IUSS
Scuola Universitaria Superiore Pavia

Scuola Universitaria Superiore IUSS Pavia

Seismic Risk Assessment for RC Buildings Including Earthquake Sequences

A Thesis Submitted in Partial Fulfilment of the Requirements
for the Degree of Doctor of Philosophy in

EARTHQUAKE ENGINEERING AND ENGINEERING SEISMOLOGY

Obtained in the framework of the Doctoral Programme in
Understanding and Managing Extremes

by

Nevena Šipčić

December, 2023

Scuola Universitaria Superiore IUSS Pavia

Seismic Risk Assessment for RC Buildings Including Earthquake Sequences

A Thesis Submitted in Partial Fulfilment of the Requirements
for the Degree of Doctor of Philosophy in

EARTHQUAKE ENGINEERING AND ENGINEERING SEISMOLOGY

Obtained in the framework of the Doctoral Programme in
Understanding and Managing Extremes

by

Nevena Šipčić
Supervisor: Professor Paolo Bazzurro – Scuola Universitaria Superiore Pavia (IUSS)

December, 2023

ABSTRACT

Seismic risk assessment models have played a pivotal role in guiding decision-making for a wide variety of purposes in recent decades. Ideally, these models would rely on empirical ground motion, damage and loss data derived from historical seismic events. However, due to the limited availability of such data, risk models resort to analytical frameworks where future earthquake scenarios, with some annual occurrence rates, are realistically simulated. Despite the progress that has been facilitated by new tools and increased data availability in recent years, several modeling decisions that are still routinely adopted require some scrutiny.

Firstly, the rate of occurrence of events in these models is derived from the historical and instrumental seismicity catalogues that are declustered, i.e. earthquake clusters (in time and space) are detected and only one event in each cluster (classified as the mainshock) is kept, while the remaining events (aftershocks, foreshocks and other triggered events) are disregarded. The process of declustering yields (or at least it should) catalogues of independent events that enable the analysts to use the relatively simple Poisson process for modeling the occurrence of future events. However, it has been shown several times that all events in the cluster, and not just the mainshock, can damage structures and humans, hence disregarding them may result in the underestimated hazard and risk estimates at the site(s) of interest.

In this thesis, we accounted for all earthquake events regardless of whether they are classified as mainshocks or not. For modeling realistic earthquake sequences, we used the Epidemic-Type-Aftershock-Sequence (ETAS) model, which is considered the state-of-the-art approach for generating realistic earthquake clusters. With this tool we investigated whether the spatial and temporal characteristics of earthquake sequences generated by crustal faults are region dependent or whether these characteristics share some commonality across regions. If the former, the modeling of seismic sequences in a new region would require a region-specific study; if the latter, on the other hand, the simulation of sequences could be done based on the statistical tools that have been derived using empirical data from regions with the same tectonic environment. With these premises, we examined the ability of ETAS to reproduce the statistical features of long-term historical seismicity in Italy in two different regions. Our findings revealed variations in the temporal and spatial distributions (namely, in the parameters' values defining the ETAS model) of the two regions that we argue are not intrinsic dissimilarities in earthquake sequence phenomena but can be attributed to the scarcity of observed sequences within the given period. Our argument was made stronger by a further investigation that revealed that the

ETAS model calibrated based on Central Italy data modeled the occurrence of earthquake sequences in Croatia and Turkey that matches the observed seismicity better than the ETAS model calibrated using the local data. These results suggest that in regions with an insufficient number of active seismic sequences during the earthquake catalogue period, adopting ETAS parameter values from a well-constrained region, such as Central Italy, could be a defensible approach.

Secondly, in addition to the potential underestimation of seismic hazard due to disregarding non-mainshock events, the conventional mainshock-only risk assessment approach implicitly assumes that the bulk of risk is caused by mainshocks. In other words, events beyond the mainshock do not contribute to causing additional structural damage and losses. Another simplification in these models is that buildings experiencing mainshocks of different clusters over time are always in an undamaged state. In essence, traditional seismic risk models suppose that buildings are repaired after each event, an operation that often does not happen, leaving already damaged structures in a more vulnerable state. This issue of decreased strength of already damaged buildings is even more important when one considers all events in a sequence, whose interarrival time is so short that repair actions are usually not feasible. In the rare instances when these models consider damage accumulation due to multiple shocks, the engineering demand parameter (EDP) employed for modeling damage estimation and derivation of the fragility curves is peak-displacement-based. This EDP, which is not monotonically increasing with multiple shocks, fails to accurately capture the progression of damage. In this study, we delved into the progression of damage in reinforced concrete (RC) columns, that fail in flexure, shear, and flexure-shear modes. Leveraging experimental data, we calibrated a modified Park and Ang damage index that is more suitable for modeling damage progression. Additionally, we scrutinized different modeling assumptions, validating them against experimental data. Our findings demonstrate that, while further validation with experimental data is warranted, the proposed EDP effectively identifies distinct damage states. As a result, it emerges as a good candidate for developing fragility and vulnerability curves within the context of clustered seismicity risk assessment.

Thirdly, another key ingredient for obtaining an accurate risk estimate is the link between seismic hazard at the site of interest and structural fragility. When fragility curves are analytically derived, a hazard-consistent selection of ground motions to be utilized to run nonlinear response history analysis on the structure(s) of interest is necessary. This selection process acts as a crucial interface between seismology and engineering, and the importance of utilizing record sets consistent with the seismic hazard at the site of interest has been highlighted clearly in numerous past studies. However, to enforce hazard-consistency in record selection one would need to have a large pool of strong ground motions at one's disposal. This is hardly ever the case. As a consequence, the analyst is usually left with the suboptimal option of augmenting the set by scaling weaker ground motions, an operation that potentially may bias the structural response estimates. Our investigation into this practice revealed that scaling ground motions does not cause statistically significant differences in structural response estimates, provided that hazard

consistency is carefully maintained in ground motion record selection, for example by using methods such as the Conditional Spectrum. Another practical issue that in real-life applications often hinders an effective hazard-consistent selection of ground motions is the excessive computational burden that follows. Even when a sufficient number of ground motions is available for extracting hazard-consistent sets, the computational demands of running numerous analyses can be substantial, especially for complex numerical models of structures. To help address this practical issue, we explored the optimal number of ground motion runs needed to derive fragility curves, aiming to balance computational efficiency with the accuracy of the resulting estimates.

Fourthly, given our objective of including all earthquakes and the deterioration of the structural integrity due to previous shocks into the risk assessment analysis, the derivation of site- and building-specific damage-state-dependent fragility curves is a must. To this end, we investigated the issue of selecting aftershock ground motions that are consistent with the mainshocks that may be experienced at the site of interest. This step is important for the analytical derivation of robust damage-state-dependent fragility curves. The importance of the aftershock record selection, however, did not receive as much attention in the literature as the mainshock one. To that end, we investigated different approaches for mainshock-aftershock record selection, comparing them with the results of the so-called "direct analysis", which can be considered as the benchmark. The direct analysis consists of simulating many years of clustered seismicity and selecting appropriate ground motions for each event characterized by a magnitude, M, and, source-to-site distance, R, regardless of whether such events are foreshocks, mainshocks or aftershocks. We showed that for the particular case that we considered, choices made in the aftershock record selection are not as critical as those related to the mainshock record selection.

This thesis emphasizes the significance of incorporating clustered seismicity into seismic risk models. The consideration of only mainshocks in risk assessment is simply not tenable anymore, as made abundantly clear by the many sequences that occurred all over the world in the past decades. This work addresses various critical issues pertaining to seismic hazard, fragility, and record selection, bridging existing gaps and laying the groundwork for future research.

ABSTRACT (IT)

Negli ultimi decenni i modelli di valutazione del rischio sismico hanno svolto un ruolo fondamentale nel guidare il processo decisionale per un'ampia varietà di scopi. Idealmente, questi modelli dovrebbero basarsi su dati empirici relativi al moto del suolo, ai danni e alle perdite derivanti da eventi sismici storici. Tuttavia, a causa della limitata disponibilità di tali dati, i modelli di rischio ricorrono a metodi analitici in cui vengono realisticamente simulati scenari futuri di terremoto con tassi di occorrenza annuali stimati. Nonostante i progressi compiuti negli ultimi anni grazie a nuovi strumenti e a una maggiore disponibilità di dati, diverse decisioni di modellazione che vengono ancora adottate di routine richiedono uno scrutinio più accurato.

In primo luogo, il tasso di occorrenza degli eventi in questi modelli è derivato dai cataloghi di sismicità storica e strumentale che vengono declusterizzati, cioè vengono individuati cluster di terremoti (nel tempo e nello spazio) e viene mantenuto solo un evento in ogni cluster (classificato come mainshock), mentre i restanti eventi (aftershock, foreshock e altri eventi innescati) vengono trascurati. Il processo di declustering produce (o almeno dovrebbe) cataloghi di eventi indipendenti che consentono agli analisti di utilizzare il processo di Poisson, relativamente semplice, per modellare il verificarsi di eventi futuri. Tuttavia, è stato più volte dimostrato che tutti gli eventi del cluster, e non solo la scossa principale, possono danneggiare strutture e persone, per cui non tenerne conto può portare a sottostimare le stime di pericolosità e di rischio nel sito (o nei siti) di interesse. In questa tesi, abbiamo considerato tutti gli eventi sismici, indipendentemente dal fatto che siano classificati come mainshocks o meno. Per modellare sequenze di terremoti realistiche, abbiamo utilizzato il modello Epidemic-Type-Aftershock-Sequence (ETAS), considerato lo stato dell'arte per la generazione di cluster di terremoti. Con questo strumento abbiamo indagato se le caratteristiche spaziali e temporali delle sequenze di terremoti generate dalle faglie crostali dipendono dalla regione o se queste caratteristiche sono comuni a tutte le regioni. Nel primo caso, la modellazione delle sequenze sismiche in una nuova regione richiederebbe uno studio specifico per la regione; nel secondo caso, invece, la simulazione delle sequenze potrebbe essere effettuata sulla base degli strumenti statistici derivati dai dati empirici di regioni con lo stesso ambiente tettonico. Con queste premesse, abbiamo esaminato la capacità di ETAS di riprodurre le caratteristiche statistiche della sismicità storica a lungo termine in Italia in due diverse regioni. I nostri risultati hanno rivelato

variazioni nelle distribuzioni temporali e spaziali (cioè nei valori dei parametri che definiscono il modello ETAS) delle due regioni che, a nostro avviso, non sono dissimmetrie intrinseche nei fenomeni di sequenza sismica, ma possono essere attribuite alla scarsità di sequenze osservate in un determinato periodo. La nostra argomentazione è stata rafforzata da un'ulteriore indagine che ha rivelato che il modello ETAS calibrato sulla base dei dati dell'Italia centrale ha modellato il verificarsi di sequenze sismiche in Croazia e Turchia che corrispondono alla sismicità osservata meglio del modello ETAS calibrato utilizzando i dati locali. Questi risultati suggeriscono che nelle regioni con un numero insufficiente di sequenze sismiche attive durante il periodo del catalogo sismico, l'adozione dei valori dei parametri ETAS da una regione ben vincolata, come l'Italia centrale, potrebbe essere un approccio difendibile.

In secondo luogo, oltre alla potenziale sottostima della pericolosità sismica dovuta al fatto che non si tiene conto degli eventi che non siano il mainshock, l'approccio convenzionale di valutazione del rischio legato alle sole scosse di mainshock presuppone implicitamente che la maggior parte del rischio sia causato soltanto da quelle scosse. In altre parole, gli eventi al di là del mainshock non contribuiscono a causare ulteriori danni strutturali e perdite. Un'altra semplificazione in questi modelli è che gli edifici che subiscono scosse di mainshock di diversa entità nel corso del tempo sono sempre in uno stato integro. In sostanza, i modelli di rischio sismico tradizionali suppongono che gli edifici vengano riparati dopo ogni evento, operazione che spesso non avviene, essendo le strutture già danneggiate in realtà in uno stato più vulnerabile. Il problema della diminuzione della resistenza degli edifici già danneggiati è ancora più importante quando si considerano tutti gli eventi di una sequenza, il cui tempo tra un evento e il successivo è di solito così breve che le azioni di riparazione non sono fattibili. Nei rari casi in cui questi modelli considerano l'accumulo di danni dovuto a scosse multiple, il parametro di domanda ingegneristica (EDP) utilizzato per la stima dei danni e la derivazione delle curve di fragilità è basato sullo spostamento di picco. Questa EDP, che non aumenta monotonicamente con gli nel caso di scosse multiple, non riesce a catturare con precisione la progressione del danno. In questo studio, abbiamo analizzato la progressione del danno nelle colonne in cemento armato (RC), che collassano a flessione, a taglio e a una combinazione di flessione e taglio. Sfruttando i dati sperimentali, abbiamo calibrato un indice di danno di Park e Ang modificato, più adatto a modellare la progressione del danno. Inoltre, abbiamo esaminato diverse ipotesi di modellazione, convalidandole con i dati sperimentali. I nostri risultati dimostrano che, sebbene sia necessaria un'ulteriore convalida con dati sperimentali, l'EDP proposto identifica efficacemente stati di danno distinti. Di conseguenza, emerge come un buon candidato per lo sviluppo di curve di fragilità e vulnerabilità nel contesto della valutazione del rischio di sismicità clusterizzata.

In terzo luogo, un altro ingrediente fondamentale per ottenere una stima accurata del rischio è il legame tra la pericolosità sismica del sito di interesse e la fragilità strutturale. Quando le curve di fragilità sono derivate analiticamente, è necessaria una selezione degli accelerogrammi da utilizzare per eseguire l'analisi della risposta non lineare sulla struttura

(o sulle strutture) di interesse che sia coerente con la pericolosità al sito. Questo processo di selezione funge da interfaccia tra sismologia e ingegneria e l'importanza di utilizzare un insieme di accelerogrammi coerenti con la pericolosità sismica del sito di interesse è stata evidenziata chiaramente da numerosi studi in letteratura. Tuttavia, per applicare la coerenza con la pericolosità nella selezione degli accelerogrammi è necessario avere a disposizione un ampio bacino di moti del suolo sufficientemente forti. Questo non è quasi mai il caso. Di conseguenza, all'analista viene solitamente lasciata l'opzione di aumentare l'insieme scalando i moti al suolo più deboli, un'operazione che potenzialmente può falsare le stime della risposta strutturale. La nostra indagine su questa pratica ha rivelato che scalare glia ccelerogrammi non causa differenze statisticamente significative nelle stime di risposta strutturale, a condizione che la loro coerenza con la pericolosità al sito sia mantenuta attentamente nella loro selezione, ad esempio utilizzando metodi come lo spettro condizionato. Un altro problema pratico che nelle applicazioni reali spesso ostacola un'efficace selezione di moti al suolo coerenti con la pericolosità è l'eccessivo carico computazionale che ne consegue per il calcolo della risposta strutturale. Anche quando è disponibile un numero sufficiente di moti al suolo per l'estrazione di insiemi coerenti con la pericolosità, la richiesta di calcolo per l'esecuzione di numerose analisi può essere sostanziale, soprattutto per modelli numerici di strutture complessi. Per risolvere questo problema pratico, abbiamo esplorato il numero ottimale di analisi necessarie per ricavare le curve di fragilità, con l'obiettivo di bilanciare l'efficienza computazionale e l'accuratezza delle stime risultanti.

In quarto luogo, dato il nostro obiettivo di includere nell'analisi di valutazione del rischio tutti i terremoti e il deterioramento dell'integrità strutturale dovuto a scosse precedenti, è indispensabile la derivazione di curve di fragilità specifiche per il sito e per l'edificio che tengano in conto lo stato iniziale di danno. A tal fine, abbiamo analizzato la questione della selezione di moti al suolo di aftershock che siano coerenti con quelli delle scosse principali che possono acacdere nel sito di interesse. Questo passaggio è importante per la derivazione analitica di robuste curve di fragilità dipendenti dallo stato di danno. L'importanza della selezione dei record di aftershock, tuttavia, non ha ricevuto in letteratura la stessa attenzione di quella dei record di mainshock. A tal fine, abbiamo studiato diversi approcci per la selezione dei record di mainshock-aftershock, confrontandoli con i risultati della cosiddetta "analisi diretta", che può essere considerata un benchmark. L'analisi diretta consiste nel simulare molti anni di sismicità che includano le sequenze e nel selezionare i moti del suolo appropriati per ogni evento caratterizzato da una magnitudo, M, e da una distanza sorgente-sito, R, indipendentemente dal fatto che tali eventi siano foreshocks, mainshocks o aftershocks. Abbiamo dimostrato che, per il caso particolare che abbiamo considerato, le scelte fatte nella selezione dei record di aftershock non sono così critiche come quelle relative alla selezione dei record di mainshock.

Questa tesi sottolinea l'importanza di incorporare la sismicità dovuta alle sequenze di terremoti nei modelli di rischio sismico. La considerazione dei soli mainshocks nella valutazione del rischio non è più sostenibile, come è emerso chiaramente dalle numerose

sequenze che si sono verificate in tutto il mondo negli ultimi decenni. Questo lavoro affronta diverse questioni critiche relative alla pericolosità sismica, alla fragilità e alla selezione degli accelerogrammi, tentando di colmare le lacune esistenti e gettando le basi per la ricerca futura.

ACKNOWLEDGEMENTS

I would like to thank Professor Paolo Bazzurro for being the best possible supervisor one can ask for. If I had not worked with Paolo during my Master's studies I doubt I would pursue a PhD, as he played a key role in developing my passion for research. Paolo, thank you for your patience and guidance throughout the years. Thank you for your support and for consistently keeping me motivated. It was my pleasure to collaborate with you and I feel so privileged to be given this opportunity.

I am grateful to Mohsen Kohrangi and it is hard to find the words to express how much. I was joking that I will have an entire chapter 'Acknowledging Mohsen' and that would probably be a fair testament to the influence he has had on this journey. Thank you, Mohsen, for your willingness to address my countless questions. You are an amazing researcher and a person. I have learned so much from our interactions.

I would like to thank Pablo who has contributed significantly to at least 50% of this thesis. We worked on many topics together and been to countless meetings and conferences together, he was always patient and supportive, especially in the last months of my thesis. He is probably the most unique character in the entire CAR college and I am grateful I can call him a friend.

I would like to acknowledge Athanasios Papadopoulos, whose prior work on the topic I continued during my PhD. His support in the initial years was invaluable to my progress. I would also like to thank Professor Warner Marzocchi, with whom I collaborated on Chapters 2 and 3, who was always eager to share his knowledge and who helped me a lot. Special appreciation goes to Enrico Spacone, Guido Camata and Massimo Petracca who hosted me in Pescara and have been incredibly helpful in the part of my thesis related to numerical modeling.

I would like to acknowledge the funding provided by the METIS project that contributed to the development of many topics in this thesis. I am thankful for the opportunities METIS provided, allowing me to meet remarkable people from all around the world. In particular, I am grateful for meeting Professor Dimitrios Vamvatsikos. Dimitrios, your sense of humor, your wit and your hospitality during my stay on the wonderful island of Hydra are memories I will forever cherish.

I would like to thank Lana, who has been an inseparable part of my academic journey, from our undergraduate studies in Montenegro over our shared Master's program in France to pursuing a PhD together in Pavia. We spent endless hours studying together and she became a true friend over the 10 years I have known her. Lana, thank you for always being patient with me, for always being there, and for giving me support constantly.

I would like to thank Deniz, who was an incredible friend to me in the period when I needed it the most. His curiosity and unique personality make him one of the most interesting people I've ever met. I would like to thank my lovely Maithree for bringing so much happiness into my life. Mai, I hope we will stay friends forever. Thanks to Rita for her infectious energy and the wonderful friendship she gave me. To Moe for making me laugh so many times. The third year of my PhD was the most enjoyable one, mostly due to the time spent with Lana, Maithree, Rita and Moe. I will always remember that period.

I want to thank Maud and Naveen for always making me feel welcome in their home, for all the traveling we did together, and for all the gatherings they organized in the Nascimbene kitchen. To Nesma, for her unique character and lovely personality. To Lucho, with whom it was so refreshing to work, I wish he was in Pavia for longer. And to so many other people in CAR and the Nascimbene community who enriched my life.

A special thanks goes to Tijana, who changed my life in the best possible way. Thank you for all the advice and guidance you have shared with me, I am incredibly grateful for meeting you.

I want to thank my amazing friends back in Montenegro. To my best friend, Dušanka, who will always be my person. To Miloš, for being the best possible friend I can ask for, who will always have a room (or garage) in my house for him, I am officially promising that. To Vladan, who has been an incredibly big support to me, who always believed in me more than I do. To Đuza and Aleksandra, the favourite couple of mine, for their love and understanding.

To Ivan, whose presence in my life I appreciate more than he can imagine, thank you for being like an older brother to me. To my lovely nephews Arsenije and Fedor for bringing so much joy to my life. To my parents for making me feel safe, even in my distance from home, and for their unconditional love.

I want to thank Nikola who is my family now. Thank you, N, for making me the happiest I have ever been.

Finally, my deepest appreciation goes to my sisters, Tanja and Anđela, for making me the person I am today. You are the two most important people in my life, and this thesis is dedicated to you. I hope I have made you proud.

To my sisters

TABLE OF CONTENTS

LIST OF FIGURES

LIST OF TABLES

1. INTRODUCTION

1.1 MOTIVATION

In the conventional approach to seismic hazard and risk assessment, the estimation of the probability that ground motion will exceed various intensity levels at a specific site over a given period is typically conducted through classical Probabilistic Seismic Hazard Analysis (PSHA). In PSHA, all dependent seismic events, such as aftershocks, foreshocks, and triggered events, are systematically disregarded. In simpler terms, to predict the rate, magnitude, and location of future seismic events, we rely on earthquake catalogues that have been "declustered" to include only the independent mainshock events. As an illustrative example, if one were to decluster earthquake catalogues encompassing seismic sequences occurring in Italy in 2009, 2012, and 2016, they would omit 289, 294, and 1298 dependent events, respectively, with moment magnitudes ≥ 3, as well as more importantly seven, six, and nine events with moment magnitudes ≥ 5.

The motivation behind the exclusion of dependent events from earthquake catalogues is rooted in mathematical simplicity. It has been demonstrated that when declustering is performed skillfully, the occurrence of the remaining events in the catalogue conforms well to the tenets of the Poissonian stochastic process. A Poissonian process implies that (i) event occurrences are independent, such that the number of events in any interval of time is independent of the number of events in any other (non-overlapping) interval of time within a short time interval; (ii) the probability of two or more events occurring in a short interval of time is negligible; and (iii) the process remains stationary over time (with a constant average rate of occurrence in each time interval). Under these assumptions, the time T to the next event can be described as an exponentially distributed random variable. This approach to describing earthquake occurrence is often referred to as "memory-less", as it lacks any recollection of the timing, size, or location of previous seismic events. While acknowledging the inconsistency of the Poissonian assumption with the elastic rebound theory and the clustering of aftershocks, which are temporally and spatially correlated (and thus, dependent) Cornell [1968] stated that "the assumption that the occurrences of earthquakes follow the behavior of the Poisson process model can be removed only at a greater penalty". By greater penalty here it is meant the adoption of more complicated renewal processes to describe earthquake recurrence. Furthermore, Cornell and Winterstein [1988] studied several recurrence models with temporal and magnitude dependence showing that the Poissonian process can well represent the occurrence of earthquakes in cases when the hazard is not controlled by a single source, when the time since the last significant event is not greater than the average time between events and when the fault does not have regular, "characteristic time" behavior. In other words, the

Poissonian process is adequate when using area sources of homogeneous seismicity to compute the site hazard.

Another reason for the adoption of this simplistic approach is that the mainshock event (typically identified with the conventional declustering methods as the event with the largest magnitude in the cluster) was assumed to serve, to some extent, as a representative indicator of the overall damage potential of the entire sequence. In the design world this translates to the notion that if the building is designed to withstand the ground motion generated by the mainshock, it will resist the presumed weaker ground motions associated with the lower-magnitude events within the sequence. And, if it does not, the evacuated building would collapse in aftershocks without loss of human lives. Furthermore, the spatial bias that can arise when non-declustered catalogues are employed, which may lead to an overestimation of seismic rates in regions with numerous historical sequences and an underestimation in regions where significant clusters have not been observed in the close past [Llenos and Michael 2020; Marzocchi and Taroni 2014] is eliminated when we use declustering. Finally, the use of the mainshock-only approach in assessing seismic risk in the insurance industry is often defended by CAT modeling practitioners who claim that risk models are calibrated using insurance claims and damage data collected at the end of seismic sequences, thus encompassing the damage (or loss) caused by all events within the sequence.

We argue that the logic behind the mainshock-only seismicity approach is, at best, weak for several compelling reasons. Firstly, one of the pioneering declustering methods was developed by Gardner and Knopoff [1974], with the title "Is the Sequence of Earthquakes in California, with Aftershocks Removed, Poissonian?". Their straightforward abstract answered this question with a "Yes." To this day, this declustering method is employed in several national hazard models. However, it is critical to recognize that this method's calibration was exclusively based on the Southern California sequence, without any assurance of its applicability to other regions worldwide. Moreover, it is rarely verified whether the events left in the declustered catalogues indeed follow a Poissonian distribution. Since the publication of the Gardner and Knopoff [1974] paper, numerous alternative declustering methods have been proposed, yielding catalogues with varying numbers of events. This variability underscores the inherent challenges in accurately classifying seismic events belonging to the same cluster. Additionally, retaining the largest magnitude event in the cluster as the mainshock is overly simplistic, as the largest magnitude does not necessarily mean the largest ground-motion intensity at any given site since events within the sequence may rupture different parts of a fault or, even different faults altogether. Finally, in practice, risk models are only partially calibrated using damage or claims data. In many parts of the world, such data may not be readily available, or no recent significant earthquakes have occurred to provide relevant data. Even when data are accessible, they may come from sequences with mainshocks followed either by an intense activity or by hardly any activity. During the calibration of building vulnerability functions (i.e., the relationships linking ground-motion intensity to repair costs), which form the core of earthquake risk models, no distinction is typically made between damage caused by a

single event versus damage caused by a sequence of events. If damage data are available, they are often utilized without further scrutiny. Secondly, in most cases, risk models are compelled to rely on analytical studies to derive building vulnerability functions, particularly for relatively recent building classes that have not been tested by severe earthquakes. Given the absence of empirical data and the fact that these analytical studies often utilize only mainshock ground motions, the resulting vulnerability functions are developed without consideration of damage accumulation resulting from multiple shocks. Even if the aftershock losses were perfectly integrated into conventional vulnerability curves, which is not the case, they would be applied to estimate losses for the next event, which may or may not be followed by an intense sequence. It is abundantly clear that the current practice, strictly speaking, is far from being rigorous and an improvement is needed. This has been demonstrated on several occasions in history when significant seismic sequences occurred, revealing that traditional approaches are inherently unconservative and may not fully capture the complexity of the process.

For instance, in September 2010, Canterbury, New Zealand, experienced a magnitude 7.1 earthquake that caused substantial damage but fortunately no fatalities. However, this event was followed by a significant aftershock sequence, most notably the February 2011 earthquake with a moment magnitude of 6.2. Despite its lower magnitude, this aftershock resulted in additional damage, disruption of services, and the loss of 182 lives [EEFIT 2011]. In March 2011, a large magnitude 9 earthquake struck Japan, followed by numerous aftershocks. Among these, five had magnitudes greater than 7, and 82 exceeded a magnitude of 6 within the first three months after the main event. These aftershocks extended the area where damage was observed to locations that were not severely affected by the initial mainshock, illustrating the consequences of seismic sequences [Kazama and Noda 2012]. In 2016, Central Italy experienced a strong earthquake sequence. The first event, with a magnitude of 6, occurred close to Amatrice and caused some damage. This damage was further compounded by subsequent shocks. After the first event in August, only the eastern part of Amatrice was damaged. However, after the October events, nearly the entire village was destroyed. The progression of structural damage during the subsequent events revealed that, after the first event, 72% of buildings were not damaged, while only 4% collapsed or were near collapse. Following the entire sequence, no building remained without damage, and 65% collapsed or were near collapse [Sextos et al. 2018a]. Similar observations have been made in other seismic events, such as the 1985 Michoacan earthquake in Mexico [McNally et al. 1986], the Taiwan earthquake [Shin 2000], the Chilean earthquake [Chung et al. 2011], and the earthquake sequence in Croatia in 2020 [Atalić et al. 2021]. These examples illustrate that the damage and impact of seismic events can be substantially amplified when considering the entire sequence, as opposed to focusing solely on the mainshock.

Motivated by these examples, several researchers started investigating seismic sequences, trying to integrate them into seismic hazard and risk assessments. Initial efforts predominantly focused on the short-term hazard given the critical nature of risk underestimation in the immediate aftermath of an event, i.e. in the post-mainshock

conditions. The objective was to facilitate decision-making in emergency planning following an event (e.g., re-occupancy decisions) and to aid communities in preparing for potentially devastating future earthquakes during periods of low seismic activity. Gallagher et al. [1999] proposed a simplified approach, considering the mainshock magnitude and the number of days elapsed since the mainshock, to provide guidelines for assessing the safety of damaged buildings following an earthquake and determining whether they could be re-occupied. Yeo and Cornell [2009] expanded on this concept by introducing a methodology that accounted for increased hazard using a procedure referred to as Aftershock Probabilistic Seismic Hazard Analysis (APSHA), where the occurrence of subsequent events is modeled conditional on the occurrence of the mainshock via the Modified Omori law [Omori 1894; Utsu 1961]. In addition to the elevated hazard they also considered the damage state of the building after the mainshock, based on the residual capacity of the damaged building, following the approach of Bazzurro et al. [2004]. This work derived aftershock collapse fragility curves through nonlinear static pushover analysis on both undamaged and damaged structures, assessing the reduction in capacity by pushing the damaged structure to collapse. In recent years, more detailed models have emerged, aiming to better understand the damage patterns that can affect the reduction in the collapse capacity. For instance, Raghunandan et al. [2015] calculated the increase in the vulnerability of damaged code-conforming reinforced concrete (RC) frames subjected to ground motion sequences and explored various system and component damage indicators to identify the most effective proxies for assessing structural safety reduction. They claimed that a significant reduction in safety is observed only when the mainshock damage is substantial, and that the maximum interstory drift is the best indicator of the capacity reduction. Shokrabadi and Burton [2018] demonstrated that the increase in seismic hazard, estimated using APSHA, combined with the reduction in the capacity of RC frame buildings, imposes significant seismic risk on the structures in post-mainshock conditions. Zhang et al. [2018] extended this methodology by proposing an approach to assess the reduction in a building's capacity using a machine learning framework, which is subsequently used as a criterion for determining the safety of occupancy. The reduction in capacity is evaluated based on the damage response pattern, encompassing peak global and local responses. More recently, Galvis et al. [2023] introduced a simulation-based methodology to identify damage indicators and safety thresholds for determining the suitability for occupancy of a damaged structure. This approach considered ductile RC frame buildings, incorporating factors such as drift, ground motion intensity, the fraction of damaged components, and floor damage indexes as damage indicators. Their findings highlighted that floor damage indices, derived from beam and column hinge damage, were the most efficient predictors of collapse capacity for damaged structures. These studies underscore the critical need to establish a link between the damage state of a structure and post-event hazard analysis to assess the risk levels associated with building re-occupancy.

Moving beyond post-mainshock conditions, Boyd [2012] and Iervolino et al. [2014] extended the concept of aftershock probabilistic seismic hazard analysis (APSHA) initially developed by Yeo and Cornell [2009]. They identified independent event clusters and combined probabilistic seismic hazard analysis (PSHA) with APSHA to calculate the annual

exceedance rate of ground motion intensity levels due to all events in clusters, rather than solely to mainshocks. Along a similar line but using a different approach, Marzocchi and Taroni [2014] proposed a simplified method within classical PSHA that corrected for the negative bias caused by catalogue declustering. More recently, Papadopoulos et al. [2021]) proposed a simulation-based framework where the Epidemic-Type-Aftershocks-Sequence (ETAS) model [Ogata 1988, 1998], which is arguably the state of the art, is used to simulate realistic seismic sequences and estimate the hazard accounting for all events in a sequence. In the framework of seismic risk assessment accounting for clustered seismicity, several probabilistic frameworks have been proposed, explicitly considering damage accumulation and earthquake clustering [Iervolino et al. 2016; Jalayer and Ebrahimian 2016; Shokrabadi and Burton 2018]. These studies developed damage-dependent curves by subjecting numerical models of buildings to mainshock-aftershock ground motions. The impact of damage accumulation was studied both in single-degree-of-freedom (SDOF) systems [Goda 2012; Goda and Taylor 2012; Hatzigeorgiou and Beskos 2009; Zhai et al. 2014] and multi-degree-of-freedom (MDOF) systems [Hatzigeorgiou and Liolios 2010; Raghunandan et al. 2015; Ruiz-García and Negrete-Manriquez 2011]. These studies primarily employed non-cumulative, displacement-based Engineering Demand Parameters (EDPs) to assess the influence of seismic sequences on structural response. This choice was dictated mainly by the convenience that lies in its easy documentation during experiments and numerical analysis. Experimental studies showed that peak noncumulative indices can effectively represent damage in well-detailed RC members that are not supposed to experience shear failure or bond slip [Cosenza and Manfredi 2000] and their use may be suitable in cases when structures are subjected to impulse-type or short-duration earthquakes. However, recent research has highlighted the limitations of such EDPs [Baraschino et al. 2023; Ge et al. 2022; Pedone et al. 2023] and underscored the advantages of adopting energy-based EDPs in state-dependent fragility analysis.

To analytically derive damage-dependent fragility curves, nonlinear response history analyses have to be performed by subjecting the structure to both the mainshock and aftershock ground motions in a back-to-back fashion. Due to the scarcity of high-intensity mainshock-aftershock ground motions recorded at the same station, several authors decided to use mainshock ground motions to represent the ground shaking induced by both the mainshock and the aftershock events [Amadio et al. 2003; Luco et al. 2004; Raghunandan et al. 2015; Wen et al. 2017] or, to make these scenarios more realistic, they would randomly pair mainshock ground motions and scale down the aftershock ground motion [Aljawhari et al. 2020; Jeon et al. 2015; Ryu et al. 2011]. While the importance of hazard consistency in selecting ground motions for response analysis has been recognized and studied by several researchers in the mainshock-only framework [Bradley, 2010; Lin et al., 2013; Kohrangi et al., 2017], there is comparatively less research done on this topic concerning seismic sequences. Nonetheless, given the correlation between the mainshock and aftershock causal parameters (e.g., magnitude and distance), as well as the "similarity" in the spectral shape of the mainshock and aftershock ground motions at the same station, it is reasonable to assume that site dependency is also pertinent for clustered seismicity. To

the authors' knowledge, there are only a few studies on this topic [Ghotbi and Taciroglu 2020; Papadopoulos et al. 2020; Zhu et al. 2017].

1.2 OBJECTIVES AND SCOPE

Within this thesis, our primary aim is to comprehensively explore the impact of seismic sequences on seismic risk, encompassing both hazard and vulnerability aspects. Furthermore, we aim to address knowledge gaps in the field. We will focus on the three separate yet related aspects of the earthquake engineering practice and probabilistic earthquake risk assessment.

- Our initial objective is to estimate the annual hazard, taking into account all events within the sequence, rather than solely focusing on the mainshock. To achieve this, we will generate memory-full stochastic catalogues using the ETAS model. We will specifically explore two cases: "unconditional case" which will be employed to quantify the average increase in seismic hazard due to seismic sequences, and "conditional case", which will be utilized to assess the increase in hazard at a specific point in time. The former case can be useful when one is developing seismic hazard maps for applications that cannot absorb the variability of the hazard with ease, such as the definition of design ground motions. Both cases instead hold particular relevance for other stakeholders, such as insurance companies that, for example, need to establish fair earthquake policy premiums and adequate financial reserves to ensure solvency. We will further calibrate ETAS parameters for two different regions in Italy and investigate the variability of ETAS parameter estimates. We will compare the hazard estimates obtained from the ETAS model with those generated through alternative models. Specifically, for the two sites in Central Italy, we will contrast the ETAS model's results with those derived from the mainshock-only approach, i.e., the Poisson model, and from the Omori model which is often used as a simpler alternative to ETAS to model seismic sequences. Finally, we will expand our research to other regions such as Croatia and Turkey, where significant seismic sequences have been recently observed, to test the applicability of the proposed set of parameters.
- In the second part of the thesis, we will delve into the modeling of the progression of damage in RC columns. Here, our primary focus will be on the calibration of a newly proposed energy-based damage index. We will define the onset of distinct damage states using gathered experimental data and existing research findings. Our objective in this part of the research is to quantitatively define the framework for the development of damage-dependent fragility and vulnerability curves in the realm of clustered seismicity risk assessment.
- We will then focus on addressing some of the practical issues that plague the implementation of hazard-consistent mainshock record selection for the purpose of fragility curve development. Given that an ample database of sufficiently strong ground motions is not available and it likely will not be for decades, analysts have resorted to scaling the amplitudes of weaker motions. In this work, we took a closer look at whether this practice may create ensembles of strong ground

motions that could potentially cause bias in structural response estimates. To address this, we employed an ensemble of structures, modeled as SDOF systems with different material models, located in Central Italy, and we selected hazard-consistent sets of records using the Conditional Spectrum approach [CS, Jayaram et al. 2011] and different limits for scaling factors (low and high scaling factors). Additionally, we explored the optimal number of ground motion runs required within the CS-based Multiple Stripe Analisys framework [MSA, Jalayer 2003] in order to obtain reliable fragility curve estimates with a level of computational burden affordable in real-life applications. We considered and assessed three distinct approaches: back-to-back Incremental Dynamic Analysis (B2B-IDA) [Vamvatsikos and Cornell 2002], the mainshock-consistent aftershock record selection scheme developed by Papadopoulos et al. [2020], and a combination of the two. These three methods were used to develop damage-dependent fragility curves for different SDOF systems using different Engineering Demand Parameters (EDPs) and conditioning ground motion Intensity Measures (IMs). We then computed with the derived fragility curves, the annual probabilities of exceeding different damage states for these structures, modeling the seismic hazard with the ETAS model. A comparative analysis is then conducted against the results of the so-called "direct analysis", which is considered the benchmark in this context. By direct analysis, we mean simulating many years of seismicity and selecting appropriate ground motions for each event characterized by a magnitude, M, and, source-to-site distance, R.

The sections within this thesis are written independently, as they have been (or will be shortly) published as separate journal articles. Therefore, the repetition of certain contents in different sections of the thesis is unavoidable.

2.THE EFFECT OF SEISMIC SEQUENCES IN PROBABILISTIC SEISMIC HAZARD ANALYSIS

2.1 INTRODUCTION

Traditionally, seismic hazard and risk assessment studies consider Poissonian occurrences of mainshocks and disregard spatially and temporally dependent events (foreshocks and aftershocks), which are removed from earthquake catalogues before computing historical earthquake occurrence rates. The justification for this simplification is that the mainshock event (which is usually characterized as the event with the largest magnitude in a cluster) could, to some extent, represent the damage potential of the entire sequence. In the design world, this translates into implying that if the building is designed to withstand the ground motion shaking of the mainshock, it will resist the assumed weaker ground motions of the other lower magnitude events in the sequence. However, several studies showed that this is an overly simplistic notion as the different events in a sequence may have different epicentral areas, and the largest magnitude event does not imply the largest ground motion intensity at any site. It is undeniable that earthquake sequences pose an additional risk to society because of the increment in financial losses due to increased direct damage to the built environment and to longer business interruption that follows. The underestimation of seismic risk by the traditional approach (here, by risk we refer to the ground-up losses to repair physical damage and not to insurance losses) is expected to be especially important in the period after the occurrence of a significant event due to the elevated short-term hazard (post-mainshock conditions). This issue was extensively studied in past decades with the primary objectives of both supporting the decision-making process associated with emergency planning in the aftermath of an event, and of helping communities prepare in periods of low seismicity for potentially destructive future earthquakes. These studies modeled the occurrence of subsequent events conditional on the occurrence of mainshock usually via the Modified Omori law [Omori 1894; Utsu 1961] (e.g., [Gee et al. 2021; Reasenberg and Jones 1989; Wiemer 2000; Yeo and Cornell 2009]) or, more rarely, via the ETAS model [Ogata 1988, 1998], such as in the studies of Field and Milner [2018] or Taroni et al. [2018].

Going beyond the post-mainshock conditions, Boyd [2012] and Iervolino et al. [2014] extended the aftershock probabilistic hazard analysis (APSHA) developed by Yeo and Cornell [2009]. They identified independent clusters and combined PSHA and APSHA to calculate the annual exceedance rate of a ground motion intensity level at a specific site due to all the events in clusters (SPSHA) rather than just to all the mainshocks. Along the same line, but using a different approach, Marzocchi and Taroni [2014] proposed a simple method based on the classical PSHA that introduced a correction for the negative bias (i.e., underestimation) caused by catalogue declustering. For each cell in the domain, they suggested a correction to the total seismicity rate and the magnitude-frequency distribution to make them equal to those computed from the whole (non-declustered) catalogue.

However, our objective is neither to perform the short-term forecast (i.e., to find the probabilities of exceeding ground motion level conditional on the occurrence of the mainshock) nor to provide the seismic hazard estimates during the sequence. Similar to Papadopoulos et al. [2021], our goal is to include all the events in a sequence and not only the mainshock into the estimation of annual hazard and, later, risk to specific structures and portfolios of them. We will do so by generating sets of memory-full stochastic catalogues using as initial conditions the seismicity occurred until the time of the analysis. For this task, we will utilize the ETAS model, which is arguably state-of-the-art for modeling seismic sequences, both temporally and spatially.

Including all events in a sequence to calculate seismic rates is relevant, for example, to the insurance industry, where it is well known that traditional seismic risk assessment studies based on declustered catalogues underestimate the risk by neglecting sequences. To cover for such an unknown bias and other unknowns, insurance companies traditionally add significant loadings to the pure premium (i.e., the one based on the average annual loss) of earthquake insurance policies. Given that this bias is not well estimated, for business reasons this practice necessarily leads to an overcorrection of earthquake insurance premiums offered to the public. It is worthwhile noting, however, that exceptions to this practice exist as some risk models make an attempt to somewhat consider seismic sequences. For instance, Shome and Williams [2014] included the occurrence of aftershocks while estimating the change in seismic risk in Japan, after the Tohoku earthquake, by using the rates calculated with the Reasenberg and Jones [1989] methodology and averaging them over a 5-year long period.

As for the case of earthquake-resistant design, arguments in favor of using simplified approaches based on mainshock-only seismicity for risk assessment are not lacking. For example, the use of the mainshock-only approach in assessing seismic risk in the insurance industry is often supported by the logic that risk models are calibrated with the total damage (or claims) data collected at the end of sequences that include both damage (or loss) caused by mainshocks and damage (or loss) caused by aftershocks. This reasoning holds some truth when the time elapsed between the mainshock and the following events is short, and building inspection between events could not be done. This logic, however, is weak at best, for at least two reasons. First, in reality, risk models are only partially calibrated using damage or claims data. In many parts of the world, these data are simply not available, or

no recent strong earthquakes have occurred in recent time, and the only data available may be for old events that affected a different building stock. Even when available, damage or loss data may come from sequences with mainshocks followed either by an intense activity or by hardly any activity. No difference between damage caused by one event or by a collection of events is considered during the calibration of the building vulnerability functions (i.e., relationships that link ground motion intensity with repair cost) that are at the core of such earthquake risk models. The damage/loss/claims data, if available, are just used without further scrutiny. Second, in most cases, risk models are forced to use analytical studies to derive building vulnerability functions, at least for the relatively recent building classes never tested by any severe earthquake. For these building classes, given the lack of empirical data and given that such analytical studies use only mainshock ground motions, the vulnerability functions are derived with a complete disregard of damage accumulation caused by multiple shocks. Even if the aftershock losses were perfectly embedded in the conventional vulnerability curves, which they are not, they would be applied to estimate the losses for the next event that may, or may not, be followed by an intense sequence. Therefore, it is abundantly clear that the current practice, strictly speaking, is far from being rigorous and should be improved. In this paper, however, the focus is on seismic hazard rather than risk and, hence, these important considerations related to risk assessment in presence of clustered seismicity will be discussed in more detail in a future article.

To better understand the impact of sequences on seismic hazard estimates (which, in turn, affect risk estimates), we consider two cases. The first is the "unconditional case" (or "random year"), where we sample multiple 1-year long stochastic catalogues, each one starting with different initial conditions. This exercise is meant to identify the average long-term increase in seismic hazard estimates due to sequences. This information could be helpful for applications that need stable hazard estimates that do not change whenever a significant event occurs (e.g., hazard maps informing building codes). The second is the "conditional case," which again considers multiple 1-year long stochastic catalogues, but in this case, each one starts with the same initial conditions. This exercise is meant instead to identify the average long-term increase in seismic hazard estimates due to sequences at a particular point in time, information that is useful for applications such as pricing estimation for insurance policies to be issued in the period covered by the computation length (i.e., one year here).

Therefore, in the former case, the estimate of a hazard rate increase could have been computed by averaging the hazard estimates for simulated catalogues of any time length. We chose one year here because usually hazard rates are presented for that time unit. In the latter case, however, we are interested in estimating the hazard at a specific time (perhaps after or during an intense sequence), conditional on the past seismicity in previous years. In this case, as alluded to above, the selection of the time length of the stochastic catalogues is clearly driven by the application. The time length of the simulated catalogues is the consequence of a practical decision rather than a conceptual one. Taking a one-year-long period is motivated by many real-world applications, particularly in the insurance industry,

where earthquake risk estimates over 1-year long horizon starting at the time of the policy issuance are required since earthquake policies are annual contracts. However, suppose an application calls for assessing the hazard increase over a longer period starting from the time of computation (e.g., 3-year-long cat bonds). In that case, the proposed methodology can be replicated in an identical manner by simply lengthening the time of the simulated catalogues, as needed.

In the following sections, we first describe the ETAS model vis-à-vis the simpler Omori law approach for modeling earthquake sequences and compare both with the Poissonian approach that, taken at face value, disregards them. Then we investigate the variability of the estimates of the ETAS parameters in different regions of Italy and show that the ETAS model is capable of modeling realistic sequences with several tests. We then define the Poisson and Omori model, followed by the discussion about the effects of declustering on the Poisson model and the consistency of the Omori model with the available data. Finally, we estimate the hazard curves at the two selected sites with the three described methods, and we summarize our findings.

2.2 Initial considerations about ETAS, Omori and Poisson models

Using a complex approach, such as ETAS, to model seismic sequences can be considered impractical and this consideration motivated us to investigate two alternative, simpler models. The final considerations on the appropriateness of these three modeling choices that will follow are based on the comparison of seismic hazard curves for two sites in Central Italy computed in three ways: a) using the ETAS model; b) the classical mainshock-only Poissonian model, and c) an approach that combines mainshock Poissonian modeling and aftershock modeling via modified Omori law (e.g, Iervolino et al. [2014]). We compare the hazard curves for the conditional and unconditional cases mentioned earlier in all three modeling choices. To estimate the seismicity rate using the b and c models, it is necessary to agree on the (arbitrary) definition of what constitutes a mainshock. This definition guides the selection of the declustering method to adopt and, given the method adopted, of the specific values of the temporal and spatial parameters utilized for sifting out the foreshocks and aftershocks events in a cluster. Moreover, the parameter values of the modified Omori law to be used have to be coherent with the declustering technique adopted. It is well known that the selection of the declustering technique and its details can significantly affect the characteristics of the processed catalogue and, therefore, the ensuing historical seismicity rates and, from there, the hazard results [Marzocchi and Taroni 2014; Mizrahi et al. 2021; Teng and Baker 2019]. Hence, as a part of this exercise, we examine some of the declustering methods available in the literature, namely Gardner and Knopoff [1974], Reasenberg [1985] and Zaliapin et al. [2008].

However, for the correct utilization of the ETAS model, some considerations are in order. The ETAS model is calibrated based on the earthquake data available in the region of interest. Intuitively, we may assume that some ETAS parameters' values depend on the seismotectonic characteristics of the specific region. Several studies investigated the variability of the values of the ETAS parameters across different tectonic zones. For

instance, Chu et al. [2011] explored the variability and fit of ETAS parameter values across different tectonic zones globally and identified significant differences. Similarly, Page et al. [2016] showed that aftershock productivity and decay rate vary with the tectonic regime. Utsu and Ogata [1995] found high variability of ETAS temporal parameter values and speculated that this variation might be related to the tectonic conditions of the region (such as structural heterogeneity, stress, or temperature). Nandan et al. [2017] applied ETAS in different regions of California and showed a significant spatial variation of the parameters' values. Conversely, Zhang et al. [2020] investigated the global variability of ETAS parameters' values in subduction zones that experienced megathrust earthquakes with a magnitude larger than M7.5 and showed no apparent systematic regional dependency. Stallone and Marzocchi [2019] also found no reason to assume a dissimilarity in the properties (in terms of productivity, duration, and spatial distribution) of clusters occurring in different active crustal regions.

It remains unclear whether it is justified to use the same set of ETAS parameters' values in a large area, such as a continent or a country. Ideally, one could distinctly consider regions with different seismotectonic characteristics and estimate parameters' values specific for each region. However, there are often practical complications in doing so. For example, scarcity of data sometimes poses difficulties in obtaining robust estimates in each region. Even when enough data are available, a somewhat complicated mathematical framework is required to properly treat the parameter variation around the boundaries of the two regions, given that events in one region could trigger events in the adjacent one and vice-versa. In order to address these practical issues, we explore the variability of the estimates of ETAS parameters in two different regions in Italy fitted using a common instrumental catalogue.

2.3 BUILDING THE ETAS MODEL

To familiarize the reader with the ETAS model, we first review its fundamentals defined by Ogata [1988, 1998]. The ETAS model is one of the space-time point Hawkes processes formulated as the combination of background seismicity and triggered seismicity. Every background (or parent) event can trigger offspring events potentially capable of producing offspring of their own. Thus, the overall rate of events (sometimes called conditional intensity) with magnitude m at a certain point in time and space, conditional upon the history of prior earthquakes, H_t, can be characterized by the general form given with Equation (2.1) [Seif et al. 2017; Zhuang et al. 2004]:

$$\lambda(t,x,y,m \mid H_t) = \mu(x,y) + \sum_{j:t_j<t}^{n} g(t-t_j, x-x_j, m_j) \tag{2.1}$$

The index j refers to all past earthquakes. For simplicity and computational benefit, we assume that the background rate is stationary in time, i.e., $\mu(x,y,t)=\mu(x,y)$, even though this assumption may not always be valid [Lombardi and Marzocchi 2007]. A triggering function $g(t-t_j,x-x_j,y-y_j,m_j)$ which comprises a productivity function, a temporal distribution and a spatial distribution, gives the rate of triggered events. The function g has the following form [Ogata 1998]:

$$g(t-t_j, x-x_j, y-y_j, m_j) = k(m_j) \cdot v(t-t_j) \cdot f(x-x_j; y-y_j, m_j) \quad (2.2)$$

The productivity term $k(m_j)=Ae^{\alpha(mj-mc)}$ represents the mean number of events directly triggered by an earthquake of a magnitude m_j, where m_c is the minimum magnitude considered. The temporal decay of triggered earthquakes, namely $v(t-t_j)=(p-1)\, c^{p-1}(t-t_j+c)^{-p}$, is modeled with the so-called Modified Omori law [Omori 1894; Utsu 1961]. While productivity and temporal distribution adopted by researchers are typically the same, spatial distribution $f(x-x_j,y-y_j,m_j)$ can be found in several formats. The one adopted in our study showed good performance in Papadopoulos et al. [2021] and Zhuang et al. [2004]:

$$f(x-x_j; y-y_j, m_j) = \frac{q-1}{\pi \cdot d \cdot e^{\gamma(m_j-m_c)}}\left[1+\frac{x^2+y^2}{d \cdot e^{\gamma(m_j-m_c)}}\right]^{-q} \quad (2.3)$$

It is worthy of note that the adopted spatial distribution uses a simple isotropic kernel. This means that the spatial distribution has no knowledge of the location of existing faults in the region and it does not eliminate the possibility that an aftershock is triggered exactly at the same location of the mainshock, which is a rather unrealistic case. Ogata and Zhuang [2006] corrected this deficiency by using an anisotropic kernel instead but showed that the model's performance did not change significantly. More recently, Fitzenz and Langenbruch [2021] showed that using magnitude-dependent kernel weights can improve earthquake forecast performance (seen using the log-likelihood score) for large events. However, given its heavy computational burden, these enhancements are not considered here.

The magnitude distribution $s(m)$ of both background and triggered events, which is assumed to be independent of the other terms, follows the exponential Gutenberg-Richter (GR) law, truncated at maximum magnitude m_{max}. Other models for $s(m)$ can also be used (e.g., tapered Gutenberg-Richter).

$$s(m) = \frac{\beta \cdot e^{-\beta(m-m_c)}}{1-e^{-\beta(m_{max}-m_c)}} \quad (2.4)$$

The constant β is equal to $\ln(10)b$, where b is estimated independently from other parameters using the maximum likelihood method [Aki 1965] and accounting for the magnitude binning correction [Utsu 1966]. One should keep in mind that the method of Aki [1965] was developed for non-truncated magnitude distribution and, hence, the b-value estimate in Equation (2.4) might be biased. Marzocchi et al. [2020] showed, however, that the bias is not significant when M_{max}-$M_{min}\geq 3$.

As in all empirically-based exercises, to obtain reliable estimates of the ETAS parameters' values (A, α, p, c, d, γ, and q), it is necessary to have a complete and homogenous catalogue with a "sufficient" amount of data. The catalogue should: a) extend beyond the considered region to prevent estimating an artificially lower density near the geographical boundaries by excluding offspring inside the border generated by earthquakes in the outer region [Wang et al. 2010]; and b) extend beyond a temporal window before the starting time T_0 of the investigation period to include events within the investigation period that may be

triggered by earthquakes that occurred before T_0. For these reasons, we extend the studied region for 75 km outside of the borders and include two years of seismicity as initial conditions before the beginning of the investigation period, T_0.

In our application, the estimates of the values of the ETAS parameters are found by maximizing the log-likelihood function expressed with:

$$\log L(\boldsymbol{\theta}) = \sum_{j=1}^{n} \log[\lambda(t_j, x_j, y_j) \mid H_t] - \int_0^{S,T} \lambda(t, x, y \mid H_t) dtds \tag{2.5}$$

in which S and T are the spatial and temporal windows, respectively, while *n* represents the number of events in them [Seif et al. 2017]. The background seismicity rate *μ(x,y)* can be written as $v \cdot u(x,y)$, where *v* is the total rate and *u(x,y)* is the spatial distribution of the background events. To simplify the maximization procedure, the spatial distribution, *u(x,y)*, of the background seismicity rate is computed separately from all the other parameters using first the mainshock-only catalogue (obtained using the original Gardner and Knopoff [1974] declustering algorithm) and then smoothing the mainshock rate using the Gaussian kernel-based smoothing approach proposed by Frankel [1995] with a correlation distance of 20 km.

For an interested reader, the effect of different background models and different correlation distances can be found in Papadopoulos et al. [2021]. The value of *v* is estimated together with the rest of the ETAS parameters.

The value of the productivity parameter, α, controls the triggering capability of events with respect to the magnitude. A high value of α implies that a higher triggering capability is given to the events with higher magnitudes, while low value gives more capability to lower-magnitude events. Several studies showed that the value of α is found to be lower than $\beta = \ln(10)b$ [Chu et al. 2011; Console et al. 2003; Ogata and Zhuang 2006]. However, other researchers claimed that this trend is observed due to the unrealistic assumptions of the model (such as isotropic kernel for aftershock distribution) and that, in reality, $\alpha \cong \beta$, an alternative that agrees with the Baths law [Felzer et al. 2003] and stress triggering models [Hainzl et al. 2010]. Furthermore, [Hainzl et al. 2013] found that when the aftershock incompleteness and time variance of the background rate are accounted for, results imply that $\alpha \cong \beta$. One should keep in mind that setting α=β can lead to the values of branching ratio, representing the proportion of the triggered events amongst all events, above one [Zhuang and Ogata 2006] indicating the critical process, except in the cases where we impose a maximum magnitude.

While the debate about the appropriate α value remains open in the scientific community, we adopt here α=β and consider a vector of unknown parameters as:

$$\boldsymbol{\theta} = \{v, A, c, p, d, q, \gamma\} \tag{2.6}$$

A more comprehensive overview of the ETAS model can be found in Ogata and Zhuang [2006].

2.4 SEISMICITY DATA

Several studies showed that the estimates of the ETAS parameters are highly susceptible to the assumptions made, such as magnitude cutoff, magnitude type, time dependency of the background rate, anisotropic aftershock triggering, and aftershock incompleteness [Seif et al. 2017; Zhuang et al. 2017]. Keeping the above in mind, it is evident that it is not straightforward to compare parameters' values from different studies that use different catalogues (with varying quality, magnitude of completeness, and spatial and temporal windows). In addition, the underlying statistical correlation of the parameters is complicating the comparison even further. Detecting the source of the potential differences between parameters' values can become very challenging, as different sets of values can lead to very close values of the log-likelihood functions [Lombardi 2017].

The first objective of our study is to compare the discrepancies of the parameters' values across two different regions in Italy. To make the comparison more straightforward and consistent, we use the same earthquake catalogue, identical temporal windows, and the same minimum magnitude of completeness. The spatial extent of the defined regions is shown in Figure 2.1. Region 1 is associated with the part of Italy where significant sequences were observed in the recent past, while Region 2 is an area of high seismicity but with less observed activity in the recent past. The data used in this study are obtained from the instrumental earthquake catalogue of [Lolli et al. 2020] (the HOmogenized instRUmental Seismic (HORUS) catalogue can be downloaded at ingv.it), homogenized to the moment magnitude M_w within a polygon that covers the mainland of Italy. We select the time window between 1983 and 2020 as the investigation period, with the previous two years (1981-1983) as the auxiliary window. In the considered investigation period, five events with $M_w \geq 6$ with a maximum magnitude of $M_w=6.6$ occurred in Region 1, while all events have $M_w<6$ in Region 2. The data are restricted to events with a maximum hypocenter depth of 40 km. Using this dataset, we estimate the Gutenberg-Richter law's *b*-value as 1.03 and 1.04 for regions 1 and 2, respectively. In addition, the minimum completeness magnitude M_w of 3 of this catalogue is estimated as the value at which the hypothesis of exponentially distributed data cannot be rejected at a significance level of 0.05 [Lilliefors 1969]. The same dataset is used later in this study for underpinning the Poisson and Omori models.

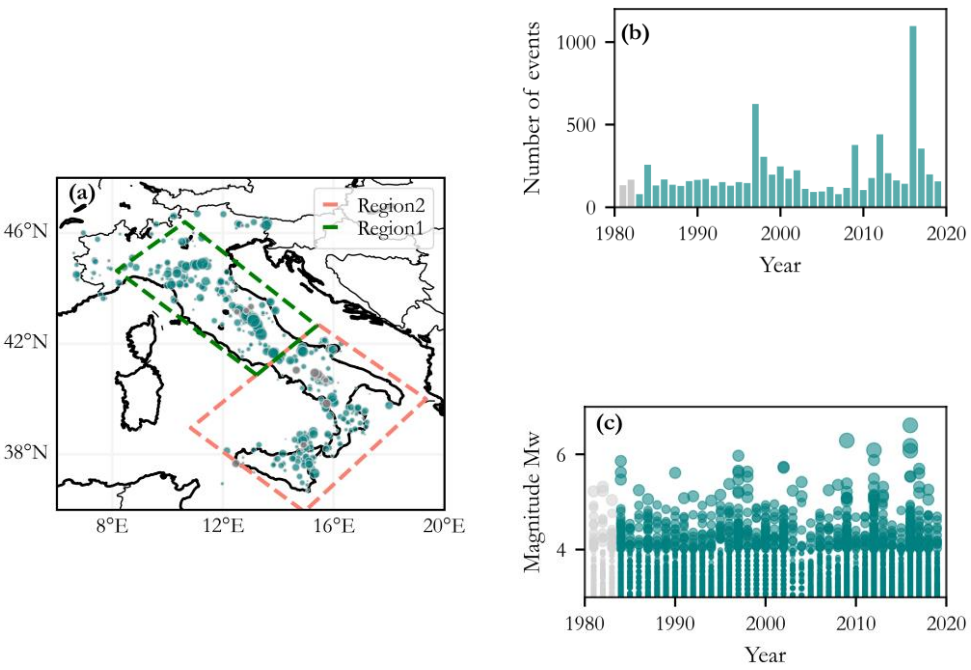

Figure 2.1. (a) Spatial extend of the considered regions. Dots represent the earthquakes' epicenters, and their size is proportional to the magnitude(only earthquakes with magnitude above 4 are shown); (b) the number of earthquakes per year; and (c) the temporal distribution of the events shown in (a). In all the figures, green is used for events in the target temporal window (1983–2020) and gray for events in the auxiliary temporal window (1981–1983).

2.5 REGIONAL DEPENDENCY AND COMPARISON OF THE ETAS MODEL WITH HISTORICAL DATA

Using the model described in the previous sections and the HORUS instrumental catalogue, we find the maximum likelihood estimates (Table 2.1) of the ETAS parameters for the two considered regions. To test the robustness of these estimates, we use different lengths of the auxiliary windows (from two to ten years) and observe minor differences in estimates (see Appendix A1 for details). Furthermore, we estimate the standard errors of the parameters following the procedure of Wang et al. [2010], simulating 200 stochastic catalogues and using the values given in Table 2.1. The standard error of each parameter's estimate is given in the brackets. We also show the total background rate calculated by integrating the spatial distribution $u(x,y)$ over the target region and multiplying it by the estimated value of the total rate ν. Finally, we estimate the branching ratio, to get a better

insight into the triggering properties. The branching ratio, for the case when $\alpha=\beta$, is estimated as [Zhuang et al. 2013]:

$$n = \int_{m_c}^{m_{max}} k(m) \cdot s(m) dm = \frac{A \cdot \beta (m_{\max} - m_c)}{1 - e^{-\beta (m_{max} - m_c)}} \tag{2.7}$$

Table 2.1. Estimated mean values and standard errors (within brackets) of the Epidemic-Type Aftershock Sequence (ETAS) parameters

ETAS parameters estimates	Region 1	Region 2
ν	0.92(0.11)	0.945(0.088)
A (events/day/km^2)	0.093(0.014)	0.09(0.044)
c (days)	0.02(0.004)	0.0054(0.0029)
p	1.18(0.02)	1.08(0.044)
d (km^2)	0.9(0.15)	1.66(0.28)
q	2.0(0.17)	1.81(0.16)
γ (magnitude^{-1})	0.59(0.12)	0.36(0.14)
Number of events	4323	2835
Total background rate (events/day)	0.076	0.106
Branching ratio	0.96	0.92

There are some evident differences in these sets. For instance, the branching ratio in Region 1 is higher, which was expected given that significant sequences were observed in this region since 1983. Furthermore, based on the temporal parameters p and c, one can find that 50% of the triggered events are expected to occur within one day in Region 1 while 32 days are needed in Region 2. It is difficult to establish with certainty the origin of these differences, as it could be attributed to parameter bias, model deficiency, actual differences in the properties of the earthquake phenomenon, or a combination of the above.

That said, we perform several Turing-style tests [Page and Elst 2018] to verify that the ETAS-generated synthetic catalogues can be considered a realistic representation of the physical phenomenon (i.e. if they are statistically consistent with the observed seismicity). To this end, we generate 500 stochastic catalogues describing the seismicity from 1983 to 2020, conditioned on the history of the two previous years (1981-1983), and compare their characteristics with those of the observed data. If the ETAS-based catalogues are significantly different from the observed data, one could conclude that the model cannot reproduce the characteristics of the observed seismicity. In this section, we show only two of these tests for conciseness. Additional tests can be found in Appendix A2. These tests are by no means exhaustive but are nonetheless indicative of the robustness of the approach.

First, we compare in Figure 2.2 the cumulative magnitude frequency distribution (MFD) of observed and ETAS-simulated events in the 37 year-long observation period. The observed number of earthquakes lies within the 5th and 95th percentiles extracted from the simulated catalogues, for Region 1, while some discrepancy is observed for Region 2.

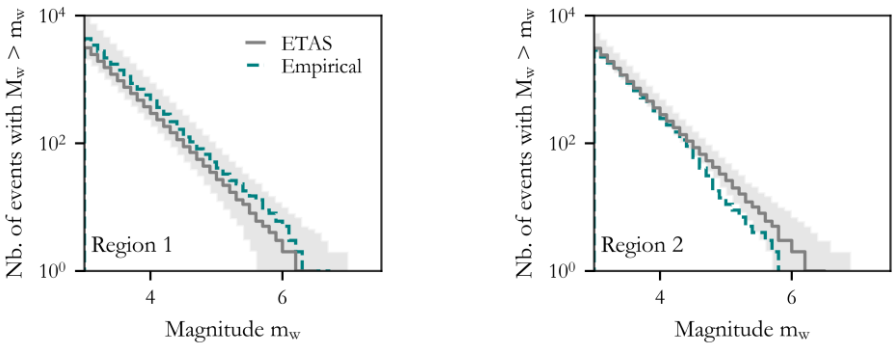

Figure 2.2. Magnitude–frequency distribution (MFD) of the events in the observed and stochastic catalogs for the period of 1983–2020 in Region 1 and Region 2. The green dashed line refers to the instrumental HOmogenized instRUmental Seismic (HORUS) catalog, the solid gray line is the median of 500 epidemic-type aftershock sequence (ETAS)-generated catalogs, and the shaded area represents the 5th and 95th percentiles of the ETAS simulations.

We also compare the ETAS model's clustering behavior with that of the observed seismicity adopting the analysis of Zaliapin et al. [2008]. Identifying clusters with this method is centered on estimating the proxy inversely proportional to the strength of the "bond" between two earthquake events. This proxy represents the nearest-neighbor distance in a multidimensional domain (time, location, and magnitude), and it separates the space into two subdomains: one (with lower η_{ij}) likely contains clustered events, and the other (with higher η_{ij}) likely contains background events. Nearest-neighbour distance can be found as per Equation (2.8) where τ_{ij} is the temporal distance, r_{ij} is the spatial distance between events i and j, and d is a constant taken equal to 1.3 following Peresan and Gentili [2020].

$$\eta_{uj} = \begin{cases} \tau_{ij} \cdot r_{ij}^{d} \cdot 10^{-bm_i}, & \tau_{ij} > 0 \\ \infty, & \tau_{ij} \leq 0 \end{cases} \tag{2.8}$$

Again, stochastic catalogues are used to find the η_{ij} distribution. Figure 2.3 compares the median and the 5th and 95th percentiles of ETAS simulated catalogues with the observed seismicity for both regions. The separation between the background and clustered modes is clear in Region 1, while in Region 2, the background peak dominates the distribution. We can see that in Region 1 the ETAS-based median of the clustered mode is overestimated

and that of the background is slightly underestimated. However, in general, the characteristics of simulated and observed catalogues show a good match.

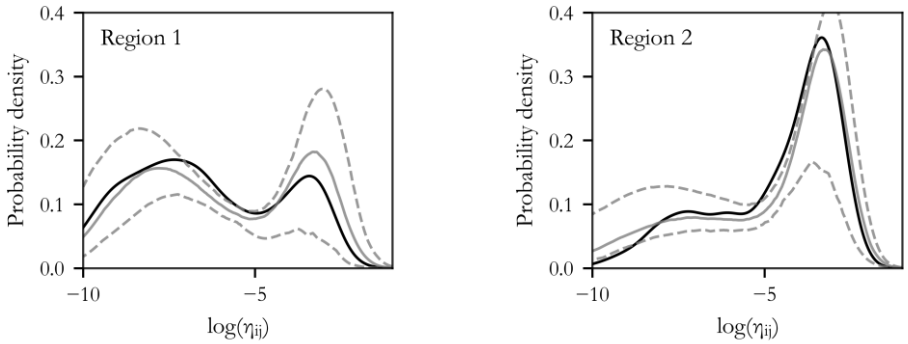

Figure 2.3. Distribution of the nearest-neighbor distance η_{ij} for the period of 1983–2020 for Region 1 and Region 2. The solid gray line refers to the median of 500 ETAS generated catalogues; the black one to the instrumental catalogue and the dashed lines represent the 5th and 95th percentiles of the ETAS-generated catalogues.

Even though we can see non-negligible differences in the clustering properties between these regions, we argue that this is a matter of the limited amount of sequences in Southern Italy rather than due to intrinsic dissimilarities in the earthquake phenomena. In fact, very few rich sequences were observed in this period outside of Central Italy. To test the validity of this assumption, we use the CPTI15 catalogue [Rovida et al. 2020] (that can be downloaded at ingv.it) to get more information regarding the high-magnitude events which are not plentiful in the HORUS catalogue. This catalogue, assembled as a combination of harmonized macroseismic and instrumental Italian data, covers the period from 1000 to 2017, and it is considered complete for events of M6 and above.

We simulate 100 stochastic catalogues of events spanning from 1717 to 2017 in Region 1 using the parameters calibrated based on the HORUS catalogue and Region 1. Then, we repeat the exercise for Region 2 but using two sets of parameters' values: the set of parameters calibrated for Region 2 (second column in Table 2.1) and the set of parameters calibrated for Region 1 (first column in Table 2.1). The M6+ events of all simulated catalogues are then compared with the M6+ events included in the CPTI15 catalogue. First, it is essential to acknowledge that in Region 1 ETAS can predict the historical seismicity well even though the model is calibrated using a different catalogue (see Figure 2.4a). There is some overestimation of results, possibly because the last 40 years, for which the parameters are calibrated, were particularly active, but not significantly. Second, in Region 2, one can observe that the set of parameters from Region 1 provides MFD closer to the observed one (see Figure 2.4b and Figure 2.4c). Based on these results, we speculate that using the set of parameters from Region 1 where the observed seismic sequences are

plentiful and, therefore, the parameters' values are well-constrained yields more defensible seismicity estimates in Region 2.

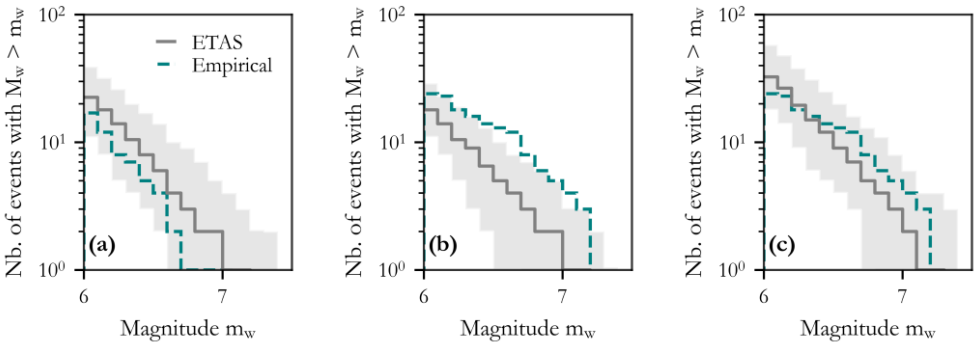

Figure 2.4. MFD of the observed and stochastic catalogues for the period of 1717–2017 in (a) Region 1, using parameters of Region 1, (b) Region 2, using parameters of Region 2, and (c) Region 2, using the parameters of Region 1. The gray dashed line refers to the historical CPTI15 catalogue, the green line is the median and the shaded area is 5th and 95th percentiles of the 100 ETAS-generated catalogues.

It is worth noting that assuming that the ETAS parameters in these regions are the same does not mean that the total background rates are equal. More specifically, we assume that the ratio between background events (computed within the maximization procedure) and the events in the declustered catalogue we used is the same for the three regions. However, this assumption does not imply that the total background rate is the same.

2.6 POISSON AND OMORI MODELS

In order to use the model that combines Poisson and Modified Omori law, it is necessary first to simulate Poissonian mainshock events. To do so, we decluster the catalogue, then calculate MFDs and rates using a correlation distance of 20 km, which is also used for the background seismicity in ETAS. For every mainshock event, we generate aftershocks following the Reasenberg and Jones [1989] methodology. Within this formulation, the rate of aftershocks with magnitude $\geq m_c$ at time t (time elapsed since the mainshock event) is found using the combination of the temporal [Omori 1894] and productivity [Utsu 1961] laws as:

$$\lambda(t, m_c) = 10^{a+b(m_j - m_c)}(t+c)^{-p} \tag{2.9}$$

where a, c and p are model parameters, while b is the value from the Gutenberg-Richter law. To estimate the parameters' values, we maximize the log-likelihood function, given by:

$$\ln L(a,c,p) = \sum_{i=1}^{N} \ln \lambda(t_i) - \int_{t_0}^{t_{end}} \lambda(t)dt \tag{2.10}$$

where N is the number of aftershocks, while t_o and t_{end} refer to the beginning and the end of the period considered. Reasenberg and Jones [1989] proposed probability distributions for these parameters, fitting several California sequences, later extensively used in seismic forecasting. Estimating the Omori parameters with sequence-specific fits can be challenging as many sequences do not have aftershocks above completeness magnitude, while simply disregarding these sequences causes a positive bias in the estimate of the productivity parameter *a*. That said, it is now well recognized that Reasenberg and Jones [1989] overestimated the value of *a* as they only considered sequences with a sufficient amount of aftershocks [Felzer et al. 2003]. In our study, we use instead the methodology proposed by Page et al. [2016], utilized as a foundation for short-term aftershock forecasting at USGS, where, to get better-constrained results, all sequences relative to the corresponding mainshock's time are stacked together, and mean Omori parameters are estimated. Based on the sequences identified with the chosen methodology (which we discuss in the following subsections), the equivalent earthquake magnitude is estimated as $(1/b)\log_{10}\sum_{j=1}^{K}10^{b\cdot M_j}$ in which K is the number of mainshocks in the stack [Hardebeck et al. 2019]. As the proposed model is purely temporal, to model aftershocks' spatial distribution, we use a simple circular area around the mainshock with a radius equal to three rupture lengths estimated with the Wells and Coppersmith [1994] scaling law. While we are aware that this model might be overly simplistic, a detailed investigation of the aftershocks' spatial distribution is outside the scope of our work.

The approach described above is extensively used in the literature to model earthquake sequences because it has the advantage of having fewer parameters to estimate than ETAS, and it builds on the familiar mainshock-only Poissonian model and upgrades it. We believe, however, that this approach has some critical weaknesses, which we address in the following subsection.

2.6.1 Effect of declustering on the Poisson model

The Poissonian rates of occurrence of mainshocks are empirically estimated from declustered catalogues, which are obtained using declustering techniques. These techniques, however, are plagued by several arbitrary decisions that inevitably color the final results. To investigate the declustering caveats, we apply here three different techniques to the HORUS catalogue for Region 1, minimum magnitude M3, and the period from 1981-2020.

The most used and the simplest declustering technique is the window-based Gardner and Knopoff [1974] method (GK74). The algorithm identifies the largest M event in a sequence and removes all other events within a window with M-specific pre-specified temporal and spatial parameters centered at the identified event. A more complex declustering approach was later proposed by Reasenberg [1985] (R85), who extended the work of Savage [1972]. Their idea was to link every event to a cluster via a spatio-temporal proxy. Every event linked with the prior one joins its cluster and, therefore, clusters grow by association. In this manner, the spatio-temporal window does not solely depend on the mainshock magnitude (as it does in GK74) but instead varies with events' behavior. More precisely, the spatial extension is based on the stress distribution pattern, which is assumed

to depend on the cluster's last and largest event. The temporal extension is developed based on the probabilistic model and Omori law. More details about the model can be found in [Molchan and Dmitrieva 1992; Reasenberg 1985; Stiphout et al. 2012]. Lastly, we use the nearest-neighbor proxy defined by Zaliapin et al. [2008] (ZNN) to identify the sequences, the largest event of which is kept as the mainshock. More details about this model are given in the previous section. One should bear in mind that the declustering methods mentioned above might be affected by the parameters that define them, calibrated based on a particular region and a limited amount of data. They may or may not be the optimal set of parameters for other regions but are nonetheless used extensively in the literature. Besides the GK74, R85 and ZNN considered here, several other methods for identifying sequences can be found in the literature, from simple deterministic ones to more advanced stochastic ones such as [Llenos and Michael 2020; Zaliapin and Ben-Zion 2020; Zhuang et al. 2004]. This high number of available declustering methods clearly reflects the true difficulties in reliably classifying earthquake events.

As stated earlier, one of the main objectives of declustering is to obtain a catalogue of earthquakes (mainshocks) whose temporal occurrences can be modeled as a Poissonian distribution. A check of whether the Poissonian process assumption holds is rarely carried out in practice. As Luen and Stark [2012] showed, whether the declustered catalogue could be considered Poissonian depends on the declustering method, available catalogue, magnitude range, and the statistical test utilized. Therefore, we first test the Poissonian assumption with the Kolmogorov-Smirnov one-sample test following Luen and Stark [2012], and we show its p-values in Table 2.2. The p-values obtained for all three declustered catalogues are low (below 5%), with the GK74 catalogues yielding the highest values and the R85 ones yielding the lowest. This trend, also observed in other studies, led to the use of GK74 for declustering the catalogues adopted in National Seismic Hazard Models, e.g., MPS19 for Italy [Meletti et al. 2021] and NSHM for the USA [Petersen et al. 2020]. Table 2.2 also compares the number of events in the entire catalogue with the number of events in the three declustered catalogues. From these results, one can see that the R85 method retains by far the highest number of mainshocks while GK74 and ZNN yield similar results.

Table 2.2. Properties of the declustered catalogues (Region 1, Mmin=3, Period 1981-2020)

Method	GK74	R85	ZNN
Number of MS	1191	2240	1151
Number of AS	2513	1857	2610
Ratio[a]	26.8	50	25.9
p-value (M_{min}=3)	$3.7 \cdot 10^{-2}$	10^{-18}	$3 \cdot 10^{-4}$
p-value (M_{min}=3.5)	$4.0 \cdot 10^{-2}$	$1 \cdot 10^{-5}$	$42 \cdot 10^{-2}$

[a] Number of events in entire catalogue to the number of events in declustered catalogue

On a different note, keeping only the largest events in the clusters might affect the *b*-value due to the Gutenberg-Richter law's inevitable distortion. The declustering technique removes a disproportionately much larger number of lower magnitude events than higher magnitude ones (i.e., it does not sample the Gutenberg-Richter distribution randomly) and, therefore, it tends to lower the estimate of the *b*-value. To check that the magnitude of the events in the three declustered catalogues can still be reasonably modeled with an exponential distribution, we use the Lilliefors [1969] test and conclude that the hypothesis of exponential distribution cannot be rejected at a significance level of 5% in all three cases. Figure 2.5 shows the Gutenberg-Richter distribution and associated b-values for the three declustered catalogues to illustrate that significantly lower values were obtained for GK74 and ZNN models. On the contrary, the catalogue declustered with R85 has the same b-value as the full catalogue. The issue related to the distortion of the GR b-value due to declustering was acknowledged in the Uniform Californian Earthquake Rupture Forecast version three [UCERF3; Field et al. 2014], where, for the MFD of the gridded seismicity model, the *b*-value of the declustered catalogue was used only before the point where MFDs of the full and declustered catalogues crossover. Nonetheless, a common practice in PSHA is still to take the *b*-value of the declustered catalogue as is and, therefore, to overestimate the rate of high-magnitude events in hazard calculations possibly considerably [Mizrahi et al. 2021].

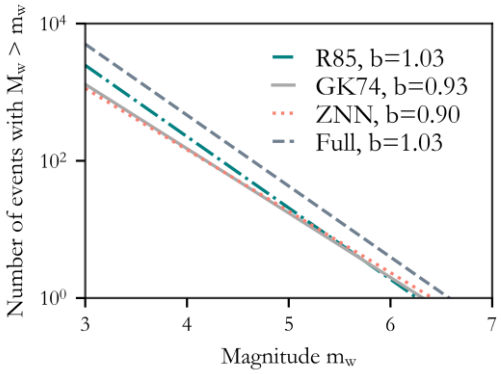

Figure 2.5. Gutenberg–Richter law for the full HORUS catalog and for three different declustered catalogs extracted from it (figure refers to Region 1)

Lastly, one should note that the declustering also affects the spatial distribution of the events as recently illustrated by Llenos and Michael [2020]. The spatial distribution of events declustered with the three different methods can be found in Appendix 0.

Keeping the above discussion in mind, one needs to be careful with the interpretation of the declustering results, as it is not guaranteed that the occurrence of the remaining events can be reasonably modeled with a Poisson distribution. Additionally, it is necessary to be

aware of the sensitivity to the chosen method as different catalogues declustered from the same initial catalogue can have significantly different numbers of events and different *b*-values of Gutenberg-Richer law.

2.6.2 Consistency of Omori model with the available data

Using the three models previously described (GK74, R85, and ZNN) and the methodology presented in the previous section, we estimate the values of the Omori parameters for Region 1, minimum magnitude M3, and the period 1981-2020. It is essential to highlight that the values of the set of Omori parameters obtained here differ from the values of the set estimated in the ETAS model (first column of Table 2.1) because the values of the Omori parameters in ETAS are applied locally, i.e., to every generation of aftershocks. In the Modified Omori law model, on the other hand, all aftershocks are assumed to be triggered by a single mainshock event, and, hence, the parameters' values refer to entire sequences. Therefore, the applicability of the Modified Omori-Utsu law is questionable in cases with complex sequences as frequent occurrence of large aftershocks, which might trigger their own sequences, can break the Omori law assumed for the entire sequence [Spassiani and Marzocchi 2018]. Furthermore, several studies showed that aftershock productivity could significantly vary from sequence to sequence, suggesting that differences in the tectonic region [Chu et al. 2011; Page et al. 2016], the geometry of source [Dascher-Cousineau et al. 2020], mainshock stress drop variability [Marsan and Helmstetter 2017] and heat flow [Zaliapin and Ben-Zion 2016] might be potential reasons. Hence, assuming the same value of the productivity parameter (a in Omori and A in ETAS) for all sequences can cause bias, reducing the sequence-to-sequence variability. Even though this problem is mutual for both the ETAS and Omori models, ETAS benefits from some natural variability intrinsic in the model.

The derived parameter estimates are presented in Figure 2.6. To better assess the reasonability of the Omori law parameter values obtained from the GK74, R85, and ZNN declustering methods, we generate 500 stochastic catalogues in Region 1 over the 1983-2020 period (the previous two years of seismicity are used to feed the model, similarly as in the ETAS case) using Monte Carlo simulation. In this exercise, we estimate the number, magnitude, location, and time of the aftershocks generated by each mainshock event simulated via the Poisson model and compare them with the observed values in the HORUS catalogue. The *b*-value for simulating the mainshocks is given in Figure 2.5, while for the aftershocks, we use 1.03 (*b*-value of the full catalogue), as this is a common approach in the literature. In addition, the magnitudes of the generated aftershocks are constrained to be lower than the corresponding mainshock's magnitude for consistency with the assumption adopted in the three declustering techniques. Figure 2.7a compares the magnitude frequency distribution of the earthquakes in the 500 simulated catalogues with the one of the HORUS catalogue. In all cases, the match is satisfactory even though the parameters used are somewhat different.

As we use different b-values for simulating mainshocks and aftershocks in the Omori model, the b-value of the resulting simulated catalogue remains unclear. That said, we

estimate the median and 90% confidence interval based on the 500 Omori simulated catalogues and compare them with those of the 500 ETAS simulated catalogues and with the original b-value of the HORUS full catalogue (Figure 2.7b). With all Omori variants, the b-value of the simulated catalogues is higher than the original, while in the case of ETAS, this value is perfectly recovered. To the authors' knowledge, this issue with the Omori model is not recognized in the literature, and the *b*-value of the resulting stochastic events, which is somewhat arbitrary, is left unchecked.

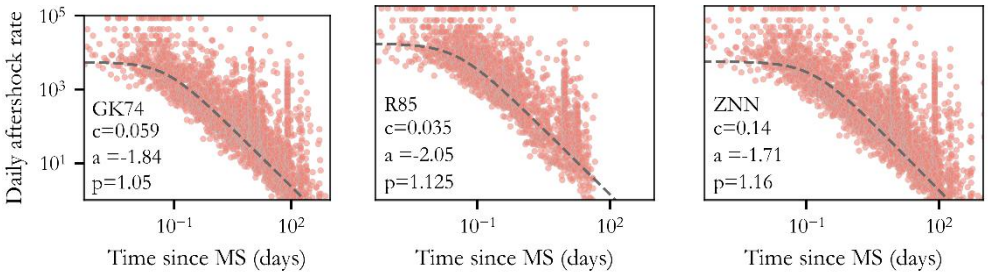

Figure 2.6. The stacked rate of aftershocks following mainshocks from 1981 to 2020 in Region 1 (the minimum magnitude considered for both mainshock and aftershock events is M3). The gray solid line shows the aftershock rate obtained with the Reasenberg and Jones [1989] model, whereas the empirical aftershock rate was found from two consecutive aftershocks in the stack as $1/(t_{j+1}-t_j)$ [Hardebeck et al. 2019]. From left to right, the method used to identify sequences is Gardner and Knopoff [1974] (referred to as GK74), Reasenberg [1985] (referred to as R85), and Zaliapin et al. [2008] (referred to as ZNN), respectively.

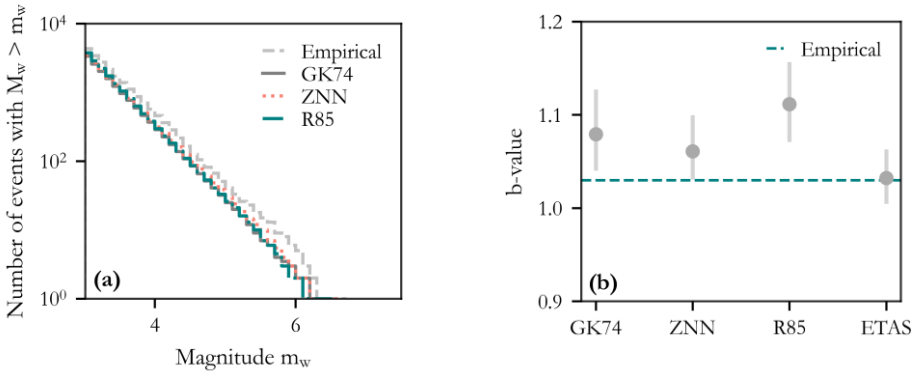

Figure 2.7. (a) MFD of the observed and simulated catalogues for the 1983–2020 period in Region 1. The dashed gray line refers to the instrumental HORUS catalogue, whereas other lines refer to the median of 500 Omori-generated catalogues using different sets of parameters' values; (b) Median and the confidence intervals for *b*-value estimated based on the 500 simulations, for different models.

2.7 HAZARD ESTIMATES

In this section, we compare and contrast the hazard estimates in terms of Sa(0.3s) (spectral acceleration at the period of 0.3 s), at two rock sites (shear wave velocity in the top 30 m of 800 m/s) in Norcia and Perugia (Region 1, Central Italy) obtained from different catalogues that use the Poisson, Poisson + Omori, and ETAS approaches to model earthquake occurrences. More specifically, we simulate 20,000 1-year-long stochastic catalogues of seismicity in Region 1 using these three approaches. To each event in the catalogue, rupture properties, such as a rake, dip, slip, and seismogenic depth, are generated using the SHARE seismic source model [Woessner et al. 2015] following the procedures implemented in the OpenQuake software [Pagani et al. 2014]. We used the Abrahamson et al. [2014] GMPE to characterize the ground motion generated by each earthquake. As explained in the Introduction section, following Papadopoulos et al. [2021], we produce two sets of ETAS hazard estimates. In the first so-called 'unconditional' case, we generate 11 years of seismicity with no initial conditions (i.e., no auxiliary period), and we retain only the last simulated year. This procedure guarantees an unbiased seismicity level (i.e., neither high nor low compared to the long-term one) as the initial conditions for the catalogues used for hazard calculations. In the second so-called 'conditional' model, the initial conditions are controlled and fixed to a specific auxiliary 2yr-period and, again, the seismicity of the following year is simulated. Herein, as an auxiliary period, we choose the high seismicity period 26/04/2015 - 26/04/2017 with active ongoing sequences, and we simulate the seismicity of 26/04/2017- 26/04/2018.

For the Poisson + Omori model (in the following text, for brevity, we simply refer to this model as the Omori model), we also consider these two cases. The 'unconditional case' is conceptually the same, while in the 'conditional' case, we feed the model with the seismicity observed in the auxiliary 2yr-long initial window extracted this time from the declustered catalogue as, by definition, only mainshock events can generate aftershocks within this model. Naturally, as the Poisson model is time-independent, there is no distinction between the 'conditional' and 'unconditional' cases. In all the hazard analysis computations, we only consider events with magnitude ≥M4. The seismic hazard curves are derived by counting the number of events that exceed each given level of spectral acceleration and dividing it by the total number of stochastic 1-year long catalogues, i.e., annual rates are estimated. If the annual probabilities of one or more exceedances are needed, one needs to count the number of stochastic catalogues in which each given level of spectral acceleration is exceeded at least once and divide it by the total number of stochastic 1-year long catalogues simulated.

2.7.1 Poisson and Omori model comparison

In Figure 2.8, we compare the annual rate of exceedance of Sa(0.3s) obtained via both the Poisson and Omori models, considering the three different declustering techniques of GK74, R85 and ZNN. First, we can observe that the hazard estimates obtained with the Omori model are higher than those from the Poisson ones for all declustering methods and both considered sites, as expected, given that the rates are higher in the former case.

The GK and ZNN models yield similar results for both the Poisson and Omori models and for both sites. ZNN hazard estimates are slightly higher for larger intensities in the Poisson case, possibly due to the lower GR *b*-value that causes a higher rate of large-magnitude events. R85 results in higher hazard estimates in the Poisson case for both Norcia and Perugia, which was expected as the R85 declustered catalog contains more events (Figure 2.5). On the other hand, in the Omori model, the difference is observed only for Norcia, where R85 again predicts the highest hazard estimates, while in Perugia, the three curves are almost indistinguishable. This might be due to the differences in the spatial distribution of the events in different Omori models as R85 retains more events in the Central part of the region, where Norcia is located (figures illustrating spatial distribution can be found in Appendix A4). One should remember that the earthquake occurrences in the R85 declustered catalog do not follow a Poisson distribution, and, hence, the obtained hazard curve is not coherent with the hypothesis.

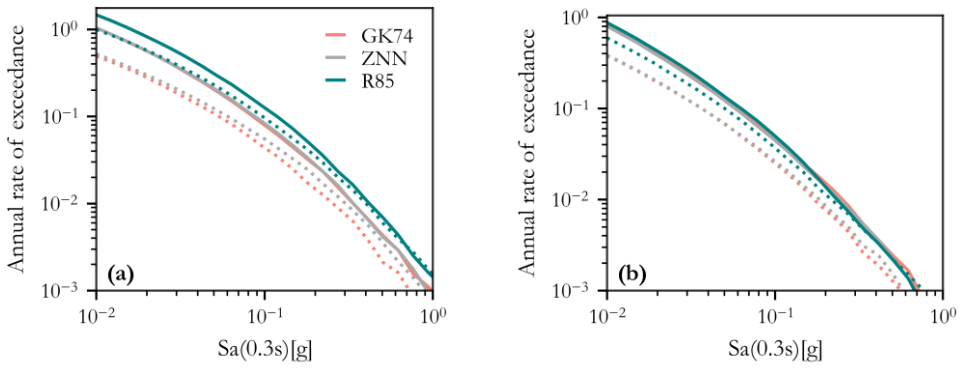

Figure 2.8. The annual rate of exceedance for (a) Norcia and (b) Perugia. The rates from the Omori model are shown with a solid line and those from the Poisson model with a dotted line. Random initial conditions are assumed, that is, the "unconditional" case.

2.7.2 Omori and ETAS model comparison

Figure 2.9 compares the Norcia and Perugia hazard curves produced by the Omori, ETAS and Poisson models. For brevity, we only consider here Poisson and Omori model based on the GK74 declustered catalog. As expected, in all cases considered, both Omori and ETAS generate hazard curves that are undoubtedly higher than the Poisson-based one. In the unconditional case, the annual rates found with the ETAS model are consistently higher than those found with the Omori model, although not significantly higher. This result implies that both models are equally suitable to compute hazard in periods of average seismicity. However, in the conditional case, the year of hazard computations follows a period plagued by an active sequence. In this case, the ETAS results are considerably higher than those based on the Omori model. The reason for this is that 102 events with magnitude ≥M4 occurred in the investigated region in the auxiliary period used as initial

conditions for the ETAS model. Only seven such events, which survived the declustering, are fed to the Omori model. Some of the events removed by the declustering process are the high-magnitude events (≥M5) that preceded and followed the M6.6 mainshock earthquake that occurred on 30/10/2016 near Norcia. Based on the findings of this example, we infer that the Omori and ETAS models can predict significantly different results in periods of higher-than-average seismicity during ongoing active sequences.

The statement above, however, seems to apply only to sites close to the sequences. For Perugia, which is significantly farther from the focus of the activity, ETAS yields higher rates for lower intensities but lower rates for higher intensities. Hence, it is intuitive to expect that the Omori model may provide hazard estimation similar to the ETAS at sites away from the bulk of the active sequences even in the period of heightened activity. These are only simple considerations, and more investigations should be conducted. However, it should be underlined that finding the reasons that may cause differences in the hazard estimates from ETAS and Omori models is anything but simple. Besides the apparent difference in how productivity and temporal distribution of aftershocks are modeled, their spatial distributions can also affect the hazard estimates. As described previously, the spatial distribution of background events in ETAS is estimated based on the declustered catalogs, while the distribution of triggered seismicity is described with an isotropic kernel without considering the fault geometry. In the Omori model, the spatial distribution of the aftershocks is modeled with a simple scaling law. The effect of these assumptions needs further investigation but is outside our study's scope.

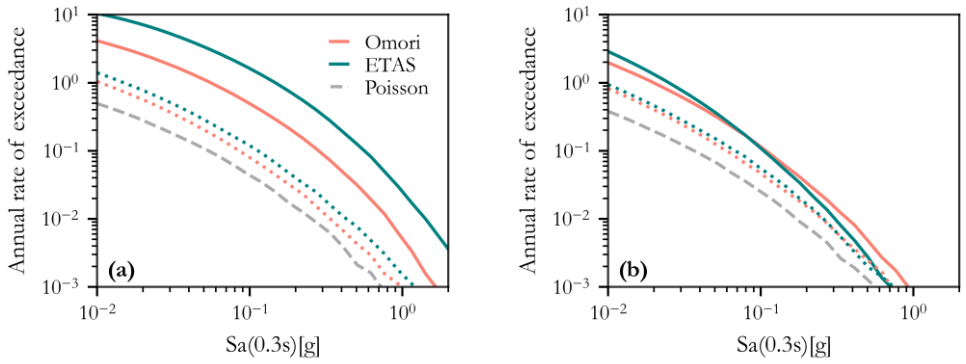

Figure 2.9. Annual rate of exceedance for (a) Norcia and (b) Perugia obtained using Omori and ETAS models. The conditional case (active ongoing sequences) is illustrated with a solid line and the unconditional case (average seismicity) with a dotted line.

2.8 DISCUSSION AND CONCLUSIONS

The objective of this study was threefold: (1) to estimate seismic hazard using the ETAS model, (2) to investigate the spatial variability of the ETAS parameters, and (3) to compare hazard estimates from ETAS with those based on Poisson and Omori models.

First, by comparing the MFD of the historical CPTI15 catalogue with the MFD of the ETAS-generated stochastic catalogues, we have shown that the ETAS model can adequately describe the past seismicity in the two considered regions in Italy. Furthermore, this study has shown that models based on the mainshock-only view of seismicity are often used despite several limitations, leading to hazard estimates that are significantly lower compared to those obtained with more advanced tools capable of accounting for the triggered seismicity, such as the Omori or ETAS models. In addition, a PSHA approach based on the ETAS model for simulating future seismicity also appears to be able, unlike the Omori model, to capture the temporal variation in seismic hazard both in quiet and active periods of clustered seismicity.

The application of the ETAS model for seismic hazard estimation, however, is complex. There are many regions where an insufficient number of active sequences have occurred in the (short and recent) period of the earthquake catalog that can be considered as complete for lower magnitude events, as required by the method. Hence, our second objective was to investigate if it is legitimate to use ETAS parameters' values from a region well constrained by data and apply them elsewhere. We have defined two regions, Central Italy (Region 1) and Southern Italy (Region 2), and used the recent instrumental HORUS catalog, which covers the period from 1981 to 2020, to calibrate the ETAS model. We found that the parameter estimates are different for these two investigated regions with similar tectonic environments. However, at least in the area considered, we can speculate that this discrepancy is more likely due to the scarcity of sequences in the observed period rather than to intrinsic differences in the earthquake sequence phenomena. Our conjecture is supported by comparing the magnitude frequency distributions for M6+ events of 100 ETAS simulated catalogs with the historical CPTI15 catalog covering the period from 1717 to 2017. These findings show a better agreement between simulated and observed frequency distributions when the more robust values of the ETAS clustering parameters from Central Italy are used to model sequences in the South, where sequences were scarce in the past few decades.

Lastly, for the sake of comparison, we have examined the classical Poissonian model that considers mainshocks only and the model that combines the Poissonian model for mainshocks and the Modified Omori law for modeling aftershocks (Omori model), which is considered to be an approach for clustered seismicity modeling less complicated than ETAS. Since the Omori model is sensitive to the identification of mainshocks, we have investigated three different declustering methods, namely Gardner and Knopoff [1974], Reasenberg [1985] and Zaliapin et al. [2008]. We have found that these methods return catalogs with a different number of events, different b-values of GR law, different *p*-values of the K-S test for assessing the suitability of the Poisson distribution, different sets of Omori parameters' values, and a magnitude-frequency distribution not comparable to the

observed one. Among the three, we favor GK74, which is the simplest and yields a catalog of events with occurrences distributed more closely to the Poisson distribution. We have investigated if the differences in the models described above significantly impact the hazard estimates, expressed in terms of the annual rate of exceedance of ground motion intensity measures at two sites in Central Italy. We have first compared the Omori and Poisson models, using the three different declustering methods. We have illustrated that the results might vary depending on the declustering method adopted. We then compared the three alternative models (Poisson, Omori, and ETAS) using two different initial conditions: an 'unconditional' case, with initial conditions characterized by average seismicity, and a 'conditional case' whose initial conditions included an ongoing active earthquake sequence. As expected, our findings indicate that the traditional Poissonian approach for earthquake occurrence modeling tends to provide lower hazard estimates. Taking the aftershocks in the Omori model and all the events in the ETAS model into consideration significantly increases the hazard estimates to more realistic values because it accounts for the effect of all earthquakes and not only those of the largest ones. These promising results suggest the need to additionally investigate and improve the models used for describing spatiotemporal clustering. Furthermore, we have shown that the Omori and ETAS models yield similar hazard estimates during periods of average seismic activity for particular sites and intensity measure. However, during periods of increased activity, such as those following an active sequence, and for a site close to the sequence, the Omori model predicts lower hazard as it is unable to consider the temporally varying hazard stemming from the heightened initial conditions.

There are several appealing features in the ETAS model: it incorporates the non-Poissonian nature of the earthquake occurrence phenomenon, it does not require the somewhat arbitrary classification of events into the mainshocks, foreshocks and aftershocks, it relies on the Gutenberg-Richter law of the entire catalog circumventing the subjective choice of labeling mainshock, foreshocks and aftershocks, it is adaptive, and it is well-suited for performance-based methodology as it does not neglect, unlike the Poisson and Omori models, any events that may increase the chance of observing certain levels of ground motions at a site. Although the use of the ETAS model for hazard computations is undoubtedly promising, several aspects of it can be improved. For example, fault geometry and anisotropic kernel for aftershock distribution, the time-varying magnitude of completeness, potential inter-sequence variability of the parameters, time-dependent background rate, and effect of the temporal and spatial window are some of the traits that deserve further investigation.

3.INVESTIGATING REGIONAL CHARACTERISTICS OF EARTHQUAKE SEQUENCES: THE CASE OF CROATIA AND TURKEY

3.1 INTRODUCTION

As discussed at length in the previous section, spatial and temporal clustering of the earthquake occurrences can be well described by the ETAS model. ETAS model is the combination of the background seismicity, denoted as $\mu(x, y)$, which, for the sake of simplicity, is assumed to occur uniformly over time, and the triggered seismicity, characterized by the function $g(t-t_j,x-x_j,y-y_j,m_j)$ that can be further described using temporal, productivity and spatial distribution. The overall rate of earthquake occurrence, with magnitude m, at a specific point in space and time, conditioned upon the history of prior earthquakes, H_t, can then be represented by the general form given by Equation (3.1) [Seif et al. 2017; Zhuang et al. 2004]:

$$\lambda(t, x, y, m \mid H_t) = \mu(x, y) + \sum_{j:t_j<t}^{n} g(t-t_j, x-x_j, m_j) \tag{3.1}$$

The index j refers to all past earthquakes. The triggering function has the following form [Ogata 1998]:

$$g(t-t_j, x-x_j, y-y_j, m_j) = k(m_j) \cdot v(t-t_j) \cdot f(x-x_j; y-y_j, m_j) \tag{3.2}$$

For simplicity, the background rate, $\mu(x,y)$, can be expressed as $\mu(x,y) = v \cdot u(x,y)$, where v represents the total background rate and $u(x, y)$ is the spatial distribution of the background events. The productivity term $k(m_j)=Ae^{\alpha(mj-mc)}$ represents the mean number of events directly triggered by an earthquake of a magnitude m_j, where m_c is the minimum magnitude considered. Parameter A quantifies the overall triggering capability, independent of earthquake magnitude, while α governs the role of magnitude; a larger α gives more influence to larger-magnitude events in terms of triggering capability, while a smaller α places greater emphasis on the triggering capability of smaller earthquakes. The temporal decay of triggered earthquakes, $v(t-t_j)=(p-1)\ c^{p-1}(t-t_j+c)^{-p}$, is modeled by the Modified Omori law [Omori 1894; Utsu 1961], where the parameter p governs the temporal decay rate, and c represents a small constant denoting the delay between the end of the triggering event

rupture and the start of the triggered activity. The spatial distribution function used in this study is given by Equation (3.3)[Zhuang et al. 2004]:

$$f(x-x_j; y-y_j, m_j) = \frac{q-1}{\pi \cdot d \cdot e^{\gamma(m_j - m_c)}} [1 + \frac{x^2 + y^2}{d \cdot e^{\gamma(m_j - m_c)}}]^{-q} \quad (3.3)$$

Hence, the ETAS model can be characterized by a set of eight correlated parameters: $\theta = \{\nu, A, \alpha, c, p, d, q, \gamma\}$, in addition to the spatial distribution of the background seismicity, *u(x, y)*. These parameters are typically calibrated using empirical data from the region of interest.

It is intuitive to expect that some ETAS parameters' values depend on the seismotectonic characteristics of the specific region. Ideally, one would distinctly consider regions with different seismotectonic characteristics and estimate the ETAS parameters' values using empirical earthquake data specific to each region. However, there are often practical complications in doing so. There are many regions where an insufficient number of active sequences have occurred in the (short and recent) period in which the instrumental earthquake catalog can be considered complete for lower-magnitude events or where the local instrumentation network is poor or missing altogether and, therefore, an instrumental catalog of events complete to lower magnitudes is simply missing. Furthermore, even when sufficient data are available, it becomes challenging to account for parameter variation near the boundaries of adjacent regions, as earthquakes in one region can trigger events in another, and vice versa. In Šipčić et al. [2022] (i.e., Chapter 2 of this thesis), we investigated the feasibility of using ETAS parameters derived from the well-constrained region in Central Italy and applying them to the Southern Italy region. Our preliminary findings indicate that the parameter estimates at first glance appear to differ between these two regions, despite their similar tectonic environments. However, based on several Turing-style tests [Page and Elst 2018], we concluded that this discrepancy is likely a consequence of the limited number of observed sequences in Southern Italy rather than an indication of intrinsic differences in earthquake sequence phenomena. We argue that the values of the parameters derived for the well-constrained region of Central Italy are superior in describing the clustered seismicity in Southern Italy.

Based on similar findings and recognizing the complexity of ETAS model parameterization and aiming to develop a model suitable for areas lacking reliable earthquake catalogs, Mancini and Marzocchi [2023] introduced a simplified version of the ETAS model called simplETAS. The underlying assumption behind simplETAS is that the clustering process in crustal regions is time and space-independent. In this approach, the values of all the ETAS parameters, except for A (the triggering capability) and the total background rate ν, are fixed using physical constraints and/or heuristic motivations based on the previous empirical findings. A maximum likelihood method is then used to calibrate the values of the remaining two parameters. They demonstrated that while this approach may not be the top-performing clustering model possible, it can be considered a reliable forecasting tool for practical applications.

The objective of this study is to explore ways to utilize the ETAS model more effectively, recognizing the importance of incorporating clustered seismicity into classical hazard assessment and, at the same time, finding a balance between accuracy and practicality. To this end, we have collected data from two European regions, specifically Croatia and Turkey. In the following sections, we will compare the accuracy of the ETAS model in three different setups:

- Using the set of ETAS parameters calibrated based on the Central Italy region (called the SCI parameter set), where many seismic sequences occurred and the catalogue used is of good quality.
- Using the set of ETAS parameters calibrated based on the region of interest (Croatia and Turkey) (called the SR parameter set).
- Fixing all parameters of the ETAS model to the values calibrated based on the Central Italy region, except for the total background rate ν and the productivity term A, akin to the simplETAS methodology (called the SE parameter set).

The first two setups are similar to the aforementioned exercise that involved Central and Southern Italy. The subsequent sections will delve into the available data in Croatia and Turkey, provide insights into how the ETAS model will be tested, and ultimately present and discuss the results.

3.1 DATA

The unclustered seismic catalog of events for the region of Croatia, obtained from Professor Herak [2023, personal communication], encompasses the geographical area of Croatia, including a buffer zone outside its borders, and it covers the period from 20/02/1990 to 06/10/2021. It includes events with local magnitude M_L greater than 3.45, above which it can be considered complete. To convert the local magnitude into moment magnitude (M_w), a conversion equation provided by Herak [2020] was employed. This conversion equation has been calibrated using data from the Croatian Earthquake Catalogue, specifically based on the analysis of 153 earthquakes recorded from 1959 to 2020.

$$M_w = (-0.106 \mp 0.122) + (1.022 \mp 0.027) M_L \tag{3.4}$$

For further analysis we only considered the events in the catalogue with $M_w > 3.4$, resulting in a total of 727 events. Figure 3.1a displays the number of events per year. Notably, there is a significant increase in the number of events in 1996, primarily attributed to the Slot-Slano earthquake that occurred on September 5th with an M_w of 5.9. This event was followed by numerous aftershocks, the largest of which had an M_w of 5.5. Similarly, in March 2003, near the island of Jabuka, an earthquake with an M_w of 5.5 occurred, which triggered several cascading events, as depicted by the second large peak in the same figure. Figure 3.1b illustrates the magnitude-frequency distribution of the events in the catalogue with the Gutenberg-Richter law fitted to the data, and the b-value estimated using the approach of [Aki 1965]. It is worth noting that the data do not perfectly align with the

fitted line. The Kolmogorov-Smirnov test rejected at the 5% significance level the hypothesis that data follow an exponential distribution.

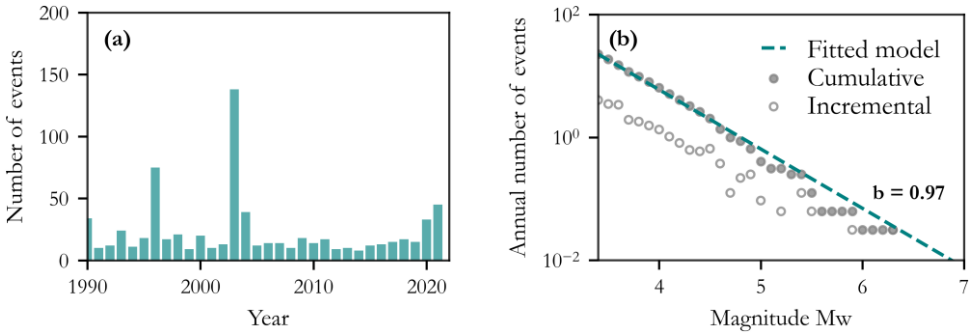

Figure 3.1. (a) The number of earthquakes per year and (b) magnitude-frequency distribution of events and Gutenber-Richter fit. Results refer to the data in the Croatian catalogue.

Figure 3.2 shows the spatial distribution of the events in the catalogue, before and after the declustering that we carried out using the algorithm developed by Gardner and Knopoff [1974], which is arguably the simplest and the most used method. This figure highlights significant clustering around 43.0°N and 18.0°E, which corresponds to the location of the aforementioned Slot-Slano earthquake.

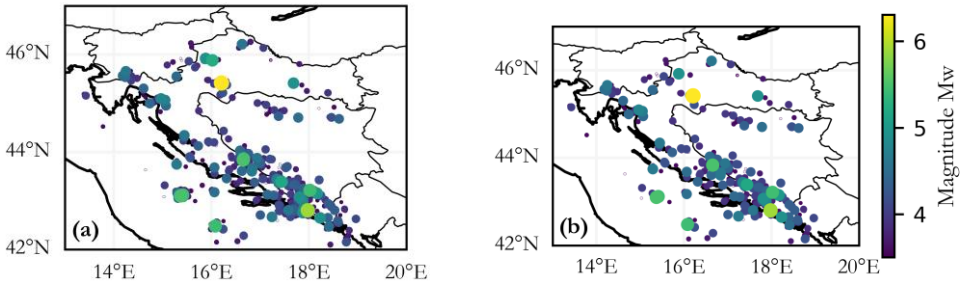

Figure 3.2. The catalogue of events used for the region in Croatia: (a) before declustering and (b) after declustering. Dots represent the earthquakes' epicenters, and their size and colour are magnitude-dependent.

In the region of Turkey, we obtained the catalogue from Erdik [2023, personal communication]. The catalogue spans over the period from 01/01/2000 to 12/05/2023 and it covers the entire country. However, for our study, the region considered spans from

32.0°N to 44.0°N and 34.0°E to 42.0°E. Similarly to the case of Croatia, Figure 3.3a displays the number of events per year. The increased number of earthquakes in 2011 can be attributed to the sequence that occurred near the city of Van in October 2011, which included a mainshock with a magnitude of 7.1. The elevated number of earthquakes in 2023 is associated with the Kahramanmaraş sequence that began on February 6th and involved 53 events with $M_w \geq 5.0$ out of which two had $M_w \geq 7.5$. Figure 3.3b illustrates the magnitude-frequency distribution of the events in the catalogue and the Gutenberg-Richter law fitted to the data, utilizing a minimum magnitude of three. In this case, the Kolmogorov-Smirnov test indicated that the hypothesis of exponential distribution cannot be rejected at the 5% significance level. Figure 3.4 displays the spatial distribution of events in the catalog both before and after declustering. The declustering procedure yielded a catalog of 6742 earthquakes with $M_w \geq 3.0$ from the original of 18293 events.

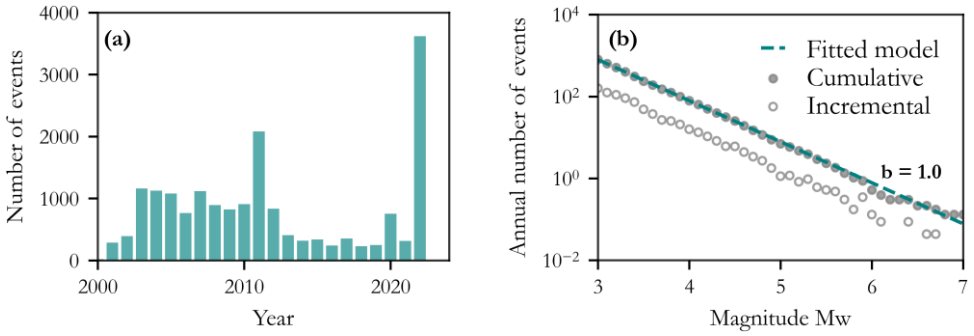

Figure 3.3. (a) The number of earthquakes per year and (b) magnitude-frequency distribution of events and Gutenber-Richter fit. Results refer to the data in the Turkish catalogue.

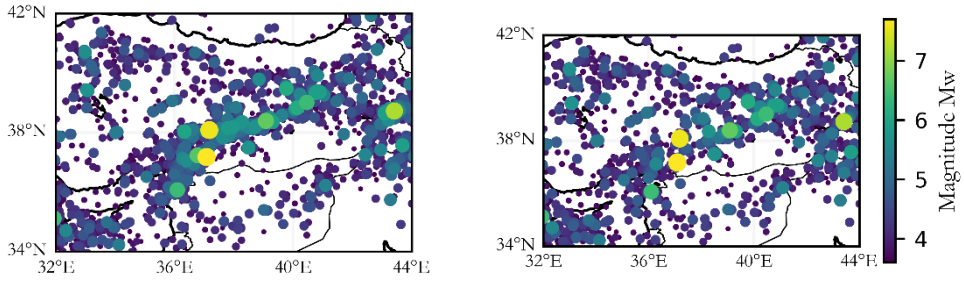

Figure 3.4. The catalogue of events used for the region in Turkey: (a) before declustering and (b) after declustering. Dots represent the earthquakes' epicenters, and their size and colour are magnitude-dependent.

3.2 PARAMETRIZATION OF ETAS MODELS

As referred to in the Introduction, we seek to compare different ETAS model parameterizations for the two considered regions. First, the spatial distribution of background events is estimated a priori from the declustered catalogues for both regions using the smoothed seismicity approach, with a correlation distance of 20 km [Frankel 1995]. Figure 3.5 shows the daily rate density in each grid cell (events per day per square kilometer) that results from this operation. To estimate the values of the ETAS parameters, the spatial distribution of background events and the first two years of the respective event catalogues are used as the conditioning period. This period corresponds to the years 1990-1992 for Croatia and 2000-2002 for Turkey. The value of α is held fixed to $\ln(10)b$ [e.g., Seif et al. 2017; Zhang et al. 2020]. A minimum magnitude of 3.4 is used for Croatia, while for Turkey, a minimum magnitude of 3.5 is employed to avoid convergence issues of the maximum likelihood estimator for lower magnitude values. This set of parameters' values is denoted as "SR", indicating that it is calibrated based on the specific data from the region. Subsequently, the parameters' values are re-estimated using the same assumptions, but with the difference that all parameters' values are fixed to the estimates obtained from the Central Italy data except for the productivity A and of the total background rate ν, whose values are, of course, estimated from the data of the considered region. This set of parameters' values is denoted as "SE", referring to the simplETAS. Lastly, the set of parameters' values calibrated based on the region in Central Italy is referred to as "SCI".

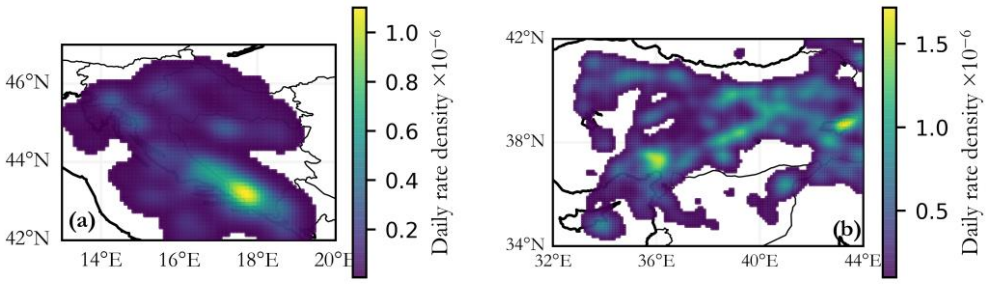

Figure 3.5. The background seismicity rate for (a) Croatia and (b) Turkey obtained using the smoothed seismicity approach and a Gaussian kernel with a correlation distance of 20km.

It's important to clarify that the total rate of background events in a region is equal to the sum of the rates obtained using the smoothed seismicity approach of the declustered catalog, multiplied by the value of the parameter ν, which is estimated with the same maximum likelihood method used for all the other ETAS parameters. The parameter ν, in this context, represents the ratio between the total background rate and the total rate of events in the declustered catalog. More specifically, if the parameter ν is the same for two

regions, then the ratio between background events and the events in the declustered catalog is the same for both regions. However, this assumption does not imply that the total background rate is identical in both regions.

The estimated parameters' values for all cases mentioned above are presented in Table 3.1. When comparing the background rate ν from the SCI set of parameters with the SR and SE sets, it becomes evident that the last two cases yield higher background rates for both regions. Additionally, the obtained values of p and c reveal that when SCI parameters are used, 50% of the triggered events are expected to occur within one day. In contrast, the SR set suggests that it would take around 10 days for Croatia and more than a year for Turkey to reach the same 50% probability of triggered events. It is important to note that these differences in the ETAS parameters' values may be attributed to parameter bias, model deficiency, actual differences in the properties of the earthquake phenomenon, or a combination of all of the above. To gain more insight, the following section compares these sets of parameters' values using Turing-style tests. This approach can help to shed light on the underlying reasons for the variations observed in the parameter estimates.

Table 3.1. Estimates of the ETAS parameters' values for the different cases considered

ETAS parameters estimates	SCI	Croatia		Turkey	
		SR	SE	SR	SE
ν	0.92	1.17	1.26	1.07	1.25
A (events/day/km^2)	0.093	0.11	0.081	0.078	0.04
c (days)	0.02	0.03	0.02	0.03	0.02
p	1.18	1.12	1.18	1.06	1.18
d (km^2)	0.9	4.46	0.9	0.27	0.9
q	2.0	2.84	2.0	2	2.0
γ (magnitude-1)	0.59	0.21	0.59	0.69	0.59

3.3 TESTING THE PERFORMANCE OF DIFFERENT ETAS MODEL PARAMETERIZATIONS

To assess the performance of different ETAS model parameterizations, we simulated 500 stochastic catalogues in the two considered regions using the SCI, SR, and SE sets of parameters' values. In all simulations, a fixed b-value of 1.03, obtained from the data in Central Italy, is used for consistency. For Croatia, the conditioning period covers the years 20/02/1990 to 20/02/1992, and the simulations span from 20/02/1992 to 20/02/2021. In the case of Turkey, the conditioning period encompasses the years 12/05/2000 to 12/05/2002, with simulations conducted from 12/05/2002 to 12/05/2023.

First, in Figure 3.6, we compare the magnitude distribution of the generated stochastic catalogues with the observed data for Croatia. It is evident that the median of the 500 simulations aligns well with the observed data in all cases. However, there is a slightly higher

dispersion in the low magnitude range when the SCI parameters are used. This effect may be attributed to the fact that this parameter set contains fewer background events and more triggered events, as indicated in Table 3.1.

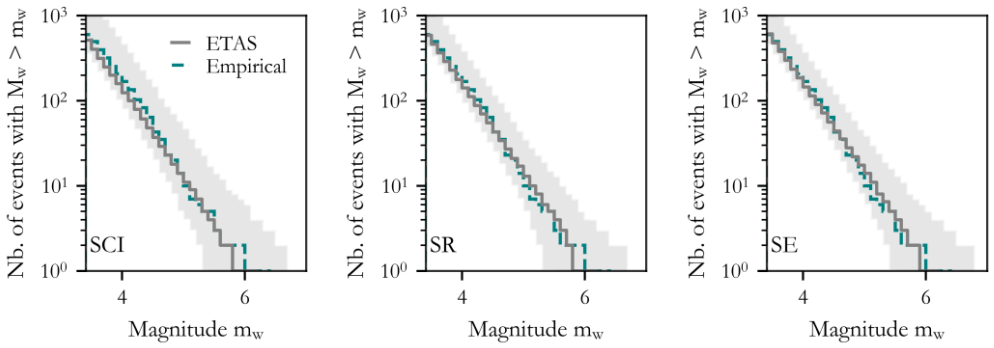

Figure 3.6. Magnitude–frequency distribution (MFD) of the events in the observed and stochastic catalogs obtained with different sets of parameters's values for Croatia for the period of 20/02/1992–20/02/2021. Solid grey lines represent the median of 500 stochastic catalogues while shaded area represents the 5th and 95th percentile. The blue line refers to the empirical data.

In Figure 3.7, we compare the ETAS model's clustering behavior with that of the observed seismicity adopting the analysis of Zaliapin et al. [2008]. Basically, with this method, the identification of clusters is centered on estimating the proxy inversely proportional to the strength of the "bond" between the two earthquake events. This proxy represents the nearest-neighbor distance, η_{ij}, in a multidimensional domain (time, location, and magnitude), and it separates the space into two subdomains: one (with lower η_{ij} values) likely contains clustered events, and the other (with higher η_{ij} values) likely contains background events. The separation between the background and clustered modes is clear in all cases, with the background peak (the one on the right) being dominant. One can see that in the SCI case, the background peak is less pronounced, as expected given the obtained parameters' values. Finally, we compared the median spatial distribution of events in the stochastic catalogs. These values are derived by counting the number of events within each grid cell and calculating the median across the 500 simulated catalogs. It is important to note that these values are normalized because our focus is on the spatial distribution rather than the actual rates. A simple visual inspection of Figure 3.8 makes clear that all models effectively represent the spatial distribution of events that was observed in the considered period.

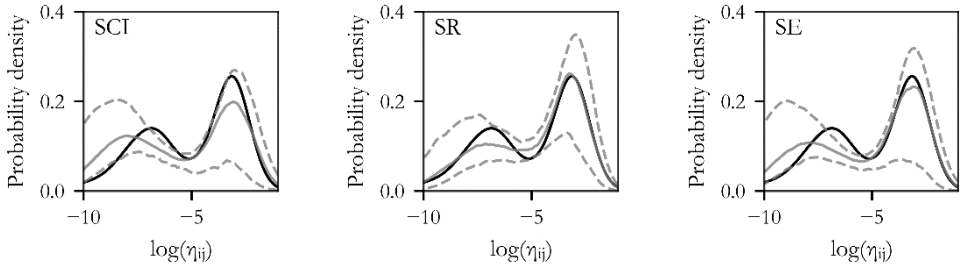

Figure 3.7. The distribution of the nearest-neighbor distance, η_{ij}, for Croatia, computed using the three considered sets of parameters' values. The solid gray line refers to the median of 500 ETAS-generated catalogs; the black one to the instrumental catalog and the dashed lines represent the 5th and 95th percentiles of the ETAS-generated catalogs.

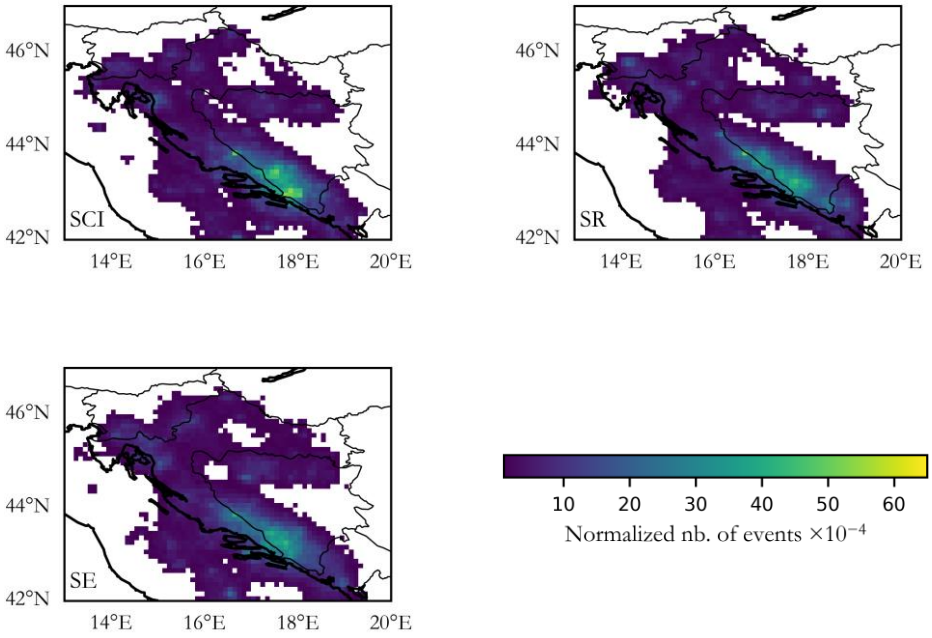

Figure 3.8. Normalized number of events for Croatia. The median of 500 stochastic catalogues is shown. Only grid cells with values above 1x10-4 are shown.

The same set of tests was conducted for Turkey. Figure 3.9 provides a comparison of the magnitude-frequency distribution, indicating that the SR and SE parameter sets tend to underestimate the number of events while the SCI set yields a good match. Additionally, it is noticeable that the dispersion in the lower magnitude range is low for the SR and SE sets,

implying that these sets might classify more events as background events when compared to the SCI set. As Figure 3.10 shows, the distribution of the n_{ij} proxy exhibits two distinct modes, which are almost equally prevalent. The clustering behavior is better described by the SCI parameter set, however, while both the SR and SE sets tend to overestimate the number of background events (right peak).

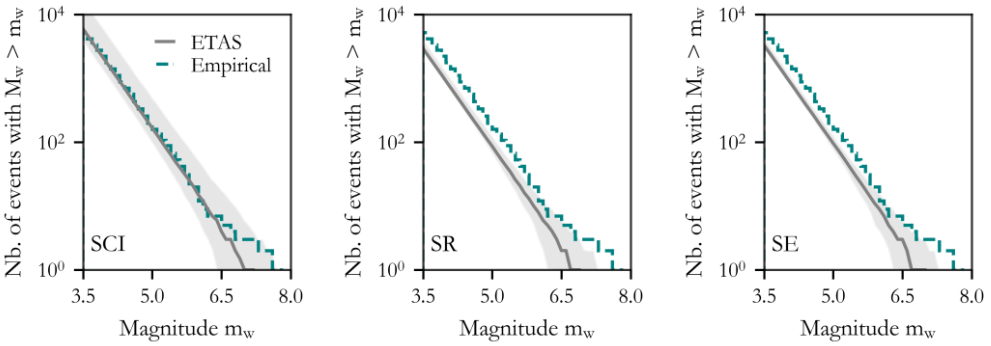

Figure 3.9. Magnitude–frequency distribution (MFD) of the events in the observed and stochastic catalogues obtained with different sets of parameters's values for Turkey for the period of 12/05/2000–12/05/2023. Solid grey lines represent the median of 500 stochastic catalogues while shaded area represents the 5th and 95th percentile. The blue line refers to the empirical data.

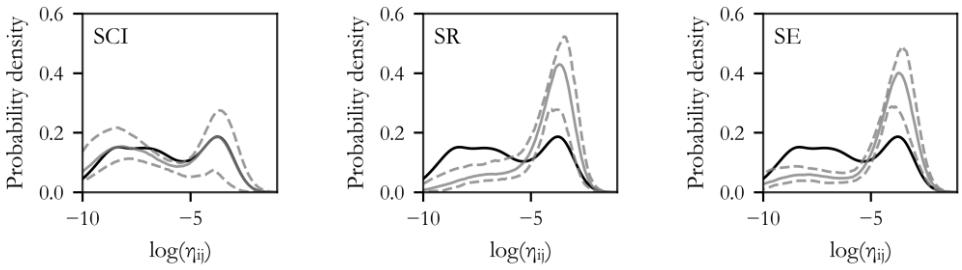

Figure 3.10. The distribution of the nearest-neighbor distance, η_{ij}, for Turkey computed using the three considered sets of parameters' values. The solid gray line refers to the median of 500 ETAS-generated catalogues; the black one to the instrumental catalog and the dashed lines represent the 5th and 95th percentiles of the ETAS-generated catalogs.

When it comes to the spatial distribution of events, a visual inspection of Figure 3.11 shows that the obtained results are in good agreement with the pattern of events in the undeclustered seismic catalogue (Figure 3.4b). It can be noticed that in the SCI case, events seem more diffused than in the other two cases, a pattern that may indicate that this set yields more triggered events than the other two.

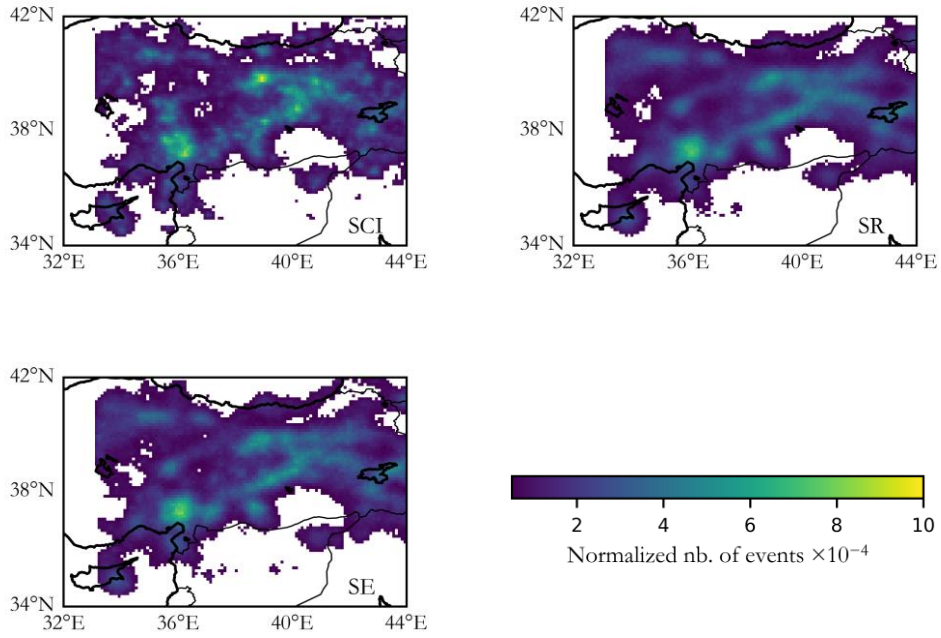

Figure 3.11. Normalized number of events for Turkey. The median of 500 stochastic catalogues is shown. Only grid cells with values above $1x10^{-4}$ are shown.

3.4 CONCLUSIONS

The primary objective of this study is to propose an optimal parameter set for the Epidemic-Type Aftershock Sequences (ETAS) model, a state-of-the-art method for modeling seismic sequences, to be applied in Croatia and the considered region of Turkey. To achieve this, we explored various parametrizations of the ETAS model. More extensively, this study tries to answer whether an ETAS-calibrated model based on a well-constrained region can be applied to other regions with the same tectonic environment but with poorer or missing instrumental catalogs.

Initially, we employed a parameter set calibrated based on the seismic activity in Central Italy, as demonstrated to be effective by Šipčić et al. [2022]. This set of parameters (denoted here as SCI) was derived using the HORUS instrumental catalogue [Lolli et al. 2020] spanning from 1981 to 2020, with a completeness magnitude of M3. It encompasses both quiet periods (absence of clustering) and active periods (significant clustering), rendering it suitable for calibrating the ETAS model, which is highly sensitive to data quality. Subsequently, we estimated the ETAS parameters's values using seismic data collected in the two specified regions (denoted here as SR): a catalogue of earthquakes from 20/02/1990 to 06/10/2021 with a completeness magnitude of 3.4 for Croatia, and another

catalogue spanning from 01/01/2000 to 12/05/2023 with a completeness magnitude of 3.5 for Turkey. Finally, we fixed all ETAS parameters to the values of the first set (SCI), except for the background seismicity rate ν and productivity term A, which were calibrated based on the available data in the respective regions.

To compare these different parameterizations, we generated for each parameterization 500 stochastic catalogues for the periods 20/02/1992 to 20/02/2021 and 12/05/2002 to 12/05/2023 in Croatia and Turkey, respectively. These catalogues were conditioned on the preceding two years of seismicity. We then compared the magnitude-frequency distribution, clustering behavior (via the η_{ij} proxy defined by Zaliapin et al. [2008]), and spatial distribution of events with empirical data. Our findings revealed that in the case of Croatia, all defined parameter sets demonstrated good agreement with empirical data. Conversely, in the case of Turkey, the SR and SE parameter sets underestimated the observed number of events, predicting a more dominant background term than observed in the empirical catalogue. This discrepancy may be attributed to the poor quality of the Turkish catalogue. We speculate that the underestimation of the productivity term may be linked to "interrupted" data related to the seismic sequence that was initiated in February 2023, which is likely still ongoing. Nonetheless, the SCI parameter set generated catalogues that aligned well with observations.

Based on the findings of this study, we can conclude that the set of ETAS parameters' values calibrated based on the Central Italy region, which is well-constrained, can be used to represent seismicity in Croatia and Turkey.

4.MODELING DAMAGE ACCUMULATION IN RC COLUMNS

4.1 INTRODUCTION

In the current Performance-Based Earthquake Engineering (PBEE) framework [Cornell and Krawinkler 2000] the seismic performance of a structure is evaluated by using performance measures that are meaningful to the stakeholders. Following the methodology developed by PEER, this framework encompasses four steps. Firstly, the seismic hazard at a site is characterized in a probabilistic manner, commonly via Probabilistic Seismic Hazard Analysis, or PSHA, in terms of Mean Annual Frequency (MAF) of exceeding predetermined levels of a ground motion Intensity Measures (IMs) (e.g., spectral accelerations at given vibration periods) considered independently. Less frequently, seismic hazard is defined in terms of MAF of equaling multiple IMs considered jointly, in which case Vector-valued PSHA is used [Bazzurro 1998]. Secondly, response analysis is performed, using either static or dynamic analysis, resulting in a vector of engineering demand parameters (EDPs) (e.g., maximum inter-story drift or peak floor acceleration) that serve as predictors of damage to structural components (e.g., columns or beams) or to the entire structure (in this study we will focus on components). This prediction yields the probability that different EDP values are reached or exceeded when the structure is subject to ground motions of any given IM value. Subsequently, the damage measures (DMs), such as cracking, yielding, or fracture, which effectively reflect the condition of the component and serve as an indicator of the level of damage sustained, are estimated based on these EDPs. Specific values of these EDPs are then associated with the onset of the aforementioned physical damage states. These two past steps are then joined to generate sets of fragility functions, each one of which provides the probability that the component will end up in a given damage state or worse should it experience a ground motion of different IMs. Lastly, DMs are related to the decision variable of interest (DV), such as repair cost, downtime, fatalities, and, more recently, sustainability metrics [Wei et al. 2016].

To perform a comprehensive loss assessment of a single building, one first needs to identify anticipated damage mechanisms and, based on them, identify the component groups such as joints, beams, columns, or infill walls for which fragility curves need to be developed. Although damage can arise from complex relationships between damageability and component demands of various types, as alluded to earlier the occurrence of damage states within a component group is typically predicted using a single EDP. This parameter is

selected to be a reliable indicator of the entity of the damage and, therefore, of seismic response.

In this study, the focus is on assessing the damage sustained in reinforced concrete (RC) columns, which are the most critical elements in RC frame structures as the loss of a column's bearing capacity can result in severe structural damage and, eventually, in partial or complete structural collapse.

Given the highly complex inelastic response of RC buildings, numerous damage variables and indices have been proposed in the literature. The aim is to establish a correlation between the damage level (e.g., cracking and yielding) and demand quantities whose values can be calculated analytically. Peak noncumulative damage indices, such as ductility ratio, maximum inter-story drift, maximum rotation, stiffness degradation, and maximum curvature, have conventionally been favored due to their simplicity and practicality. In particular, maximum inter-story drift, although not a component-specific demand parameter but rather a story-specific one, has consistently demonstrated its effectiveness as the primary indicator of potential damage in columns, as shown in several studies [Bearman 2012; Elwood et al. 2005; Pagni and Lowes 2006]. Its convenience lies both in its easy documentation during experiments and its calculation during numerical analysis. Experimental studies showed that peak noncumulative indices can effectively represent damage in well-detailed RC members that are not supposed to experience shear failure or bond-slip [Cosenza and Manfredi 2000] and their use may be suitable in cases when structures are subjected to impulse-type or short-duration ground motions. However, one can easily think of a scenario where cumulative EDPs could be a more rational choice, such as in situations when structures are subject to very long ground motions, such as those caused by large-magnitude interface events occurring in subduction zones or when the accumulation of damage is expected. Being able to reliably estimate cumulative damage is especially relevant in the aftermath of severe earthquakes when financial constraints or short intervals between subsequent earthquakes limit the time available for repairs. We will focus on this latter case here. The recent seismic sequences, such as the 2010–2011 Darfield-Christchurch in New Zealand [Shcherbakov et al. 2012], the 2011 Van in Turkey [Di Sarno et al. 2013], the Great East Japan Earthquake [Goda et al. 2013], the 2016-17 earthquake sequences in central Italy [Sextos et al. 2018a], as well as the recent Zagreb-Petrinja 2020-2021 earthquakes in Croatia [Atalić et al. 2021], highlighted the potential increase in building vulnerability due to limited repair opportunities and elevated hazard. Nonetheless, traditionally, when estimating risk, structures are assumed to be in pristine condition, an assumption that can lead to underestimating damage and losses, ultimately resulting in misinformed decisions.

The impact of adopting this assumption in assessing the risk of RC structures has been investigated in several studies that primarily employed simplified models and noncumulative EDPs to assess the influence of seismic sequences on the response of different structures. Recent studies have shed light on the limitations of such EDPs. Baraschino et al. (2023) examined the efficacy of inelastic peak displacement demand in describing the structural damage sustained during seismic sequences. Their findings

revealed counterintuitive results, suggesting that in certain instances, the probability of collapse decreased when considering pre-existing damage in the structure. Pedone et al. [2023] emphasized the advantages of adopting energy-based EDPs in state-dependent fragility analysis, using a reinforced concrete building as a case study and highlighted the need to calibrate these EDPs further with experimental data. Ge et al. [2022] explored the performance of RC bridge piers subjected to seismic sequences, comparing drift and energy-based performance measures through both experimental and analytical models, and concluded by stating the superiority of energy-based metrics. Wen et al. [2017] studied a five-story RC concrete bare frame, and investigated the effectiveness of different EDPs (peak roof displacement, peak inter-storey drift, residual displacement and hysteretic energy). The conclusions were, again, that energy-based damage measures can more efficiently reflect the additional damage induced by seismic sequences.

This study aims to delve into the modeling of the progression of damage in RC columns and focuses on the calibration of a novel energy-based EDP based on the modified Park and Ang damage index [Kunnath et al. 1997; Park and Ang 1985]. This index is expected to effectively identify various damage states and, consequently, serve as a strong candidate for the development of fragility and vulnerability curves in the realm of clustered seismicity risk assessment. We first assemble a comprehensive database of experimental tests conducted on RC columns and we provide a detailed description of the characteristic points on the force-displacement curve, such as the cracking point and yield points extracted from the data, that are key elements in the proposed index calibration process. Subsequently, we define and describe the damage states based on the available experimental data and existing literature, categorizing the columns into those failing in flexure mode, or in shear mode, or in flexure-shear mode, as their responses can differ significantly. We proceed to calibrate the newly proposed damage index for each of the aforementioned column failure modes using the assembled database. To validate the effectiveness of the calibrated index, we compare its predictions with additional experimental tests reported in the literature. Lastly, we model several single-degree-of-freedom systems (SDOFs) and a multi-degree-of-freedom system (MDOF), subjecting them to back-to-back (B2B) Incremental Dynamic Analysis (IDA)[Vamvatsikos and Cornell 2002]. This analysis aims to explore the progression of damage and reduction of capacity under seismic sequences, employing both the proposed energy-based damage index and the more conventional peak displacement-based EDP.

4.2 COLUMN DATABASE

To assemble the database of experimental tests (we will refer to it simply as DB in the remaining text), we use two main sources: (1) data gathered by the ACI committee 369 described in more detail in Sivaramakrishnan [2010], as the primary source for the database, and (2) the database developed for the SERIES research project, described in more detail in Perus et al. [2014]. These databases are built on the Pacific Earthquake Engineering Research Center (PEER) Structural Database [Berry et al. 2004], with some additional experiments extracted from published reports of different authors. In the current version, only rectangular RC columns are included and all specimens are subjected to the pseudo-

static cyclic loading. The compiled database provides force-displacement histories that are either obtained directly from the researchers or digitized from force-displacement plots in source documents. As the columns in the database have different test configurations (single cantilever, double-ended, double-curvature), for consistency, the provided force-displacement histories are transformed to correspond to the cantilever case regardless of the test configuration. For each column the DB includes details about the geometrical and material properties, reinforcing details, test configuration, applied axial load, and other relevant information. In total, there are 370 specimens, 54 of which are from the SERIES and 316 from the ACI369 database; 251 columns are flexure-dominated, 36 shear-dominated and the remaining 83 flexure-shear dominated. More detailed description of the assembled DB can be found in Appendix B1.

In addition to the given properties, from the available force-displacement data we extracted the values corresponding to the characteristic points on the force-displacement curve, such as the cracking point, yield point, point of the maximum applied load, and point where the ultimate displacement is reached. The cracking point corresponds to the point where flexural cracking occurs when the concrete tensile stress exceeds the tensile strength. The cracks mainly appear at the bottom and top 1/3 of the column, perpendicular to its axis. To estimate the cracking point, we perform sectional analysis using the OpenSees software. We create the zero-length section with the fiber discretization of the cross-section. We use the *Steel02* uniaxial constitutive model to model the behavior of steel with the yield strength as provided in the database, strain-hardening ratio equal to 0.01, and elastic modulus of 210GPa. We use the *Concrete02* uniaxial material model with compressive strength as given in the database for unconfined concrete. The ultimate strength of concrete is taken as 5MPa, tensile strength as 10% of the compressive strength, tension softening stiffness as 5GPa, strain at maximum strength as 0.002, and strain at ultimate strength as 0.005. The properties of the confined concrete are then calculated using the Mander model. We apply axial load and rotation of 0.001 to the section (equivalent to curvature for a zero-length section) and, in this manner, we can get the moment-curvature M-ϕ curve and detect the point where the tensile strength of concrete is exceeded. Once the curvature and moment at cracking are found, displacement and force are calculated as:

$$d_{cr} = \frac{\phi_{cr} \cdot L^2}{3}, F_{cr} = \frac{M_{cr}}{L} \tag{4.1}$$

where L is the shear span of the column. It is assumed that the column is fixed at the base and that curvature varies linearly along its height.

The point of yielding is usually associated with longitudinal cracking (parallel to the axis of the column), the onset of concrete spalling, or cracking at an angle (shear cracking). The definition of the yielding point is not straightforward, and several approaches exist in the literature. To find this point we distinguish columns with flexure and shear mode failure. In the case of flexure failure (and flexure-shear failure), we define the yield displacement as the sum of the displacements due to flexure, bar slip, and shear:

$$d_y = d_{y,f} + d_{y,s} + d_{y,sh} \tag{4.2}$$

Flexural displacement, similarly to the displacement at cracking, can be found as:

$$d_{y,f} = \frac{\phi_y \cdot L^2}{3} \tag{4.3}$$

To find yield curvature ϕ_y we again use the results of the moment-curvature analysis. We define the point of "first yield" as the one where either the first reinforcing bar yields in tension or the concrete reaches a maximum compressive strain of 0.002. Corresponding moment and curvature are noted as M'_y and ϕ'_y. The point of "nominal yield" is defined as the point where either the concrete compressive strain of 0.004 or the steel tensile strain of 0.015 is reached. The corresponding moment is noted M_y and curvature at yield is found as:

$$\phi_y = \frac{\phi'_y \cdot M_y}{M'_y} \tag{4.4}$$

In this manner, we obtained the idealized moment-curvature backbone curve, as illustrated in Figure 4.1a. Contribution of the displacement due to slip is found following the methodology of Elwood and Eberhard [2006]:

$$d_{y,s} = \frac{L \cdot d_b \cdot f_s \cdot \phi_y}{8 \cdot u} \tag{4.5}$$

Where f_s is the stress in the tension reinforcement (see Elwood and Eberhard [2006] for details), and u is the average bond stress between the longitudinal reinforcement and the footing, assumed as $0.041\sqrt{f_c}\,[MPa]$. Displacement due to shear, which usually has small values that can be neglected, is estimated using Equation (4.6), and then the total displacement at yield is found using Equation (4.2).

$$d_{y,sh} = \frac{M_y}{(A \cdot G)_{eff}} = \frac{5 \cdot M_y}{6 \cdot b \cdot d \cdot 0.4 \cdot E_c} \tag{4.6}$$

As pointed out by Elwood and Eberhard [2006], the yielding point can be estimated as described above in cases where the maximum effective force measured is at least 105% of the force at yield. However, when pure shear occurs, the maximum force is reached before the first yield of the section, and, in that case, we define the yield point using the secant method. We first define the yielding force F_y as 0.95 of the maximum effective force, F_{max} (without the P-delta effects). The yield displacement is defined as the point where the line that connects the zero point and the point on the force-displacement curve where $F=0.5 \cdot F_{max}$ intersects with the horizontal line passing through the $0.95 \cdot F_{max}$ as illustrated in Figure 4.1b.

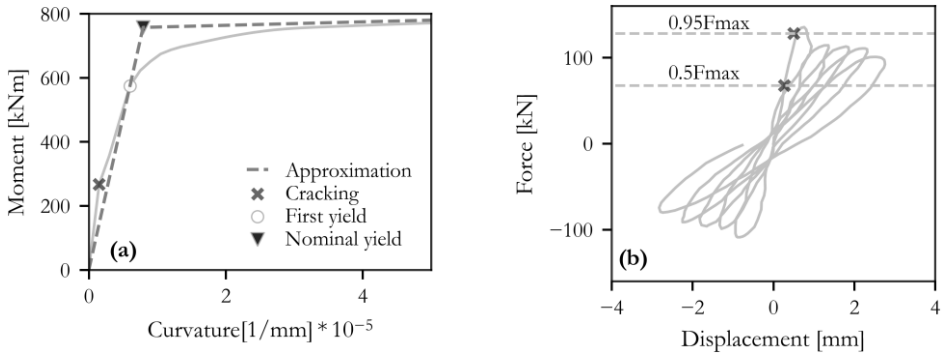

Figure 4.1. Estimation of the yield point for (a) flexure-dominated columns (Test 25 from the DB) and (b) shear-dominated columns (Test 258 from DB).

The capping point is the point at which the maximum force is attained, indicating the onset of decay. The ultimate displacement is determined as the maximum displacement recorded during the experimental testing. However, these values pertain to the cyclic backbone response. To obtain the ultimate displacement under monotonic loading, we adhere to the guidelines of ATC-2, which state that the plastic displacement d_p under cyclic loading is considered to be 70% of the plastic displacement observed under monotonic loading. Similarly, the post-capping displacement d_{pc} under cyclic loading is estimated as 50% of the corresponding displacement observed under monotonic loading (see Figure 4.2a). In some cases, the ultimate displacement under cyclic loading coincides with the capping displacement, indicating no loss in strength. In such cases, the ultimate displacement under cyclic loading was estimated as 1.1 times the displacement at the capping point under cyclic loading, which represents the lower bound value.

As an example, we show in Figure 4.2b the response of specimen C1-2 from Mo and Wang [2000] with displacement at yield, capping displacement, and ultimate displacement under cyclic and monotonic loading found as explained above. It is worth noting, however, that in some instances the aforementioned procedure for determining the characteristic points yielded results that lacked coherence. In these cases, the results were corrected through a visual examination of the force-displacement curve and reference to the information provided in the reports of the original experimenters, if available. Alternatively, if the correction was not feasible or reliable, the data was disregarded and flagged as unreliable.

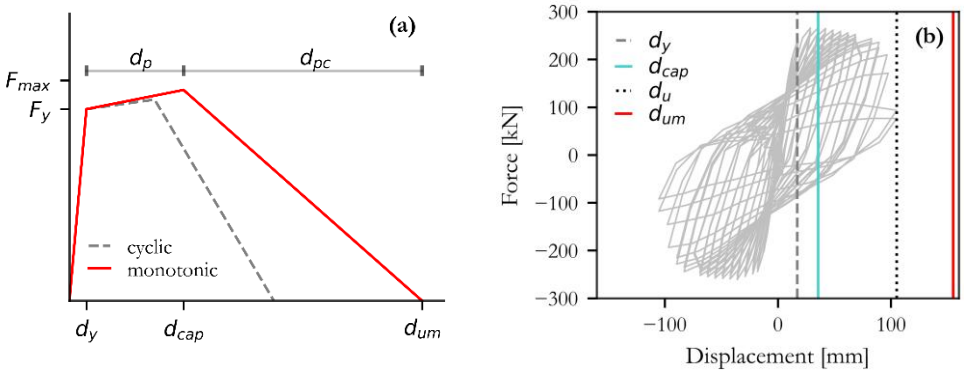

Figure 4.2. (a) Idealized monotonic and cyclic backbone response (b) cyclic response of the specimen C1-2 from Mo and Wang [2000] (Test 107 from DB) with characteristic points indicated.

4.3 DAMAGE PROGRESSION IN RC COLUMNS

Depending on the several critical parameters, such as axial ratio, reinforcement ratio, confinement details, etc. RC columns can experience failures either in flexure mode, or flexure-shear mode, or pure shear mode [Camarillo 2003]. In this section, we describe the damage progression in these different cases. In subsequent sections, for brevity, we refer to flexure-critical columns as FC, shear-flexure columns as SFC, and shear-critical columns as SC.

The flexural mode of failure in RC columns occurs when the shear force developed is below the shear strength. Typically, these column types can take relatively large lateral deformations. To define the damage states, we rely on the experimental tests conducted by several researchers, as well as the accompanying reports and photos [Bae 2005; Bearman 2012; Berry and Eberhard 2003; Borg 2015; Mo and Wang 2000; Sivaramakrishnan 2010; Tanaka 1990].

- Damage state one (DS1) corresponds to the point where flexural cracking occurs when the concrete tensile stress exceeds the tensile strength. The cracks mainly appear at the bottom and top third of the column, perpendicular to its axis. Additionally, this damage state includes longitudinal cracking (parallel with the column axis) near the column-beam interface, followed by the yielding of steel bars in tension [Tanaka 1990; Mo and Wang 2000], the propagation of cracks toward the inner part of the column, and shear cracking (typically oriented at an angle of 35 to 65 degrees from the horizontal) [Bearman 2012]. Significant residual crack may occur (exceeding 1.5cm) requiring epoxy injections (ATC-58, Porter et al. [2006]).
- Damage state two (DS2) is associated with the onset of concrete cover spalling exposing the transverse but not the longitudinal reinforcement. Typically, it first occurs on the flexural side, but upon loading reversals, it also extends to the side faces. The onset of concrete cover spalling is the first damage state where safety implications are possible (although marginal), and related repair costs might be high [Berry and Eberhard 2008]. The point at which the onset of spalling occurs is usually associated with the maximum compressive strain being reached and, hence, can be associated with the point where maximum force is obtained.
- Damage state three (DS3) is associated with a more significant spalling of concrete, with steel (also longitudinal) being exposed (ATC-58) at the top and the bottom of the column and ties potentially starting to yield.
- Damage state four (DS4) is associated with major safety implications and usually requires partial or total replacement [Berry and Eberhard 2008]. It corresponds to the buckling of longitudinal bars (i.e., the bar is curved outwards), crushing of the concrete core, bar fracture and loss of axial capacity. DS4 corresponds to complete failure of the column. Concrete crushing typically occurs when transverse reinforcement has yielded (usually due to the buckling of longitudinal reinforcement).

In Figure 4.3a, as an example, we show the response of a column subject to cyclic loading that fails in flexure with the damage description as reported by the authors [Mo and Wang 2000].

Columns that experience failure before flexural yielding are classified as SC columns. They are characterized by brittle failure and significant degradation in force-displacement behavior. Compared to FC columns, they can typically sustain lower deformations. As in the case of flexure-dominated RC columns, to define the damage states associated with the progression of damage, we use the experimental data provided by several researchers [Henkhaus et al. 2013; Lynn et al. 1996; Sezen 2000] along with the reports and photos accompanying these experiments.

- Damage state one (DS1) corresponds to the point where we have flexure-shear cracks that are intersecting followed by the formation of splitting cracks along the tensioned reinforcement and longitudinal cracks in the compressed concrete [Sezen 2000].
- Damage state two (DS2) occurs before the failure of the column and is associated with the widening and localization of the shear cracks. This is followed by the spalling of concrete.
- Damage state three (DS3) is associated with the failure of the column – longitudinal bar buckling which can occur quickly after the spalling of the concrete, yielding of transverse reinforcement, which triggers the crushing of the concrete core, after which axial failure is reached.

In Figure 4.3b we show the response of a column subject to cyclic loading that fails in shear with the damage description as reported by the authors [Umehara and Jirsa 1982].

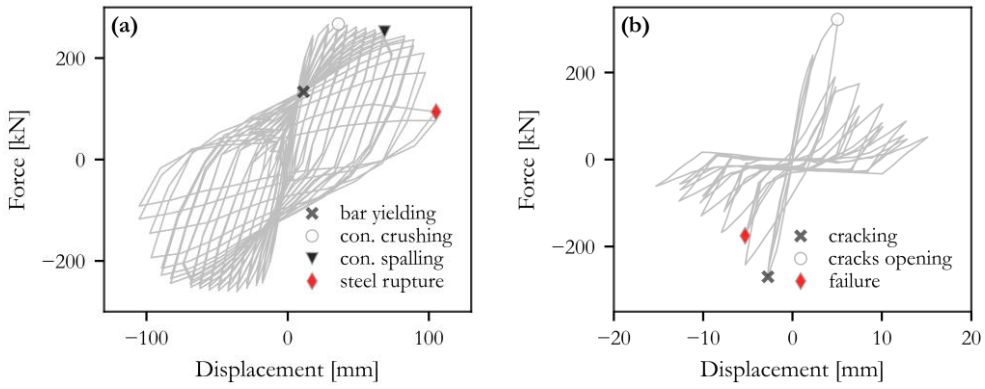

Figure 4.3. Typical behavior of (a) flexure-critical column (specimen C1-2 from Mo and Wang [2000]) and (b) shear-critical column (specimen CUS from Umehara and Jirsa [1982]).

The response of the flexure-shear-dominated columns is the combination of flexure and shear-dominated response previously described. First, the column behaves in a flexural

mode, with the damage progression corresponding to the damage states one and two in the flexure-dominated case. Then the specimen fails in the shear manner, as described in the damage state three of the shear-dominated case.

Table 4.1 provides a concise and clear synthesis of the proposed damage states.

Table 4.1. Description of damage states for different failure modes (FC:flexure-critical, FSC:flexure-shear-critical, SC:shear-critical)

	FC	FCS	SC
DS1	Flexural cracking and longitudinal cracking (parallel with the column axis) near the column-beam interface, followed by the yielding of steel bars in tension; significant residual cracks may occur;	Flexural cracking and longitudinal cracking (parallel with the column axis) near the column-beam interface, followed by the yielding of steel bars in tension; significant residual cracks may occur;	Flexure-shear cracking followed by the formation of splitting cracks along the tensioned reinforcement and longitudinal cracks in the compressed concrete;
DS2	The onset of concrete cover spalling exposing the transverse reinforcement; safety implications are possible (although marginal);	The onset of concrete cover spalling exposing the transverse reinforcement; safety implications are possible (although marginal);	Widening and localization of the shear cracks, followed by the spalling of concrete;
DS3	A more significant spalling of concrete, with steel being exposed at the top and the bottom of the column; ties potentially starting to yield;	Failure of the column – longitudinal bar buckling, spalling of the concrete, yielding of transverse reinforcement, crushing of the concrete core, axial failure;	Failure of the column – longitudinal bar buckling, spalling of the concrete, yielding of transverse reinforcement, crushing of the concrete core, axial failure;
DS4	Major safety implications; buckling of longitudinal bars, crushing of the concrete core, bar fracture, and complete failure of the column;		

4.4 DAMAGE INDEX CALIBRATION

Despite the attention that energy-based EDPs recently received in the research community, there is a limited number of well-defined EDPs. One such example, arguably the most used one, is the rather old Park and Ang damage index [Park and Ang, 1985], which assumes a linear relationship between energy and deformation terms and is defined as follows:

$$DI_{PA} = \frac{d_{\max}}{d_{u,m}} + \frac{\beta \cdot \int dE}{F \cdot d_{u,m}} \tag{4.7}$$

where d_{max} represents the maximum displacement during the analysis, $d_{u,m}$ represents the ultimate displacement under monotonic loading, $\int dE$ represents the dissipated energy, F_y represents the yield force, and β is a parameter calibrated based on the experimental data. Dissipated energy is found by integrating the force-displacement curve as shown below:

$$\int dE = \int_0^{d_{\max}} F(d)dF = \sum_0^{d_{i+1}=d_{\max}} \frac{F_{i+1} - F_i}{2}(d_{i+1} - d_i) \tag{4.8}$$

where i is the number of points used for discretization. Kunnath et al. [1997] later proposed a modified version of the damage index by replacing displacement with curvature and subtracting the elastic term, resulting in:

$$DI_{PA_k} = \frac{\phi_{\max} - \phi_y}{\phi_{u,m} - \phi_y} + \frac{\beta \cdot \int dE}{M_y \cdot \phi_{u,m}} \tag{4.9}$$

In this equation, $\phi_{\max}$ represents the maximum curvature, $\phi_{u,m}$ represents the ultimate curvature under monotonic loading, ϕ_y is the yield curvature, M_y represents the yield moment and the remaining variables are defined as in the original DI_{PA}.

In this study, we consider the DI given by Equation (4.10) and proceed by calibrating the values of the parameters in it based on our larger DB of experimental tests.

$$DI_{M_k} = \frac{d_{\max} - d_y}{d_{u,m} - d_y} + \frac{\beta \cdot \int dE}{F_y \cdot (d_{u,m} - d_y)} \tag{4.10}$$

Estimating the value of the parameter β has been recognized as the critical component when using the proposed damage index and different authors have reported significantly dissimilar values based on their respective databases. [Cosenza et al. 1993] stated that observed values of β range from -0.3 to 1.2, with a median value of 0.15. This value, derived from regression analysis of experimental data, has been adopted in several studies. We calibrate the value of β depending on the expected failure mechanism of the column. To calibrate the damage index for flexure-critical columns, we use Equation (4.10) as the starting point. The ultimate displacement under monotonic loading, yield force and yield displacement are extracted from each experiment considered, as described in Section 4.2. Subsequently, using Equation (4.11) we determine the value of the parameter β for each experiment, assuming that the damage index reaches a value of one at the point of collapse.

Out of all the tests collected, we selected 90 experiments with reliable data (an additional 5 experiments were retained for validation). In this manner, we obtained the median value of β=0.1, while the standard deviation of the DI calculated with the median β is 0.31.

$$\beta = \frac{E_{mon}}{\int dE} \cdot (1 - \frac{d_{\max} - d_y}{d_{u,m} - d_y}) \tag{4.11}$$

To reduce the variability, we modified the damage index by adding the parameter γ, as can be seen in Equation (4.12). Upon analyzing the data, we observed that the ratio between displacement and energy terms differs for cases with many cycles (at least 17) compared to those with fewer cycles. Therefore, using linear regression, we established a relationship between γ and the number of cycles (as shown in Figure 4.4). By employing the proposed median value of β=0.1 and calculating γ using the derived equation, we found that the standard deviation in the calculated damage index reduced from the initial 0.32 to 0.13. Note that the number of cycles in this context, refers to the number of cycles after the yielding point, not to the total number of cycles.

$$DI_N = \frac{d_{\max} - d_y}{d_{u,m} - d_y} + \frac{\beta \cdot \int dE}{\gamma \cdot (d_{u,m} - d_y)} \tag{4.12}$$

To validate the proposed model, we used five experiments not included in the calibration process. We calculated the DI for each experiment and obtained the values of 1.00, 1.03, 1.07, 1.02 and 0.86, which indicate that the damage index produces more than acceptable results.

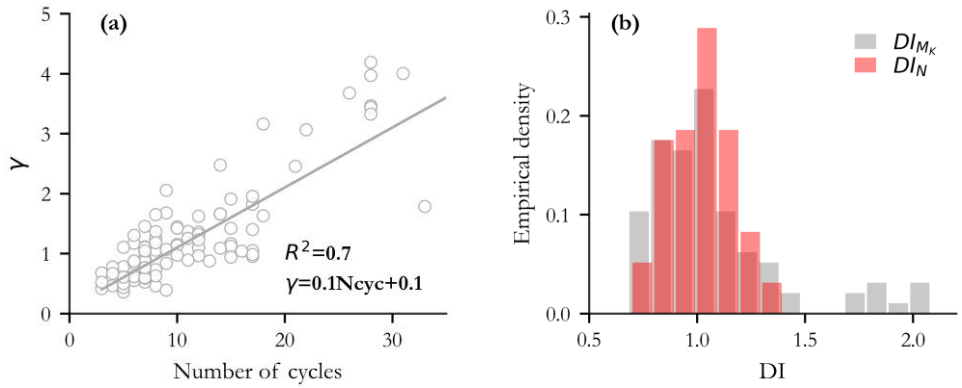

Figure 4.4. (a) Fitted linear regression between the number of cycles and γ parameter; scatter points refer to the experiments. (b) The distribution of the DI defined in two manners: using Equation (4.10) (DI_{Mk}) and using Equation (4.12) (DI_N).

It is important to highlight that although the proposed damage index reduces the standard deviation in DI given with Equation (4.10), it can be challenging to estimate the number of cycles in practical applications. This difficulty arises from the ambiguity of defining what

constitutes a cycle, which can vary depending on the context. Interested readers can explore various propositions from the literature (e.g. Hancock and Bommer [2005]). Even when clear criteria for defining a cycle are established, the task of extracting this information for each ground motion can be time-consuming and computationally heavy. For the time being, as a practical alternative, we recommend using the DI given by Equation (4.10) to circumvent the complexities associated with cycle counting.

We extend our investigation to include cases where specimens fail in shear and flexure-shear modes. It is important to note that we had a significantly smaller number of specimens with good quality in these cases, specifically 36 for SC and 40 for FSC columns. Similar to the approach used in the previous section, we initially estimated the value of parameter β using Equation (4.11). The median value obtained for SC columns is 0.3, and the standard deviation in the damage index was found to be 0.2. A higher value of β was expected considering that SC columns typically experience greater deterioration compared to FC ones. Upon introducing the parameter γ, we did not observe any correlation with the number of cycles. Generally, these specimens exhibited lower dissipation of energy and a reduced number of cycles until collapse, in comparison to the FC columns. Nevertheless, we did observe a correlation between the ductility ratio μ (calculated as the ratio between ultimate and yield displacement) and the damage index, as demonstrated in Figure 4.5. By utilizing the equation illustrated in the figure, we re-calculated the damage index, resulting in a reduced standard deviation of 0.12.

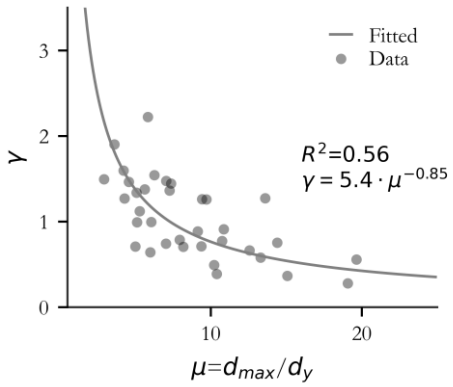

Figure 4.5. The fitted model between the ductility μ and parameter γ; scatter points refer to the experiments.

Regarding FSC columns, we found no correlation between the parameter γ and neither the number of cycles nor ductility. Consequently, we employed the damage index defined by Equation (4.10), using β =0.15 which was estimated as the median from the experiments. The standard deviation of the damage index calculated in this manner is 0.19.

The limited number of experiments conducted in these cases precluded the allocation of some specimens solely to validation, namely excluding them from the calibration process.

Nevertheless, in the subsequent sections, we utilize shake table tests to at least partially validate the proposed indices.

4.5 DI VALUES CORRESPONDING TO THE DAMAGE STATES

Damage indices, in general, are normalized quantities ranging from 0 (no damage) to 1 (total damage). Park et al. [1987] associated damage states with the damage index as follows: $0<DI<0.2$ corresponds to minor damage, $0.2<DI<0.4$ to moderate damage, $0.4<DI<1.0$ to severe (unrepairable) damage, and $DI>1.0$ to total collapse. Even though these values were proposed many years ago they are still widely used, to the authors' knowledge, without further investigation. To determine the values of the DI that correspond to the thresholds of the proposed damage states given in Table 4.1, an extensive analysis was conducted on the available experiments that provided comprehensive descriptions of damage progression. The cases considered were again divided into three categories: FC, SC, and FSC columns.

For the FC columns, a total of 17 experiments from the DB were utilized. For these experiments, detailed descriptions of damage during cyclic tests were provided. For each experiment, the instances in the force-deformation history at which damage was reported by the respective authors were identified and linked to one of the damage states. The corresponding DI values were then estimated using Equation (4.12). It should be noted that in most cases, however, the identification of the instants corresponding to the reported damage description required determining the time step at which the damage occurred based on the figures provided by the authors. This process may have introduced some slight approximations that, however, we consider negligible for all practical purposes. Additionally, it is important to highlight that this procedure is not without limitations, as the damage observed during the experiment is typically reported at the end of the cycle.

To illustrate this procedure, Figure 4.6 presents the force-displacement plot for Unit 6 from Tanaka (test 23 from DB), where the authors reported damage occurrences such as first yielding of tension reinforcement, first yield of compression reinforcement, first crashing of cover concrete, onset of concrete spalling, opening of ties, and commencement of buckling of longitudinal reinforcement. One can see points corresponding to the yielding of the steel, onset of spalling and buckling which we associate with DS1, DS2 and DS4, respectively, from Table 4.1. The figure also displays the progression of the proposed DI values and the associated reported damage. The ranges of the DI values corresponding to each damage state reported in Table 4.2 are based on the fitting of all the available experiments such as that considered here as an illustrative example.

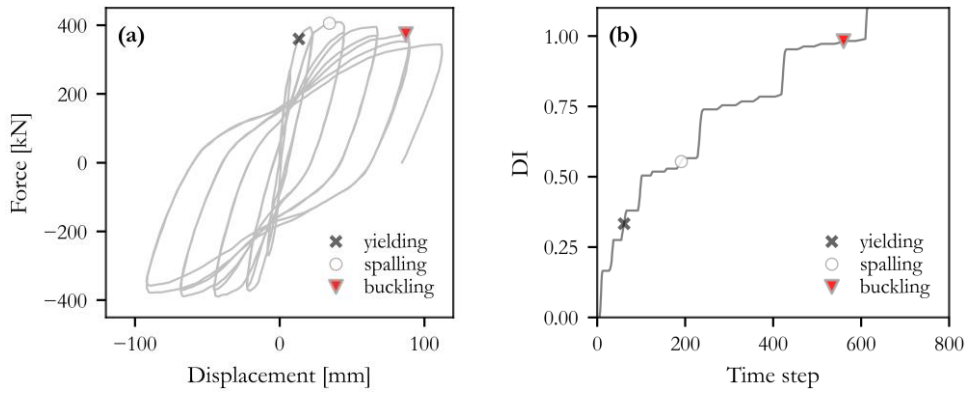

Figure 4.6. (a) Force displacement plot for Unit 6 from Tanaka (test 23 in the DB) with the different damage occurrences indicated, as reported in the corresponding experiment and (b) the progression of the proposed DI with the same damage occurrences indicated.

Table 4.2. Proposed DI ranges for FC columns and different damage states

	Median value	16th - 84th percentile	Proposed range	Description of damage
DS1	–	–	0–0.2	Flexural and longitudinal cracking, yielding of steel bars in tension, followed by shear cracking.
DS2	0.28	0.2-0.50	0.2–0.4	The onset of concrete spalling exposing the transverse reinforcement.
DS3	0.53	0.44-0.65	0.4–0.75	More significant spalling of concrete, longitudinal steel is exposed, the potential start of tie yielding.
DS4	1.0	0.88-1.10	>0.75	Major safety implications, bar buckling, concrete core crushing, fracture of the bars, complete failure.

As already mentioned, our assembled DB contains limited experimental data in the case of shear and flexure-shear critical columns. Moreover, extracting information from the corresponding reports proved to be challenging in many cases. Therefore, we resorted to utilizing force-displacement histories to define the DI ranges for damage states for these columns. To characterize the damage states, we associated DS1 with the point of yielding, DS2 with the capping point, and DS3 with either the point where the remaining capacity drops to 80% of the original value or the point of axial collapse if reported during the experiment). Based on the obtained results, we propose the values given in Table 4.3.

It is important to note that the obtained results reveal a counterintuitive observation: the median value of the DI associated with DS3 is significantly lower than 1. This discrepancy arises from the calibration process adopted here. The thresholds were established using either the point of axial collapse or the point where the capacity drops to 80% of the original value. In the latter case, although the specimen has not completely collapsed, it exhibits damage severe enough to be considered irreparable. Thus, the DI values significantly lower than 1 associated with the onset of DS3 reflect the consideration of severe damage that occurs immediately prior to complete collapse.

A similar procedure was followed for the FSC columns and the proposed ranges can be seen in Table 4.4.

Table 4.3. Proposed DI ranges for SC columns and different damage states

	Median value	16^{th} - 84^{th} percentile	Proposed range	Description of damage
DS1	–	–	0–0.25	Flexure-shear cracking, formation of splitting cracks.
DS2	0.27	0.15-0.4	0.25–0.45	Widening and localization of the shear cracks, the onset of concrete spalling.
DS3	0.73	0.45-0.90	>0.45	Longitudinal bar buckling yielding of transverse reinforcement, crushing of the concrete core, axial failure.

Table 4.4. Proposed DI ranges for FSC columns and different damage states

	Median value	16^{th} - 84^{th} percentile	Proposed range	Description of damage
DS1	-	-	0–0.15	Flexural and longitudinal cracking, yielding of steel bars in tension, followed by shear cracking.
DS2	0.33	0.14-0.74	0.15–0.60	The onset of concrete spalling exposing the transverse reinforcement.
DS3	0.9	0.6-1.2	>0.60	Longitudinal bar buckling yielding of transverse reinforcement, crushing of the concrete core, axial failure.

4.6 VALIDATION WITH THE SHAKE TABLE TESTS

To further validate our results, we examined the available data from shake-table tests. We utilized the shake table tests column database compiled by Li [2012]. This database includes large-scale columns within two-dimensional frames, derived from seven shaking table test programs. It provides detailed information about column properties, including geometry, material composition, axial load, mode of failure, etc. In total, the database comprises 59 columns, with 36 categorized as non-ductile featuring inadequate confinement, and 23 classified as ductile with sufficient transverse reinforcement. Specifically, for non-ductile flexure-shear critical columns, the database offers crucial details about each experiment, such as the point of yielding, the capping point, and the point at which columns experience axial failure. For 23 columns from the shake table tests available, we identified the time step at which these points occurred and associated them with the damage states outlined in Table 4.4. More specifically, we associated the point of yielding with DS1, the capping point with DS2 and the point of axial failure with DS3. For each damage state, we calculated the DI using Equation (4.10) and β value of 0.15, as the considered columns are classified as FSC. Displacement at yield was extracted from the corresponding references while the ultimate displacement under monotonic loading was found using the ultimate displacement under cyclic loading, which is extracted from the experimental data, following the guidelines of ATC-2, as explained in Section 4.2.

As mentioned in the Introduction, drift is commonly employed as an EDP. Therefore, for comparison, we also determined the drift values associated with the indicated damage states for these 23 tests. To accomplish this, we referred to the research conducted by Bearman [2012], who utilized data and results from [Bae 2005; Berry and Eberhard 2003; Sezen 2000]. They distinguished between cases characterized by low and high axial loads, emphasizing the distinct patterns of damage progression observed in each scenario. Specimens with an axial load ratio below 0.5 were categorized as having low axial loads, while those with an axial ratio equal to or greater than 0.5 were classified as having high axial loads. Table 4.5 shows the proposed maximum drift values corresponding to different failure modes and levels of axial load. Specifically, "LAL" denotes low axial load, while "HAL" indicates high axial load.

For each considered test, the obtained values of DI and the associated maximum drift values can be found in Appendix B2. These values are compared with the damage states defined in Table 4.4, in the case of DI, and with the values defined in Table 4.5, in the case of maximum drift. It should be highlighted that in the latter case, DS3 and DS4 were merged into one DS (i.e. DS3) and that all columns considered here have a low axial load ratio and are FSC.

Table 4.5. Values of maximum drift (%) associated with different damage states

Failure mode	FC		SC		FSC	
Axial load	LAL	HAL	LAL	HAL	LAL	HAL
DS1	0.3-1.5	0.5-1.0	0.25-2.0	0.25-1.75	0.3-1.5	0.5-1.0
DS2	1.5-2.0		2.0-2.5		1.5-2.0	
DS3	2.0-4.0	1.0-2.0	>2.5	>1.75	2.0-2.5	1.0-1.75
DS4	>4.0	>2.0	-	-	>2.5	>1.75

The proposed DI predicts the DS1 and DS3 well in all tests while DS2 is satisfactorily predicted in all but three out of 23 tests. Similarly, drift effectively predicts DS1 and DS3 in all cases, but it tends to overestimate the damage associated with DS2 in 17 out of 23 tests (more than 70% of cases). As an example, Figure 4.7a illustrates the experimental results for Test 8. Estimated values of DI for DS1, DS2 and DS3 are 0.01, 0.4 and 1.04 which means that they are well predicted when compared with the values in Table 4.4. On the other hand, values of maximum drift associated with these damage states (1.0%, 2.77% and 4.98%) indicate that DS2 is not well predicted (see FSC/LAL column in Table 4.5). In Figure 4.7b we show the results for Test 21 from Table B.3. Estimated values of DI are 0.01, 0.23 and 0.86, while the maximum drift are 1.2%, 1.81% and 2.48% for DS1, DS2 and DS3, respectively, which means that both EDPs in this case predict the damage state well.

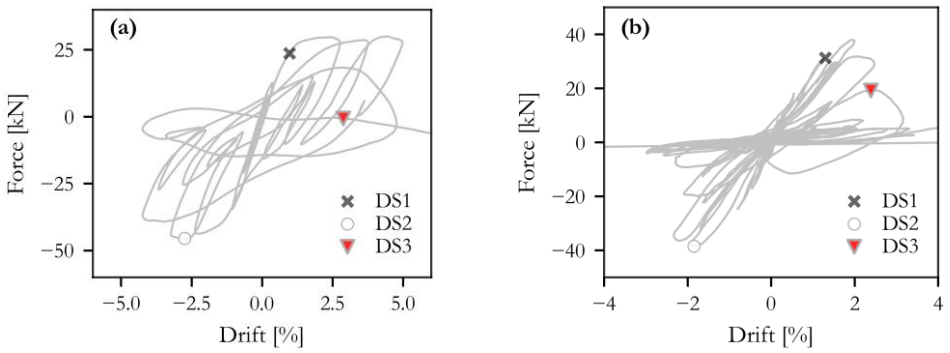

Figure 4.7. Hysteretic response of the columns from shake table tests with the indicated damage states: (a) NCREE 2005-P2-C1 (Test 8 in Table B.3) and (b) Shin 2005-III-Test 10-Chile-0.24-West C (Test 21 in Table B.3)

It is crucial to emphasize that additional experimental data are necessary to validate the effectiveness of the proposed DI and to make meaningful comparisons with drift. Specifically, having experimental data under mainshock-aftershock sequences would be

particularly beneficial in order to test how well the reduction of capacity is captured by the proposed DI.

4.7 MODELLING OF RC COLUMNS

As mentioned earlier, in most cases the nonlinear behavior of RC frames is predominantly concentrated at the ends of their members. Therefore, we considered it reasonable and computationally efficient to model these elements as elastic with rotational springs at the ends and assigned phenomenological laws (so-called lumped plasticity approach). Previous studies have explored various types of phenomenological laws, ranging from simple elasto-plastic models to more complex curvilinear hysteretic models that incorporate the deterioration of strength and degradation of stiffness. It has been demonstrated that strength deterioration and stiffness degradation can lead to a significant increase in peak displacement demand, particularly when structures are subjected to a large number of cycles, such as during earthquake sequences. As a result, several degrading phenomenological laws have been developed in the past, incorporating stiffness degradation, pinching, cyclic degradation, in-cycle degradation, or a combination of these [Ibarra et al. 2005; Kunnath et al. 1991; Leborgne and Ghannoum 2013].

Phenomenological nonlinear models are appealing as they allow us to account for the aforementioned phenomena by calibrating the model based on relevant experimental data. However, it is important to note that these models rely on empirical observations rather than fundamental mechanics principles, and estimating cyclic deterioration parameters can be particularly challenging since experimental tests are typically conducted for either monotonic or cyclic loading protocols, but not both. Additionally, a limitation of these models is that they do not consider the interaction between the bending moment and axial load (M1-M2-N interaction). As emphasized in Taucer et al. [1991], the axial load in columns can undergo significant fluctuations during ground motion, and the response of an element is generally influenced by its loading history. Moreover, energy dissipation is closely related to the axial load [Haselton et al. 2007], underscoring the importance of incorporating this interaction in the modeling process. On the other hand, fiber-based models, whether displacement-based [Bazant and Bhat 1977] or force-based [Spacone 1996], inherently account for M1-M2-N interaction. Nonetheless, employing such a model comes with substantial computational costs and may require modeling bar slip, rebar buckling, and fatigue which can cause numerical instabilities. Due to these considerations, we opted for the perhaps less refined but certainly simpler and more stable lumped plasticity approach.

As described in the Introduction, the behavior of a structural element depends greatly on the hierarchy of its strength, leading to the classification of RC columns based on their failure mechanism, namely flexural mode failure, shear mode failure, and flexure-shear mode failure. In response to the increasing interest in modeling shear-dominated columns, the research community has proposed several approaches of varying complexities. Earlier attempts, such as those by Spacone [1996] and Zeris and Mahin [1991], involved modifying flexure elements to incorporate the shear response. Elwood [2004] introduced a modeling

technique that utilized a shear spring in conjunction with a nonlinear beam-column element to simulate shear behavior. They developed a hysteretic uniaxial material with strength degradation to represent the shear spring, which was implemented in OpenSees. Once a critical lateral drift value was reached, strength degradation commenced, simulating shear failure as captured by the shear spring. Jeon [2013] later adopted this model due to its computational efficiency and demonstrated its good agreement with experimental findings. However, this model did not account for pinching or cyclic degradation. To address these limitations, Leborgne and Ghannoum [2013] extended the model by incorporating a rotation-based shear spring instead of a drift-based one, accounting for pinching and cyclic degradation. As these approaches possess limited applicability and rely on a single hysteretic model within OpenSees, O'Reilly and Sullivan [2019] used uncoupled shear spring aggregated into the lumped plasticity beam-column element. This modeling approach implies that the weaker of the two mechanisms (shear and flexure) would govern. The shear spring was described using a backbone curve with 4 phases, and its characteristic points were determined using expressions from Zimos et al. [2015].

Following De Risi et al. [2022] our approach entails an initial step of pre-classifying the columns to determine the anticipated mode of failure. Based on the expected mode we define the phenomenological laws at the member ends, using in that manner a single spring, which is a more practical and computationally efficient approach. Different empirical approaches have been proposed in the literature to classify columns based on their design parameters (e.g., axial load ratio, shear span, amount of reinforcement, etc.) and/or their bearing capacity. Recently, machine-learning techniques have gained popularity as an alternative method for column classification, utilizing basic design parameters as input variables and failure modes as outputs [Feng et al. 2020; Mangalathu et al. 2019].

However, within this study, we adopt a simpler procedure outlined by De Risi et al. [2022]. This approach utilizes the ratio between plastic shear demand V_p and shear strength V_n, transverse reinforcement ratio ρ", and aspect ratio a/d. The shear strength can be expressed as follows [Sezen and Moehle 2004]:

$$V_n = kV_0 = k\left(\frac{0.5\cdot\sqrt{f_c'}}{a/d}\sqrt{1+\frac{N}{0.5\cdot\sqrt{f_c'}\cdot A_g}}\cdot 0.8\cdot A_g + \frac{A_{sw}f_{yw}}{s}d\right) \tag{4.13}$$

$$k = \begin{cases} 1 & , \quad \mu \le 2 \\ 0.7 & , \quad \mu_\delta \ge 6 \\ 1.15 - 0.075\cdot\mu_\delta & , \quad 2 < \mu_\delta < 6 \end{cases} \tag{4.14}$$

where A_g is the column gross cross-section area; N is the column axial load, f_c' is the concrete compressive strength (in MPa), A_{sw} is the area, f_{yw} yielding strength, and s the spacing of the transverse reinforcement; a is the shear span while d is the effective height of the cross-section. The factor k defines the shear strength degradation with increasing displacement ductility μ_δ. If $V_p/V_o \ge 1$ then the column is defined as shear-dominated, if $V_p/V_o \le 0.7$ as flexure dominated and if $1 < V_p/V_o < 0.7$ as flexure-shear dominated.

4.7.1 Flexure-critical columns

To model the RC columns that fail in flexure we use the hysteretic model developed by [Ibarra et al. 2005], referred to as IMK model in the following text. The IMK model, which includes in-cycle and cyclic degradation directly modeled as a function of dissipated energy, has been extensively used as it showed good agreement with the experimental results. However, its performance entirely relies on the robust definition of the parameters' values, which in most cases are derived from empirical relations based on experimental data [Haselton et al. 2007; Panagiotakos and Fardis 2001]. The parameters used to describe IMK law can be divided into two groups: one describing monotonic response and another describing cyclic response. Figure 4.8 displays the model's monotonic backbone curve and Table 4.6 provides a description of the parameters.

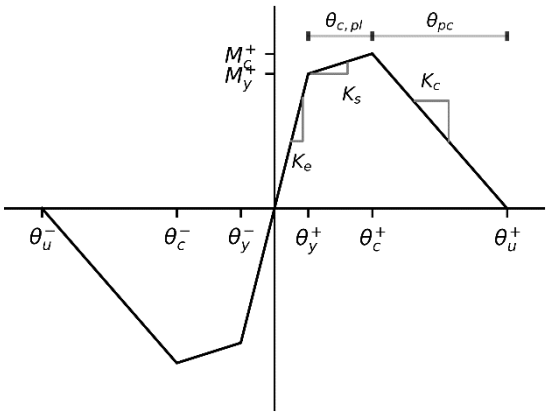

Figure 4.8. The backbone curve of the component model developed by Ibarra et al. [2005] (IMK)

First, we find the yielding moment M_y using the cross-sectional analysis. Then, using the predictive equations proposed by Haselton et al. [2007], which were obtained based on the extensive database of 255 RC members from the PEER database (220 flexure critical and 35 flexure-shear critical), we derive the ratio between the secant stiffness and gross stiffness, and the rotation at yield θ_y (assuming that we have a cantilever) with Equations (4.15) and (4.16), respectively:

$$\frac{EI_y}{EI_g} = -0.07 + 0.59 \cdot \left(\frac{N}{A_g f_c'}\right) + 0.07 \cdot \left(\frac{L_s}{H}\right), \qquad 0.2 \le \frac{EI_y}{EI_g} \le 0.6 \tag{4.15}$$

$$\theta_y = \frac{M_y \cdot L}{3 \cdot EI_y} \tag{4.16}$$

The capping moment M_c and plastic rotation at capping $\theta_{c,pl}$ can be found using Equations (4.17) and (4.18), respectively. Summing Equations (4.16) and (4.18) one can get the rotation at the capping point θ_c. To get the ultimate rotation we can sum θ_c with the post-capping rotation θ_{pc} given by Equation (4.19).

$$M_c = 1.25 \cdot 0.89^{\nu} \cdot 0.91^{0.01 \cdot f_c'[MPa]} \tag{4.17}$$

$$\theta_{c,pl} = 0.12 \cdot (1 + 0.55 \cdot a_{sl}) \cdot 0.16^{\nu} \cdot (0.02 + 40\rho_{sh}) \cdot 0.54^{0.01 f_c'[MPa]} 0.66^{0.1 s_n} \cdot 2.27^{10\rho} \tag{4.18}$$

$$\theta_{pc} = 0.76 \cdot 0.031^{\nu} \cdot (0.02 + 40\rho_{sh})^{1.02} \leq 0.10 \tag{4.19}$$

To estimate the cyclic deterioration parameters' values, we assume that λ_S, λ_C, λ_A and λ_K are equal [Lignos and Krawinkler 2011] and we utilize Equation (4.20) to calculate them. The rate of cyclic degradation (c_s, c_c, c_A, c_K) is set equal to one (i.e., a constant rate of deterioration) following the recommendations from the literature [Haselton et al. 2007].

$$\lambda = 170.7 \cdot 0.27^{\nu} \cdot 0.1^{\frac{s}{d}} \tag{4.20}$$

It is important to consider the limitations of using these predictive equations, as they have been developed based on a limited dataset. Specifically, the tests utilized focus solely on flexure-dominated columns with deformed bars and often are not tested up to the point of failure.

Table 4.6. Description of the parameters used to define the IMK model

Parameter	Description	Parameter	Description
K_e	Initial stiffness	θ_c^+, θ_c^-	Capping plastic rotation in the positive and negative direction
M_y^+, M_y^-	Yield moment in the positive and negative direction	$\theta_{pc}^+, \theta_{pc}^-$	Post-capping rotation in the positive and negative direction
θ_y^+, θ_y^-	Yield rotation in the positive and negative direction	K_c	Post-capping stiffness
K_S	Hardening stiffness	c_S, c_C, c_A, c_K	rate of strength, post-capping, reloading stiffness and unloading stiffness degradation
M_c^+, M_c^-	Capping moment in the positive and negative direction	λ_S, λ_C, λ_A, λ_K	cyclic deterioration parameter for strength, post-capping, reloading stiffness and unloading stiffness degradation

To validate the modeling process explained, we use the Scientific Toolkit for OpenSees STKO [Petracca et al. 2017]. The experimental tests were modeled as cantilever columns, comprising an elastic beam-column element and a zero-length rotational spring described with the IMK law, as illustrated in Figure 4.9. In OpenSees we used *ModIMKPeakOriented02*

unixial material model as proposed by [Ribeiro and Barbosa 2015]. More details about the model can be found in Appendix B3. By employing the loading protocols from the corresponding experiments, we conducted cyclic pushover analysis and recorded the base shear force and top displacement. As an illustrative example, Figure 4.10a shows a good match between experimental and numerical results for Test 8 from the DB.

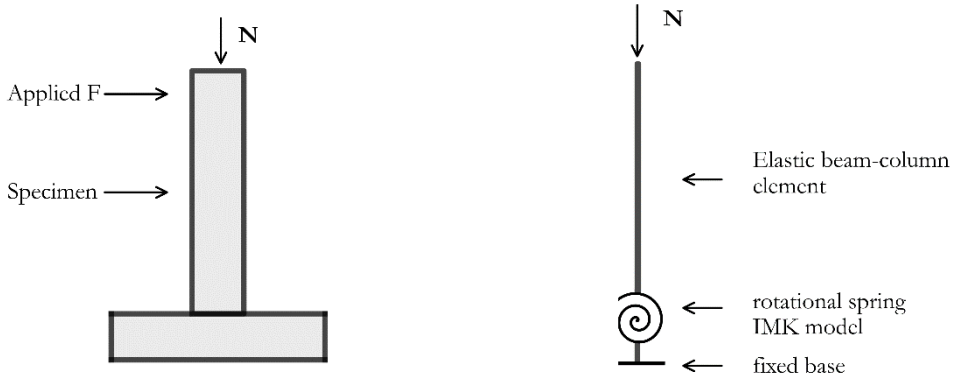

Figure 4.9. Experimental setup and the numerical model in STKO

4.7.2 Shear and flexure-shear-critical columns

When columns are categorized as shear-dominant and susceptible to failure through shear or flexure-shear, it is common to model them using a simplified backbone curve with only two points representing peak and collapse [ATC 2017; Risi et al. 2022]. For the sake of simplicity and practicality, in our study we decided to employ the same IMK model used for flexural-critical columns (Figure 4.8). However, we define the characteristic points of the curve differently. For columns dominated by flexure-shear, the yield moment is estimated using sectional analysis, the same as for the flexure-critical columns. For shear-critical columns, however, we utilize a predictive equation proposed by [Lee and Han 2018] and represented by Equation (4.21). This equation, which was derived from a comprehensive analysis of 40 shear and flexure-shear critical columns, employing multivariate regression techniques, demonstrated a good agreement with experimental results. The remaining points were estimated in the same manner for both FSC and SC columns. The initial stiffness (K_e in Figure 4.8) was determined using their proposed equation, denoted by Equation (4.22) here. Based on an examination of specimens in the database, we assumed that the capping moment is 1.08 times the yield moment, a value that aligns with the findings of [O'Reilly and Sullivan 2019] when investigating older reinforced concrete structures prone to shear failure. Additionally, the post-capping stiffness K_c was set to 0.2 times the initial stiffness K_e. The rate of deterioration parameter, c, was kept constant at one, and the cyclic deterioration parameter, λ, was determined using Equation

(4.20) proposed by Haselton, following the approach for flexure-critical columns. We recognize that strictly speaking this approach is limited to FC columns, as the equation by Haselton was derived solely from data for such columns, but we had to adopt it due to the scarcity of data and information regarding cyclic deterioration parameters for shear-dominant and flexure-shear-dominant columns. The failure point is found by assuming a moment of zero, with the corresponding rotation calculated as proposed by Elwood et al. [2005] and given by Equation (4.23).

$$M_y = e^{-0.95} b^{0.93} h^{1.23} L^{0.49} \rho_l^{0.54} \rho_t^{0.14} \tag{4.21}$$

$$K_e = e^{0.40} b^{0.99} h^{1.87} (v + 0.1)^{0.64} \rho_t^{-0.23} \left(\frac{a}{d}\right) \left(\frac{\tau}{31.62\sqrt{f_c'}}\right)^{0.09} \tag{4.22}$$

$$\theta_u = \frac{4}{100} \frac{1 + \tan^2(\theta)}{\tan(\theta) + N \dfrac{s}{A_{sw} f_{yw} d \tan(\theta)}} \tag{4.23}$$

Similarly to the case of FC columns, to validate the proposed approach we compared the available experimental data with the numerical results obtained using the STKO model. Figure 4.10b shows a good match for Test 252 from the DB.

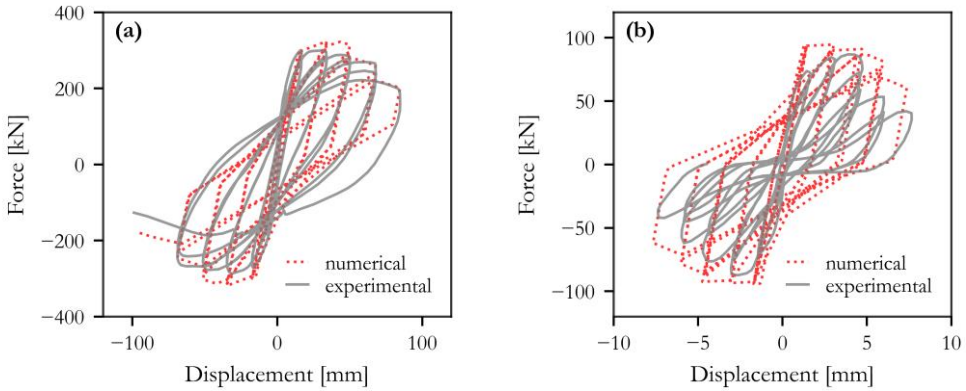

Figure 4.10. Cyclic pushover comparison of experimental and numerical results obtained using STKO model and IMK model for (a) Test 8, FC column, and (b)Test 252, FSC column. P-delta effects are removed.

4.8 NUMERICAL PREDICTION OF DAMAGE STATE PROGRESSION

In the previous sections, we demonstrated that the Modified Ibarra model represents realistically the behavior of RC columns under cyclic loading, and, based on the available experimental data, we calibrated the DI, which can be used as an EDP, to ascertain which damage state the column is in after an earthquake. In the following, our objective is to

compare the damage predicted by our proposed DI vis-à-vis that predicted with the more conventional, displacement-based EDP. Additionally, we aim to investigate the extent of capacity reduction foreseen by these two EDPs when the structure is subjected to mainshock-aftershock sequences. For that purpose, we will derive damage-dependent fragility curves for five structures, four simple SDOF systems and a four-story RC bare frame 3D structure.

4.8.1 Analysis set-up

The comparison is done using this analysis set-up. We decided to conduct back-to-back incremental dynamic analysis (B2B-IDA), a method that builds upon the original IDA technique and extends it to derive fragility curves dependent on the initial damage state. To perform the analysis we use a set of 30 ground motion records from the NGA2-West database, as explained in more detail in Bakalis et al. [2018]. The initial step involves subjecting an intact structural model, to each of the 30 input ground motions (GMs) individually, with successive scaling until the considered system collapses.

To calculate the fragility function, we assume it follows a lognormal distribution. Based on the results of the structural analysis, we estimate the median and standard deviation of the fragility function using the method of moments [Baker 2015] as follows:

$$\ln \hat{\mu} = \frac{1}{n}\sum_{i=1}^{n} \ln(IM_i) \tag{4.24}$$

$$\hat{\beta} = \sqrt{\frac{1}{n-1}\sum_{i=1}^{n} (\ln(IM_i) - \ln(\hat{\mu}))^2} \tag{4.25}$$

where $\hat{\mu}$ is the estimate of the median intensity measure (IM) level associated with the exceedance of the damage state and $\hat{\beta}$ the estimate of the standard deviation of ln(IM) of the fragility function. The number of ground motions considered is n, while IM_i is the intensity level corresponding to the onset of the DS for the i^{th} ground motion.

For each ground motion, we then determine the scale factors by which we need to scale it to obtain a ground motion strong enough to be "damaging". By that, we mean a ground motion that is supposed to bring the structure to an initial damaged state (IDS) larger than DS0 (i.e., no damage). We subsequently carried out IDA again by applying the 30 ground motions incrementally, this time on the structure that was already damaged. With the resulting data, we then fit the fragility curves, using Equations (4.24) and (4.25). In this manner, we obtain fragility curves that are conditioned on the initial damage state of the structure.

4.8.2 RC columns

(a) *Results for systems representing SC columns*

We first consider two SDOFs that are expected to experience a shear mode of failure, each with a fundamental period, T_1, of 0.2 seconds. The IMK model is characterized in a manner to resembles the columns that we have in the DB, which are expected to exhibit shear behavior. The ductility (found as the ratio between the displacement at the capping and the yielding point) of the model is set to 2.5 while two different cyclic parameter λ characterizations are investigated: one that reflects systems with a moderate rate of cyclic deterioration (λ=50) and another that reflects systems with a rapid rate of cyclic deterioration (λ=25). In the following text, these models will be denoted as MS1 and MS2, with "M" referring to the model, "S" to shear mode, and "1" and "2" to systems with medium and rapid cyclic deterioration, respectively.

The 30 selected GMs are scaled at 13 $Sa(T_1)$ intensity levels corresponding to intensities ranging from 0.075g to 0.7g and nonlinear response history analyses (NLRHA) are run on the intact system. For each conducted analysis we recorded the value of DI, found with Equation (4.12) where β=0.3 and γ is found as indicated in Figure 4.5. Upon analyzing the IDA curves of the intact system and based on the investigation conducted in the previous sections, we defined three DS, which represent light damage, moderate damage and severe damage, respectively. These damage states are defined in terms of the two EDPs, namely DI and maximum ductility (found as the ratio between the displacement at the top of the SDOF and displacement at the yielding point). The description of the damage states is given in Table 4.7. To bring the SDOF systems to IDS1 we scaled the ground motions in such a way that the resulting DI is in the range between 0 and 0.25 Similarly, for IDS2 the ground motions were scaled such that the resulting DIs are in the range between 0.25 and 0.45. For SDOFs to reach IDS1 defined in terms of maximum ductility, we scaled the ground motions so that the resulting ductility is in the range between 0 and 2.0, and to reach IDS2 we scaled them so that the resulting ductility is in the 2.0 to 4.0 range. Note that the ductility values used are fully consistent with the corresponding DI values for defined damage states.

Table 4.7. Damage states used for MS models in terms of DI and the maximum ductility

	DI	Maximum ductility	Description of damage
DS1	0-0.25	1.5-2.0	Flexure-shear cracking, formation of splitting cracks
DS2	0.25-0.45	2.0-4.0	Widening and localization of the shear cracks, onset of concrete spalling;
DS3	>0.45	>4.0	Longitudinal bar buckling yielding of transverse reinforcement, crushing of the concrete core, axial failure;

Figure 4.11 and Figure 4.12 show the IDA curves for intact damage state and model MS1, along with collapse fragility curves conditioned on the different IDSs, using DI and maximum ductility as an EDP, respectively. Similarly, we show the results for MS2 in Figure 4.13 and Figure 4.14. It's evident that in all cases, the fragility curves shift leftward, as expected, indicating a reduction in structural capacity with increasing initial damage. However, for both MS1 and MS2, the reduction in collapse capacity is more pronounced when DI is employed as an EDP. This suggests that DI may be more effective at capturing the effects of damage accumulation. Notably, the reduction in collapse capacity is more significant for MS2 due to its greater cyclic degradation.

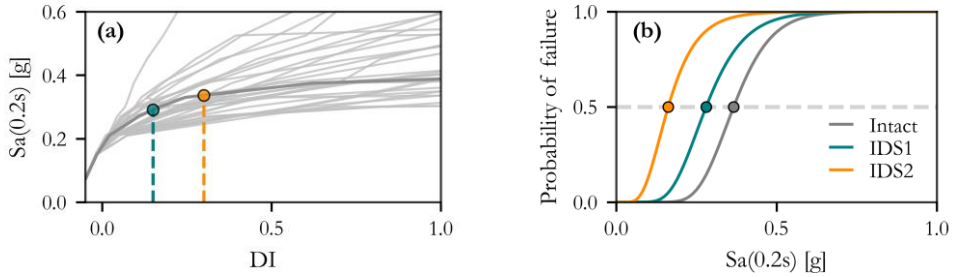

Figure 4.11. (a) IDA curves for the intact MS1 SDOF system, highlighting initial damage states for one ground motion, (b) Collapse fragility curves of the same system conditioned on the initial damage state. DI is used as an EDP.

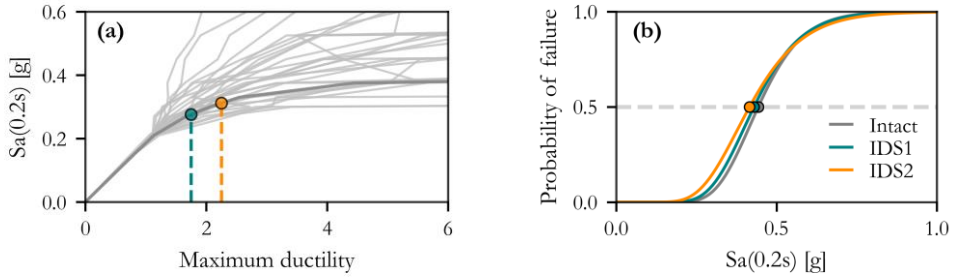

Figure 4.12. (a) IDA curves for the intact MS1 SDOF system, highlighting initial damage states for one ground motion, (b) Collapse fragility curves of the same system conditioned on the initial damage state. Maximum ductility is used as an EDP.

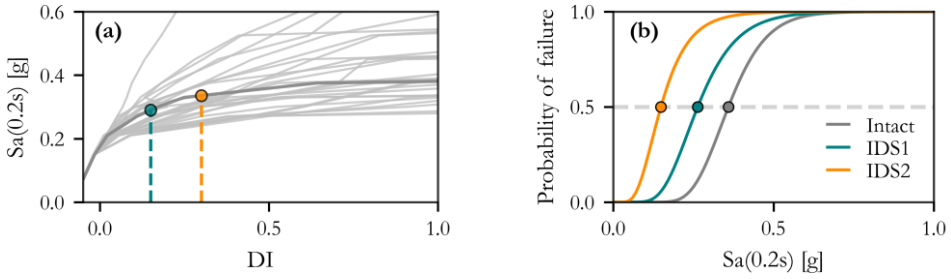

Figure 4.13. (a) IDA curves for the intact MS2 SDOF system, highlighting initial damage states for one ground motion, (b) Collapse fragility curves of the same system conditioned on the initial damage state. DI is used as an EDP.

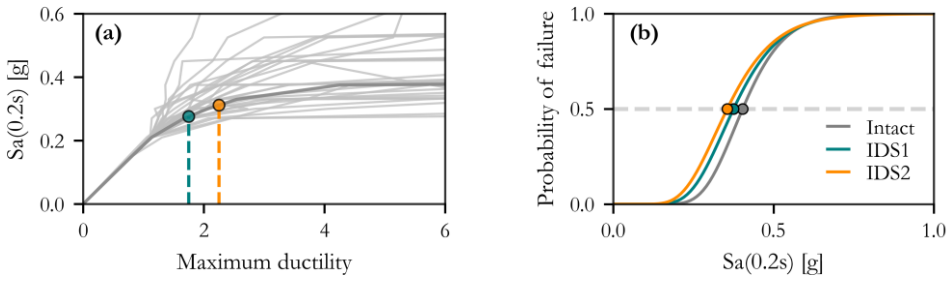

Figure 4.14. (a) IDA curves for the intact MS2 SDOF system, highlighting initial damage states for one ground motion, (b) Collapse fragility curves of the same system conditioned on the initial damage state. Maximum ductility is used as an EDP.

The superior ability of DI to capture the reduction in capacity can also be observed when the capacity refers to damage states less severe than collapse. To provide support to this statement, we calculate for MS2 the probability of exceeding a ductility of 2.0 and a DI of 0.25, conditioned on the IDS1. These two thresholds correspond to the onset of DS2 for SC columns. The resulting fragility curves for DS2 in Figure 4.15 make evident that DI results in a more substantial reduction in DS2 capacity as well. For brevity, we present results only for MS2 but similar conclusions hold for MS1.

To provide a clearer perspective on these differences, Figure 4.16 illustrates the reduction in collapse capacities and DS2 capacities for both models and EDPs. For instance, when ductility is used as the EDP, the collapse capacity of MS1 decreases by 4% and 7% for IDS1 and IDS2, respectively. However, when DI is used, this reduction is 23% and 55%, significantly higher than the reduction observed with ductility although the thresholds for onset of collapse are consistent in both EDPs. In the case of MS2, where cyclic degradation is more pronounced, the reduction is even greater. Specifically, with ductility, the reduction is 7% and 12% for IDS1 and IDS2, while with DI, the reduction is 27% and

59%. Similarly, when it comes to the reduction in DS2 conditioned on the IDS1, one can see in Figure 4.16b that the reduction predicted with maximum ductility is 9% and 12% and 57% and 60%, for columns MS1 and MS2, respectively.

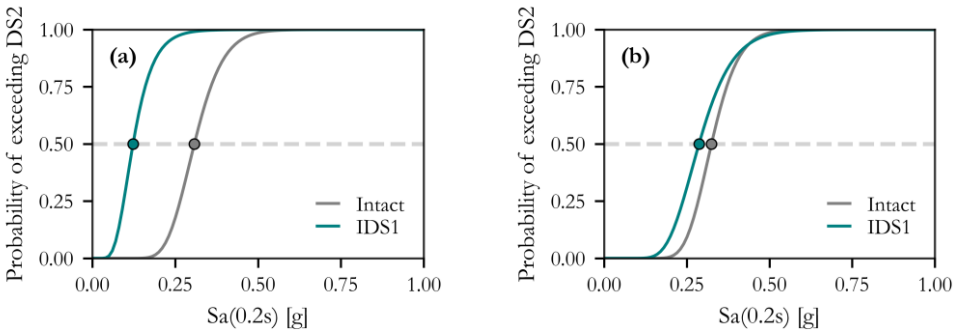

Figure 4.15. (a) Probability of exceeding DI of 0.25 (i.e., DS2) and (b) maximum ductility of 2.0 (i.e., DS2) conditioned on the IDS1. Results for model MS2 are illustrated.

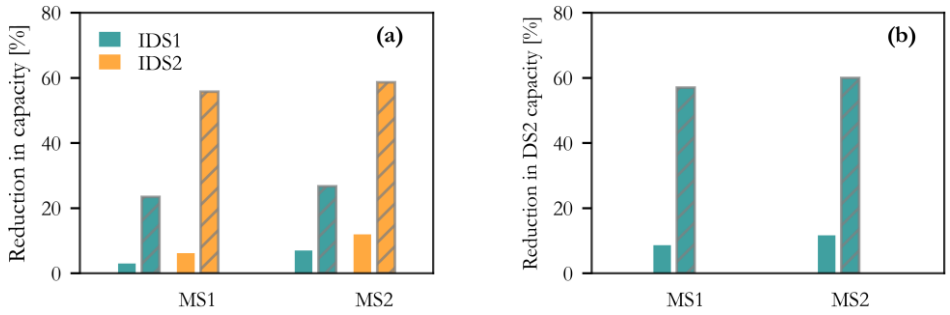

Figure 4.16. Reduction in the (a) collapse capacity and (b) DS2 capacity, conditioned on the initial damage state for shear-dominated columns MS1 and MS2. Solid bars refer to the case when maximum ductility is used and hatched when DI is used.

(b) *Results for systems representing FC columns*

The same approach has been applied to an SDOF system that is expected to fail in flexural mode. This system, with a fundamental period of 0.2 seconds, has been characterized using the IMK model to simulate columns in our database, which are anticipated to exhibit flexural behavior. The ductility capacity of the model at collapse has been set to 4, and we have employed different cyclic deterioration parameters, as in the previous case. These models are designated as MF1 and MF2, where "F" denotes flexural mode failure, and "1" and "2" correspond to λ=50 (moderate rate of cyclic deterioration) and λ=25 (rapid rate of cyclic deterioration), respectively. For each conducted analysis we recorded the value of

DI, found with Equation (4.10) where β=0.1. In this case, we have defined four damage states in terms of DI and maximum ductility, as described in Table 4.8.

To bring the SDOF systems to IDS1, we have scaled the ground motions to achieve the DI values in the range between 0 and 0.20. For IDS2, the range is between 0.20 and 0.40, and for IDS3, it is within the range of 0.4 to 0.75. Alternatively, when using maximum ductility as the EDP, IDS1 is reached when the response to scaled ground motions has a ductility ratio in the range between 0 and 2, IDS2 when the ductility ratio is between 2 and 3.5 and, finally, IDS3 when the ductility ratio ranges from 3.5 and 6.

As observed in the previous case of shear-dominated models, all fragility curves have shifted leftward, indicating a reduction in capacity. Again, this reduction is more pronounced when DI is used, as depicted in Figure 4.17 and Figure 4.19, compared to when maximum ductility is employed, as illustrated in Figure 4.18 and Figure 4.20.

Table 4.8. Damage states used for MF models in terms of DI and the maximum ductility

	DI	Maximum ductility	Description of damage
DS1	0-0.20	0-2.0	Flexural and longitudinal cracking, yielding of steel bars in tension, followed by shear cracking
DS2	0.20-0.40	2.0-3.5	The onset of concrete spalling exposing the transverse reinforcement
DS3	0.4-0.75	3.5-6.0	More significant spalling of concrete, longitudinal steel is exposed, the potential start of tie yielding
DS4	>0.75	>6.0	Major safety implications, bar buckling, concrete core crushing, fracture of the bars, complete failure

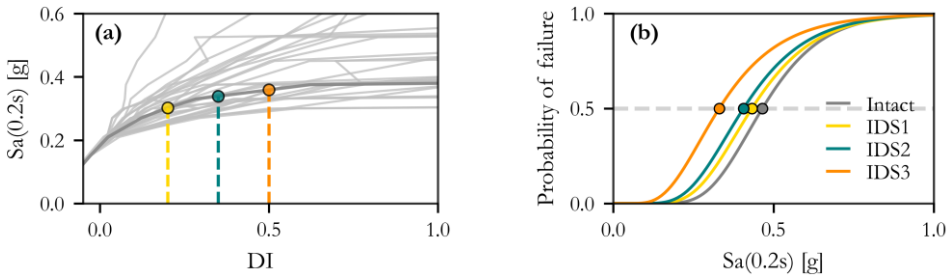

Figure 4.17. (a) IDA curves for the intact MF1 SDOF system, highlighting initial damage states for one ground motion, (b) Collapse fragility curves of the same system conditioned on the initial damage state. DI is used as an EDP.

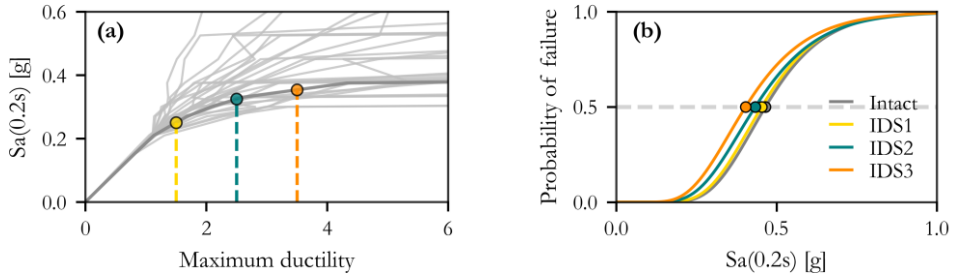

Figure 4.18. (a) IDA curves for the intact MF1 SDOF system, highlighting initial damage states for one ground motion, (b) Collapse fragility curves of the same system conditioned on the initial damage state. Maximum ductility is used as an EDP.

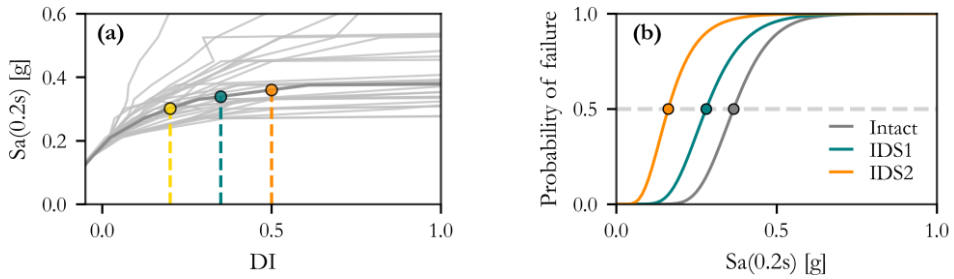

Figure 4.19. (a) IDA curves for the intact MF2 SDOF system, highlighting initial damage states for one ground motion, (b) Collapse fragility curves of the same system conditioned on the initial damage state. DI is used as an EDP.

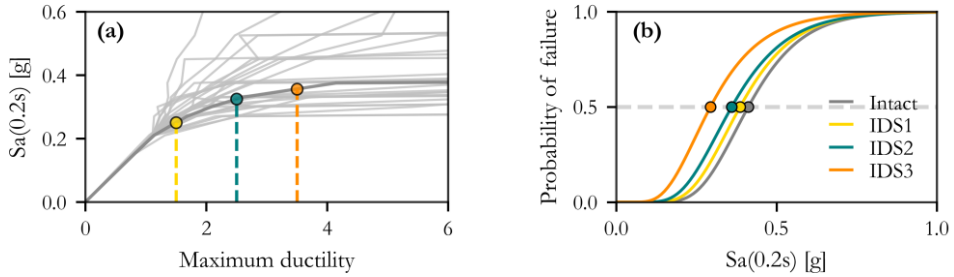

Figure 4.20. (a) IDA curves for the intact MF2 SDOF system, highlighting initial damage states for one ground motion, (b) Collapse fragility curves of the same system conditioned on the initial damage state. Maximum ductility is used as an EDP.

Similarly to the previous case, we have investigated the reduction in capacity for less severe damage states, focusing on ductility values of 3.5 and DI values of 0.40, corresponding to the DS3. The obtained results are shown in Figure 4.21. Once again, it is evident that DI predicts more reduction in capacity.

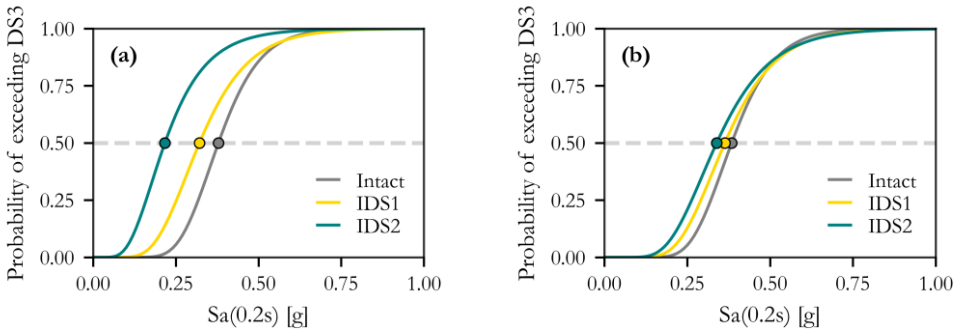

Figure 4.21. (a) Probability of exceeding DI of 0.40 (i.e., DS3) and (b) maximum ductility of 3.5 (i.e., DS3) conditioned on the IDS1 and IDS2. Results for model MF2 are illustrated.

In Figure 4.22 the reduction in collapse and DS3 capacities is illustrated for both FC models and EDPs.

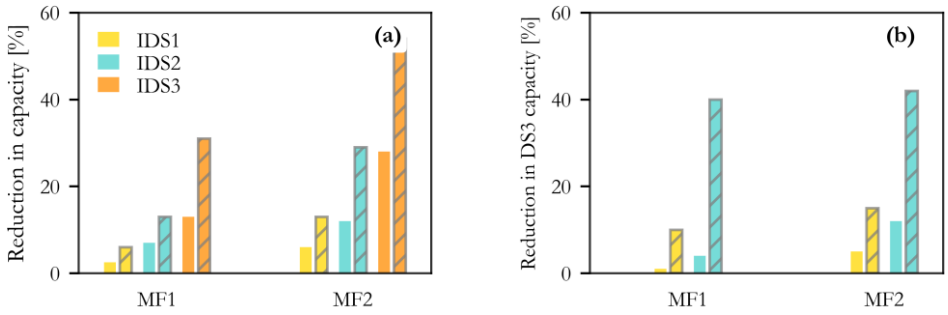

Figure 4.22. Reduction in the (a) collapse capacity and (b) DS3 capacity, conditioned on the initial damage state for flexure-dominated columns MF1 and MF2. Solid bars refer to the case when maximum ductility is used and hatched when DI is used.

For model MF1, when ductility is used as the EDP, the collapse capacity decreases by 2%, 7%, and 13% for IDS1, IDS2, and IDS3, respectively. However, when DI is employed, this reduction is 6%, 13%, and 31%. In the case of MF2, characterized by more pronounced cyclic degradation, the reduction is even more substantial. Specifically, with ductility, the reduction is 6%, 12%, and 28% for IDS1, IDS2, and IDS3, while with DI, the reduction is 12%, 29%, and 54%. When it comes to the reduction in DS3, when maximum ductility is employed reduction is 1% and 4% for MF1 and IDS1 and IDS2, respectively, while for

MF2 is higher (5% and 12%). On the other hand, more reduction is predicted with DI, 10% and 40% for MF1 and 15% and 42% for MF2, conditioned on the IDS1 and IDS2, respectively.

4.8.3 RC bare frame structure

(a) *Description and modeling of the frame*

The same exercise described in Section 4.8.1 is repeated for the RC bare frame structure designed in accordance with the previous Italian code [DM 1996]. The building, measuring 28.0m x 18.0m in plan area, consists of four stories, each with a height of 3.5m, resulting in a total building height of 14.0m. The concrete used is assumed to have a compressive strength of 30 MPa, while the reinforcement steel has a yield strength of 440 MPa. Figure 4.23 provides a plan view of the building, denoting the column sections on the first two floors. For the third and fourth floors, the column section names are enclosed in parentheses. Although not explicitly depicted in the figure, beams are color-coded for clarity – green lines correspond to Section 9, orange lines to Section 10, and grey lines to Section 11. Table 4.9 provides details about the geometry (width B and height H) of each column and beam section within the building. Longitudinal reinforcement consists of Ø20 diameter bars, while transversal reinforcement comprises Ø8 bars spaced at 200 mm for all beams and columns. Values of the structural, non-structural, and live load that are applied on the building are shown in Table 4.10. The weight of beams and columns is calculated separately and added to the loading.

Table 4.9. Geometry (width B and height H) of the column and beam sections

Section	S1	S2	S3	S4	S5	S6	S7	S8	S9	S10	S11
Width B (mm)	350	500	400	450	300	450	350	450	300	800	1000
Height (mm)	500	350	400	900	450	300	350	900	600	240	240

Table 4.10. Loads applied on the building

	Structural	Non-structural	Live load
Floor level	3 kN/m^2	2 kN/m^2	2 kN/m^2
Roof level	3 kN/m^2	1 kN/m^2	2 kN/m^2

The building is modeled in OpenSees as a 3D MDOF system using the pre- and post-processor STKO [Petracca et al. 2017], as illustrated in Figure 4.24. It is assumed that the building is fixed at the base and that diaphragms are rigid, i.e. nodes at each floor are linked through a *rigidDiapgrahm* constrain in the plane orthogonal to the global Z axis. To perform gravity and modal analysis all members in the building are modeled using *elasticBeamColumn* element defined in OpenSees, with the geometry as specified in Table 4.9. The moment of inertia of the members is adjusted using the empirical relationship proposed by Haselton et al. [2007] as expressed in Equation (4.15). The floor masses are computed based on dead

loads and 30% of live loads, and they are lumped at the nodes of each floor according to the tributary area.

On this model, we first performed gravity and modal analysis. Table 4.11 shows the periods of oscillation for the first five modes, along with the corresponding participating masses (PMF) and cumulative participating masses (∑PMF). Notably, fundamental periods in X and Y directions are similar, with the cumulative mass participation exceeding 90% after the first 5 modes.

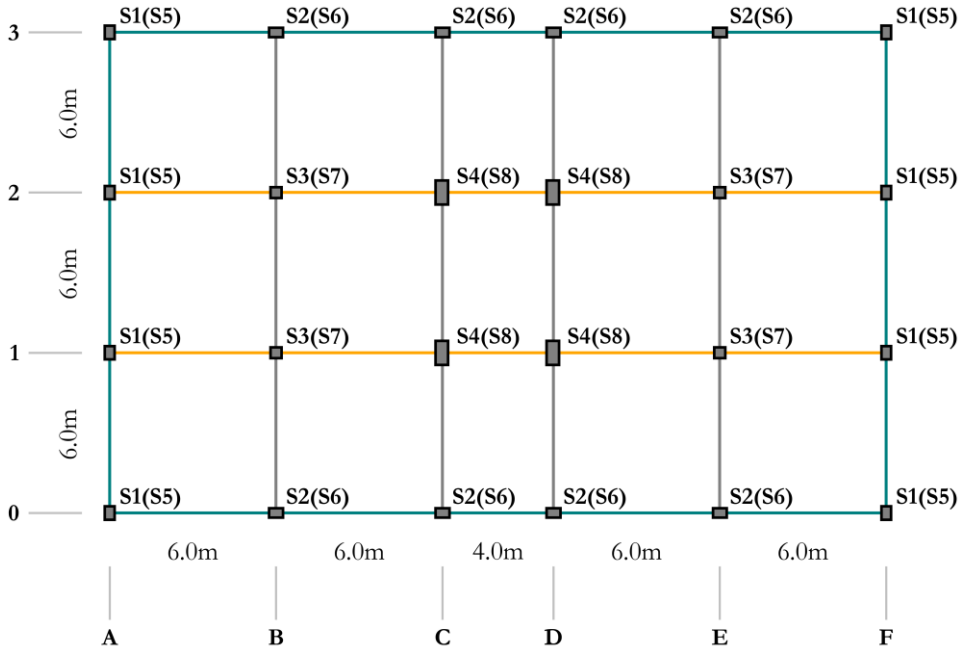

Figure 4.23. Plan of RC bare frame building, with the column section names of 1st and 2nd story indicated. Column section names of 3rd and 4th storey are given in parentheses. Beams sections S9, S10, and S11, are color-coded using green, orange and grey, respectively.

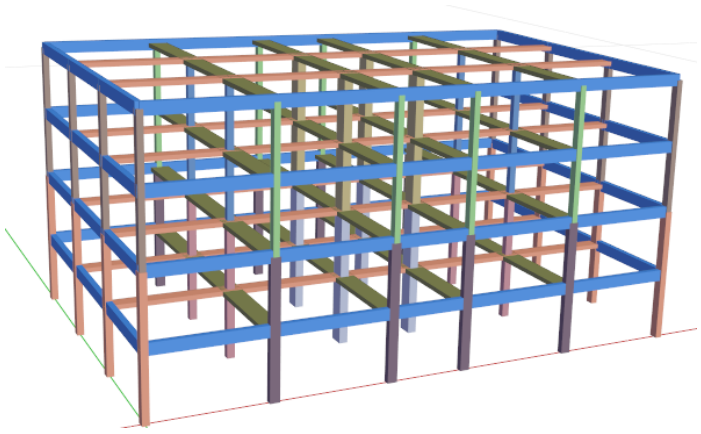

Figure 4.24. 3D model of the building made using STKO

Table 4.11. Periods and participation masses for translational (X and Y) and rotational degrees of freedom. The first five modes of oscillation are shown.

Mode	Period (s)	PMFX (%)	PMFY (%)	PMFXY (%)	∑PMFX (%)	∑PMFY (%)	∑PMFXY (%)
1	1.08	0	80.2	0	0	80.2	0
2	1.02	82.1	0	0	82.1	80.2	0
2	0.81	0	0	82.3	82.1	80.2	82.3
4	0.34	0	12.7	0	82.1	92.9	82.3
5	0.34	12.1	0	0	94.2	92.9	82.3

To perform the nonlinear static (i.e. pushover) and dynamic analysis we modeled beams and columns using the lumped plasticity approach and *HingedBeam* element in STKO, i.e. elastic beam-column element with two *zeroLenght* rotational springs at its ends in OpenSees. Each spring is defined using IMK model for both X and Y direction. Characteristic points of the IMK model are defined, assuming at first that all members would experience a flexural mode of failure and following the procedure described in Section 4.7.1. Preliminary pushover analyses are then performed in both horizontal directions using linear lateral force distribution and setting the top floor center of mass as the control node, to provide the maximum shear demand V_p in each column. These values are then compared with the shear strength V_n and columns are classified as flexure, shear or flexure-shear dominated, as explained in more detail in Section 4.7. Subsequently, rotational springs are redefined based on the mode of failure, and pushover analyses are performed again. Figure 4.25a and Figure 4.26a illustrate the results in terms of the total base shear and maximum inter-story drift in the X and Y directions, respectively. Figure 4.25b and Figure 4.26b show the inter-story drifts along the height of the building, in the X and Y directions, respectively. The

frame exhibits higher capacity in the Y direction, and the drift demand gradually increases from top to bottom in both directions.

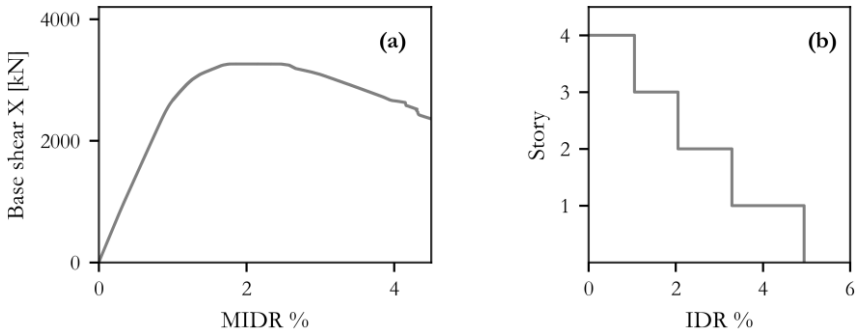

Figure 4.25. (a) Pushover curve obtained for the X direction and (b) inter-story drifts (IDR) along the height of the building

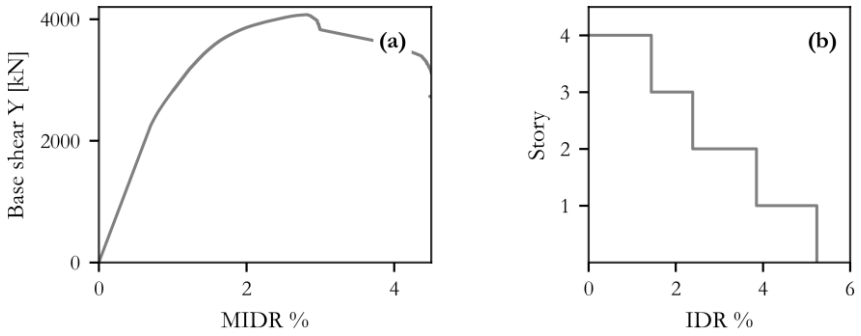

Figure 4.26. (a) Pushover curve obtained for the Y direction and (b) inter-story drifts (IDR) along the height of the building

Finally, we run NLRHA, adopting the Rayleigh damping model with a 5% damping ratio proportional to the current stiffness matrix. The analysis employs the same 30 GMs as in Section 4.8.1. As a conditioning IM we use Sa(1.0s), determined as the geometric mean of the values extracted from the two horizontal ground motion components.

(b) *Damage state definition*

We use two approaches to define the damage states for the building of interest:

(i) The global approach where maximum inter-story drift (MIDR) is used as an EDP;

(ii) Component-based approach (also called local) where the DI defined in Section 4.4 is used.

In the global approach, we use the results of the pushover analysis, IDA curves and recommendations from the literature [Rossetto and Elnashai 2003] to define four damage states, as given in Table 4.12.

Table 4.12. Damage states used for the RC building in terms of MIDR (global approach)

	Proposed MIDR range (%)	Description of the damage
DS1	1.2–1.75	Slight damage, start of structural damage; hairline cracking in beams and columns near joints (<1mm).
DS2	1.75–2.6	Flexural and shear cracking in most beams and columns. Some yielding in a limited number. Shear cracking and spalling are limited.
DS3	2.6–4.3	Loss of bond at lap-splices, bar pull-out, broken ties. The main rebar may buckle, or the element may fail in shear.
DS4	>4.3	Shear failure of many columns of impending soft-story failure.

When it comes to the component or local approach we estimate the DS of every column in the building. To do so, we use the moment-rotation results (to obtain dissipated energy by integration) and the properties of each column, to find the DI in both horizontal directions and at both ends of the column. The final DI of the column is then found as the maximum value between the two directions and two ends, as shown in Equations (4.26) and (4.27).

$$DI_{column} = \max\{DI_i, DI_j\} \tag{4.26}$$

$$\begin{matrix} DI_i = \max\{DI_{i,x}, DI_{i,y}\} \\ DI_j = \max\{DI_{j,x}, DI_{j,y}\} \end{matrix} \tag{4.27}$$

For FC columns we defined four damage states (Table 4.2), while for the SC and FSC columns, we defined three damage states (Table 4.3 and Table 4.4, respectively). To make the procedure straightforward FC columns in DS2 and DS3 are reclassified as DS2 columns, and FC columns in DS4 are reclassified as DS3. This ensures that each column in the building is categorized into one of the three damage states. Once the DS for each column is defined, to ascertain in which damage state the entire building is we follow the global damage classification of the AeDES inspection forms [Baggio et al. 2007] where we consider only vertical elements. Based on the local damage states, referred to here as DSL, and based on the extent of these DSLs (<1/3; 1/3-2/3; >2/3), the building is classified into one of the four global DS, as described in Table 4.13. More specifically, if there are columns in DSL1 and none in DSL2 it means that the building is in DS1. If fewer than 1/3 of the total number of columns in the building is in DSL2, then the building is designated as DS2. If more than 1/3 of the columns are in DSL2 and none in DSL3 then the building is in DS3. Finally, if there are any columns in DSL3 the building is labeled as being in DS4.

Table 4.13. Damage states defined for the RC bare building using the local approach. In this case DS refers to the global damage state of the entire building while DSL refers to the damage state of the components (columns here). Extent refers to the percentage of components in the corresponding DSL.

Global DS of the building	Local DS	Extent	Description of the damage
DS1	DSL1	<1/3 1/3-2/3 >2/3	Slight damage, start of structural damage; hairline cracking in beams and columns near joints (<1mm).
DS2	DSL2	<1/3	Flexural and shear cracking in most beams and columns. Some yielding in a limited number. Shear cracking and spalling are limited.
DS3	DSL2	1/3-2/3 >2/3	Loss of bond at lap-splices, bar pull-out, broken ties. The main rebar may buckle, or the element may fail in shear.
DS4	DSL3	<1/3 1/3-2/3 >2/3	Shear failure of many columns of impending soft-story failure.

(c) *Results*

Once the damage states are defined using both approaches, we run NLRHA on the intact building. Figure 4.27 shows the obtained IDA curves in terms of the MIDR with the defined damage states highlighted and corresponding fragility curves. In the component approach, however, it is not possible to obtain IDA curves as there is no continuous global EDP. Instead, for illustration, we show in Figure 4.28a the results for all GMs as stripes associated with DS achieved and corresponding IM level. In Figure 4.28b fragility curves for the four DS defined in Table 4.13 are illustrated. One should note that the fragilities obtained with these two approaches are similar (see Table 4.14).

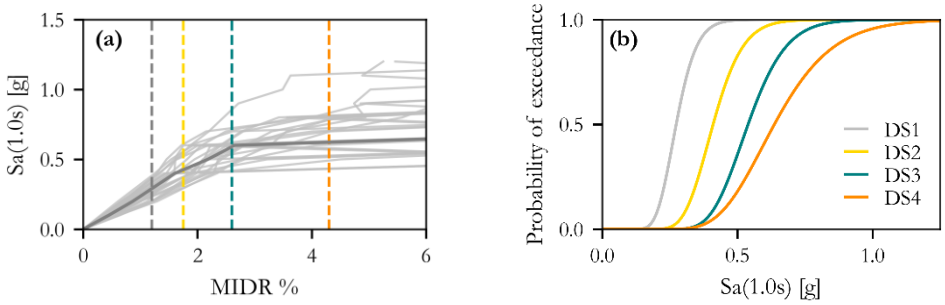

Figure 4.27. (a) IDA curves for the intact building, highlighting thresholds in terms of MIDR associated with the damage states defined in Table 4.12. (b) Corresponding fragility curves.

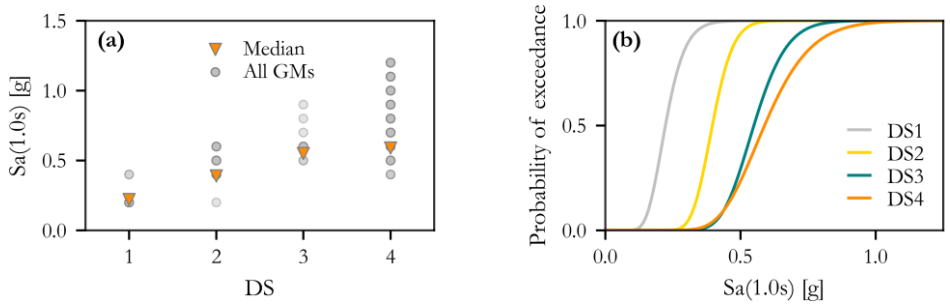

Figure 4.28. (a) Results of IDA for the intact building associated with the damage states defined in Table 4.13, using the component approach. (b) Corresponding fragility curves.

Table 4.14. Values of the fragility function parameters obtained for the intact building with global and component approach

Approach:	Global		Component	
Parameter:	Median	Standard deviation	Median	Standard deviation
DS1	0.27	0.22	0.22	0.25
DS2	0.4	0.21	0.4	0.15
DS3	0.54	0.20	0.55	0.17
DS4	0.62	0.26	0.59	0.22

Exploiting the results of the intact building, we performed IDA again, this time on the building that was already damaged. More specifically, we defined two IDSs, by scaling the GMs to the drift values of 1.4% and 2.1% that classify the building as being in IDS1 and IDS2, respectively, with both considered approaches. After some inspection, we concluded that, when the structure is in IDS3 it is so close to collapse that it would not make sense to obtain the collapse (DS4) fragility curve when the building is in this initial damage condition. Hence, we omitted it. Figure 4.29a and Figure 4.29b show the fragility curves obtained using the global approach conditional on IDS1 and IDS2, respectively. In Table 4.15 estimated median and standard deviation values are shown. One can see that for IDS1, the median DS4 capacity reduces by 35% while for IDS2 by 45%. When it comes to DS3 this reduction is 35% and 53% for IDS1 and IDS2, respectively.

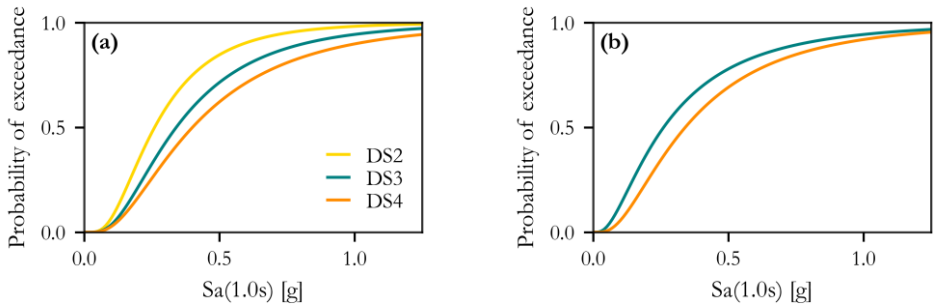

Figure 4.29. Fragility curves for different damage states conditioned on (a) IDS1 and (b) IDS2. Global approach and MIDR as an EDP are used.

Table 4.15. Estimated parameters(median and standard deviation) of the fragility curves for different damage states. Global approach and MIDR as an EDP are used. IDS refers to the initial damage state and DS to the final damage state.

IDS:	Intact		IDS1		IDS2	
Parameter:	Median	Standard deviation	Median	Standard deviation	Median	Standard deviation
DS1	0.27	0.22	-	-	-	-
DS2	0.4	0.21	0.26	0.64	-	-
DS3	0.54	0.20	0.34	0.68	0.26	0.75
DS4	0.62	0.26	0.40	0.72	0.34	0.77

Figure 4.30a and Figure 4.30b show instead the fragility curves obtained using the local approach conditional on IDS1 and IDS2, respectively, while Table 4.15 reports the estimated median and standard deviation values. Compared to the global approach one can see that there is more reduction in capacity in this case. More specifically, for IDS1 the median DS4 capacity reduces by 48% while for IDS2 by 70%. When it comes to DS3 this reduction is 53% and 77%, for IDS1 and IDS2, respectively.

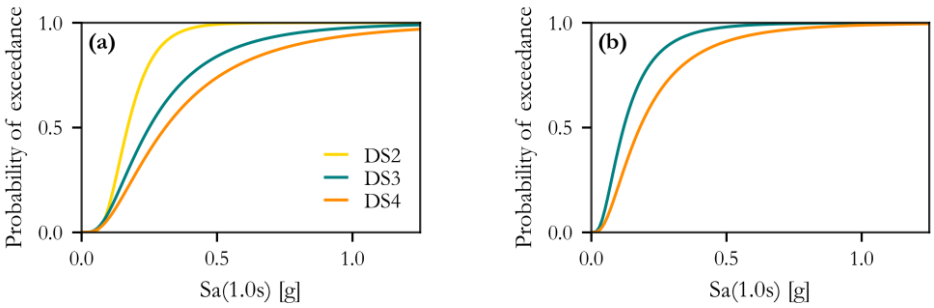

Figure 4.30. Fragility curves for different damage states conditioned on (a) IDS1 and (b) IDS2. Local approach and DI as an EDP are used.

Table 4.16. Estimated parameters(median and standard deviation) of the fragility curves for different damage states. Local approach and DI as an EDP are used. IDS refers to the initial damage state and DS to the final damage state.

IDS:	Intact		IDS1		IDS2	
Parameter:	Median	Standard deviation	Median	Standard deviation	Median	Standard deviation
DS1	0.22	0.25	-	-	-	-
DS2	0.4	0.15	0.17	0.45	-	-
DS3	0.55	0.17	0.25	0.70	0.12	0.70
DS4	0.59	0.22	0.31	0.75	0.18	0.76

4.9 DISCUSSION AND CONCLUSIONS

In the seismic risk assessment, particularly when considering the impact of clustered seismicity, it is crucial to employ numerical models capable of accurately capturing cyclic degradation phenomena. Furthermore, the importance of the EDP which can predict well the progression of damage induced by the repetitive ground motions and effects of the damage accumulation in the cases when the interval between the events in the sequence is too short to repair the building, has been highlighted in multiple studies. The objective of this section was to investigate different modeling approaches when it comes to RC columns and to propose an EDP that can be considered suitable to model damage accumulation in the context of clustered seismicity.

We first assembled a comprehensive database of experimental tests on rectangular RC columns that are subjected to cyclic pushover. The compiled database provides force-displacement histories that were either obtained directly from the researchers or digitized

from force-displacement plots in source documents. In total, there are 370 specimens, 251 were categorized as flexure critical (FC), 36 as shear critical (SC) and the remaining 83 as flexure-shear critical (FSC). For every test in the database, we provided a detailed description of the characteristic points on the force-displacement curve, such as the cracking point, yield point and the ultimate point. Subsequently, reviewing the existing literature and investigating the experimental database assembled, we defined and described the damage states recognizing the distinct responses of columns failing in flexure, shear, or flexure-shear modes.

We then calibrated an energy-based EDP based on the modified Park and Ang damage index for the three defined column types (FC, SC and FSC), using the experimental results. The performance of the proposed EDP was additionally validated against the results of the shake-table tests. Comparisons with the commonly adopted drift-based EDP demonstrated the superior efficacy of the proposed index in predicting damage accumulation more accurately.

Subsequently, we focused on the numerical modeling of the RC columns using the lumped plasticity approach and the Modified Ibarra material model. We chose this model due to its capability to capture cyclic and in-cycle degradation phenomena effectively. We again considered different modes of failure, proposing different approaches for FC and for FSC and SC columns. To validate our modeling choices we used the Scientific Toolkit for OpenSees STKO [Petracca et al. 2017] to model the columns in the experimental database using the elastic beam-column element and a zero-length rotational spring described with the Modified Ibarra model. By employing the loading protocols from the corresponding experiments, we conducted cyclic pushover analysis and compared the numerical and experimental results showing a good match.

In the last part of the study, we wanted to explore the progression of damage and reduction of capacity under seismic sequences, utilizing both the proposed energy-based damage index and the more conventional peak displacement-based EDP. We first modeled four SDOFs using the Modified Ibarra constitutive model, two that fail in shear mode and two that fail in flexure mode, with different cyclic degradation properties, and we ran B2B-IDA with the 30 ground motions. Our results showed that the proposed DI predicts more reduction in capacity, compared to maximum ductility, for all considered SDOFs and across all damage states. Finally, employing the described modeling choices we made a 3D model of the bare RC frame building and ran B2B-IDA with the same set of 30 ground motions. We considered two approaches: the global approach where maximum inter-story drift was used as an EDP and the component (or local) approach where local damage states of the vertical elements (i.e. columns) are first assessed using DI and then combined to estimate the global DS of the structure. Similarly as in the case of SDOFs, our results indicated that with the local approach and proposed DI more significant decrease in capacity is predicted.

While our findings are promising and indicate that the proposed EDP can accurately predict the damage of the RC columns, we acknowledge that there is still a lot of research ground to be covered in this field at least on two fronts. First, more experimental tests,

including shake-table tests and data from the real instrumented buildings after the occurrence of each significant event in a sequence are essential to gain insights into modeling the accumulation of damage caused by seismic sequences. Second, in this section, we focused solely on RC columns while other components, depending on the structure of the interest, might be significant (e.g., infills, joints). Of course, we believe that further analyses are necessary to determine to which extent and for which structures modeling damage accumulation is critical in risk assessment that considers seismic sequences.

To conclude, it is important to highlight that the findings of this section are relevant not only in the cases when we intend to predict damage caused by seismic sequences but also when we intend to model the progression of damage in RC buildings that experience long-duration ground motions, such as those caused by large magnitude events in active crustal areas or subduction zones.

5.PRACTICAL ISSUES IN MAINSHOCK GROUND MOTION RECORD SELECTION FOR BUILDING SPECIFIC RISK ASSESSMENT

5.1 INTRODUCTION

To estimate the probability of damage and/or losses of a structure at a specific site over a period of time, it has become customary to use analytical rather than empirical approaches primarily due to the scarcity of historical damage and loss data. These analytical approaches separate the contributions of seismic hazard, expressed as the rate of occurrence (or exceedance) of one or more ground motion Intensity Measures (IMs), from the contribution of structural response, described via one or more engineering demand parameters (EDPs). The relationship between IM(s) and EDP(s) is established through nonlinear response history analyses (NLRHA), conducted with preselected ground motions, and it is subsequently used to derive fragility functions, representing the probability of exceeding EDP values associated with the onset of given damage states should different levels of IM(s) occur at the site. Although the response of a structure to three-component ground motions depends on many characteristics of the motions, in most applications, the link between seismic hazard and structural response is left to one single ground motion IM (used as input to the fragility function). This state of practice is followed even though it is well known that different ground motions with the same level of the selected IM but different values of the other characteristics cause different levels of response. It is hence necessary to select judiciously the record sets that represent the seismic hazard at the site of interest (i.e., to enforce hazard consistency), a concept that has been highlighted many times in the literature [Bradley, 2010; Baker, 2011; Jayaram et al., 2011; Spillatura et al., 2021]. With the results of NLRHA, one can derive fragility functions anchored to specific values of the EDP corresponding to the onset of damage states (e.g., minor damage, major damage, or collapse). With the results of hazard and fragility analysis response (or demand) hazard curves can be estimated, which represent the rate of exceeding different EDP values in a given period of time.

Fragility functions are often assumed to follow a lognormal distribution with mean $\mu_{\ln(IM)}$ and standard deviation $\sigma_{\ln(IM)}$. Ideally, to obtain robust estimates of mean and standard deviation, and in turn response curves, one should select the sets of hazard-consistent ground motions (GMs) that accurately match the target distribution of intensity measure (IM) with one of the available hazard-consistent record selection variants. As in most applications it is customary to compute the hazard at a "reference rock" condition (we will

simply call it "rock" here), it would be necessary to have an extensive database of real ground motions recorded on the rock. Unfortunately, this is often not the case, particularly when it comes to the GMs with high levels of shaking. In practice, this problem is circumvented by using recordings on both rock and soil conditions scaled (often significantly) to the desired amplitude levels. While this alternative is a practical workaround, there is a legitimate concern that it might bias the structural response estimates. To mitigate the extent of this undesirable consequence, when using real ground motions, analysts often screen the ground motion database before record selection by, for instance, by limiting the values of magnitude (M), distance (R), soil shear wave velocity in the top 30 m (Vs_{30}), or maximum scaling factor (SF) [Baker and Lee 2018]. This screening identifies ground motions more consistent with those that may be experienced at the site, but it can have the negative effect of significantly reducing the number of record candidates for selection, a condition that may lead to a poor fitting of the target spectrum [Tarbali and Bradley 2016]. Hence, the analyst needs to find the balance between the rigidity in choosing the constraints and the goodness of fit of the targets, not knowing how much bias, if any, is introduced by this balancing act. The potential bias introduced by excessive ground motion amplitude scaling has been investigated in several studies in the recent literature. [Luco and Bazzurro 2007] showed that ground motion scaling could bias the nonlinear drift response of structures by an amount that depends on the scaling factor, dynamic properties of the structure and its overstrength. They anticipated that this bias might be avoided once the spectral shape is accounted for within the record selection. Indeed, this proposal was later confirmed by several studies [Baker 2007; Tsalouchidis and Adam 2022]. In contrast to those studies, [Dávalos and Miranda 2019] showed that scaling the ground motions can induce bias in the median displacement demands and collapse probability estimates, even if the spectral shape is accounted for via Conditional Mean Spectrum (CMS) [Baker 2011]. Du et al. [2019] showed that allowing high levels of scaling in Conditional Spectrum [CS, Jayaram et al. 2011] based record selection can influence the statistical distribution of IMs (e.g. arias intensity and duration) other than spectral acceleration and, consequently, some engineering demand parameters (EDPs). On the contrary, they observed that limiting the scaling to small factors can cause significant misfit to the CS target spectra. Based on these observations, they prescribed limitations on the maximum scaling factors of ground motions utilized in the CS approach, especially for structures whose response is sensitive to IMs beyond spectral accelerations.

The practical issues of mixing soil and rock ground motions and the necessity of scaling them to match the CS are not the only ones plaguing the development of fragility curves. Even with many ground motions to choose from, running numerous NLRHA can be computationally very demanding, especially for complicated structural models. This limitation leads to a reduced number of analyses, impacting the uncertainty associated with the estimates of fragility curves. Bradley [2013] explored this issue by examining the impact of the number of intensity levels considered in the Multiple-Stripe-Analysis (MSA) framework as proposed by Jalayer [2003], on the mean and standard deviation of fragility functions, comparing 'approximate' results based on the use of seismic response analyses at only a few IM levels, with the 'exact' results, based on the use of a large number of IM

levels, employing the Generalized Conditional Intensity Measure approach [GCIM, Bradley 2010] to select GMs. To reduce the computational effort that comes with running many analyses, various approaches have been proposed, including static procedures by FEMA[FEMA P-58 2012], machine learning techniques [Jeon et al. 2019], and enhanced methods like the one by Zhuang et al. [2022] which attempt to minimize the number of records while maintaining accuracy. Kiani et al. [2018] investigated the number of analyses needed for code, intensity, and risk-based seismic assessment, concluding that at least 20 ground motion pairs are required for risk assessment if a tolerance of 10% error in the mean annual rate of exceeding EDP (as compared with the benchmark case with 100 records per IM level) is accepted and maximum inter-story drift is adopted as an EDP. Baltzopoulos et al. [2019] instead examined the number of records necessary when Cloud [Jalayer 2003] and Incremental Dynamic Analysis (IDA) [Vamvatsikos and Cornell 2002] are utilized, concluding that it depends on the seismic hazard curve, with sites exposed to higher seismic hazard requiring more ground motions to achieve a similar coefficient of variation in the failure rate. The choice of the number of ground motions used in structural analysis varies among studies and hinges on the methodology adopted for assessing structural response and for record selection, on the choices of the conditioning IM and the EDP that describe the damage, and on the site-specific hazard level, among other factors.

The main motivation of this study is to answer the following two questions: (1) Given the scarcity of severe ground motions, is amplitude scaling of weaker signals to match the target CS a legitimate operation, or does it create ensembles of ground motions that could potentially cause bias in structural response estimates? and (2) how many analyses per intensity level one should run in the CS-based MSA framework for seismic risk assessment, without compromising the desired level of accuracy of the estimates and at the same time minimizing the computational burden?

In the following sections, we will first describe the methodology behind hazard-consistent record selection, explaining how we compiled the database of ground motions, performed hazard analysis for the case study site (Perugia, Central Italy) and subsequently employed CS to select records. Following this, we will explore the impact of ground motion scaling, statistically comparing distributions of different IMs, EDPs and fragility curves. In the second part of the study, we will investigate what is the optimal number of records for use in the CS-based MSA framework. This analysis involves the consideration of six distinct groups of records, each characterized by a different number of ground motions. Our investigation extends to assessing the impact of this choice on three critical aspects: fit to the target CS spectrum, the accuracy of fragility estimates and response hazard curves.

Within this analytical framework, an ensemble of hypothetical structures located at a case study site in Perugia, Central Italy, is considered. Given a large number of response analyses necessary for robust statistical inferences, we adopt a pragmatic approach: we employed single degree of freedom (SDOF) systems for their analytical simplicity but without compromising the generality of our findings.

5.2 HAZARD-CONSISTENT GROUND MOTION RECORD SELECTION

5.2.1 Assembling ground motion database

To assemble the database of ground motions from which we would select records, we use flatfiles from different data repositories. More specifically, we use the Engineering Strong-Motion (ESM) database (https://esm-db.eu) [Lanzano et al. 2019], NGA-West2 (NGA West 2 | Pacific Earthquake Engineering Research Center (berkeley.edu)) [Ancheta et al. 2014], New Zealand Strong-Motion database (Home - GNS Science) (here referred to as GNS) [Van Houtte et al. 2017] and finally, the updated version of worldwide NEar-Source Strong-motion (INGV/RELUIS NESS flat-file) (NESS) [Sgobba et al. 2021]. The ground motions from the NGA-West2 and NESS databases are retained if recorded at stations outside the geographical area covered by the other two databases to avoid double-counting. As spectral acceleration ordinates in these databases were reported at different vibration periods, we interpolated them to obtain the same array of periods that corresponds to the one available in the ESM database. A representation of the structure of the final database can be separated into six different blocks: intensity measures, event metadata, station metadata, source metadata, source-to-site distance metrics, and waveform metadata as illustrated in Figure 5.1. The assembled database is available for download at NevenaSipcic (Nevena) (github.com) as a *.mat data file. In Figure 5.2 one can see the map of the epicenters of the earthquakes with a moment magnitude M_w>5. In total, a suite of 34107 three-component ground motions is assembled.

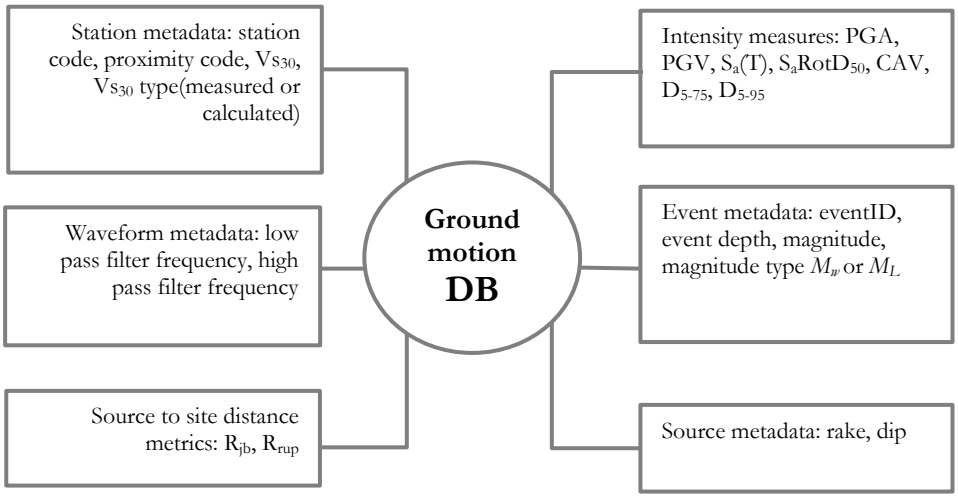

Figure 5.1. Schematic structure of the database that contains all considered ground motions.

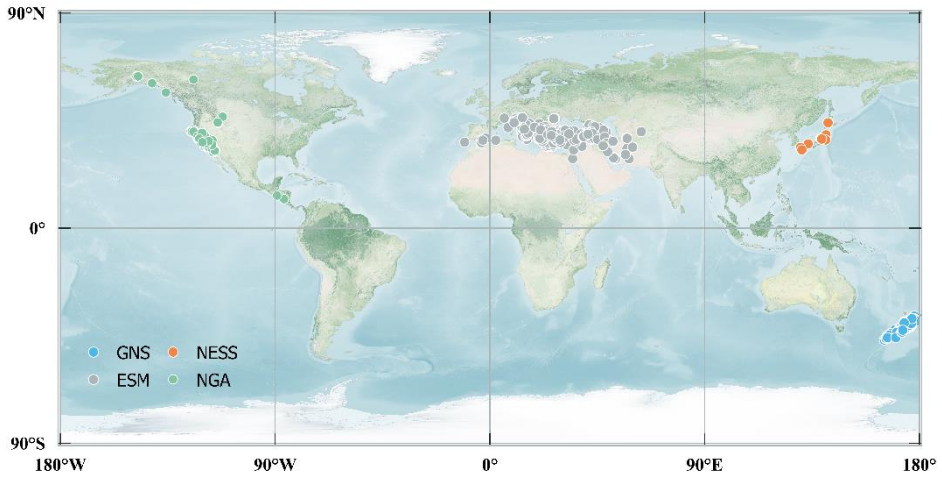

Figure 5.2. Map of epicenters of the earthquakes included in the assembled dataset, color-coded based on the original databases.

5.2.2 Hazard analysis

In both defined studies we use as a case study, a site in Perugia, Italy, located on a rock with Vs_{30}=800m/s. Probabilistic Seismic Hazard Analysis (PSHA) is carried out using the OpenQuake software [Pagani et al. 2014], the Ground Motion Prediction Equation (GMPE) of Boore and Atkinson [2008], and the SHARE seismic source model [Woessner et al. 2015]. In Figure 5.3 we show the location of the site and the mean hazard curves for different IMs, in terms of the probability of exceedance (poe) in 50 years. Seismic hazard disaggregation is performed for ten intensity levels (IMLs) corresponding to the return periods from 42 to 24975 years. Table 5.1 shows the defined IMLs with the corresponding poe in 50 years and the return period. In Appendix C1 one can find the mean magnitude and distance obtained from the disaggregation for every IML and different IMs.

Table 5.1. Considered intensity levels (IMLs) and corresponding probabilities of exceedance (poe) in 50 years and return periods.

IML	1	2	3	4	5	6	7	8	9	10
poe in 50 yrs	70%	50%	30%	10%	5%	2%	1.5%	1.0%	0.6%	0.2%
Return period	42	72	140	475	975	2475	3310	4975	8310	24975

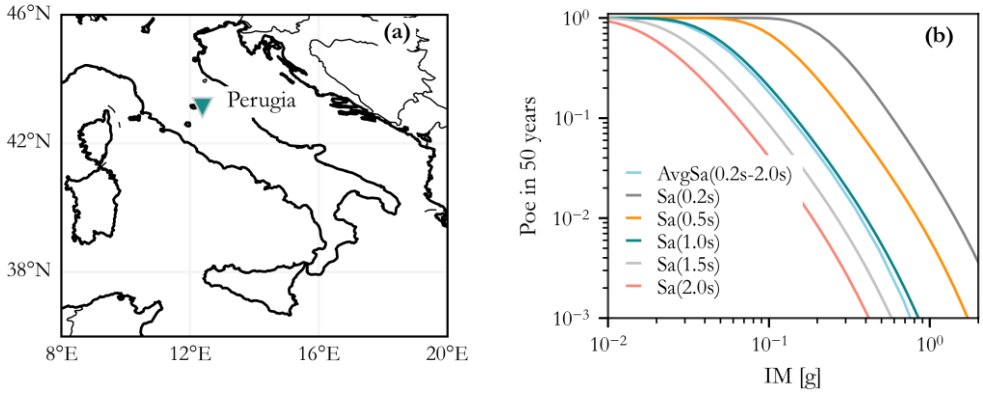

Figure 5.3. (a) Location of the case study site and (b) mean hazard curves for different IMs in terms of the probability of exceedance(poe) in 50 years.

5.2.3 CS-based record selection

To select the ground motions we use the CS approach as proposed by [Jayaram et al. 2011]. With this approach, records are selected to match the target distribution in terms of spectral ordinates conditioned on the chosen IM*(e.g. Sa(T_1), AvgSa) for the hazard level of interest extracted from the corresponding hazard curve. Results of the seismic hazard disaggregation are then used to identify the scenarios (in terms of magnitude M, distance R and residual ε for the chosen IM* level) that contribute the most to to the exceedance of that IM* level at the site. Using mean magnitude (M) and distance (R) obtained from the disaggregation, i.e. the so-called "approximate" CS method [Lin et al. 2013], target CS mean and standard deviation are found with Equation (5.1) and Equation (5.2), respectively.

$$\mu_{\ln Sa|\ln Sa(T^*)} = \mu_{\ln Sa|(T)} + \rho(T^*)\varepsilon\sigma_{\ln(Sa)} \quad (5.1)$$

$$\sigma_{\ln Sa|\ln Sa(T^*)} = \sigma_{\ln Sa|(T)}\sqrt{1-\rho(T^*)^2} \quad (5.2)$$

where $\mu_{\ln Sa(T)}$ and $\sigma_{\ln Sa(T)}$ are the unconditional logarithmic mean spectral accelerations and associated standard deviations obtained from the GMPE while ρ(T*) represents the correlation coefficient between the residuals of the IM* and Sa(T) across all periods of interest, calculated with Baker and Jayaram [2008] correlation structure.

We use the orientation-independent measure in terms of GMRotD50 [Boore 2010] to maintain full consistency with the hazard computations. For every record that we want to select we generate a random realization by sampling correlated lnSa values from the multivariate normal distribution and we select a record from an available database that best matches this realization. The simulation procedure is repeated several times and the set of records that best matches the target (given by Equations (5.1) and (5.2)) is selected. The

accuracy of the matching to the target is calculated using the use the sum of squared errors (SSEs) [Baker and Lee 2018] metric defined by Equation (5.3).

$$SSE_s = \sum_{k=1}^{p} [(m_{\ln IM_k} - \mu_{\ln IM_k})^2 + w(s_{\ln IM_k} - \sigma_{\ln IM_k})^2] \quad (5.3)$$

where IM_k is the spectral acceleration at T_k, $m_{\ln IMk}$ is the sample mean of $\ln IM_k$, and $s_{\ln IMk}$ is the sample standard deviation of lnIMk, both estimated from the selected motions. The quantities $\mu_{\ln IMk}$ and $\sigma_{\ln IMk}$ are the target conditional means and standard deviations, p is the number of vibration periods of interest in the target spectrum, and w is a weight factor here assumed equal to 2.0. This latter value is meant to assign a higher degree of importance to the mismatches in the standard deviation rather than the target mean. In our calculations, SSEs=0.12 is considered as the acceptable threshold [Iñarritu et al. 2023]. Once the initial set of records is selected, one can perform the so-called "greedy" optimization [Jayaram et al. 2011] to improve the match to the target. One should note that the record selection using AvgSa as a conditioning IM is similar to the one when Sa(T^*) is used, as explained in more detail in Kohrangi et al. [2017].

For the sake of the illustration, we show in Figure 5.4 and Figure 5.5 the record selection for the case study site and intensity level corresponding to the IML4 (i.e., 475 years return period) using Sa(1.0s) and AvgSa(0.2s-2.0s) as a conditioning IM, respectively. In the illustrated case, 22 GMs are selected to match the target mean and standard deviation of ln(Sa).

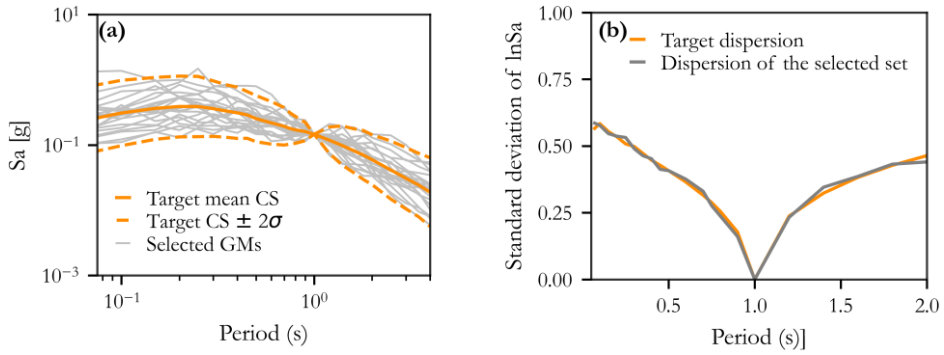

Figure 5.4. Illustration of the record selection with the conditioning IM=Sa(1.0s) corresponding to the IML4 (i.e., 475 years return period) in Perugia, Italy. (a) Mean (of the log) CS±2 standard deviations and spectra of the 22 selected records are shown. (b) Target standard deviation and standard deviation of the selected set of 22 records.

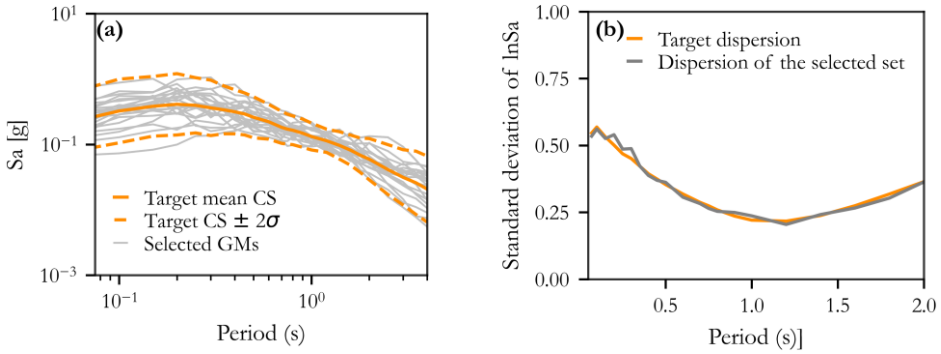

Figure 5.5. Illustration of the record selection with the conditioning IM=AvgSa(0.2s-2.0s) corresponding to the IML4 (i.e., 475 years return period) in Perugia, Italy. (a) Mean (of the log) CS±2 standard deviations and spectra of the 22 selected records are shown. (b) Target standard deviation and standard deviation of the selected set of 22 records.

5.3 EFFECT OF ACCELEROGRAMS' SCALING ON HAZARD-CONSISTENT GROUND MOTION RECORD SELECTION

5.3.1 Case study and analyses set-up

To represent a wide group of structures, we use a set of SDOF systems characterized by different fundamental periods (T_1 = 0.2, 0.5, 1.0, 1.5, and 2.0s) and with two different hysteretic models, namely, the degradation (pinching) model and the elastic-hardening model. These models were implemented in OpenSees using the "pinching4" and "Steel01" material models, respectively. To design these systems, we used the yield base shear coefficient (Cy) representative of a lateral strength corresponding to the PSHA-based spectral acceleration value of 10% in 50 years at the fundamental period of each SDOF. Cy represents the yield base shear Fy normalized by the weight W and is numerically equivalent to the yield spectral acceleration Sa_y in units of g. Namely, $Sa_y/g=Vy/W$ is obtained as $Sa_{des}(T_1)\cdot\Omega/(q\cdot g)$, where $Sa_{des}(T_1)$ is the design spectral acceleration at T_1, q is the behavior factor assumed equal to 4.0 for new ductile buildings and Ω=2.0 is the overstrength factor. Accordingly, the corresponding yield displacement, δy of the SDOF is obtained by $\delta y = Sa_y\cdot[T_1/(2\pi)]$. The responses of the SDOFs were computed assuming a 5% mass proportional Rayleigh damping.

From the compiled database of ground motions, two groups of records were extracted, differentiated by the scaling factors used to match the target CS spectra. In the low-scaling factor (LSF) group, we only allowed scale factors in the range of [1, 2] while in the high-scaling factor (HSF) group, much larger scale factors in the range of [7, 10] were adopted. For each considered SDOF system and 10 IMLs defined (Table 5.1), 40 ground motion pairs were selected using $Sa(T_1)$ as the conditioning IM, employing the methodology described in Section 5.2, from both the LSF and HSF groups. Figure 5.6 shows the goodness of fit achieved between empirical and target CS in terms of SSEs for the LSF

and HSF groups across all conditioning periods. Notably, all cases exhibit a satisfactory fit, with none surpassing the threshold SSEs value of 0.12 [Iñarritu et al. 2023]. One should note that SSEs values obtained from the HSF group are slightly higher despite using higher scaling factors, a result that may appear counterintuitive. Nonetheless, it is worth highlighting that the HSF group includes only motions with a minimum scaling value of 7 (in contrast to the LSF group's minimum of 1), hence this is an expected trend.

Figure 5.7 shows the hazard consistency verification that compares the values in the PSHA hazard curves for Sa(0.2), Sa(1.0), and Sa(2.0) with the mean annual rates of exceeding the same values extracted from the CS-selected sets of records with IM*= Sa(1.0). One can see that the match is good for both LSF and HSF group.

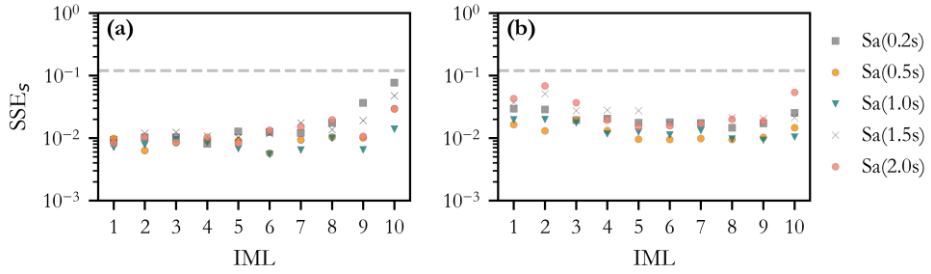

Figure 5.6. SSEs for the CS-based (a) LSF and (b) HSF record sets selected for different conditioning periods. The horizontal gray dashed line shows the acceptable SSEs threshold of 0.12.

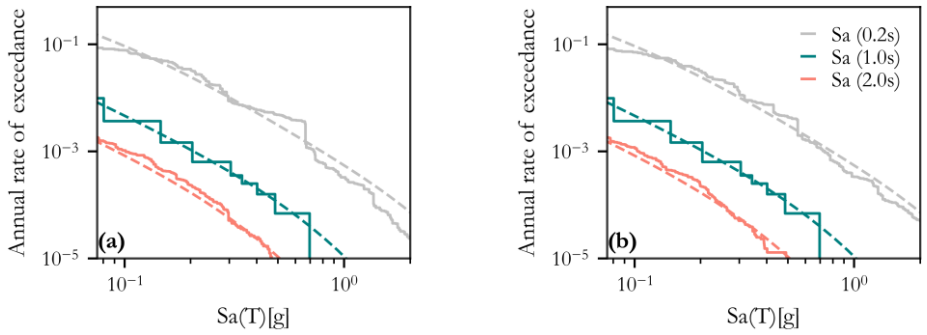

Figure 5.7. Hazard consistency verification for spectral ordinates of Sa(0.2), Sa(1.0), and Sa(2.0) using the IM*= Sa(1.0) for records selected from (a) the LSF group, and (b) the HSF group. The dashed lines show the PSHA-based hazard curves while the solid lines show the values of the mean annual frequency of each spectral ordinate as estimated from CS-based selected records.

Using the selected sets of GMs we run the NLRHA analysis for all IMLs (i.e. MSA) monitoring four EDPs relevant to risk assessment: a) maximum ductility, computed using the yield displacement of each SDOF; b) maximum acceleration, computed as the maximum absolute value found during the analysis; c) maximum velocity, computed as before; and d) dissipated hysteretic energy, computed by integrating the force–displacement response. The cases where the ductility exceeds eight are treated as collapse cases. Fragility functions for the SDOFs are derived for three arbitrarily defined ductility-based damage states (DS): Onset of Damage (DS1) when $2<\mu\leq4$, Moderate Damage (DS2) when $4<\mu\leq8$, and near collapse (DS3) defined by ductility values $\mu>8$. To derive fragility functions we assume a lognormal distribution and we use the maximum likelihood method [Baker 2015].

Our extreme choices for CS-based record selection, in the use of small versus large scaling factors, will reveal the level of importance of these choices in hazard-consistent structural response prediction. We acknowledge that the "true" response to hazard-consistent, unscaled rock ground motions is indeed unknown. However, if we do not see significant statistical differences in the response estimates resulting from our purposely extreme choices, then we can reasonably claim that there are no additional biases introduced by these practical circumventions in hazard-consistent record selection.

5.3.2 Statistical analyses of the IMs

To assess whether our choices for the SF in CS selection introduce any potential systematic discrepancies in structural responses, we first compare the empirical distribution of several IMs extracted from the selected sets of records. The IMs considered are peak ground acceleration (PGA), significant duration ($Ds_{5\text{-}75}$), cumulative absolute velocity (CAV), Arias intensity (AI), and acceleration spectral intensity (SI) [Thun et al. 1988]. Figure 5.8 compares the metrics of the distributions of the IMs using box plots, for the three conditioning periods of 0.2, 1.0, and 2.0 s. In these figures, the boundaries of each box correspond to the lower and upper quartiles, the line within the box corresponds to the median and the whiskers extend to the minimum and maximum observed values. Results for the remaining intermediate cases (0.5s and 1.5s) are provided in Appendix C2.

We see almost no differences in terms of PGA and SI, while some systematic discrepancies are present in terms of $Ds_{5\text{-}75}$, CAV, and AI. Using the t-test for hypothesis testing, we indeed observed that the null hypothesis could not be rejected at the 5% significance level for PGA and SI, whereas for $Ds_{5\text{-}75}$, CAV, and AI the null hypothesis is rejected in almost all cases. Note that $Ds_{5\text{-}75}$ is not directly affected by scaling, but as using high scaling factors naturally implies selecting suites of ground motions recorded, on average, at larger distances from the site, this systematic difference leads to selecting ground motions in the HSF group with, on average, longer durations. On the contrary, we can notice statistically significant discrepancies in the distribution of AI and CAV for the HSF and LSF groups, with the metrics for the HSF group being almost always higher. Therefore, this exercise clarifies that the distributions of the IMs that are not directly controlled by the selection algorithm can be distorted by the amount of scaling. Therefore, if such IMs are pertinent

to the response of a structure their hazard consistency must be enforced using approaches like the GCIM, to mitigate potential bias.

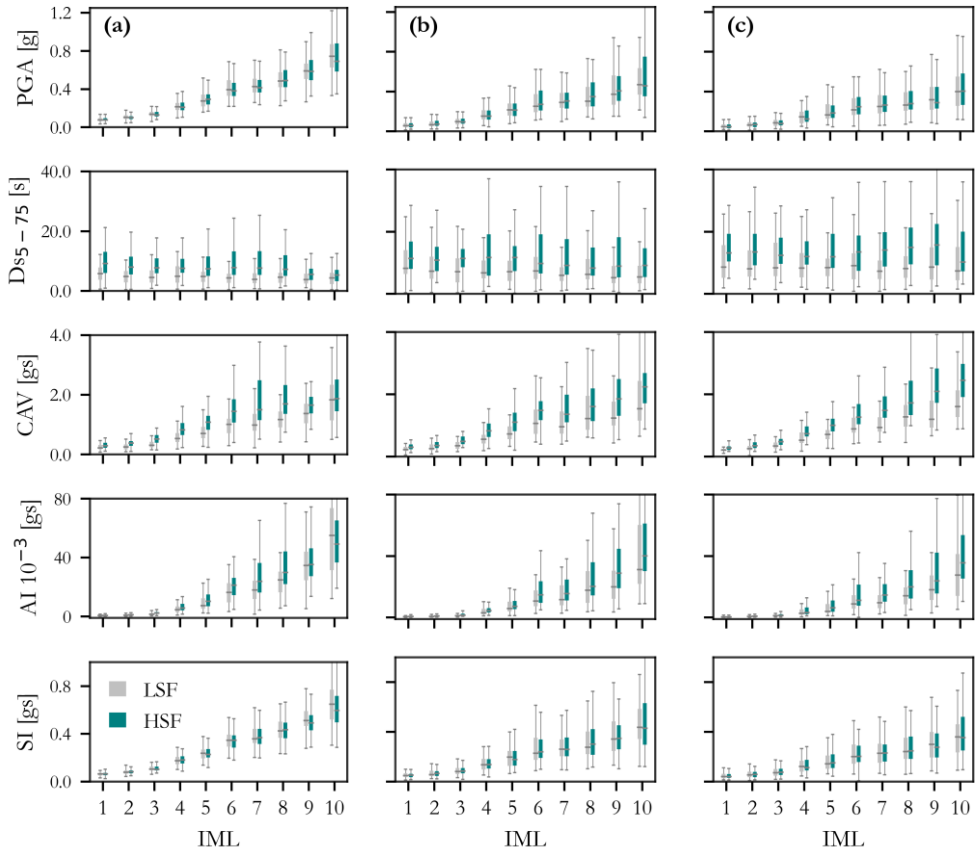

Figure 5.8. Metrics of the distributions of the different IMs: PGA, $Ds_{5\text{-}75}$, CAV, AI, and SI from the first to the last row, respectively. Results for the sets of records selected using the IM*=(a) Sa(0.2s), (b) Sa(1.0s)and (c) Sa(2.0s) are shown.

5.3.3 Structural response estimates and fragility analyses

In Figure 5.9 and Figure 5.10, we compare the ductility ratio and maximum acceleration obtained via MSA for the three SDOFs with the vibration periods of 0.2, 1.0, and 2.0 s and pinching and elastic with hardening hysteretic models, respectively. In Figure 5.11 and Figure 5.12, we show the corresponding fragility curves for the three defined damage states. Despite the differences in the IMs observed earlier, the ductility ratio and maximum acceleration responses caused by the ground motions in the two groups are similar both in terms of median and percentiles for all IMLs and SDOFs. However, the slight differences in the distribution tails yield some minor differences in the fragility curves. For the SDOF

systems with pinching, with the only exception of the T_1=2.0s SDOF at DS3, the HSF group yields slightly higher, but statistically not significantly different, exceedance probabilities for all SDOFs and ductility levels. However, in the case of SDOF system with the elastic with hardening material model, in some cases LSF yields higher and in others lower probabilities. Nonetheless, these differences, again, are not significant. The remaining cases (i.e. SDOFs with 0.5s and 1.5s and structural response in terms of the maximum velocity and dissipated energy), which show similar trends, are omitted here but can be found in Appendix C3.

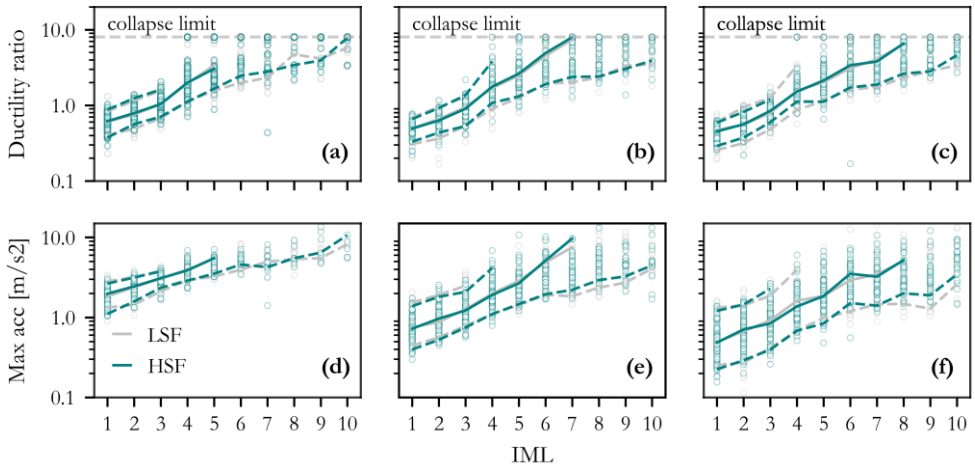

Figure 5.9. Comparison of the response estimates obtained from MSA showing the data points, the median (solid line) and 5th and 95th percentiles (dashed lines) of the data in terms of ductility ratio (a, b, c), and maximum relative acceleration (d, e, f) based on the LSF and HSF sets of ground motions. Results for the SDOF with T_1 of 0.2s(a and d), 1.0s(b and e), and 2.0s(c and f) are illustrated. These results pertain to SDOFs with pinching material model.

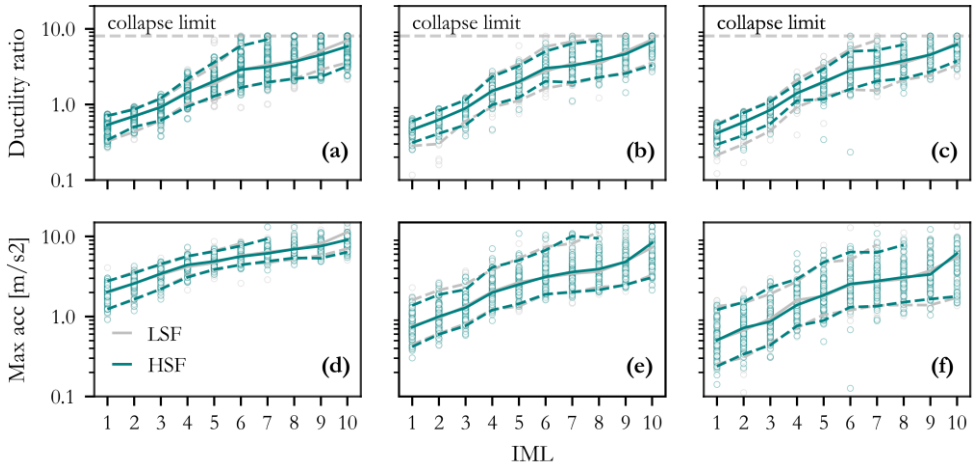

Figure 5.10. Comparison of the response estimates obtained from MSA showing the data points, the median (solid line) and 5th and 95th percentiles (dashed lines) of the data in terms of ductility ratio (a, b, c), and maximum relative acceleration (d, e, f) based on the LSF and HSF sets of ground motions. Results for the SDOF with T_1 of 0.2s(a and d), 1.0s(b and e), and 2.0s(c and f) are illustrated. These results pertain to SDOFs with elastic with hardening material model.

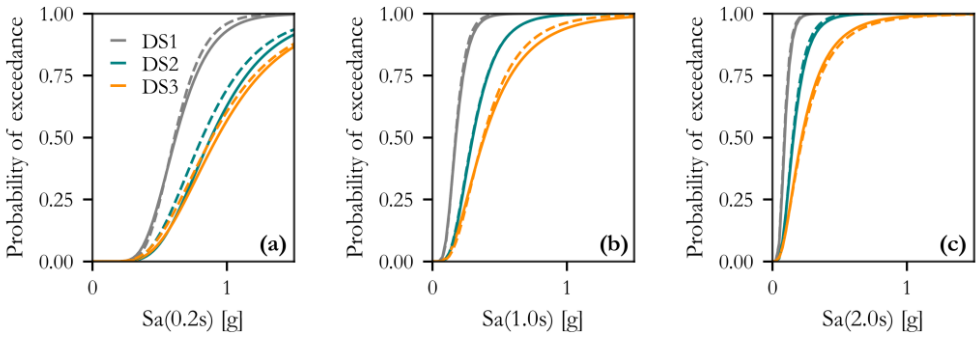

Figure 5.11. Comparison between the fragility curves obtained from LSF (solid line) and HSF (dashed line) groups for three different damage states and SDOFs with vibration period of (a) T_1=0.2 s, (b) T_1=1.0 s, and (c) T_1=2.0 s. These results pertain to SDOFs with pinching material model.

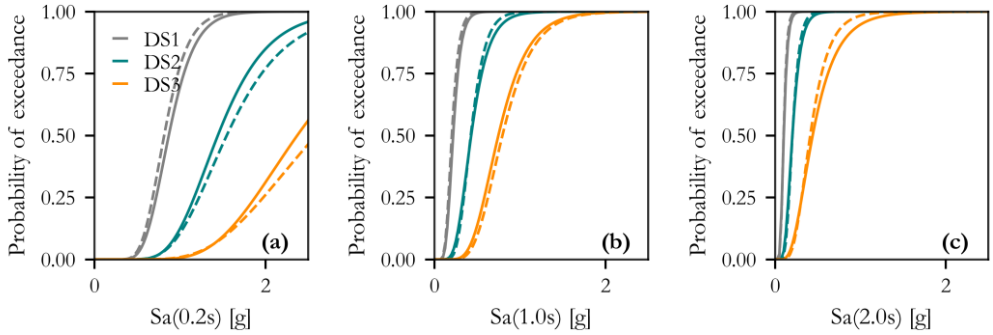

Figure 5.12. Comparison between the fragility curves obtained from LSF (solid line) and HSF (dashed line) groups for three different damage states and SDOFs with vibration period of (a) T_1=0.2 s, (b) T_1=1.0 s, and (c) T_1=2.0 s. These results pertain to SDOFs with elastic with hardening material model.

5.4 OPTIMIZING THE NUMBER OF GROUND MOTIONS PER INTENSITY LEVEL

5.4.1 Case study and analyses set-up

In the second part of this study, we focus on the estimation of the optimal number of records per IM level (or stripe) needed in MSA to achieve an acceptable level of accuracy. To do so, we use as a case study a nonlinear SDOF system with a fundamental period of T_1=1.0s, designed for the lateral strength corresponding to the PSHA-based spectral acceleration value of 10% in 50 years (see Section 5.3.1 for more details). Our chosen SDOF system is modeled in OpenSees using a zero-length element and the constitutive model proposed by Ibarra et al. [2005], which incorporates both in-cycle and cyclic strength and stiffness degradation. Three ductility-based damage states (DS) are arbitrarily defined as: Onset of Damage (DS1) when $2<\mu\leq3$, Moderate Damage (DS2) when $3<\mu\leq6$, and near collapse (DS3) defined by ductility values $\mu>6$. In Figure 5.13 we show the monotonic backbone curve of the model with defined damage states indicated.

As in the previous section, our SDOF system is located in Perugia, Central Italy. Following the methodology outlined in Section 5.2, we select the ground motions using CS for the ten IMLs defined (Table 5.1) and using two conditioning IMs, namely Sa(1.0s) and AvgSa(0.2s-2.0s), with an increment of 0.2s. We define six distinct groups with varying numbers of selected GMs: 3, 7, 11, 16, 22, and 44. To measure the statistical variability of the estimates, we repeat the selection 20 times for each group, every time disregarding part of the selected ground motions (to avoid having the same sets of records): for the case of N3 (i.e., 3 records per stripe), one record is omitted in each iteration; for N7, three records; for N11, 4 records; for N16, 5 records; for N22, 7 records; and for N44, 11 records.

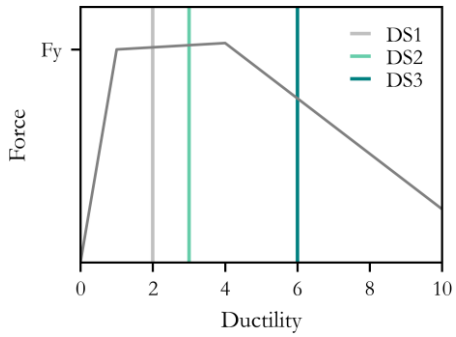

Figure 5.13. The monotonic backbone of the Ibarra et al. [2005] constitutive material model with the three defined damage states indicated, i.e., DS1(onset of damage), DS2(moderate damage) and DS3(near collapse).

5.4.2 Fitting the target CS

For each group Nx (where x refers to the number of records in a set), Figure 5.14 and Figure 5.15 show the SSEs error metric, given with Equation (5.3), used to measure the misfit of the distribution of spectral quantities from the selected set to the target CS one,

for the Sa(1.0s) and AvgSa(0.2s-2.0s) case, respectively. The points in each stripe refer to the 20 iterations conducted. For both conditioning IMs, group N3 exceeds the acceptable threshold for all intensity levels, while group N7 fluctuates around the threshold. The last four groups have acceptable fits for the first 9 IMLs. For the last IML, group N44 is close to or above the threshold in a few iterations simply because of the lack of records left in the database with the increasing number of iterations. While we acknowledge that achieving a good fit to the target CS depends on various factors, such as the choice of conditioning IM, the hazard at the site, the intensity level of interest, and the availability of records for selection, based on our findings we can say that when there are too few records in the stripe (seven or fewer), matching the target mean and standard deviation of the CS within an acceptable tolerance can be a challenging task.

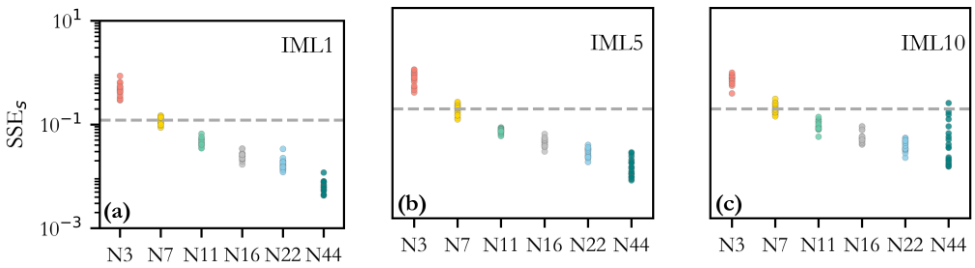

Figure 5.14. The error (SSEs) estimate for three different intensity levels: (a) IML1, (b) IML5 and (c) IML10, for six groups with different numbers of records per stripe (N3–N44) showing the improving fidelity achieved by larger record sets. The dashed grey line serves as the threshold below which the fit to the target CS can be considered accurate. Record sets are selected using Sa(1.0s) as conditioning IM.

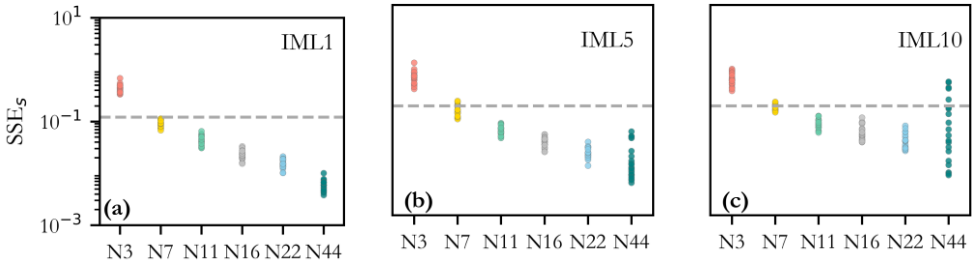

Figure 5.15. The error (SSEs) estimate for three different intensity levels: (a) IML1, (b) IML5 and (c) IML10, for six groups with different numbers of records per stripe (N3–N44) showing the improving fidelity achieved by larger record sets. The dashed grey line serves as the threshold below which the fit to the target CS can be considered accurate. Record sets are selected using AvgSa(0.2s-2.0) as conditioning IM.

5.4.3 Fragility and response hazard curves

To derive the fragility curves, we run the NLRHA for each of the 10 IMLs and each of the six Nx groups using the 20 alternative sets of records. For instance, in the case of the N3 group, we performed 600 runs by running three ground motions for 10 IMLs 20 times (as we have 20 iterations). Figure 5.16 and Figure 5.17 show the results for three groups: N3, N16, and N44, for Sa(1.0s) and AvgSa(0.2s-2.0s) cases, respectively. As expected, the variability in the fragility curves decreases, and the results become more stable as we utilize a larger number of records. This trend is not as apparent for the lower ductility levels as it is for the DS3 (near collapse). More specifically, Figure 5.18 and Figure 5.19 display the distribution of the median and dispersion of the fragility functions for each group considered. To estimate the variability associated with the fragility function parameters, we calculate the coefficient of variation (COV) for both median and dispersion, as illustrated in Figure 5.20 and Figure 5.21, for Sa(1.0s) and AvgSa(0.2s-2.0s) case, respectively. Notably, the median estimates are more stable, consistently remaining below 10% for all damage states when there are seven or more records in the stripe. On the other hand, for all damage states the dispersion estimate has a higher COV, but lower than 20%, when there are 16 or more records per stripe.

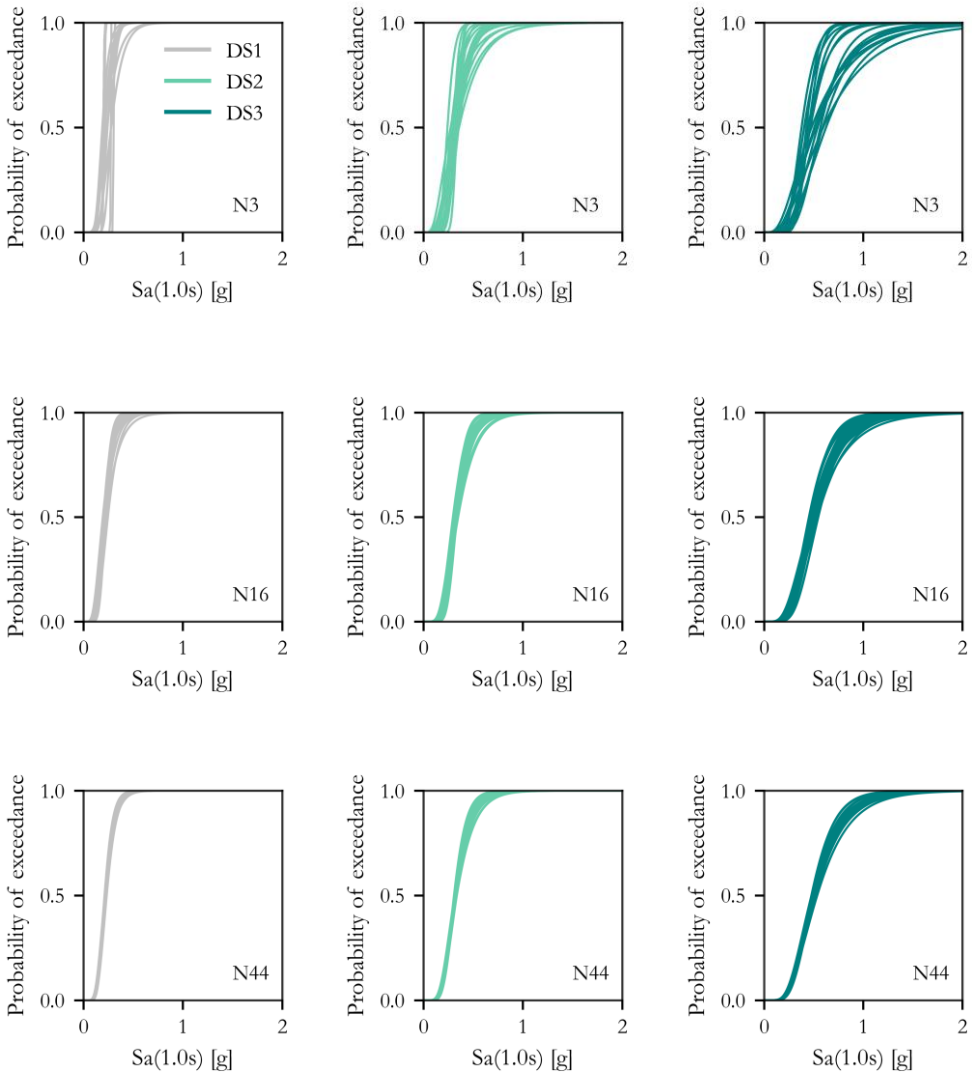

Figure 5.16. Fragility curves obtained with 20 alternative ground motion sets for three damage states DS1, DS2, and DS3 corresponding to the ductilities of 2, 3, and 6, respectively. Results for groups N3, N16 and N44 are illustrated. Record sets are selected using Sa(1.0s) as conditioning IM.

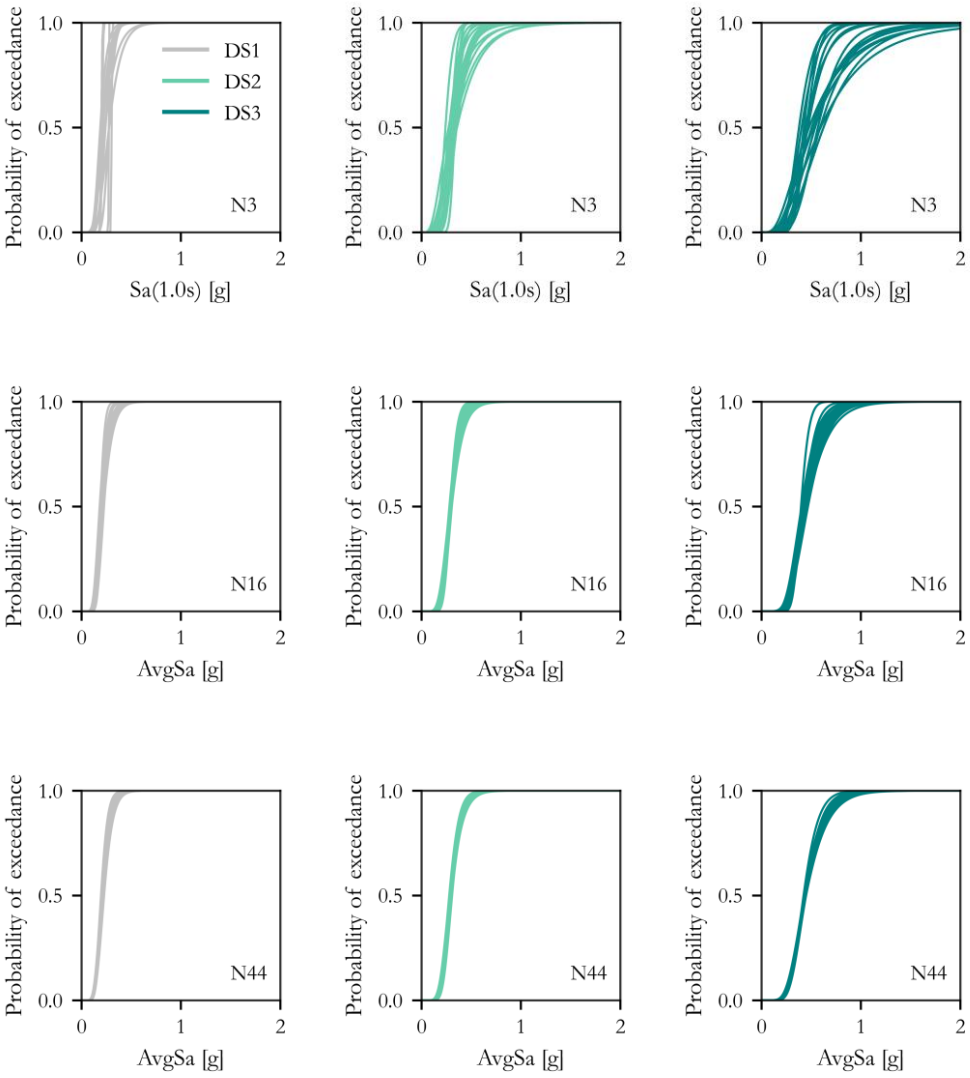

Figure 5.17. Fragility curves obtained with 20 alternative ground motion sets for three damage states DS1, DS2, and DS3 corresponding to the ductilities of 2, 3, and 6, respectively. Results for groups N3, N16 and N44 are illustrated. Record sets as selected using AvgSa(0.2s-2.0) as conditioning IM.

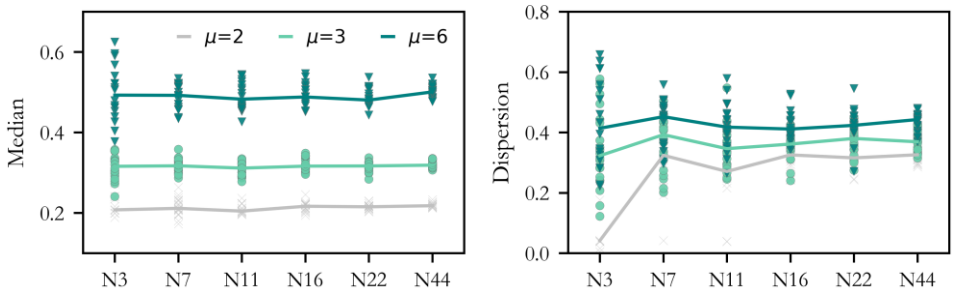

Figure 5.18. Estimates of the fragility function parameters. Scatter points refer to 20 alternative record sets while solid lines connect the median values per DS. Record sets are selected using Sa(1.0s) as conditioning IM.

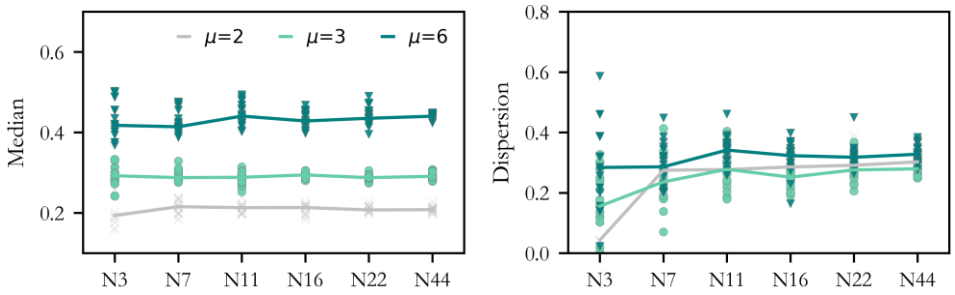

Figure 5.19. Estimates of the fragility function parameters. Scatter points refer to 20 alternative record sets while solid lines connect the median values per DS. Record sets are selected using AvgSa(0.2s-2.0) as conditioning IM.

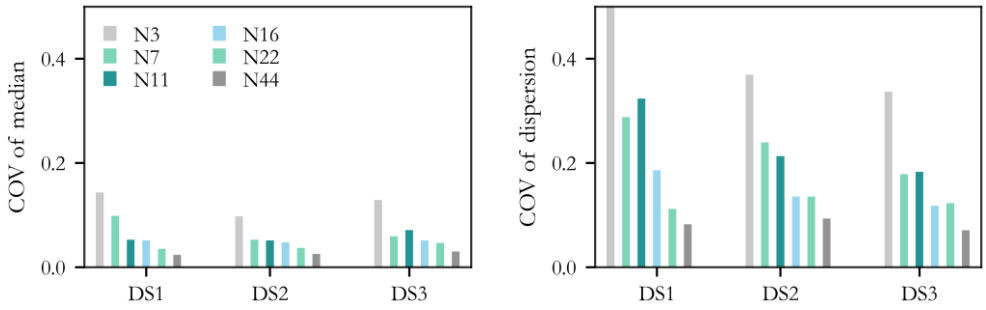

Figure 5.20. COV of the fragility curve parameter estimates. A number of 11–16 records seems to offer a stable low COV for both median and dispersion across all DSs. Record sets are selected using Sa(1.0s) as conditioning IM.

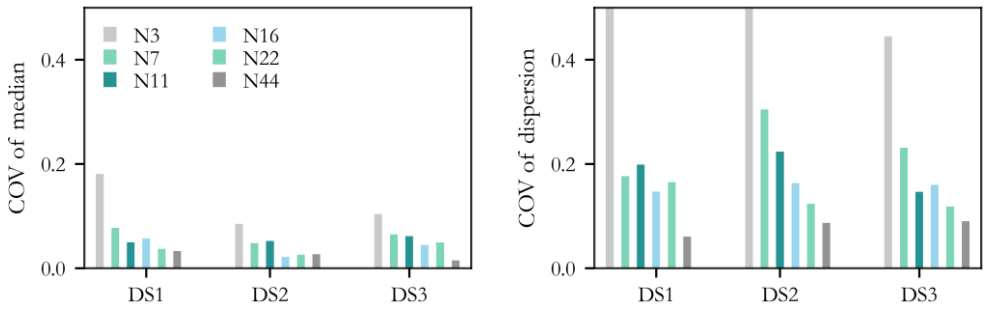

Figure 5.21. COV of the fragility curve parameter estimates. A number of 11–16 records seems to offer a stable low COV for both median and dispersion across all DSs. Record sets are selected using AvgSa(0.2s-2.0) as conditioning IM.

Lastly, we use the obtained results to derive the seismic demand hazard curves, which represent the rate of exceeding a specific *edp* level (in this case ductility) in a given period of time (e.g., one year). To calculate the seismic demand curves we combine the results of the hazard analysis with the results of the structural analysis using numerical integration over a range of intensity levels and the following expression:

$$\lambda_{EDP}(edp) = \sum_{i=1}^{N_{IM}} P(EDP > edp \mid IM) \frac{\Delta\lambda_{IM}(im)}{\Delta IM} \Delta IM \tag{5.4}$$

$\lambda_{EDP}(edp)$ is the annual rate of exceeding the *edp* level, $P(EDP>edp \mid IM)$ is the probability of exceeding a certain *edp* level for the given intensity level $IM=im$ and ΔIM is the increment in *IM* between the considered *IM* levels while the $\Delta\lambda_{IM}(im)$ is the increment in the seismic hazard curve for the associated *im*. The term associated with the hazard part is found as the first derivative of the hazard curve (which is interpolated using cubic spline interpolation in log space). To find the probability of exceeding the *edp* level for a given intensity level we follow the methodology of Shome and Cornell [1999], who separate collapse and non-collapse cases, as given in Equation (5.5).

$$\lambda_{EDP}(edp) = \sum_{i=1}^{N_{IM}} ((1 - P_{C|IM}) \cdot P(EDP > edp \mid IM, NC) + P_{C|IM}) \frac{\Delta\lambda_{IM}(im)}{\Delta IM} \Delta IM \tag{5.5}$$

$P_{C|IM}$ is the probability of collapse, found using the maximum likelihood method Baker [2015]. As performed commonly, the distribution of non-collapse cases is found assuming the lognormal distribution characterized with a mean $\mu_{\ln EDP|IM}$ and dispersion $\sigma_{\ln EDP|IM}$. To find the mean and dispersion we use the method of moments (see Equations (5.6) and (5.7)). As the structural analyses are performed only at the specific IM levels to find mean and dispersion at other intensity levels we use the piecewise linear interpolation.

$$\mu_{\ln EDP|IM} = \exp\left(\sum_{i=1}^{N_{IM}} \frac{\ln(x_i)}{n}\right) \tag{5.6}$$

$$\sigma_{\ln EDP|IM} = \left(\sum_{i=1}^{N_{IM}} \frac{(\ln(x_i) - \ln(\mu_{\ln EDP|IM}))^2}{n-1}\right)^{0.5} \tag{5.7}$$

In Figure 5.22, we show the response hazard curves cast in terms of ductility ratio for different sets of records. Similarly as in the case of fragility functions, the variability reduces as we increase the number of records used. As illustrated in Figure 5.23 the COV of the estimated exceedance rates increases, as expected, for the higher ductilities and decreases as we utilize more records. For the first two damage states the COV is below 15% if we use at least 11 records per stripe while for the last damage states at least 22 records are needed to achieve the same accuracy.

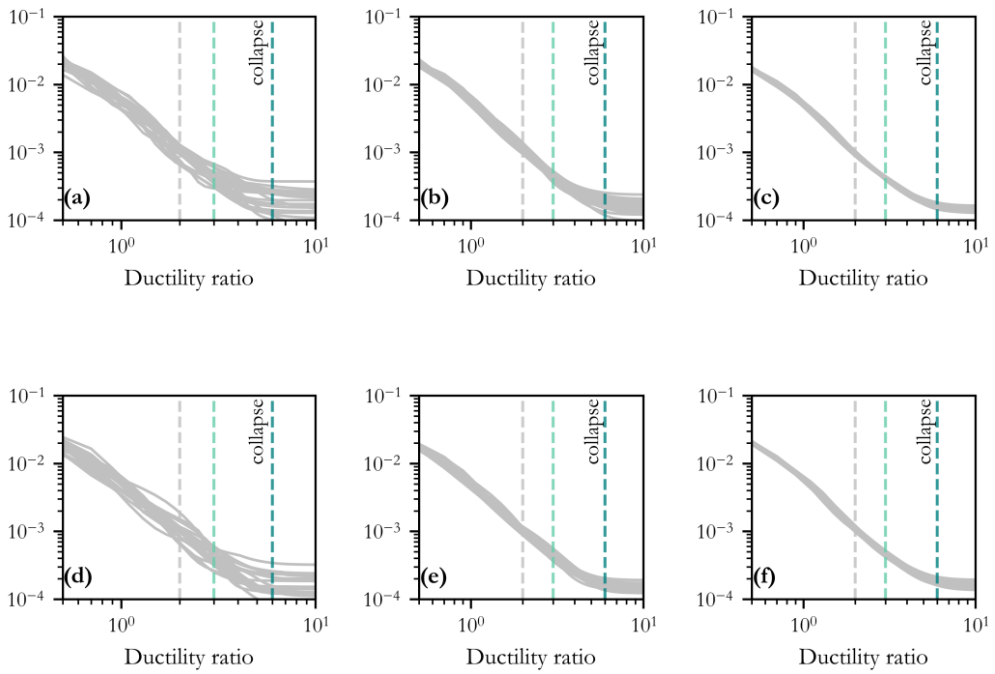

Figure 5.22. Ductility hazard curves obtained with 20 alternative ground motion sets from groups with different numbers of GMs (N3 in (a) and (d), N16 in (b) and (e) and N44 in (c) and (f)). Record sets are selected using Sa(0.1s)((a), (b) and (c)) and AvgSa(0.2s-2.0)((d), (e) and (f)) as conditioning IM.

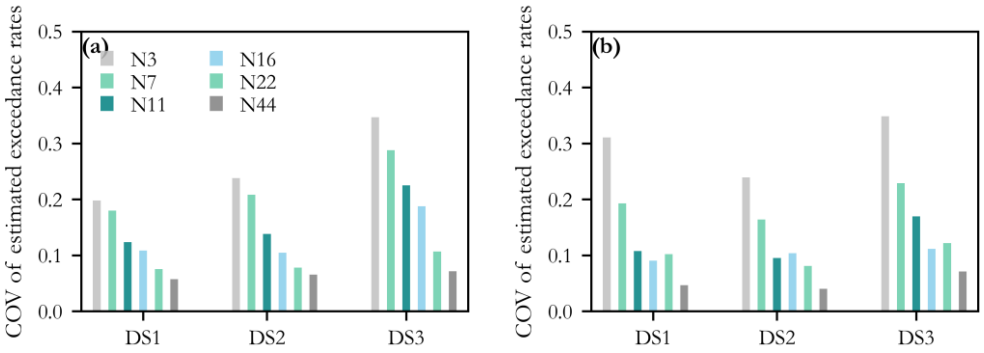

Figure 5.23. COV of estimated exceedance rates at different ductility levels and for different record sets using (a) Sa(1.0s) and (b) AvgSa(0.2s-2.0s) as a conditioning IM.

5.5 CONCLUSIONS

Hazard-consistent record selection is of paramount importance for adequate site-specific risk assessment of structures. In many high-profile applications, the hazard is computed via PSHA for reference rock conditions, while the effects of soil on surface motions are studied using soil dynamics. In these cases, to ensure hazard consistency, record selection would ideally require a large pool of rock, unscaled, real ground motions to ensure hazard consistency. However, the number of available rock ground motions is not sufficient to achieve this goal and alternative practical workarounds, such as mixing soil with rock real ground motions, scaling real ground motions to bring them up to the desired (high) amplitudes, or considering synthetic ground motions (or combinations of them), are often utilized. In the first part of this study, we investigated the possible bias in structural response arising from using scaled real ground motions for CS-based record selection. For this purpose, we considered a site in Central Italy as a case study for hazard computation; we carried out CS-based record selection for that site and with the ground motions we computed the responses of five SDOF systems (with fundamental periods ranging from 0.2 to 2.0 s), with 2 material models (pinching and elastic with hardening). The sets of CS-based records selected to match the target spectra included were separated into the two groups: ground motions scaled by high scaling factors (HSF) in the range of [7, 10] and low scaling factors (LSF) in the range of [1, 2]. For the different record sets, we compared the distributions of several intensity measures beyond spectral quantities, which are already forced to be similar by the CS-based selection approach, to identify any systematic differences in IMs that could potentially lead to different structural responses. Although we noticed some discrepancies in the distribution of some IMs among different groups exacerbated by our extreme choices in record selection, we did not observe significant statistical discrepancies between the predicted responses of the considered SDOF systems. Our results show that as long hazard consistency is carefully enforced via a CS method, and provided that none of the IMs relevant to the structural response of the specific structure show any systematic differences, the use of scaled motions can be considered

adequate to use for response assessment of structures located in active crustal seismicity regions and with a fundamental period in the 0.2–2.0 s range. If some of the IMs that can affect the response do show some systematic difference, then the use of GCIM for record selection is recommended instead. We would like to emphasize again that, by design, we tested only extreme cases, the response of structures to CS-based selected groups of very different ground motions, namely, only unscaled (or mildly scaled) records versus severely scaled records. In real applications, we see no compelling reasons to consider such extreme cases because one would rather consider using highly scaled records sparingly and only on an as-needed basis to augment the pool of unscaled records. Therefore, it is legitimate to say that in real applications one would expect to see an even smaller amount of bias, if any, than that found in some cases here.

To obtain robust fragility (and hence response hazard curve) estimates one often has to run many analyses, an exercise that can come with high computational cost. That said, the objective in the second part of this study was to investigate how one could reduce the number of response analyses needed to derive site-specific fragility curves for structures using the MSA approach. To do so, we first examined the effect of the number of ground motions per stripe on the match of the distribution of spectral accelerations of the selected ground motions with that of the target conditional spectrum and, in turn, the effect on the resulting fragility curve. We showed that to achieve a good match to the target more than 7 records per stripe are recommended and, more importantly, to obtain stable median and dispersion estimates of the fragility curve at least 11 or 16 ground motions are needed, given the desired level of accuracy sought here.

The findings of this section can facilitate the practical application of CS-based record selection for fragility curve computation and, ultimately, for site- and structure-specific risk assessment.

6.AFTERSHOCK GROUND MOTION RECORD SELECTION AND DAMAGE-DEPENDENT FRAGILITY CURVES

6.1 INTRODUCTION

In the current framework of performance-based earthquake engineering (PBEE), as established by Cornell and Krawinkler [2000], the assessment of the probability that ground motion will exceed various intensity levels at a specific site over a given period of time relies on classical Probabilistic Seismic Hazard Analysis (PSHA). In PSHA, all dependent seismic events, such as aftershocks, foreshocks, and triggered events, are systematically disregarded. In other words, earthquake catalogs that are used to predict the rates of future events have been "declustered" to include only the supposedly independent mainshock events. Additionally, it is assumed that the building is returned to an intact state immediately after the earthquake event, assuming that repairs have been fully completed since the occurrence of the previous seismic event – though, in reality, this assumption most often does not hold.

Historical seismic sequences, such as those in Canterbury, New Zealand in 2010 [EEFIT 2011], Japan in 2011 [Kazama and Noda 2012], and Central Italy in 2016 [Sextos et al. 2018] have demonstrated that these traditional approaches tend to be conservative in estimating the risk to society. These sequences illustrated that the impact of seismic events can be significantly amplified when considering the entire sequence, compared to when focusing solely on the mainshock. This amplification is particularly notable in the aftermath of major events, which are frequently followed by a cluster of damaging aftershocks. As this issue has been long recognized, several researchers have been studying how to incorporate clustered seismicity into risk assessment both in terms of hazard and vulnerability. The underestimation of hazard due to the mainshock-only view has been addressed in several previous studies where different models have been proposed [e.g., Iervolino et al. 2014; Papadopoulos et al. 2020; Yeo and Cornell 2009]. Conversely, to quantify the potential underestimation of structural vulnerability, researchers have introduced the concept of fragility functions conditioned on the damage experienced after the mainshock. These are commonly referred to as state- or damage-dependent fragility curves [Bazzurro et al. 2004; Luco et al. 2004]. Due to the lack of empirical data, these curves are often derived analytically, via nonlinear response history analysis (NLRHA) where the structure of interest is subject to both the mainshock (MS) and aftershock (AS) ground motions in a back-to-back fashion.

Due to the scarcity of MS-AS ground motions recorded at the same station, particularly in the high-intensity range, several authors used MS ground motions to represent both the MS and AS shaking effects [e.g., Amadio et al. 2003; Raghunandan et al. 2015]. To make these scenarios more realistic, either the mainshock ground motions were randomly paired with aftershock ground motions or the aftershock ground motion was taken as identical to the mainshock ground motion but scaled down [Aljawhari et al. 2020; Ryu et al., 2011]. On the other hand, Jeon et al. [2015] and Jalayer and Ebrahimian [2016] employed distinct pools of ground motions for mainshocks and aftershocks before randomly combining them. Several studies, such as those conducted by Ruiz-García and Negrete-Manriquez, [2011] and Li et al. [2014], have emphasized the significance of using real ground motion sequences. They argued that artificially paired seismic sequences, whether by repeating the mainshock ground motion or by forming random mainshock-aftershock pairs, can lead to biased results, such as overestimation of demand and reduced variability. These findings underscore the importance of maintaining the correlation between mainshock and aftershock ground motions for more accurate analyses.

To derive damage-dependent fragilities all of these studies used approaches such as Cloud Analysis [Bazzurro et al. 1998; Jalayer 2003; Shome et al. 1998], incremental dynamic analysis [IDA, Vamvatsikos and Cornell 2002] and its extension Back-to-back (B2B) IDA, introduced by Luco et al. [2004], or a combination of these. While these methods have proven valuable in certain applications, recent research has shed light on the importance of hazard consistency when developing fragility functions within the mainshock-only framework. As a result, several studies have addressed this concern by proposing various site-specific record selection methods [e.g., Baker 2011; Bradley 2010; Jayaram et al. 2011; Spillatura et al. 2021]. Nonetheless, there is comparatively less research on this topic when it comes to hazard consistency in the context of seismic sequences. Given the correlation between the causal parameters of the mainshock and aftershock, as well as the similarities observed in the spectral characteristics of their ground motions at the same station, it is reasonable to assume that site dependency also plays a relevant role in the context of clustered seismicity. The limited amount of research in this field can be attributed to the relatively recent surge in interest surrounding clustered seismic risk assessment and the inherent complexity of the topic, which demands substantial computational efforts. To the best of the authors' knowledge, only a handful of studies have explored this area, including the works of Zhu et al. [2017], Ghotbi and Taciroglu [2020] and Papadopoulos et al. [2020]. Ghotbi and Taciroglu [2020] proposed a new framework for aftershock probabilistic seismic hazard analysis (APSHA) and computed aftershock hazard curves for the given mainshock scenario. They used information from hazard disaggregation for a site in California to select hazard-consistent aftershock ground motion records using the generalized intensity measure (GCIM) approach [Bradley 2010]. Zhu et al. [2017] developed a method for generating aftershock Conditional Mean Spectrum [CMS; Baker 2011] using a copula technique, NGA-West2 [Ancheta et al. 2014] ground motion database and Abrahamson et al. [2014] ground motion prediction equation (GMPE) to model the correlation between the MS and AS spectral ordinates. However, they only provide the correlation coefficients at the same period (T_{AS}=T_{MS}). In contrast, Papadopoulos et al.

[2019] empirically derived correlation coefficients by investigating the correlation of MS-AS spectral accelerations at different vibration periods and proposed a pragmatic procedure that can be applied to the selection of MS-AS ground motion pairs using consistent causal parameters and accounting for the correlation between their spectral accelerations.

The selection of the conditioning intensity measure (IM) and its significance in record selection has been the subject of multiple investigations in the context of mainshock-only seismicity [e.g., Bakalis et al. 2018; Bradley 2012; Kohrangi et al. 2016; O'Reilly 2021]. However, in the realm of ground motion sequence selection, comprehensive studies on this aspect are limited. Typically, the employed intensity measures include peak ground acceleration (PGA) [e.g., Di Trapani and Malavisi 2019], spectral acceleration at the fundamental period of the structure ($Sa(T_1)$) [e.g., Jalayer and Ebrahimian 2016; Tesfamariam and Goda 2017] or, more rarely, inelastic spectral displacement (S_{di})[e.g., Raghunandan et al. 2015]. Jeon et al. [2015] used structure-independent intensity measures, namely peak ground acceleration, velocity and displacement (PGA, PGV, PGD), Arias Intensity (AI), Cumulative Absolute Velocity (CAV) and Sa(1.0s) for the aftershock fragility assessment of an old RC frame building in California and showed that the PGV was the optimal IM, among those considered. In a recent study, Orlacchio et al. [2021] computed state-dependent fragility functions for the Italian reinforced concrete residential structure classes. They employed four conditioning IMs: Sa(0.3s), spectral acceleration at the period of the undamaged system $Sa(T_{el})$, average spectral acceleration AvgSa and I_{NP} [Bojórquez and Iervolino 2011]. They showed that AvgSa and I_{NP} are more efficient intensity measures compared to the remaining two. The advantages of using AvgSa for the derivation of damage-dependent fragility curves, such as its ability to indirectly account for the higher-mode effects and period elongation, have been also acknowledged in the studies of Aljawhari et al. [2020] and Pedone et al. [2023].

Some of the mentioned techniques for MS-AS ground record selection are simple but crude, while others are superior but significantly more complex. Given that it is still unclear what is the optimal method to derive damage-dependent fragility curves, while balancing accuracy and computational effort, our study investigates three different approaches of varying complexity. These approaches are evaluated using a simple case study, and their relative advantages and disadvantages are discussed. To compare these methods we compute and contrast the estimates of the annual probability of exceeding different damage states from the different approaches. The probabilities that serve as the benchmark are those that we compute following the so-called "direct analysis". In the following sections, we describe the set-up of the analysis, including the description of the case study, the definition of the damage states, seismic hazard analysis, and the event-based methodology used for computing annual probabilities of exceeding defined damage states. Each approach is applied to the case study. Finally, we discuss the results and provide some practical recommendations based on the outcomes of our investigation.

6.2 ANALYSIS SET-UP

6.2.1 Case study and definition of the damage states

As a case study site, we have selected a rock site in Perugia, Central Italy, located at 43.11°N and 12.39°E with Vs_{30}=800 m/s, as shown in Figure 6.1a. The structural system under consideration is a nonlinear single-degree-of-freedom system (SDOF) with a fundamental period of T_1=0.2s. This SDOF system is described using the constitutive model defined by Ibarra et al. [2005], which incorporates both in-cycle and cyclic degradation, directly modeled as a function of the dissipated energy. It has been widely used in earthquake engineering as it demonstrated to be in good agreement with experimental results. The SDOF is designed to have the spectral acceleration at yield (Sa_y) equal to 0.1875g and accordingly, the corresponding yield displacement $\delta y=Sa_y(T_1/2\pi)$. The ductility of the system ($\mu=\delta c/\delta y$) is set to 4, categorizing it as a system of medium ductility. The spectral acceleration at the capping point Sa_c is determined as 1.1 times Sa_y, and the softening branch is defined by assuming that the ratio between the post-capping stiffness (K_c) and the initial stiffness (K_e) is -0.30. The monotonic backbone of the system, defined in this manner, is depicted in Figure 6.1b. Regarding the parameters describing the cyclic response, we employ a consistent cyclic deterioration parameter λ=25 for all modes of deterioration (strength, post-capping strength, unloading stiffness, and reloading stiffness), representing rapid cyclic degradation, while the rate of degradation is set to 1.0.

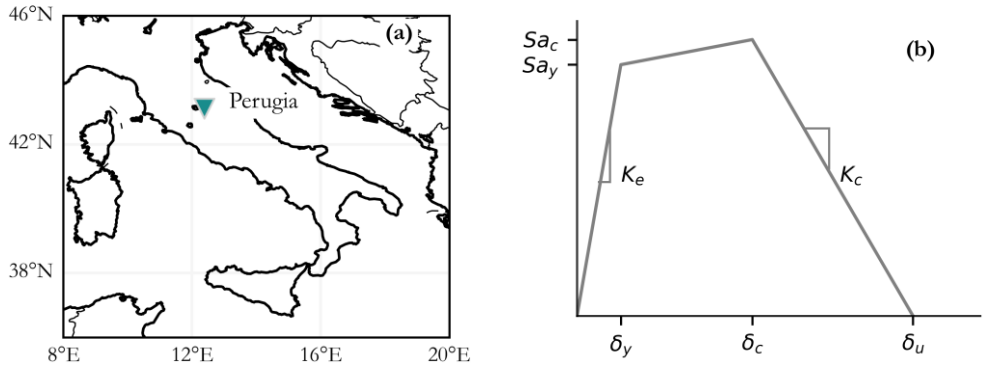

Figure 6.1. (a) Location of the case study site and (b) the monotonic backbone of the considered SDOF, with the characteristic points indicated

To define the damage states, we use two engineering demand parameters (EDPs). First, we use a conventional, displacement-based EDP, defined in this particular case through maximum ductility ratio. While displacement-based EDPs are often utilized due to their simplicity and practicality, recent studies underscored their limitations in the realm of predicting damage during seismic sequences due to their non-cumulative nature [e.g., Baraschino et al. 2023; Iñarritu et al. 2021; Pedone et al. 2023; Wen et al. 2017]. These

studies indicated that cumulative, energy-based EDPs might be a preferable choice. Therefore, in addition to the maximum ductility, we use the damage index (simply referred to as DI in the following text) that is defined in Section 4.4 of this thesis. In Table 6.1. we define the damage states using both considered EDPs, based on the findings described in Section 4.8. Keep in mind that these damage states correspond to the flexure-dominated columns, given that the SDOF considered here is expected to fail in this mode. DS0, not reported in the table, refers to the intact conditions while DS4 is considered as collapse. If at the end of an earthquake the structure, initially in the intact condition DS0, experiences a ductility μ of, say, 3.0, then the final damage state will be DS2. As discussed later, this damage state will be the initial one should another event strike the structure.

We recognize that the choice of a simple SDOF system has its limitations, but it was a pragmatic decision to facilitate fast analysis, considering the need to perform thousands of analyses for specific approaches, as elaborated upon later in this study.

Table 6.1. Damage states defined in terms of the maximum ductility and DI

	Maximum ductility	DI	Description of damage
DS1	1.5-2.0	0-0.20	Flexural and longitudinal cracking, yielding of steel bars in tension, followed by shear cracking
DS2	2.0-3.5	0.2-0.4	The onset of concrete spalling exposing the transverse reinforcement
DS3	3.5-6.0	0.4-0.75	More significant spalling of concrete, longitudinal steel is exposed, the potential start of tie yielding
DS4	>6	>0.75	Major safety implications, bar buckling, concrete core crushing, fracture of the bars, complete failure

6.2.2 Seismic Hazard Analysis

To perform the probabilistic seismic hazard analysis, we adopt the event-based methodology and we consider two cases: (i) clustered seismicity case where we use the ETAS model, as proposed by Papadopoulos et al. [2020], to simulate seismic sequences and (ii) mainshock-only case where the Poisson model is used.

The ETAS model is one of the space–time point Hawkes processes formulated as the combination of background seismicity $\mu(x, y)$ and triggered seismicity characterized by the function g, treating all events uniformly without distinguishing between foreshocks, mainshocks, and aftershocks. Every background (or parent) event can trigger offspring events capable of producing offspring of their own. The overall rate of events with magnitude m at a specific time and location, given the history of prior earthquakes, H_t, can be characterized by the general form given with the following equation [Seif et al. 2017; Zhuang et al. 2004]:

$$\lambda(t, x, y, m \mid H_t) = \mu(x, y) + \sum_{j:t_j<t}^{n} g(t - t_j, x - x_j, m_j) \tag{6.1}$$

The index *j* refers to all past earthquakes. The triggering function has the following form [Ogata 1998]:

$$g(t - t_j, x - x_j, y - y_j, m_j) = k(m_j) \cdot v(t - t_j) \cdot f(x - x_j; y - y_j, m_j) \tag{6.2}$$

where the productivity term $k(m_j)=Ae^{\alpha(mj-mc)}$ represents the mean number of events directly triggered by an earthquake of a magnitude m_j, the minimum magnitude considered is m_c. Parameter A quantifies the overall triggering capability, independent of earthquake magnitude, while α governs the role of magnitude. The temporal decay of triggered earthquakes, $v(t-t_j)=(p-1)\ c^{p-1}(t-t_j+c)^{-p}$, is modeled by the Modified Omori law [Omori 1894; Utsu 1961], while the spatial distribution function used in this study is the one proposed by Zhuang et al. [2004].

To employ the ETAS model effectively, it is essential to calibrate it based on available seismic data for the region of interest and estimate the sets of unknown parameters:

$$\theta = \{v, A, \alpha, c, p, d, q, \gamma\} \tag{6.3}$$

In this study, we utilize parameter values provided by Šipčić et al. [2022] (i.e. Section 2), which have been calibrated for the Central Italy region, where Perugia, our case study site, is located, and the HORUS [Lolli et al. 2020] instrumental earthquake catalog.

When it comes to the Poissonian model we use the b-value of 0.93 to describe the magnitude-frequency distribution which is assumed to follow the Gutenberg-Richter law, and smoothed seismicity approach proposed by Frankel [1995], with the correlation distance of 20km. These parameters are estimated based on the HORUS instrumental catalogue for the region in Central Italy, declustered with the Gardner and Knopoff [1974] method, as described in Šipčić et al. [2022].

To calculate hazard curves, we employ the calibrated models (ETAS in the clustered seismicity case and Poisson in the mainshock-only case) and conduct Monte Carlo simulations, generating 100,000 stochastic earthquake catalogs, each one spanning one year. The ETAS model is conditioned on seismicity before the start of the investigation period, which, in this case, is the year between 26/04/2017 and 26/04/2018, following a period of heightened seismic activity in Central Italy. Naturally, as the Poisson model is time-independent, there is no conditioning period in this case. For each simulated earthquake event, we sample rupture properties (rake, dip, slip, and seismogenic depth) based on SHARE seismic source model [Woessner et al. 2015] following the procedures implemented in the OpenQuake software [Pagani et al. 2014]. Subsequently, we utilize the GMPE of Abrahamson et al. [2014] to estimate the mean and standard deviation of spectral acceleration at various vibration periods, assuming a lognormal distribution [Jayaram and Baker 2008].

To reduce the computational effort, for both Poisson and ETAS cases, we only consider events with magnitude M≥4 as we assume that lower magnitude events are not damaging.

In this manner, for every event in all of the 100,000 stochastic catalogues, we simulate at the case study site a spectral acceleration (Sa) value. To determine the annual rate of exceeding various intensity levels, in each catalogue we count the number of exceedances of a specific level of spectral acceleration, we sum all of them for all the one-year-long catalogues and then divide the sum by the total number of catalogues as given by Equation (6.4). To find the annual probability of at least one exceedance we count the number of stochastic catalogues in which each given level of spectral acceleration is exceeded at least once and divide it by the total number of stochastic one-year-long catalogs simulated, as given by Equation (6.5).

$$\lambda(IM > im) = \frac{1}{N_{cat}} \sum_{n=1}^{N_{cat}} \sum_{k=1}^{N_{rup}} I(IM > im \mid rup_{n,k}) \tag{6.4}$$

$$P(IM > im) = \frac{1}{N_{cat}} \sum_{n=1}^{N_{cat}} I(IM > im \mid cat_n) \tag{6.5}$$

In these equations, $\lambda(IM>im)$ is the annual rate of exceeding *im* level, N_{cat} is the number of simulated catalogues (in our case 100,000), N_{rup} is the number of ruptures (i.e., simulated earthquakes) in each stochastic catalogue and $I(IM>im)$ is the indicator function which is equal to 1 if *im* is exceeded and 0 otherwise. For a comprehensive description of the hazard calculation methodology, including details about the ETAS and Poisson models used, please refer to Šipčić et al. [2022].

We compute hazard curves, and subsequently fragility curves, by employing two conditioning IMs. First, we use spectral acceleration at the fundamental period of the considered SDOF, i.e. Sa(0.2s), as it is a commonly used IM. As explained in the Introduction, due to the period-elongation and higher-mode effects, AvgSa might be a better choice for the derivation of damage-dependent fragility curves. To that end, we also use AvgSa, defined for the range [0.2s-0.6s] with the 0.1s step. Figure 6.2 shows the hazard curves for both IMs, and both Poisson and ETAS models, in terms of the annual probability of exceedance (poe). As expected, these curves demonstrate that the annual probabilities of exceedance are consistently higher across the entire range of intensities when the ETAS model is utilized, particularly in the lower-intensity range.

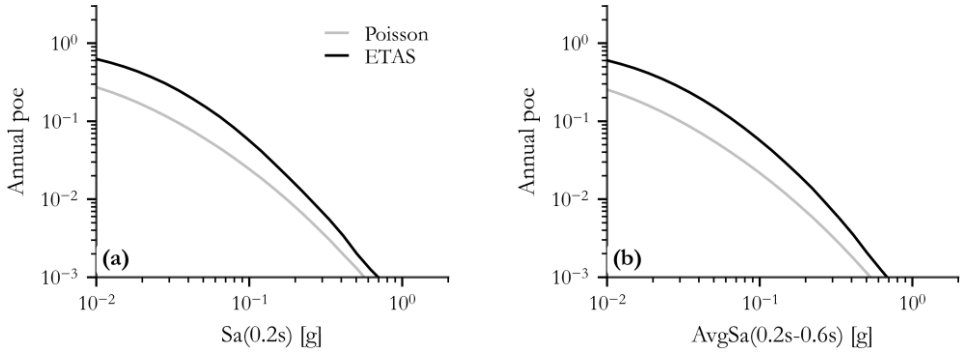

Figure 6.2. Hazard curves in terms of the annual probability of exceedance (poe) obtained using ETAS and Poisson models for the year from 26/04/2017 to 26/04/2018. Results for (a) Sa(0.2s) and (b) AvgSa(0.2s-0.6s) are illustrated.

Additionally, we perform the seismic hazard disaggregation [Bazzurro and Cornell 1999] for the Poissonian case, to obtain the probabilities that, for a given *im* value, the *im* exceedance is caused by rupture scenario with magnitude M_j and distance R_j. We first discretize all magnitude and distance values into the bins with width of 0.5 and 10km, respectively. We then use the expression given by Equation (6.7):

$$P(M_j, R_j \mid IM > im) = \frac{\lambda(IM > im, M = M_j, R = R_j)}{\lambda(IM > im)} \tag{6.6}$$

To obtain the numerator in Equation (6.7), which represents the rate of exceeding *im* level given the rupture scenario with M_j and R_j, we count all scenarios in the simulated catalogues where *im* level is exceeded for that scenario. The denominator, which represents the rate of exceeding *im* level is simply found as the sum of all *im* exceedances. We repeat this procedure for every *im* level considered. In Table 6.2, we show the mean M and R values associated with ten intensity levels defined in terms of Sa(0.2s). Similarly, in Table 6.3 we show the results in terms of AvgSa(0.2s-0.6s).

Table 6.2. Disaggregation results in terms of mean magnitude M and distance R, obtained using Sa(0.2s) as conditioning IM for ten intensity levels (IMLs).

IML	**1**	**2**	**3**	**4**	**5**	**6**	**7**	**8**	**9**	**10**
Sa(0.2s) [g]	0.1	0.2	0.3	0.4	0.45	0.50	0.55	0.60	0.84	1.10
M	5.48	5.65	5.76	5.88	5.89	5.92	5.94	5.98	6.1	6.2
R(km)	32.0	25.2	21.5	18.9	18.3	17.5	16.4	16.3	14.9	13.5

Table 6.3. Disaggregation results in terms of mean magnitude M and distance R, obtained using AvgSa(0.2s-0.6s) as conditioning IM for ten intensity levels (IMLs).

IML	1	2	3	4	5	6	7	8	9	10
AvgSa(0.2s-0.6s) [g]	0.1	0.2	0.3	0.4	0.45	0.50	0.55	0.65	0.70	0.75
M	5.77	5.98	6.1	6.21	6.24	6.28	6.31	6.4	6.42	6.45
R(km)	38.2	29.9	25.4	22.8	21.4	20.5	19.7	18.3	17.7	16.9

6.2.3 Event-based methodology for the estimation of the annual probability of exceeding a given damage state: fragility-based approach

To compare different methods for the derivation of damage-dependent fragility curves, with the obtained fragilities, we compute with the obtained fragilities annual probabilities of exceeding a given damage state, defined in Table 6.1. We follow the event-based methodology, building upon the framework used for hazard computation. The steps followed are outlined below:

1. Develop damage-dependent fragility curves: we derive the fragility curves dependent on the level of initial damage (IDS), using one of the three approaches described in the following section;
2. Use the same 100,000 1-year-long stochastic catalogs that are generated using the ETAS model in the hazard analysis phase;
3. For each stochastic catalogue:
    a. Initialize the computation by assuming the structure is in the intact damage state (IDS=0);
    b. For each earthquake event in the stochastic catalogue:
        i. Determine the value of the conditioning intensity measure (IM^*);
        ii. Based on the fragility functions for all pertinent DS (say, DS2, DS3 and DS4) corresponding to the initial DS of the structure before the earthquake (say IDS1) and on the IM level, simulate the DS of the structure at the end of the earthquake using Monte Carlo simulations[b];
        iii. Set the DS at the end of the earthquake as the initial DS for the following earthquake and select the set of fragility curves conditioned on that IDS;
    c. Repeat for all earthquakes in that year
    d. Save the DS of the structure at the end of the year;

[b] DS is simulated 10 times, to add uncertainty due to the DS definition into the calculation. Investigation showed that after 10 simulations results become stable

4. Compute the annual rate of exceeding any given DS by counting the number of catalogs where that DS was reached or exceeded and divide it by the total number of generated catalogs using Equation (6.7):

$$P(DS > ds) = \frac{1}{N_{cat}} \sum_{n=1}^{N_{cat}} I(DS > ds \mid cat_n) \tag{6.7}$$

In this equation, *P(DS>ds)* represents the annual probability of exceeding the specified *ds*, N_{cat} is the total number of stochastic catalogs (in our case, 100,000), and *I(DS>ds)* is the indicator function, equal to 1 if the *DS* exceeds *ds* and 0 otherwise. In case one is interested in the computation of annual probabilities in the traditional MS-only context, the procedure described above would be used with two adjustments – in the second step instead of using stochastic catalogues generated with the ETAS model one would use those generated with the Poisson model and step 3biii would be omitted as it would be assumed that the structure is always in the intact state DS0.

6.3 COMPUTATION OF DAMAGE-DEPENDENT FRAGILITIES

6.3.1 Approach 1

In the Introduction section, we mentioned the commonly employed approach for deriving damage-dependent fragility curves, which is the back-to-back incremental analysis (B2B-IDA) method. This method builds upon the original incremental dynamic analysis (IDA) technique and extends it to derive fragility curves dependent on the initial damage state. To perform the analysis we use a set of 30 ground motion records from the NGA2-West database, as explained in more detail in Bakalis et al. [2018]. The initial step involves subjecting an intact structural model, to each of the 30 input ground motions individually, with successive scaling. In this particular case, we scale these ground motions to 13 successive intensity levels. To calculate the fragility function, we assume it follows a lognormal distribution. Based on the results of the structural analysis, we estimate the median and standard deviation of the fragility function using the method of moments [Baker 2015]. These estimates are calculated as follows:

$$\ln \hat{\mu} = \frac{1}{n} \sum_{i=1}^{n} \ln(IM_i) \tag{6.8}$$

$$\hat{\beta} = \sqrt{\frac{1}{n-1} \sum_{i=1}^{n} (\ln(IM_i) - \ln(\hat{\mu}))^2} \tag{6.9}$$

In these equations, $\hat{\mu}$ is the estimate of the median IM level associated with the exceedance of the damage state and $\hat{\beta}$ the estimate of the standard deviation of ln(IM) of the fragility function. The number of ground motions considered is *n*, while IM_i is the intensity level corresponding to the onset of the DS for the i^{th} ground motion. The hat sign above the median and standard deviation implies that these are only estimates of the true values. However, for simplicity, we will omit the hat in the remainder of the text.

Figure 6.3a shows the obtained IDA curves, for the case of the IM*=Sa(0.2s) and maximum ductility as an EDP. The median, 5th and 95th percentile curves are indicated with darker grey lines. Figure 6.3b displays the corresponding fragility curves for the four defined damage states. Keep in mind that these results correspond to the intact structure. Similarly in Figure 6.4 we show the results for IM*=Sa(0.2s) and DI as an EDP. In addition, we show in Figure 6.5 the fragility curves obtained using IM*=AvgSa(0.2s-0.6s).

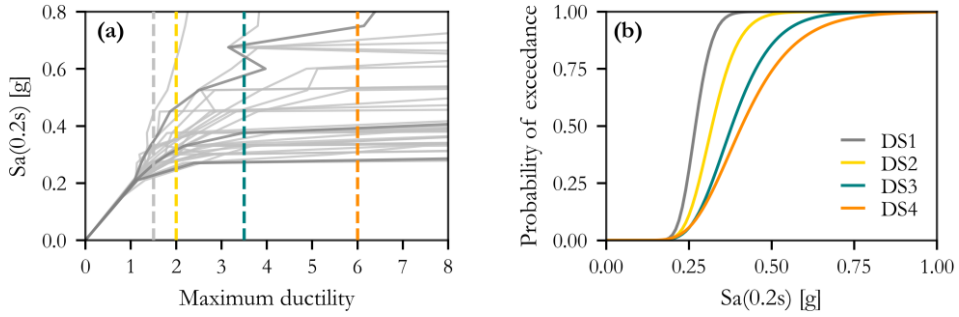

Figure 6.3. (a) IDA curves for the intact system using IM*=Sa(0.2s) and maximum ductility as an EDP. Median, 5th and 95th percentile are indicated with the darker lines (b) Corresponding fragility curves for the four damage states that are defined in Table 6.1.

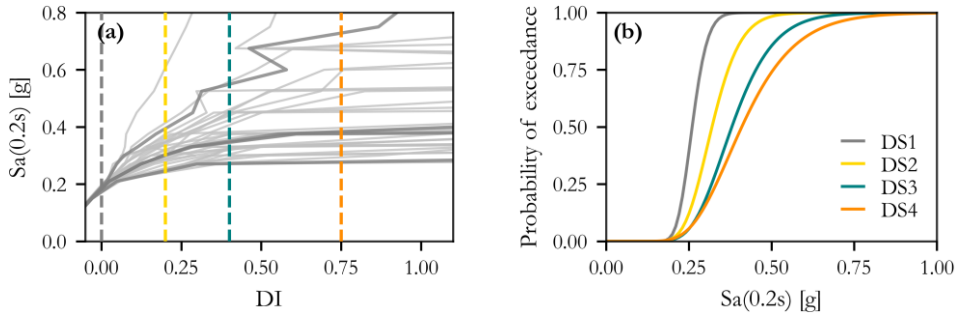

Figure 6.4. (a) IDA curves for the intact system using IM*=Sa(0.2s) and DI as an EDP. (b) Corresponding fragility curves for the four damage states that are defined in Table 6.1.

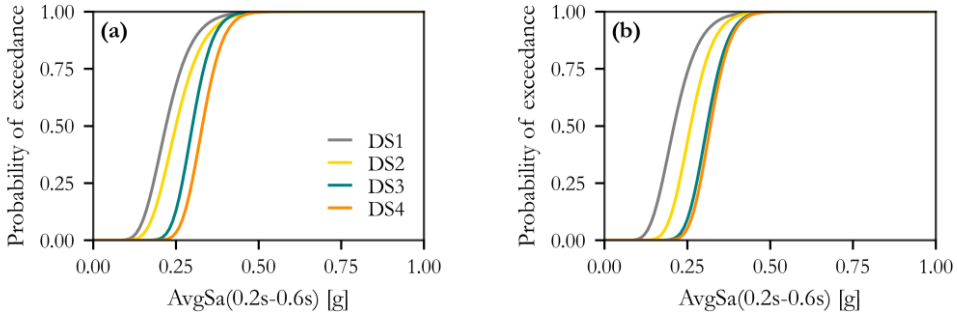

Figure 6.5. Fragility curves for the four damage states that are defined in Table 6.1 using IM*=AvgSa(0.2s-0.6s) and (a) maximum ductility and (b) DI as an EDP.

Having completed the analysis of the intact structure, we proceed to calculate scaling factors that will cause the ground motions to be strong enough to be "damaging" to a given level of severity. These scaled ground motions are intended to induce a given damage state at the end of the shaking that will be utilized as the initial damaged state (IDS) of the structure for successive ground motions. For instance, to bring the structure to IDS1, we scale the "natural" ground motion to cause the maximum ductility in the structure within the [1.5 – 2.0] range. We then carry out IDA by applying the 30 ground motions incrementally again, following the same procedure as for the intact case. Using the same methodology as previously outlined, we compute fragility functions (i.e., DS2|IDS1, DS3|IDS1, and DS4|IDS1) that are now conditioned on the IDS1 of the structure. This process is repeated for the damage states DS2 and DS3 to compute damage-dependent fragility curves (namely, DS3|IDS2 and DS4|IDS2 and DS4|IDS3). The same procedure is then repeated for the case when DI is used, and for both conditional IMs.

Figure 6.6a shows, for the case of IM*=Sa(0.2s), the damage-dependent fragility curves for the collapse case (DS4) for the three initial damage states (i.e. IDS1, IDS2 and IDS3) along with the fragility curve for the intact structure, obtained when the maximum ductility ratio is used. The results for DI are illustrated in Figure 6.6b. Similarly, Figure 6.7 shows the results for the case of IM*=AvgSa(0.2s-0.6s). In all cases, the reduction in capacity with increasing levels of severity of the IDS is evident: the more damage the system suffers from a previous shock, the lower its residual capacity.

The estimated parameters of the damage-dependent fragility curves can be found in Table 6.4. Damage-dependent fragility function parameters (μ/β) obtained with Approach 1 and IM*=Sa(0.2s).Table 6.4 and Table 6.5, for both EDPs considered and for the case when IM*=Sa(0.2s) and IM*=AvgSa(0.2s-0.6s), respectively. The estimated median and standard deviation values of the capacity in the fragility curves for all DSs developed for the intact structure are almost insensitive to the EDP used for gauging the occurrence of each damage state, for both conditioning IMs. This is not entirely surprising since the DI has a significant contribution from the maximum displacement, which is the numerator of the

ductility ratio. However, the estimates of these two quantities differ significantly for the fragility curves developed when the structure is already damaged (i.e., IDS from 1 to 3).

It is interesting to note, however, that the reduction in capacity is more pronounced when DI is used, due to the superior ability of DI to capture the accumulation of damage, as shown in Section 4 of this thesis. As an example (see Table 6.4), when DI is used as the EDP the median estimate of the collapse capacity (i.e., of DS4) reduces by approximately 1.17, 1.46, and 2.3 when the structure is already in IDS1, IDS2 and IDS3, respectively. This reduction is only approximately 1.08, 1.14, and 1.41 when the maximum ductility ratio is used.

When AvgSa(0.2s-0.6s) is used as a conditioning IM, the difference between the estimates of the capacity at DS3 and DS4 is reduced. Furthermore, when compared with the Sa(0.2s) case, the dispersion estimates of the capacities are lower for the more severe damage states and higher for the less severe ones.

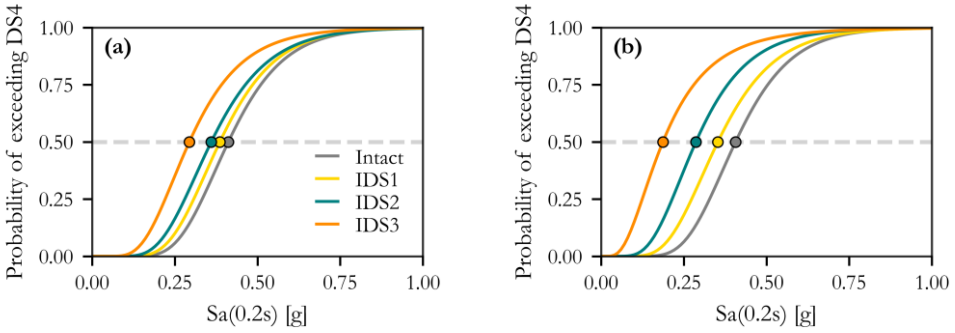

Figure 6.6. Collapse (i.e., DS4) fragility curves of the system conditioned on the different initial damage states, obtained using IM*=Sa(0.2s) and measured in terms of (a) maximum ductility ratio and (b) DI. Fragility curves are estimated using Approach 1.

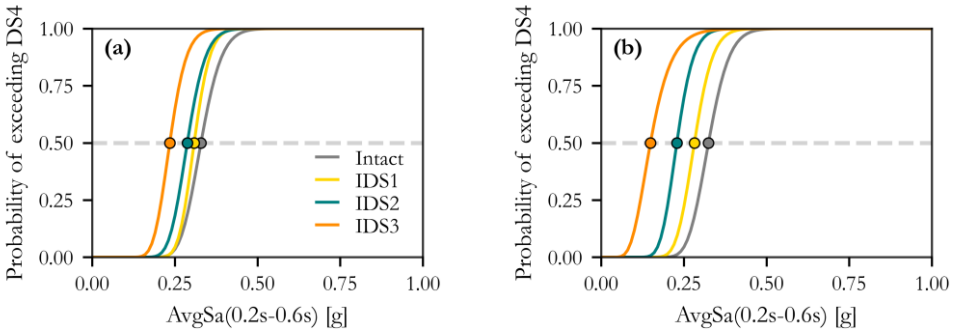

Figure 6.7. Collapse (i.e., DS4) fragility curves of the system conditioned on the different initial damage states, obtained using IM*=AvgSa(0.2s-0.6s) and measured in terms of (a) maximum ductility ratio and (b) DI. Fragility curves are estimated using Approach 1.

Table 6.4. Damage-dependent fragility function parameters (μ/β) obtained with Approach 1 and IM*=Sa(0.2s).

	Ductility ratio				DI			
	IDS0	IDS1	IDS2	IDS3	IDS0	IDS1	IDS2	IDS3
DS1	0.27/0.15	-	-	-	0.26/0.14	-	-	-
DS2	0.32/0.20	0.28/0.30	-	-	0.32/0.21	0.13/0.40	-	-
DS3	0.38/0.26	0.36/0.33	0.33/0.37	-	0.38/0.26	0.33/0.27	0.25/0.43	-
DS4	0.41/0.31	0.38/0.34	0.36/0.37	0.29/0.42	0.41/0.31	0.35/0.37	0.28/0.43	0.18/0.6

Table 6.5. Damage-dependent fragility function parameters (μ/β) obtained with Approach 1 and IM*=AvgSa(0.2s-0.6s).

	Ductility ratio				DI			
	IDS0	IDS1	IDS2	IDS3	IDS0	IDS1	IDS2	IDS3
DS1	0.22/0.28	-	-	-	0.21/0.28	-	-	-
DS2	0.25/0.26	0.23/0.25	-	-	0.26/0.21	0.11/0.23	-	-
DS3	0.30/0.16	0.29/0.13	0.27/0.15	-	0.31/0.16	0.26/0.15	0.20/0.17	-
DS4	0.33/0.15	0.30/0.12	0.28/0.15	0.23/0.17	0.32/0.15	0.28/0.15	0.23/0.17	0.15/0.33

6.3.2 Approach 2

While IDA and B2B-IDA offer valuable insights for various applications, they do not inherently ensure site hazard consistency, which can potentially lead to biased fragility estimates, as demonstrated in prior studies for both mainshock-only [e.g., Kohrangi et al. 2017] and clustered seismicity [Papadopoulos et al. 2020] cases. Here we investigate further an alternative approach originally proposed by Papadopoulos et al. [2020] to derive the damage-dependent fragility curve where MS ground motions are selected in a hazard-consistent manner followed by the MS-consistent AS ground motion selection. This method is based on the following four steps.

Step 1: Select MS ground motions

The first step in this methodology involves selecting MS ground motions using the Conditional Spectrum (CS) approach [Jayaram et al. 2011], as it is commonly done when one wants to ensure hazard consistency. With this approach, records are selected to match the target distribution in terms of spectral ordinates conditioned on the chosen IM*(e.g. $Sa(T_1)$, AvgSa) for the hazard level of interest extracted from the corresponding hazard

curve. Seismic hazard disaggregation is then performed to identify the scenarios (in terms of magnitude M, distance R and residual ε for the chosen IM* level) that contribute the most to to the exceedance of that IM* level at the site. For every scenario, we can then compute the mean and standard deviation of the natural logarithm of the spectral ordinates as:

$$\mu^{i}{}_{\ln Sa|\ln(IM^*)} = \mu^{i}{}_{\ln Sa} + \rho(T^*)\varepsilon_i\sigma^{i}{}_{\ln(Sa)} \tag{6.10}$$

$$\sigma^{i}{}_{\ln Sa|\ln(IM^*)} = \sigma^{i}{}_{\ln Sa}\sqrt{1-\rho(T^*)^2} \tag{6.11}$$

where i represents the scenario, $\mu^{i}{}_{\ln(Sa)}$ and $\sigma^{i}{}_{\ln(Sa)}$ are the unconditional logarithmic mean spectral accelerations and associated standard deviations obtained from the GMPE, $\rho(T^*)$ represents the correlation coefficient between the residuals of the IM* and Sa(T) across all periods of interest, which can be calculated with Baker and Jayaram [2008] or Abrahamson et al. [2014] correlation structure. Every i^{th} scenario is associated with a weight, p_i, obtained from the disaggregation, which is then used to compute the target conditional mean and standard deviation of spectral accelerations Sa(T) given IM*, by combining all scenarios as follows:

$$\mu_{\ln Sa|\ln(IM^*)} = \sum_i \frac{p_i}{\bar{p}}\mu^{i}{}_{\ln Sa|\ln(IM^*)} \tag{6.12}$$

$$\sigma_{\ln Sa|\ln(IM^*)} = \sqrt{\sum_i \frac{p_i}{\bar{p}}[(\sigma^{i}{}_{\ln Sa|\ln(IM^*)})^2 + (\mu^{i}{}_{\ln Sa|\ln(IM^*)} - \mu_{\ln Sa|\ln(IM^*)})^2]} \tag{6.13}$$

In this equation, $\bar{p}$ is the sum of all the weights for the considered scenarios. For every record that we want to select (for a total of, say, N_{rec}), we then randomly draw a rupture scenario (M and R) from the seismic disaggregation probability mass function (pmf) for that IM* level, and for the given i^{th} rupture we create the conditional spectrum with mean and standard deviation found with Equations (6.10) and (6.11), respectively. We then generate a random realization by sampling correlated lnSa values from the multivariate normal distribution and select a record (usually scaled) from an available database that best matches this realization. One should keep in mind that the target CS is defined in terms of GMRotD50 [Boore 2010] to maintain full consistency with the hazard computations.

As an illustrative example, we show in Figure 6.8a the target mean spectra found with Equation (6.12) for our case study site, for IM*=0.2s and IML5 (i.e. Sa(0.2s)=0.45g, see Table 6.2). Additionally, we show for record *r=1* mean CS calculated with Equation (6.10) for the rupture with M=5.25 and R=5km, sampled from the pmf of the seismic disaggregation. In Figure 6.8b we then show a realization of that CS and the ground motion that is selected to match it.

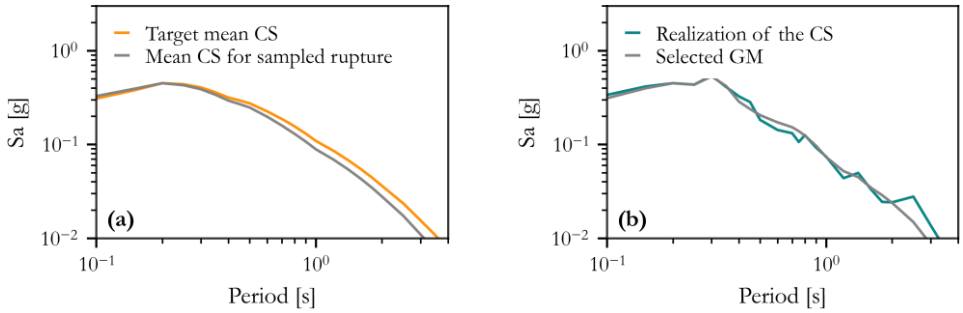

Figure 6.8. (a) Target mean CS calculated with Equation (6.12) and mean CS for the sampled rupture (M=5.25 and R=5km); (b) Realization of the mean CS obtained for the sampled rupture and GM selected to match that CS. Illustrated example refers to the case when IM*=Sa(0.2s) and IML5 (i.e. Sa(0.2s)=0.45g)

The described process is repeated for every record, ensuring that each one is associated with the previously drawn M-R rupture scenario. This is a crucial piece of information for the next step of the framework (unlike the procedure proposed by Jayaram et al. [2011] that is typically used for this purpose). The simulation procedure is repeated several times and the set of records that best matches the target, given by Equations (6.12) and (6.13), is selected. The accuracy of the matching to the target is calculated using the sum of squared errors (SSEs) [Baker and Lee 2018] metric defined with Equation (6.14).

$$SSE_s = \sum_{k=1}^{p} [(m_{\ln IM_k} - \mu_{\ln IM_k})^2 + w(s_{\ln IM_k} - \sigma_{\ln IM_k})^2] \quad (6.14)$$

where IM_k is the spectral acceleration at T_k, $m_{\ln IMk}$ is the sample mean of $\ln IM_k$, and $s_{\ln IMk}$ is the sample standard deviation of lnIMk, both estimated from the selected motions. The quantities $\mu_{\ln IMk}$ and $\sigma_{\ln IMk}$ are the target conditional means and standard deviations, p is the number of vibration periods of interest in the target spectrum, and w is a weight factor here assumed equal to 2.0. Once the initial set of records is selected, one can perform the so-called "greedy" optimization [Jayaram et al. 2011] to improve the match to the target (refer to Papadopoulos et al. [2020] for more details).

Using the results of the disaggregation and procedure described above, we calculate the target mean and standard deviation for each intensity level, with both conditioning IMs. Finally, we select 100 ground motions for each intensity level using the database described in more detail in Iñarritu et al. [2023] and allowing for the maximum scaling factor of 10. In Figure 6.9a, we show, for IML5 and IM*=Sa(0.2s) the target mean CS and target mean CS ± two target standard deviations along with the mean and mean ± two standard deviations of the selected set of records. Similarly, results for IM*=AvgSa(0.2s-0.6s) are illustrated in Figure 6.9b.

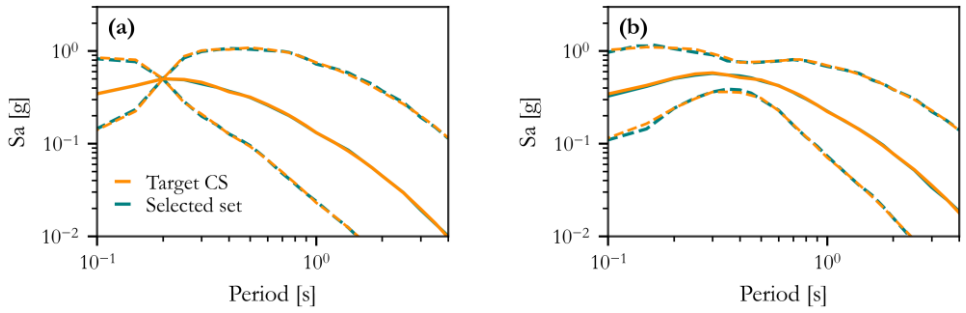

Figure 6.9. Mean (solid line) and mean ± 2 standard deviations (dashed lines) of the target CS and of the selected set of 100 records for IML5. Results obtained with (a) IM*=Sa(0.2s) and (b) IM*=AvgSa(0.2s-0.6s) are shown.

Once we have the selected mainshock ground motions, we run the NLRHA on our SDOF system. Using the results of the structural analysis and the maximum likelihood method [Baker 2015] we estimate the median and standard deviation of the fragility curve which is assumed to follow a lognormal distribution, similar to Approach 1. In Figure 6.10, we show the response of the system in terms of maximum ductility for each intensity level considered and the derived fragility curves for the intact state of the structure and defined damage states, using maximum ductility ratio as an EDP and IM*=Sa(0.2s). Similarly, results for DI are illustrated in Figure 6.11. One should note that in Figure 6.11a DS1 is not indicated as it corresponds to DI=0, which can't be illustrated due to the logarithmic scale used.

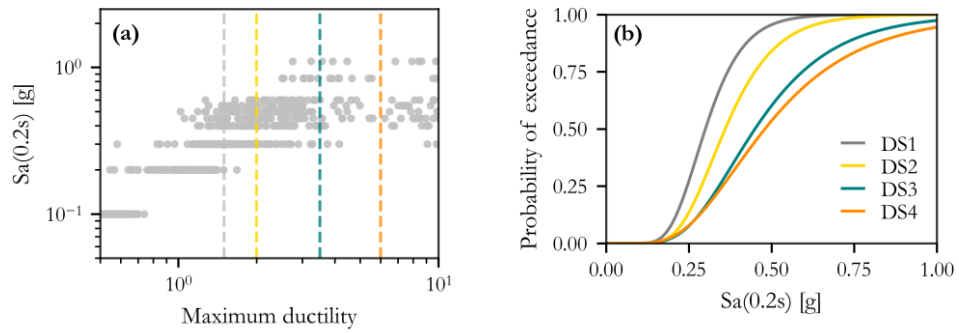

Figure 6.10. (a) Maximum ductility ratio response of the SDOF under MS ground motions with the damage states, as defined in Table 6.1, indicated with vertical dashed lines, and (b) corresponding fragility curves based on Sa(0.2s).

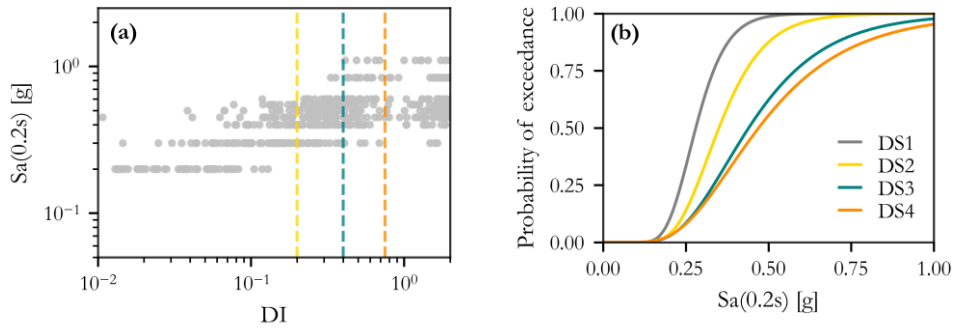

Figure 6.11. (a) DI of the SDOF under MS ground motions with the damage states, as defined in Table 6.1, indicated with vertical dashed lines and (b) corresponding fragility curves based on Sa(0.2s).

In Figure 6.12 we show the fragility curves of the intact system, for both EDPs, obtained using IM*=AvgSa(0.2s-0.6s).

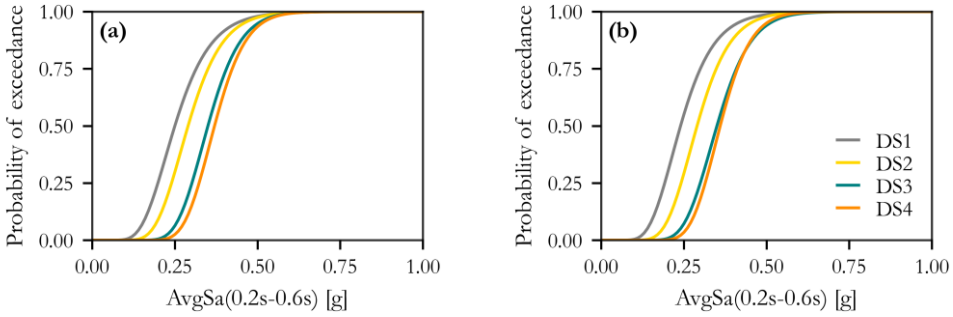

Figure 6.12. Fragility curves based on IM*=AvgSa(0.2s-0.6s) for damage states as defined in Table 6.1, using (a) maximum ductility ratio and (b) DI.

Table 6.6 provides the estimates of the parameters'values of the capacity associated with the fragility functions for each considered case.

There are two important considerations to make here. First, the parameters of the fragility functions obtained through the MSA and CS differ from those derived via IDA (in Approach 1). Specifically, the median capacity and dispersion for all damage states are higher in the MSA-CS scenario. The increase in median capacity can be attributed to the fact that the set of records adapted from Bakalis et al. [2018] and used for IDA in our study is selected for a location in Greece, which is characterized by higher seismic hazard than that of Perugia, our case study site. Consequently, this set of records is, on average, more "aggressive" for this structure than the one employed for Perugia. Additionally, the IDA

record set exhibits, by chance and not by design, a lower IM dispersion compared to that of the CS record set, resulting in reduced variability in structural response.

Secondly, such an extensive dataset of 100 records per stripe was not necessary to derive robust fragility curves. Even with a significantly lower number of records, the estimated mean and standard deviation did not substantially differ (as confirmed by testing with 30 records per stripe). Nonetheless, the rationale behind using such a high number of records will become evident in the subsequent sections.

Table 6.6. Values of the fragility function parameters (μ/β) obtained with Approach 2 for the intact structure.

	Sa(0.2s)		**AvgSa(0.2s-0.6s)**	
	Ductility ratio	DI	Ductility ratio	DI
DS1	0.30/0.30	0.28/0.26	0.25/0.33	0.24/0.33
DS2	0.36/0.33	0.36/0.32	0.30/0.28	0.30/0.27
DS3	0.45/0.41	0.45/0.41	0.35/0.23	0.35/0.23
DS4	0.48/0.46	0.48/0.45	0.36/0.20	0.37/0.20

Step 2: Simulate seismic sequences

The second step involves generating realistic aftershock sequences using the M and R values associated with each MS ground motion selected in the previous step. There are different ways to accomplish this and we will mention three here. Following Papadopoulos et al. [2020] one can use the ETAS model and the outlined steps:

- Consider the selected MS as the parent event;
- Sample the number of direct offspring from the productivity function (Poisson distribution with the mean number of offspring events k given in Equation (6.15) for the mainshock with magnitude m_i);
- Determine the location of offspring events based on the spatial distribution, estimating the distance r from the mainshock with magnitude m_i, and the angle θ (the polar coordinate) with Equation (6.16);
- Calculate the inter-arrival time Δt between parent and offspring events using Equation (6.17).
- Estimate the magnitude of each sampled aftershock event using the Gutenberg-Richter (GR) law and Equation (6.18)

In these equations, A, a, p, c, D, q, γ and b are ETAS parameters, as explained in the hazard analysis part (i.e., Section 6.2.2), u_r, u_θ, u_m and u_t represent uniformly distributed random

variables over the range (0, 1), and m_{min} is the minimum magnitude considered. This simulation process is repeated until there are no new events triggered or the triggered events fall outside the defined spatiotemporal window of interest.

$$k(m_i) = Ae^{\alpha(m_i - M_{min})} \tag{6.15}$$

$$r(m_i) = de^{(m_i - M_{min})}\sqrt{u_r^{\frac{1}{1-q}} - 1}, \theta = 2\pi u_\theta \tag{6.16}$$

$$\Delta t = -c + c(1-u_t)^{1/(1-p)} \tag{6.17}$$

$$m_{AS} = -\ln\frac{(1-u_m)}{b\ln 10} + m_{\min} \tag{6.18}$$

Alternatively, one can use the generalized Omori model [Shcherbakov et al. 2005] to simulate sequences, namely the number of events with associated magnitude and time stamps, given the M-R values of the causative event of the selected mainshock record. These are the steps:

- Draw the number of triggered events from a Poisson distribution with the mean number of events calculated using Equation (6.15);
- Calculate the timestamp and magnitude of the triggered events based on Equations (6.17) and (6.18), respectively;
- Ensure that the maximum aftershock magnitude does not exceed the magnitude of the triggering mainshock.

In the case of the Omori model, the parameters to be estimated are *a*, *c*, *p,* and *b*. It is worth noting that the literature provides different values of the ETAS and Omori parameters, which depend on the region of interest and the quality of the available data used for calibration [Seif et al. 2017; Šipčić et al. 2022]. It is crucial to highlight that the values of the set of Omori parameters differ from those estimated in the ETAS model because the values of the Omori parameters embedded in ETAS are applied locally to every generation of aftershocks. More specifically, in the ETAS model, every event is capable of triggering new events while in the generalized Omori law model, all aftershocks are assumed to be triggered by a single MS event and, therefore, the parameter values refer to entire sequences.

$$k(m_i) = 10^{a+b(m_i - M_{min})}c^{(1-p)/(p-1)} \tag{6.19}$$

To simplify the process even further, one can assume that the entire sequence of events can be represented by a single aftershock with, on average, a magnitude $m_{AS}=m_{MS}$-1.2 [Båth 1965]. Since the generalized Omori law and Bath's law models do not consider the spatial distribution of aftershocks, one can assume that aftershocks occur within a circular area around the mainshock with a radius equal to three rupture lengths estimated using the scaling law of Wells and Coppersmith [1994]. Alternatively, one can assume, more unrealistically, that the epicenter locations of the mainshock and aftershock are the same, as done in previous studies [e.g., Goda and Taylor, 2012; Yeo and Cornell, 2009].

Within our study, we use the ETAS model to generate seismic sequences of events with the set of ETAS parameters adopted from Šipčić et al. [2022], similar to the hazard analysis part.

Step 3: Select AS ground motions

To select realistic ensembles of AS ground motions (possibly for multiple AS) for each single MS ground motion obtained in the first two steps, we need to consider the distribution of the AS spectral accelerations at different periods of vibration that are conditional on the spectral accelerations of the specific MS record. To do so we use the MSAS-CS technique developed by Papadopoulos et al. [2020]. As shown by Baker and Jayaram [2008] for individual records and confirmed later by Papadopoulos et al. [2019] for MS-AS pairs, the joint distributions of spectral accelerations at multiple periods are well represented by a multivariate lognormal distribution. The unconditional mean and variance-covariance matrix of the joint MS-AS log-spectral acceleration distribution are found using Equations (6.20) and (6.21). The conditional (on the MS ground motion spectral ordinates) mean and variance-covariance matrix for the AS ground motion are given by Equations (6.22) and (6.23)

$$\mu_0 = \mu_{01} \mid \mu_{02} = [\mu_{\ln Sa(T_1^{AS})}, \ldots \mu_{\ln Sa(T_n^{AS})}] \mid [\mu_{\ln Sa(T_1^{MS})}, \ldots \mu_{\ln Sa(T_n^{MS})}] \tag{6.20}$$

$$\Sigma_0 = [\frac{\Sigma_{11} \mid \Sigma_{12}}{\Sigma_{22} \mid \Sigma_{22}}] \tag{6.21}$$

$$\mu'_c = \mu'_{01} + \Sigma_{12}\Sigma'_{22}(x^{MS} - \mu'_{02}) \tag{6.22}$$

$$\Sigma_c = \Sigma_{11} + \Sigma_{12}\Sigma'_{22}\Sigma_{21} \tag{6.23}$$

where x^{MS} is the vector of observed MS logarithmic spectral accelerations, $\mu_{\ln Sa(Ti)}$ and $\sigma_{\ln Sa(Ti)}$ are unconditional mean and standard deviation of the spectral accelerations extracted from the GMPE. To find the covariance matrix it is necessary to have an estimate of $\rho(T_i, T_j)$ which represents the correlation coefficient between the logarithmic spectral accelerations at T_i and T_j of either MS or AS GM. More specifically, to find Σ_{11} and Σ_{22} it is necessary to have $\rho(T_i^{AS}, T_j^{AS})$ and $\rho(T_i^{MS}, T_j^{MS})$, respectively, and such quantities can be found using the model proposed by Baker and Jayaram [2008] or Abrahamson et al. [2014], similarly as done in the first step of the process. To evaluate Σ_{12} and Σ_{21} we need $\rho(T_i^{AS}, T_j^{MS})$ and $\rho(T_i^{MS}, T_j^{AS})$, which can be found using the correlation structure developed by Papadopoulos et al. [2019]. For more details regarding the MSAS-CS procedure briefly discussed here, see Papadopoulos et al. [2020].

With the M-R of the MS, the spectrum of the MS ground motion and the M-R of the AS, we can first generate a realization of the AS response spectrum by sampling from the joint MS-AS Sa distribution and then select the ground motion (which is usually scaled) that best matches the AS sampled target spectrum (i.e., it has the lowest sum of the squared errors across periods). For computational simplicity, only one realization of the AS ground motion is drawn. As many selected AS ground motions will have very low intensity, one can set a threshold below which all sampled GMs are discarded and the simulation is repeated. As shown by Papadopoulos et al. [2020] the potential bias caused by systematically disregarding low-intensity AS ground motions is not expected to be of importance as long as the intensity threshold for discarding is kept reasonably low, i.e., the

small magnitude and/or large distance MS ruptures are not forced to produce AS sequences with unrealistically large M and associated ground motions.

Here, we retain only those events that lead to a Sa(0.2s) greater than 0.1g, as it is tenable to assume that the lower-intensity ground motions would not be damaging to the considered SDOF system.

Step 4: Derive the damage-dependent fragility curves

To derive damage-dependent fragility curves, we first assess the damage state of the structure after the mainshock event. Subsequently, we categorize the response data into four distinct groups, each corresponding to IDS0, IDS1, IDS2, and IDS3 (recall that DS4 means collapse here). As an example, after the MS analysis, when IM*=Sa(0.2s) is used and damage states are categorized using maximum ductility ratio, we have 267 ground motions in IDS0, 98 in IDS1, 139 in IDS2, and only 31 in IDS3. The remaining 465 GMs already caused collapse. The reason for employing 100 MS records per stripe was to ensure that we had a sufficient number of ground motions available for these different damage states. Based on the sample of intensity-response pairs in each considered IDS we estimate the median and standard deviation of the fragility curve, dependent on that IDS, using the maximum likelihood method.

Figure 6.13a shows, for the case of IM*=Sa(0.2s), the damage-dependent fragility curves for the collapse case (DS4). These curves correspond to the four initial damage states (i.e. IDS0, IDS1, IDS2 and IDS3) and the maximum ductility ratio as an EDP. Analogous results for DI are illustrated in Figure 6.13b. Similarly, Figure 6.14 shows the results for the case of IM*=AvgSa(0.2s-0.6s). The estimated parameters of the damage-dependent fragility curves can be found in Table 6.7 and Table 6.8Table 6.4. Damage-dependent fragility function parameters (μ/β) obtained with Approach 1 and IM*=Sa(0.2s)., for both EDPs considered and for the case when IM*=Sa(0.2s) and IM*=AvgSa(0.2s-0.6s), respectively.

First, it is important to highlight that, unlike in Approach 1, fragility curves conditioned on the IDS0 are not the same as those corresponding to the intact case (see Table 6.6). This is because when fragility curves are estimated for the intact case (Figure 6.10, Figure 6.11 and Figure 6.12) MS ground motions are used. On the contrary, fragility curves conditioned on the IDS0 illustrated in Figure 6.13 and Figure 6.14 are obtained using both MS and AS ground motions, resulting in different hazard compared to the MS-only case. Therefore, this difference is not surprising.

Secondly, one can see from the figures below that in all cases we have a reduction in the median capacity with increasing levels of severity of the IDS, as expected. However, there is a significant increase in dispersion, which, for some intensity levels causes the crossover of the fragilities. This implies that the structure that experienced more damage has lower probability of collapse compared to the less damaged structure, particularly evident at very high intensities where data points are limited. It is important to notice, nonetheless, that this counterintuitive phenomenon, seems to be mitigated to some extent when we use AvgSa(0.2s-0.6s) as a conditioning IM and DI as an EDP. Note that in Table 6.8, values for

the DS4|IDS3 are not reported as the standard deviation is unreasonably high. Instead, in the rest of the study for that fragility curve we will use the parameters obtained for DS4|IDS2.

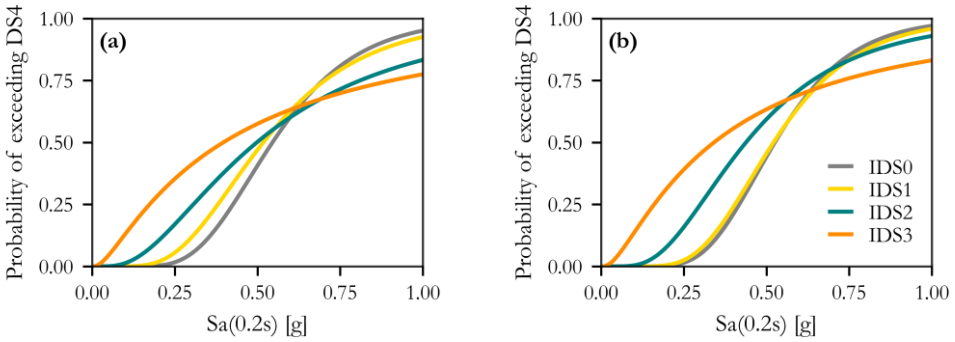

Figure 6.13. Collapse (i.e., DS4) fragility curves of the system conditioned on the different initial damage states, obtained using IM*=Sa(0.2s) and measured in terms of (a) maximum ductility ratio and (b) DI. Fragility curves are estimated using Approach 2.

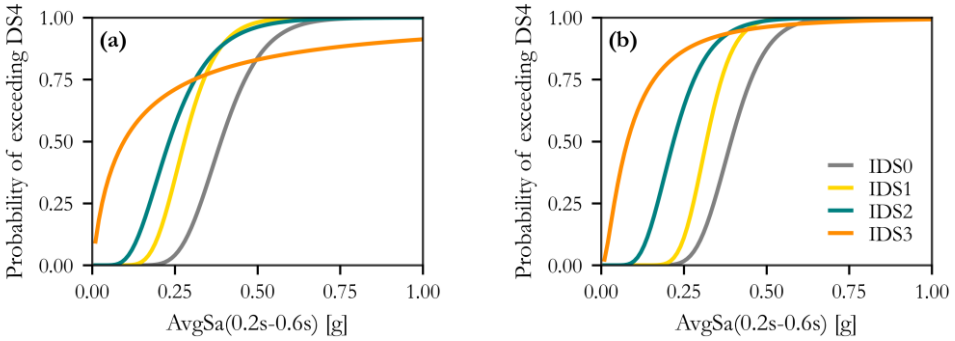

Figure 6.14. Collapse (i.e., DS4) fragility curves of the system conditioned on the different initial damage states, obtained using IM*=AvgSa(0.2s-0.6s) and measured in terms of (a) maximum ductility ratio and (b) DI. Fragility curves are estimated using Approach 2.

The approach described here, developed by Papadopoulos et al. (2020), offers a MS-AS record selection scheme where the spectral correlation between the MS and AS ground motion pairs is respected and the generated AS events are realistic. Additionally, it is flexible in the sense that MS ground motion record selection can be performed separately from the AS one, even with different approaches (e.g., CS, GCIM, cloud), if so desired. This approach eliminates the need for distinct databases of MS and AS ground motions, thus avoiding the task of identifying seismic sequences. However, it is important to acknowledge certain limitations of this approach.

Firstly, although this method maintains consistency between MS and AS ground motions, it does not enforce hazard consistency for the aftershock ground motions. Unlike MS ground motions, which have target mean and variance spectra, AS ground motions are randomly sampled. Secondly, this approach requires a seismic sequence generation model (e.g., Omori, ETAS), which often necessitates parameter calibration. Furthermore, the generated seismic sequences are usually not consistent with the MS hazard assessment. Specifically, in our case, MS ground motions are selected based on hazard computed using the Poisson model, while AS ground motions are generated using the ETAS model, which does not differentiate between MS and AS events but rather defines seismicity in terms of background and triggered events. Lastly, to obtain stable fragility estimates, a substantial number of MS and AS ground motions are required, making the method computationally intensive. Finally, while it is clear that hazard-consistent mainshock record selection can have a significant effect on the fragility estimates it is still unclear how important this is for the aftershock GMs given their secondary effect.

With this in mind, we propose Approach 3, which aims to make a balance between Approaches 1 and 2.

Table 6.7. Damage-dependent fragility function parameters (μ/β) obtained with Approach 2 and IM*=Sa(0.2s).

	Ductility ratio				**DI**			
	IDS0	IDS1	IDS2	IDS3	IDS0	IDS1	IDS2	IDS3
DS1	0.31/0.26	-	-	-	0.25/0.42	-	-	-
DS2	0.38/0.25	0.35/0.42	-	-	0.36/0.24	0.30/0.57	-	-
DS3	0.50/0.34	0.46/0.44	0.36/0.61	-	0.49/0.31	0.45/0.33	0.33/0.58	-
DS4	0.54/0.36	0.51/0.45	0.49/0.72	0.39/1.22	0.52/0.34	0.52/0.37	0.43/0.56	0.34/1.11

Table 6.8. Damage-dependent fragility function parameters (μ/β) obtained with Approach 2 and IM*=AvgSa(0.2s-0.6s).

	Ductility ratio				**DI**			
	IDS0	IDS1	IDS2	IDS3	IDS0	IDS1	IDS2	IDS3
DS1	0.26/0.37	-	-	-	0.25/0.51	-	-	-
DS2	0.31/0.27	0.21/0.28	-	-	0.32/0.26	0.23/0.57	-	-
DS3	0.36/0.22	0.26/0.27	0.20/0.43	-	0.37/0.21	0.31/0.2	0.18/0.50	-
DS4	0.39/0.25	0.28/0.28	0.23/0.43	-	0.39/0.21	0.32/0.20	0.22/0.37	0.08/1.03

6.3.3 Approach 3

Approach 3 is the combination of the two previous approaches. More specifically, we first compute the fragility of the undamaged structure, employing the hazard-consistent CS and MSA to select ground motions, as described in Step 1 of Approach 2. These values can be found in Table 6.6. Subsequently, we apply the B2B-IDA procedure, as explained in Approach 1, to determine the reduction in the median capacity of the intact structure. These values are obtained by dividing the median capacities given in Table 6.4 and Table 6.5 corresponding to different IDSs with the median capacities of the structure in the intact state. We then use these ratios to multiply the capacity of the structure in the intact state obtained with Approach 2, as given in Table 6.6. Similarly, we do the same with the standard deviation that increases with the severity level of the pre-existing damage. In this manner, we obtain the parameters in Table 6.9 and Table 6.10 for IM*=Sa(0.2s) and IM*=AvgSa(0.2s-0.6s), respectively.

Table 6.9. Damage-dependent fragility function parameters (μ/β) obtained with Approach 3 and IM*=Sa(0.2s).

	Ductility ratio				**DI**			
	IDS0	IDS1	IDS2	IDS3	IDS0	IDS1	IDS2	IDS3
DS1	0.30/0.30	-	-	-	0.28/0.26	-	-	-
DS2	0.36/0.33	0.31/0.50	-	-	0.36/0.32	0.15/0.60	-	-
DS3	0.45/0.41	0.43/0.52	0.39/0.58	-	0.45/0.41	0.39/0.42	0.29/0.67	-
DS4	0.48/0.46	0.44/0.50	0.42/0.54	0.34/0.62	0.48/0.45	0.41/0.53	0.32/0.62	0.21/0.87

Table 6.10. Damage-dependent fragility function parameters (μ/β) obtained with Approach 3 and IM*=AvgSa(0.2s-0.6s).

	Ductility ratio				**DI**			
	IDS0	IDS1	IDS2	IDS3	IDS0	IDS1	IDS2	IDS3
DS1	0.25/0.33	-	-	-	0.24/0.33	-	-	-
DS2	0.30/0.28	0.28/0.27	-	-	0.30/0.27	0.13/0.30	-	-
DS3	0.35/0.23	0.34/0.19	0.31/0.21	-	0.35/0.23	0.29/0.21	0.22/0.24	-
DS4	0.36/0.20	0.33/0.16	0.305/0.20	0.26/0.23	0.37/0.20	0.32/0.20	0.26/0.23	0.17/0.40

6.4 EVENT-BASED METHODOLOGY FOR THE ESTIMATION OF THE ANNUAL PROBABILITY OF EXCEEDING A GIVEN DAMAGE STATE: DIRECT ANALYSIS METHOD

In this section, we compute the annual probabilities of exceeding different damage states using the so-called direct analysis, which serves as a benchmark in this context. We perform the direct analysis for two variants: (i) the MS-only case where the seismic hazard is modeled with Poisson model and it is assumed that the structure is repaired after each event and (ii) the case where all events in the sequence are considered using the ETAS model and damage accumulation is accounted for. The procedure for computing annual probabilities of exceedance via direct analysis is outlined below for both cases.

MS-only Case:

1. Use the same 100,000 1-year-long stochastic catalogs generated in the hazard assessment phase with the Poisson model (refer to Section 6.2.2 for detailed information)
2. For each stochastic catalogue *n*:
   - For each i^{th} rupture in catalogue *n*:
     - Using the associated properties (e.g., rake, dip, slip, seismogenic depth) and the Abrahamson et al. [2014] GMPE, determine the mean and standard deviation of the Sa's all oscillator periods and related covariance matrix and use them to construct a multivariate normal distribution. Keep in mind that Sa is defined in terms of GMRotD50 [Boore 2010];
     - Generate a random realization of the ground motion response spectrum by sampling correlated lnSa values from the multivariate normal distribution;
     - Select the ground motion from an available database that best matches this realization;
     - Using the selected record run the NLRHA;
     - Save the DS of the structure at the end of the run;
3. Compute the annual probability of exceeding different damage states by simply counting the number of catalogs in which exceedance occurs and dividing that number by the total number of catalogs as expressed by Equation (6.7).

Seismic sequences Case:

1. Use the same 100,000 1-year-long stochastic catalogs generated in the hazard assessment phase with the ETAS model (refer to Section 6.2.2 for detailed information)
2. For each stochastic catalogue *n*:
   - For each i^{th} rupture in the catalogue:
     - If it is the first event in the catalogue (i=1):
       - Using the associated properties (e.g., rake, dip, slip and seismogenic depth) and Abrahamson et al. [2014] GMPE,

determine the mean, standard deviation, and unconditional covariance matrix;

- Else:
  - Using the associated properties, (e.g., rake, dip, slip and seismogenic depth) and Abrahamson et al. [2014] GMPE, determine the mean and standard deviation of the Sa's all oscillator periods and related covariance matrix and use them to construct a multivariate normal distribution conditional on the Sa's of the ground motion of the $(i-1)^{th}$ rupture using Equations (6.20)-(6.23);
- Generate a random realization by sampling correlated lnSa values from this multivariate normal distribution;
- Select the ground motion from an available database that best matches this realization;
- Add 10 seconds of zero acceleration at the end of the ground motion allowing for the system to come to rest when subject to this zero-padded ground motion;
- Using this zero-padded record run the NLRHA;

- Save the DS of the structure;

3. Compute the annual probability of exceeding different damage states by simply counting the number of catalogs in which the exceedance of the EDP value corresponding to the onset of such a DS occurs and dividing by the total number of catalogs, as expressed by Equation (6.7).

We argue that the results obtained with direct analysis serve as a benchmark against which the results of the other three fragility curve-based approaches should be compared. This approach circumvents the need for conditioning on an IM and avoids the computation of fragility curves. However, it is important to note that direct analysis poses a substantial computational burden due to the many analyses one needs to run. In our specific case, this exercise was made feasible primarily due to the simplicity of the SDOF system. As stated earlier, to mitigate the computational load to some extent, we restricted the analysis to ground motions with Sa(0.2s) exceeding 0.1g, considering lower-intensity motions as non-damaging. Consequently, we performed a reduced set of 2394 analyses in the MS-only case and 5673 analyses in the case of seismic sequences, optimizing computational efficiency while still providing meaningful results.

6.5 RESULTS

In the previous sections, we described four approaches that can be used to find the annual probabilities of exceeding different damage states, discussing the advantages and disadvantages of each approach. The first three are based on the calculation of damage-dependent fragility curves (or simply fragility curves in the MS-only case) while the last one, which serves as the benchmark, is based on the results of direct analysis. Two variants of the direct analysis approach were carried out: the mainshock-only seismicity case and the

clustered seismicity case. Of course, for consistency, the thresholds of the EDP (either maximum ductility or DI) assigned to the onset of each one of the four damage states are identical in all four cases.

We first show the annual probabilities of exceeding different damage states in the MS-only case (Figure 6.15 and Figure 6.16), which utilizes the Poisson model for hazard calculations and assumes that the structure is repaired after each seismic event. In this case, by design, results obtained with Approach 3 are the same as those obtained with Approach 2. One can see that the results obtained using Approach 2, which is a hazard-consistent approach, are much closer to the benchmark results than those derived from the IDA (Approach 1). These results were expected given the differences we observed in the fragility curves as the obtained median capacity and dispersion for all damage states are higher in Approach 2.

It is also interesting to notice that the ratio between the annual probability of exceedance obtained with IM*=AvgSa(0.2s-0.6s) and that obtained with IM*=Sa(0.2s), is significantly lower when we use Approach 2, for both considered EDPs, as illustrated in Figure 6.17. These findings prove once again the superiority of the hazard-consistent methods for record selection.

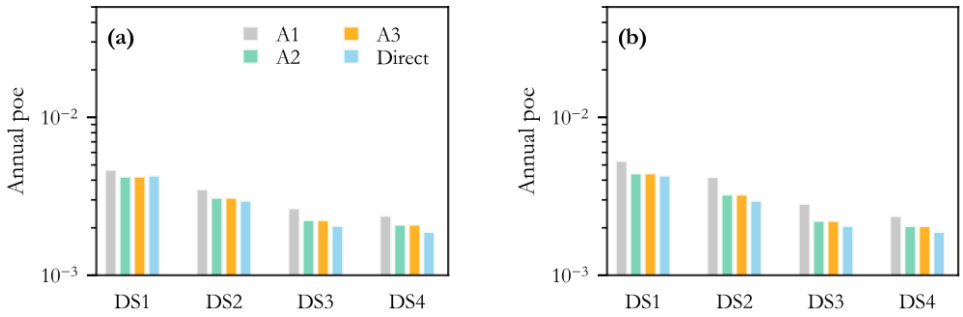

Figure 6.15. Annual probabilities of exceedance (poe) of the four DSs for the MS-only case when maximum ductility ratio is used as the EDP. Results obtained using (a) Sa(0.2s) and (b) AvgSa(0.2s-0.6s).

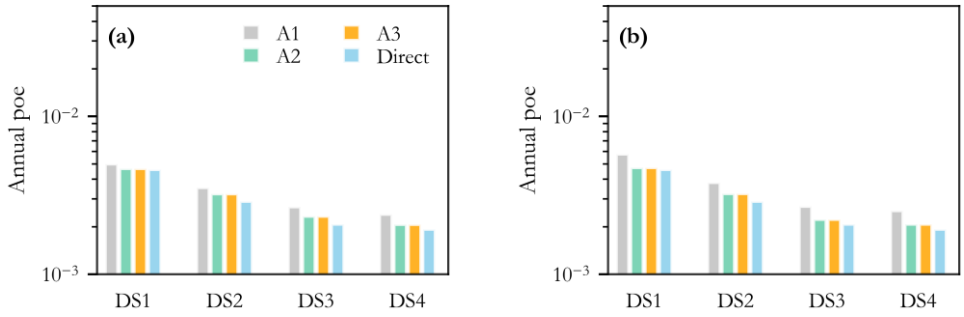

Figure 6.16. Annual probabilities of exceedance (poe) of the four DSs for the MS-only case when DI is used as the EDP. Results obtained using (a) Sa(0.2s) and (b) AvgSa(0.2s-0.6s).

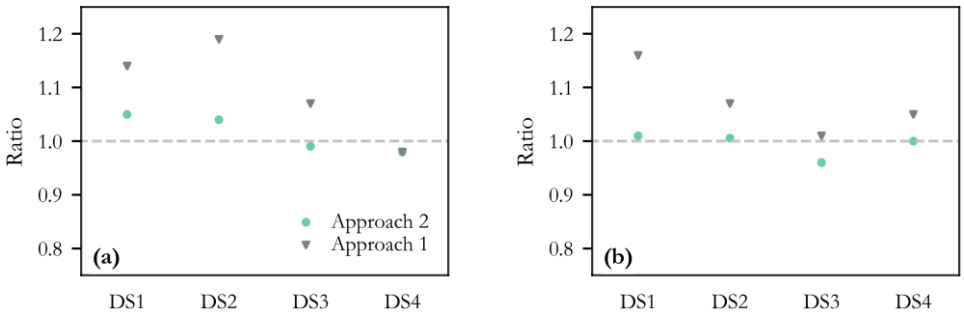

Figure 6.17. The ratio between the annual probability of exceeding given DS obtained when IM*=AvgSa(0.2s-0.6s) and when IM*=Sa(0.2s) for the case when EDP is (a) maximum ductility ratio and (b) DI. Illustrated results refer to the Poissonian (MS-only) case.

In Figure 6.18 and Figure 6.19, we show the results obtained for the clustered seismicity case, using maximum ductility ratio and DI as EDPs, respectively. It is important to note that the direct approach yields annual probabilities of exceedance that are approximately twice as high across all damage states and for both considered EDPs when compared to the Poissonian model. In Figure 6.20, we show the ratio between the annual probability of exceedance obtained with IM*=AvgSa(0.2s-0.6s) and that obtained with IM*=Sa(0.2s) for all approaches considered. The differences between the two conditioning IMs are significantly more pronounced than in the Poissonian case. However, it is noteworthy that these differences are considerably lower in Approaches 2 and 3 compared to those in Approach 1.

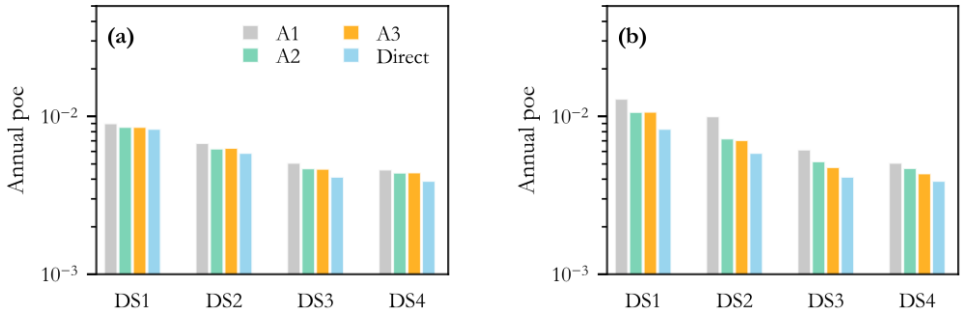

Figure 6.18. Annual probabilities of exceedance (poe) of the four DSs for the clustered seismicity case when maximum ductility ratio is used as the EDP. Results obtained using (a) Sa(0.2s) and (b) AvgSa(0.2s-0.6s).

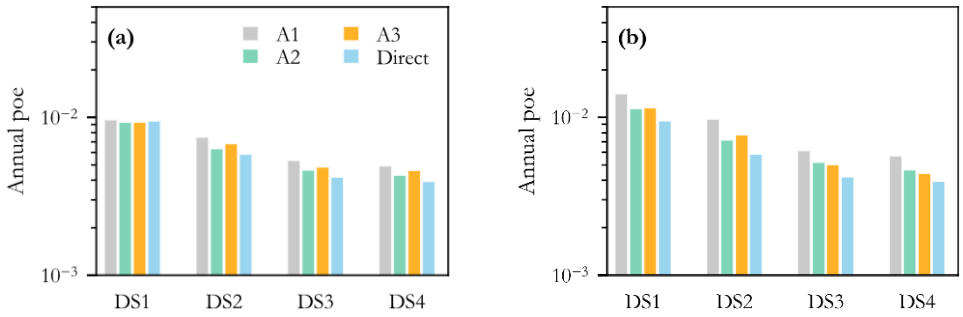

Figure 6.19. Annual probabilities of exceedance (poe) of the four DSs for the clustered seismicity case when DI is used as the EDP. Results obtained using (a) Sa(0.2s) and (b) AvgSa(0.2s-0.6s).

In Figure 6.21, we show the ratio between the annual probability of exceedance obtained with the direct approach with those obtained with the three discussed methods. This figure refers to the case where the maximum ductility ratio is used as an EDP. Similarly, results for DI are shown in Figure 6.22. One can note that all considered approaches tend to overestimate the probabilities when compared to the benchmark, regardless of the EDP and conditioning IM. Approach 1 consistently produces results farthest from the benchmark, supporting our observations in the Poissonian case. The closest approximation to the benchmark is achieved when DI is utilized in conjunction with Approach 2 and IM*=Sa(0.2s).

When DI is used as an EDP and IM*=Sa(0.2s), Approach 2 yields lower annual probabilities of exceedance compared to Approach 3-an outcome anticipated due to the higher median capacities of fragility curves obtained with Approach 2 in this specific case. In other cases, however, the reasons for the difference between the results of these two

methods are less straightforward, owing to the intricate interplay between median values and standard deviations (i.e., slopes) of the fragility curves. However, one can notice that the differences in results obtained with these two approaches are not considerable.

The results obtained with IM*=AvgSa(0.2s-0.6s) overall give us higher probabilities of exceedance in Approaches 2 and 3, compared to the case with IM*=Sa(0.2s). This was expected as there are small differences between the two conditioning IMs in the intact case and the reduction in capacity predicted with IM*=AvgSa(0.2s-0.6s) is higher, leading to higher annual probabilities of exceedance.

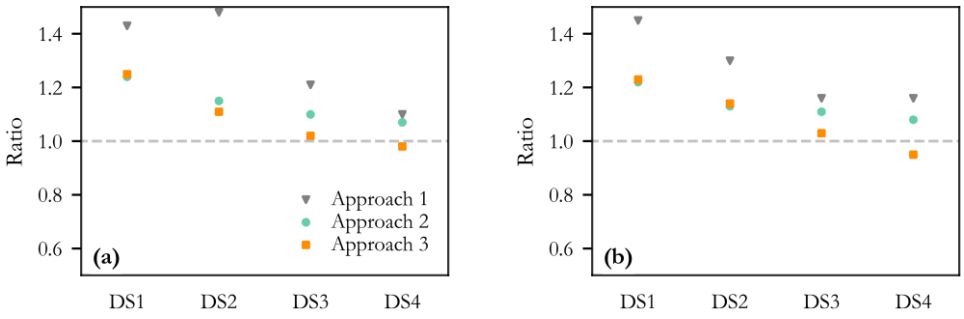

Figure 6.20. The ratio between the annual probability of exceeding given DS obtained when IM*=AvgSa(0.2s-0.6s) and when IM*=Sa(0.2s) for the case when EDP is (a) maximum ductility ratio and (b) DI. Illustrated results refer to the clustered seismicity case.

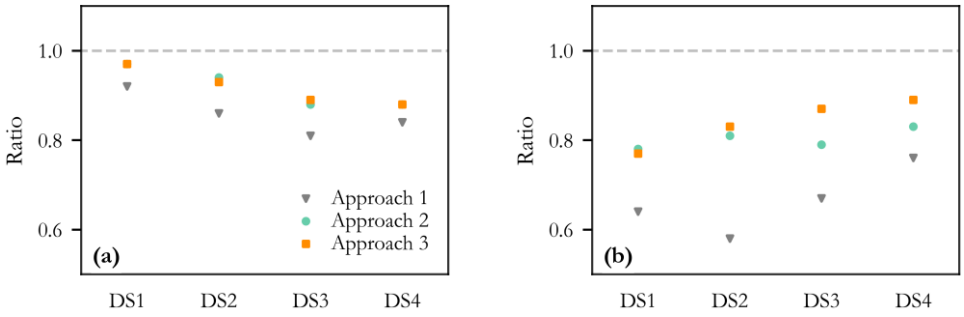

Figure 6.21. The ratio between the annual probability of exceedance obtained with the direct approach and the annual probability of exceedance obtained with the three defined approaches. Results for maximum ductility ratio and (a) IM*=Sa(0.2s) and (b) IM*=AvgSa(0.2s-0.6s) are illustrated.

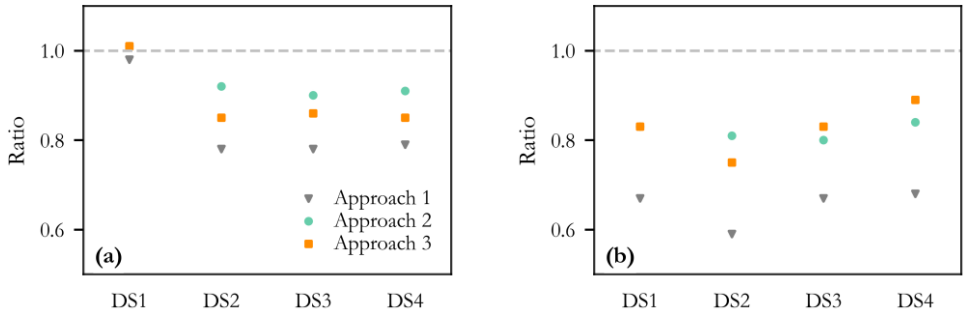

Figure 6.22. The ratio between the annual probability of exceedance obtained with the direct approach and the annual probability of exceedance obtained with the three defined approaches. Results for DI and (a) IM*=Sa(0.2s) and (b) IM*=AvgSa(0.2s-0.6s) are illustrated.

Based on the results obtained, it is evident that Approaches 2 and 3, which incorporate hazard consistency in the selection of mainshock records, outperform Approach 1, where IDA is employed without guaranteed hazard consistency. Additionally, our findings suggest that when utilizing Approach 2 for selecting aftershock ground motions, the stability of fragility curves is achieved more rapidly when AvgSa is employed as a conditioning IM and the DI is used as an EDP. However, given the complexity and computational demands of Approach 2, an alternative in the form of Approach 3 proves viable. This alternative method combines hazard-consistent mainshock record selection with the outcomes of B2B-IDA, yielding results with only minor discrepancies compared to Approach 2.

6.6 Conclusions

In light of the limited research on the development of damage-dependent fragility curves and the significance of aftershock record selection, our study addresses these gaps in the context of clustered seismic risk assessment. We explore three distinct approaches for deriving damage-dependent fragility curves and we compare them on the basis of annual probabilities of exceeding different damage states.

The investigation is conducted on a simple SDOF system characterized by the Modified Ibarra material model, with moderate ductility and a fundamental period of 0.2s. The site that we considered is Perugia, in Central Italy, where significant seismic sequences were observed in recent history. We first computed the hazard for our case study site following the event-based methodology. We considered two cases: (i) clustered seismicity case and (ii) mainshocks-only case. For the former, we utilized the Epidemic-Type-Aftershock Sequence (ETAS) model – a state-of-the-art approach for modeling clustered seismicity. To characterize the model we used the set of parameters calibrated by Šipčić et al. [2022] (i.e., Section 2 of this thesis) for Central Italy. In the latter, mainshock-only case, we employed the Poisson model, calibrated through the smoothed seismicity approach and the HORUS instrumental catalogue of events [Lolli et al. 2020], declustered using Gardner and Knopoff [1974] method. With the simulated catalogues of events, Abrahamson et al.

[2014] GMPE and SHARE seismic source model [Woessner et al. 2015] we computed the hazard using two conditioning IMs, Sa(T_1=0.2s), commonly used metric, and AvgSa(0.2s-0.6s) which might be a better choice in the context of clustered seismicity where period elongation can occur due to the loss of stiffness caused by the accumulation of damage. We defined damage states through two EDPs: traditional displacement-based EDP (expressed in terms of maximum ductility ratio) and Modified Park and Ang DI that combines displacement with dissipated energy, calibrated using an extensive database of RC columns.

We then described the three approaches for the derivation of damage-dependent fragility curves: (i) Approach 1 which used B2B-IDA without any consideration of hazard-consistency in the ground motions used; (ii) Approach 2 where mainshock records are selected to be consistent with the hazard at the site using Conditional Spectrum (CS), while the aftershock ground motions are selected to be consistent with the selected mainshock ground motions following the methodology proposed by Papadopoulos et al. [2020] and (iii) Approach 3, which combines the mainshock record selection from Approach 2 with the results of B2B-IDA to estimate the reduction in capacity due to pre-existing damage.

With the damage-dependent fragility curves derived through these three methods, we calculated the annual probabilities of exceeding defined damage states for both EDPs and conditioning IMs under consideration. We explored both mainshock-only and clustered seismicity cases. To establish a benchmark, we employed a direct analysis approach where we computed annual probabilities of exceedance by selecting ground motions for each simulated rupture in the simulated stochastic catalogues. This approach circumvents the need to derive fragility curves but poses a substantial computational burden, feasible in our study due to the simplicity of the SDOF system used.

Our results showed that annual probabilities of exceedance obtained with the direct approach in the clustered seismicity case are twice those obtained in the mainshock-only case. Additionally, we observed that, for both cases, results obtained with Approach 1 deviated farthest from the benchmark, as expected, given the lack of hazard consistency in this approach. Our findings suggest that when employing Approach 2, the stability of fragility curves is achieved more rapidly when AvgSa is used as a conditioning IM and DI as an EDP. However, it is worth noting that Approach 2, despite maintaining consistency between mainshock and aftershock ground motions, can be complex due to the requirement of a seismic sequence generation model and a substantial number of analyses needed for stable fragility estimates. In light of this, we showed that Approach 3 may be a practical alternative, as the differences in results compared to Approach 2 are minor and the computational burden is much lower.

It is crucial to highlight, however, that, for more comprehensive conclusions, similar analyses need to be conducted for different types of structural systems, including both SDOF and MDOF systems, as well as for sites with different seismic characteristics.

7.CONCLUSIONS

7.1 SUMMARY

The main objective of our work was to scrutinize some of the common modeling decisions in seismic risk assessment, with emphasis on the significance of including clustered seismicity.

The conventional practice in seismic risk models is to neglect any event that is not the so-called mainshock, namely the largest magnitude earthquake of a cluster that occurred within a certain period in a certain area. This implies that the derivation of the rate of occurrence of future events is (mostly) based on the analysis of "declustered" historical and instrumental seismicity catalogues. The various declustering techniques identify earthquake clusters and then keep the mainshocks, while all remaining events, whether "proper" foreshocks and aftershocks (namely those events that break part of the same rupture of the mainshock) or "triggered" events (namely those that break other segments of the same fault or other adjacent faults) are disregarded. While this process enables analysts to use the relatively simple Poisson process for modeling the occurrence of future events, numerous studies demonstrated that keeping just the mainshock events may result in underestimated hazard and risk estimates, highlighting the damaging potential of all seismic events.

In **Chapter 2** of this thesis, we estimated seismic hazard in two regions, namely Central Italy (Region 1) and Southern Italy (Region 2), accounting for all earthquake events regardless of whether they are classified as mainshocks or not. To model seismic sequences we employed the Epidemic-Type-Aftershock-Sequence (ETAS) model, which is considered the state-of-the-art approach for generating realistic earthquake clusters. By adopting several Turing-style tests, we demonstrated that the ETAS model can represent the statistical features of long-term historical seismicity in these two regions well. We compared the hazard estimates for sites of Norcia and Perugia, in Central Italy, obtained with the ETAS model with those based on the Poissonian model that considers mainshocks only and the model that combines the Poissonian model for mainshocks and the Modified Omori law for modeling aftershocks (Omori model), which is more practical albeit less accurate approach than ETAS for clustered seismicity modeling. We showed that the Poisson model leads to hazard estimates that are significantly lower in some cases compared to ETAS. Furthermore, our comparison of ETAS with the Omori model revealed that the former can better capture the temporal variation in seismic hazard both in quiet and active periods of clustered seismicity. In essence, there is a price to pay if one wants to use simpler

approaches for clustered modeling: these results underscored the need to refine models describing spatiotemporal clustering for more accurate risk assessments.

After having established that the ETAS model is indeed superior although more complex, the next obvious question is: can we calibrate the ETAS model in one region and use it also in other regions with the same tectonic environment? This question is addressed in the remaining part of Chapter 2 and complemented in Chapter 3.

Along these lines, we investigated whether the spatial and temporal characteristics of earthquake sequences generated by crustal faults are region-dependent or whether these characteristics share some commonality across regions. We found that there are differences in the parameters' values defining the ETAS model in these two regions but these differences are not due to different characteristics of the clustering in the two regions but rather to statistical issues due to limited sample sizes of the data available. By comparing the magnitude frequency distributions for large magnitude events of ETAS simulated catalogs with the historical CPTI15 catalogue covering the period from 1717 to 2017, we showed that the modeling of the sequences in Southern Italy is superior when the ETAS clustering parameters from Central Italy are used rather than those extracted from the sparse dataset of clusters occurred in the past decades in Southern Italy itself. More specifically, there is a better agreement between simulated and observed frequency distributions when we utilized the more robust values of the ETAS clustering parameters from Central Italy. These findings suggested that discrepancies in ETAS parameters' values are likely a consequence of data scarcity rather than intrinsic differences in earthquake sequence phenomena.

Chapter 3 further reinforced our Chapter 2 findings as we applied the ETAS model calibrated with Central Italy data to represent seismic sequences in Croatia and Turkey. Again, through several Turing-style tests, we demonstrated that the ETAS model calibrated in this manner matches the observed seismicity better than the ETAS model calibrated using local data. Our results in Chapter 2 and Chapter 3 support the premise that ETAS parameters' values from well-constrained regions, such as Central Italy, can be used in the same tectonic regions that either did not experience a sufficient number of active seismic sequences during the period of the earthquake instrumental catalogue or where the local instrumentation network is poor or missing.

In addition to the potential underestimation of seismic hazard due to disregarding non-mainshock events, which was systematically addressed in Chapters 2 and 3, the conventional mainshock-only risk assessment approach implicitly assumes that events other than the mainshock of the cluster do not contribute to causing additional structural damage and losses beyond those caused by the main event. This is clearly an oversimplification that is dispelled by the evidence from damage reconnaissance missions during active sequences. The assumption of structure always in the undamaged state is also not tenable even when only mainshocks from different clusters are considered, as is the case in the traditional approach. This assumption of immediate repair after each event often does not align with reality: in many parts of the world it takes decades before the building stock is fully repaired while in the meantime the damaged structures are left in a

heightened state of vulnerability. Simply put, the accumulation of damage due to different shocks is routinely disregarded. Even in the extremely rare cases when these models consider damage accumulation from multiple shocks, the engineering demand parameter (EDP) employed to describe damage estimation is usually peak-displacement-based. Such EDPs, which are not monotonically increasing, are poorly equipped to detect an increased level of damage caused by multiple shocks, either in the same cluster or by other mainshocks. This caveat is even more serious when other shocks cause weaker ground motions, such as those from lower-magnitude events in the same cluster. Damage data collected after earthquakes in a sequence clearly shows the progression of damage that this EDP cannot detect. Clearly, a more refined EDP is needed to address this problem.

Chapter 4 addressed these limitations as we delved into the progression of damage in reinforced concrete (RC) columns, that fail in flexure, shear, and flexure-shear modes. We concentrated our effort on RC buildings since they represent the largest fraction of structures in many parts of the world and we focused on columns because they are the main structural elements whose damage contributes the most to the progressive loss of capacity. A database of experimental tests on rectangular RC columns subjected to cyclic pushover was assembled and characteristic points (such as the cracking point, yield point, and ultimate point) were extracted from the force-displacement data. Leveraging experimental data, a modified Park and Ang damage index was calibrated. Our findings demonstrated that, while further validation with experimental data is warranted, the proposed EDP, which includes a peak displacement part and a dissipated energy part, identifies distinct damage states more effectively than previous peak displacement only EDPs. As a result, it emerges as a good candidate for developing fragility and vulnerability curves within the context of clustered seismicity risk assessment. We then focused on the numerical modeling of RC columns using the lumped plasticity approach and the Modified Ibarra material model. We explored the progression of damage and capacity reduction under seismic sequences, considering the proposed energy-based damage index and the conventional peak displacement-based EDP. Results from modeling single-degree-of-freedom systems (SDOFs) and a 3D model of a bare RC frame structure using back-to-back IDA indicated that the proposed damage index predicts a more significant reduction in capacity compared to maximum ductility, a result that is in better agreement with the data of the laboratory tests at our disposal.

In **Chapter 5,** our primary focus was on improving the applicability of existing procedures for the development of robust site-specific and structure-specific fragility curves for risk assessment purposes. The focus here is specifically on the link between the seismic hazard at the site of interest and structural fragility. This link is ensured through a hazard-consistent selection of ground motions, for the implementation of which, for example via using Conditional Spectrum (CS), a large pool of strong ground motions is needed. As this is hardly ever the case, in practical applications the suite of records is usually augmented by scaling weaker ground motions. We took a deeper look at whether the practice of scaling ground motions selected via CS may cause bias in the fragility estimates. For this purpose, we considered a site in Central Italy as a case study for hazard computation and ten

structures modeled as five SDOF systems with fundamental periods ranging from 0.2 to 2.0 seconds and with 2 material models each. We defined two groups of ground motions to select from–one with low scaling factors (LSF) and one with high scaling factors (HSF). Our findings indicated that when hazard consistency is maintained in the ground motion record selection, scaling ground motions does not lead to statistically significant differences in structural response estimates. This means that, although not encouraged, the practice of ground motion scaling can be tolerated because the scarcity of naturally strong ground motions to choose from would cause a more significant negative impact on the accuracy of the risk estimates.

This is not the only practical issue that complicates the implementation of risk assessment of structures at a specific site. Another significant issue is related to managing the computational burden needed to achieve stable and accurate risk estimates. To do so, in real-life applications, one often needs to run many analyses especially when the analysts rely on complex numerical models of structures. Therefore, in this part of our work, we investigated how to reduce the number of response analyses required to derive site-specific fragility curves using CS-based record selection and the Multiple-Stripe-Analysis approach. We showed that to achieve a good match to the target CS more than 7 records per stripe are recommended and, more importantly, to obtain stable response estimates, that is median and dispersion estimates of the fragility curve, at least 11 (for the median) and 16 (for the dispersion) ground motions are needed for a desired ±10% accuracy.

Finally, given our objective of including all earthquakes and the deterioration of the structural integrity due to previous shocks in the risk assessment analysis, we moved further than fragility curves for intact structures and ventured into the derivation of site- and building-specific damage-state-dependent fragility curves. Given the limited existing research on the subject and the importance of aftershock record selection, in **Chapter 6** we investigated three distinct approaches for deriving damage-state-dependent fragility curves with different levels of accuracy and complexity. We evaluated them by comparing the annual probabilities of exceeding different damage states with the benchmark estimates obtained via the "direct approach" discussed below. Approach 1, which is the simplest and less accurate, utilizes back-to-back Incremental Dynamic Analysis (B2B-IDA) using a set of strong ground motions extracted from the existing database without accounting for site hazard consistency. Approach 2, the most complex and arguably the most accurate, utilizes mainshock records that are selected to be consistent with the hazard at the site via CS, while the aftershock ground motions are selected to be consistent with the selected mainshock ground motions. Approach 3, a hybrid method of the previous two of intermediate complexity, combines the mainshock record selection from Approach 2 with the results of B2B-IDA to estimate the reduction in capacity due to pre-existing damage. The direct approach consists of simulating many years of clustered seismicity (via ETAS) and for each event of magnitude, M, at a source-to-site distance, R, of selecting ground motions of appropriate spectral content. The investigation was conducted on a simple SDOF system characterized by the Modified Ibarra material model, with moderate ductility and a fundamental period of 0.2s, located in Perugia, Central Italy. We defined the damage states

using the conventional displacement-based EDP and Damage Index, DI, proposed in Chapter 4. Our results showed that results obtained with Approach 1 deviate from the benchmark the most, due to the lack of hazard consistency. The application of Approach 1 is, therefore, discouraged. Furthermore, we demonstrated that the differences in results obtained with Approach 2 and Approach 3 were not significant. This implies that, at least for the specific case considered, the choices made in aftershock record selection were not as critical as those related to mainshock record selection. In all cases using DI instead of conventional displacement-based EDP yielded superior results. Hence, in practical applications, we suggest using DI for defining damage states and Approach 3 of intermediate complexity for the derivation of damage-state dependent fragility curves.

7.2 FUTURE RESEARCH

The research presented in this thesis emphasizes the significance of incorporating clustered seismicity into seismic risk models and it addresses various critical issues related to seismic hazard, fragility curves' development, and record selection for the goal of site- and structure-specific risk assessment. Of course, there remains plenty of room for further improvement and investigation of the discussed methodologies. Below are the key areas that we believe warrant additional research.

- While we believe that the use of the ETAS model is undoubtedly promising, several aspects of it can be investigated more thoroughly. For example, fault geometry and anisotropic kernel for aftershock distribution, the time-varying magnitude of completeness, potential inter-sequence variability of the parameters, time-dependent background rate, and effect of the temporal and spatial window are some of the traits that deserve further investigation.
- It is necessary to test if the set of ETAS parameters calibrated based on data in the region in Central Italy can be used in other crustal regions, expanding the study beyond Croatia and the region in Turkey, which were investigated in this thesis.
- More efforts need to be made to gain insight into the accumulation of damage during seismic sequences. It is necessary to have more experimental tests, including shake-table tests and data from instrumented buildings after each event in the sequence to further validate the proposed Damage Index. Furthermore, we focused only on the RC columns while the potential significance of other components of RC buildings, like infills and joints, needs to be assessed. More broadly, it is necessary to carry out additional analyses to determine the relevance of damage accumulation in seismic risk assessment for different structures.
- Given the scarcity (or absence) of empirical tests, it would be useful to develop high-fidelity finite element models that can accurately predict damage in RC components, enabling the exploration of different seismic sequences and the effects of damage accumulation.
- To reduce the the computational burden associated with running several response analyses in the Multiple-Stripe-Analysis framework for derivation of fragility

curves, it should be investigated what is the optimal number of stripes to run, balancing the accuracy and practicality.

- When it comes to aftershock record selection it would be valuable to develop a framework that not only maintains the consistency between the mainshock and aftershock ground motions but also enforces hazard consistency of the aftershock ground motions. Additionally, while it is clear that hazard-consistent mainshock record selection can have a significant effect on the fragility estimates it would be useful to perform additional analysis and investigate the importance of aftershock hazard consistency.
- To obtain stable estimates of the damage-dependent fragility curves, one needs to run a substantial number of analyses, an exercise that often requires a high computational burden. That said, more practical approaches for fragility analyses should be explored and developed, circumventing the need for an excessively high number of back-to-back analyses.

REFERENCES

Abrahamson, N. A., Silva, W. J., and Kamai, R. [2014] "Summary of the ASK14 ground motion relation for active crustal regions," *Earthquake Spectra*, Vol. 30, No.3, pp. 1025–1055.

Aki, K. [1965] "Maximum likelihood estimate of b in the formula log N = a - bM and its confidence limits," *Bulletin of the Earthquake Research Institute Tokyo University*, Vol. 43, pp. 237–239.

Aljawhari, K., Gentile, R., Freddi, F., and Galasso, C. [2020] "Effects of Ground-motion Sequences on Fragility and Vulnerability of Case-Study Reinforced Concrete Frames," *Bulletin of Earthquake Engineering*. Springer, Netherlands. https://doi. org/10.1007/s10518-020-01006-8.

Amadio, C., Fragiacomo, M., and Rajgelj, S. [2003] "The effects of repeated earthquake ground motions on the non-linear response of SDOF systems," *Earthquake Engineering and Structural Dynamics*, Vol. 32, pp. 291–308.

Ancheta, T. D., Darragh, R. B., Stewart, J. P., Seyhan, E., Silva, W. J., Chiou, B. S. J., Wooddell, K. E., Graves, R. W., Kottke, A. R., Boore, D. M., Kishida, T., and Donahue, J. L. [2014] "NGA-West2 database," *Earthquake Spectra*, Vol. 30, No.3, pp. 989–1005.

Atalić, J., Uroš, M., Šavor Novak, M., Demšić, M., and Nastev, M. [2021] "The Mw5.4 Zagreb (Croatia) earthquake of March 22, 2020: impacts and response," *Bulletin of Earthquake Engineering*, Springer Netherlands, Vol. 19, No.9, pp. 3461–3489.

ATC. [2017] "Recommended modeling parameters and acceptance criteria for nonlinear analysis in support of seismic evaluation, retrofit, and design", NIST GCR 17-917-45.

Bae, S. [2005] "Seismic Performance of Full-Scale Reinforced Concrete Columns," *Ph.D. Thesis*, The University of Texas at Austin.

Baggio, C., Bernardini, A., Colozza, R., Corazza, L., Bella, M. Della, Pasquale, G. D. I., Dolce, M., Goretti, A., Martinelli, A., Orsini, G., Papa, F., and Zuccaro, G. [2007] "Field Manual for post-earthquake damage and safety assessment and short term countermeasures(AeDES)," European Commission—Joint Research Centre—Institute for the Protection and Security of the Citizen, EUR, 22868.

Bakalis, K., Kohrangi, M., and Vamvatsikos, D. [2018] "Seismic intensity measures for above-ground liquid storage tanks," *Earthquake Engineering and Structural Dynamics*, Vol. 47, No.9, pp. 1844–1863.

Baker, J. W. [2007] "Measuring bias in structural response caused by ground motion scaling," *Pacific Conference on Earthquake Engineering*, Nanyang Technological University, Singapore.

Baker, J. W. [2011] "Conditional mean spectrum: Tool for ground-motion selection," *Journal of Structural Engineering*, Vol. 137, No.3, pp. 322–331.

Baker, J. W. [2015] "Efficient analytical fragility function fitting using dynamic structural analysis," *Earthquake Spectra*, Vol. 31, No.1, pp. 579–599.

Baker, J. W., and Jayaram, N. [2008] "Correlation of spectral acceleration values from NGA ground motion models," *Earthquake Spectra*, Vol. 24, No.1, pp. 299–317.

Baker, J. W., and Lee, C. [2018] "An Improved Algorithm for Selecting Ground Motions to Match a Conditional Spectrum," *Journal of Earthquake Engineering*, Vol. 22, No.4, pp. 708–723.

Baltzopoulos, G., Baraschino, R., and Iervolino, I. [2019] "On the number of records for structural risk estimation in PBEE," *Earthquake Engineering and Structural Dynamics*, Vol. 48, No.5, pp. 489–506.

Baraschino, R., Baltzopoulos, G., and Iervolino, I. [2023] "A note on peak inelastic displacement as a proxy for structural damage in seismic sequences," *Procedia Structural Integrity*, Vol. 44, No.2023, pp. 75–82.

Båth, M. [1965] "Lateral inhomogeneities of the upper mantle," *Tectonophysics*, Vol. 2, No.6, pp. 483–514.

Bazant, S., and Bhat, P. [1977] "Prediction of Hysteresis in Reinforced Concrete Members," *Journal of Structural Engineering*, Vol. 103, No.1, pp. 153–167.

Bazzurro, P. [1998] "Probabilistic Seismic Demand Analysis," *Ph.D. Thesis*, Department of Civil and Environmental Engineering, Stanford University.

Bazzurro, P., and Cornell, C. A. [1999] "Disaggregation of seismic hazard," *Bulletin of the Seismological Society of America*, Vol. 89, No.2, pp. 501–520.

Bazzurro, P., Cornell, C. A., Menun, C., and Motahari, M. [2004] "Guidelines for seismic assessment of damaged buildings," *13th World Conference on Earthquake Engineering,* Vancouver, Canada.

Bazzurro, P., Cornell, C. A., Shome, N., and Carballo, J. E. [1998] "Three proposals for

characterizing MDOF nonlinear seismic response," *Journal of Structural Engineering*, Vol. 124, No.11, pp. 1281–1289.

Bearman, C. F. [2012] "Post-Earthquake Assessment of Reinforced Concrete Frames," *Ph.D. Thesis*, University of Washington.

Berry, M., and Eberhard, M. [2003] "Performance Models for Flexural Damage in Reinforced Concrete Columns Performance Models for Flexural Damage in Reinforced Concrete Columns," *PEER Report 2003/18, Pacific Engineering Research Center*, University of California, Berkeley, California, 158 pp..

Berry, M. P., and Eberhard, M. O. [2008] "Performance Modeling Strategies for Modern Reinforced Concrete Bridge Columns," *Pacific Engineering Research Center*, the University of California, Berkeley.

Berry, M., Parrish, M., and Eberhard, M. [2004] "PEER Structural Performance Database User 's Manual", *Pacific Engineering Research Center*, the University of California, Berkeley, California, 38 pp.

Bojórquez, E., and Iervolino, I. [2011] "Spectral shape proxies and nonlinear structural response," *Soil Dynamics and Earthquake Engineering*, Vol. 31, No.7, pp. 996–1008.

Boore, D. M. [2010] "Orientation-independent, nongeometric-mean measures of seismic intensity from two horizontal components of motion," *Bulletin of the Seismological Society of America*, Vol. 100, No.4, pp. 1830–1835.

Boore, D. M., and Atkinson, G. M. [2008] "Ground-motion prediction equations for the average horizontal component of PGA, PGV, and 5%-damped PSA at spectral periods between 0.01 s and 10.0 s," *Earthquake Spectra*, Vol. 24, No.1, pp. 99–138.

Borg, R. C. [2015] "The deformation capacity of reinforced concrete elements subject to seismic loading : Determination of Empirical Equations for Assessment," *Ph.D. Thesis*, University College London.

Boyd, O. S. [2012] "Including Foreshocks and Aftershocks in Time-Independent Probabilistic Seismic-Hazard Analyses," *Bulletin of the Seismological Society of America*, Vol. 102, No.3, pp. 909–917.

Bradley, B. [2010] "A generalized conditional intensity measure approach and holistic ground-motion selection," *Earthquake Engineering and Structural Dynamics*, Vol. 39, No.12, pp. 1321–1342.

Bradley, B. A. [2013] "Practice-oriented estimation of the seismic demand hazard using ground

motions at few intensity levels," *Earthquake Engineering and Structural Dynamics*, Vol. 42, No.14, pp. 2167–2185.

Brendon A. Bradley. [2012] "The seismic demand hazard and importance of the conditioning intensity measure," *Earthquake Engineering and Structural Dynamics*, Vol. 41, pp. 1417–1437.

Camarillo, H. [2003] "Evaluation of Shear Strength Methodologies for Reinforced Concrete Columns," *M.Sc. Thesis*, University of Washington, Seattle.

Chu, A., Schoenberg, F. P., Bird, P., Jackson, D. D., and Kagan, Y. Y. [2011] "Comparison of ETAS parameter estimates across different global tectonic zones," *Bulletin of the Seismological Society of America*, Vol. 101, No.5, pp. 2323–2339.

Chung, A. I., Neighbors, C., Belmonte, A., Miller, M., Sepulveda, H. H., Christensen, C., Jakka, R. S., Cochran, E. S., and Lawrence, J. F. [2011] "The Quake-Catcher Network Rapid Aftershock Mobilization Program Following the 2010 M 8.8 Maule, Chile Earthquake," *Seismological Research Letters*, Vol. 82, No.4, pp. 526–532.

Console, R., Murru, M., and Lombardi, A. M. [2003] "Refining earthquake clustering models," *Journal of Geophysical Research: Solid Earth*, Vol. 108, No.March, pp. 1–9.

Cornell, C. A., and Winterstein, S. [1988] "Temporal and magnitude dependence in earthquake recurrence models," *Bulletin of Seismological Society of America*, Vol. 78, No.4, pp. 1522–1537.

Cornell, C. A. [1968] "Engineering Seismic Risk Analysis," *Bulletin of the Seismological Society of America*, Vol. 58, No.5, pp. 1583–1606.

Cornell, C. A., and Krawinkler, H. [2000] "Progress and challenges in seismic performance assessment," PEER Center News 3: 1–3.

Cosenza, E., and Manfredi, G. [2000] "Damage indices and damage measures," *Prog. Struct. Engng Mater.*, Vol. 2, pp. 50–59.

Cosenza, E., Manfredi, G., and Ramasco, R. [1993] "The use of damage functionals in earthquake engineering: A comparison between different methods," *Earthquake Engineering and Structural Dynamics*, Vol. 22, No.10, pp. 855–868.

Dascher-Cousineau, K., Brodsky, E. E., Lay, T., and Goebel, T. H. W. [2020] "What Controls Variations in Aftershock Productivity?," *Journal of Geophysical Research: Solid Earth*, Vol. 125, No.2.

Dávalos, H., and Miranda, E. [2019] "Evaluation of the scaling factor bias influence on the probability of collapse using SA(T1) as the intensity measure," *Earthquake Spectra*, Vol. 35,

No.2, pp. 679–702.

De Risi, M. T., Di Domenico, M., Manfredi, V., Terrenzi, M., Camata, G., Mollaioli, F., Noto, F., Ricci, P., Franchin, P., Masi, A., Spacone, E., and Verderame, G. M. [2022] "Modelling and Seismic Response Analysis of Italian pre-code and low-code Reinforced Concrete Buildings. Part I: Bare Frames," *Journal of Earthquake Engineering*, Vol. 27, No.6, pp. 1482–1513.

Di Sarno, L., Yenidogan, C., and Erdik, M. [2013] "Field evidence and numerical investigation of the Mw = 7.1 October 23 Van, Tabanli and the Mw > 5.7 November earthquakes of 2011," *Bulletin of Earthquake Engineering*, Vol. 11, No.1, pp. 313–346.

Di Trapani, F., and Malavisi, M. [2019] "Seismic fragility assessment of infilled frames subject to mainshock/aftershock sequences using a double incremental dynamic analysis approach," *Bulletin of Earthquake Engineering*, Vol. 17, No.1, pp. 211–235.

DM. [1996] "Norme tecniche per il calcolo, l'esecuzione ed il collaudo delle strutture in c.a. normale e precompresso e per le strutture metalliche."

Du, W., Long, S., and Ning, C. L. [2019] "An Algorithm for Selecting Spatially Correlated Ground Motions at Multiple Sites under Scenario Earthquakes," *Journal of Earthquake Engineering*, Vol. 2469.

Earthquake Engineering Field Investigation Team EEFIT [2011] "The Mw 6.1 Christchurch, New Zealand earthquake of 22 February 2011: A field report," Institution of Structural Engineers, London.

Elwood, K. J. [2004] "Modelling failures in existing reinforced concrete columns," *Canadian Journal of Civil Engineering*, Vol. 31, No.5, pp. 846–859.

Elwood, K. J., and Eberhard, M. O. [2006] "Effective Stiffness of Reinforced Concrete Columns," *Research Digest No. 2006-1 A publication of the Pacific Earthquake Engineering Research C*, pp. 1–5.

Elwood, K. J., Eeri, M., Moehle, J. P., and Eeri, M. [2005] "Drift Capacity of Reinforced Concrete Columns with Light Transverse Reinforcement," *Earthquake Spectra*, Vol. 21, No.1, pp. 71–89.

Felzer, K. R., Abercrombie, R. E., and Ekström, G. [2003] "Secondary aftershocks and their importance for aftershock forecasting," *Bulletin of the Seismological Society of America*, Vol. 93, No.4, pp. 1433–1448.

FEMA [2012] "Seismic Performance Assessment of Buildings, FEMA P-58-1," *Applied Technology Council for the Federal Emergency Management Agency*.

Feng, D. C., Liu, Z. T., Wang, X. D., Jiang, Z. M., and Liang, S. X. [2020] "Failure mode classification and bearing capacity prediction for reinforced concrete columns based on ensemble machine learning algorithm," *Advanced Engineering Informatics*, Vol. 45, No.April, p. 101126.

Field, E. H., Arrowsmith, R. J., Biasi, G. P., Bird, P., Dawson, T. E., Felzer, K. R., Jackson, D. D., Johnson, K. M., Jordan, T. H., Madden, C., Michael, A. J., Milner, K. R., Page, M. T., Parsons, T., Powers, P. M., Shaw, B. E., Thatcher, W. R., Weldon, R. J., and Zeng, Y. [2014] "Uniform California Earthquake Rupture Forecast, version 3 (UCERF3) -The time-independent model," *Bulletin of the Seismological Society of America*, Vol. 104, No.3, pp. 1122–1180.

Field, E. H., and Milner, K. R. [2018] "Candidate products for operational earthquake forecasting illustrated using the haywired planning scenario, including one very quick (and not-so-dirty) hazard-map option," *Seismological Research Letters*, Vol. 89, No.4, pp. 1420–1434.

Fitzenz, D., and Langenbruch, C. [2021] "A Three Kernel Approach to Earthquake Source Modeling : Incorporating Incomplete or Low Resolution Seismicity , Fault and Deformation Datasets in Continental China," *Annual Meeting of the Seismological Society of America*.

Frankel, A. [1995] "Mapping seismic hazard in the central and eastern United States," *Seismological Research Letters*, Vol. 66, No.4, pp. 8–21.

Gallagher, R. P., Reasenberg, P. A., and Poland, C. D. [1999] "Earthquake aftershocks-Entering damaged buildings," *Applied Technology Council*.

Galvis, F. A., Hulsey, A. M., Baker, J. W., and Deierlein, G. G. [2023] "Simulation-based methodology to identify damage indicators and safety thresholds for post-earthquake evaluation of structures," *Earthquake Engineering and Structural Dynamics*, Vol. 52, pp. 3455–3476.

Gardner, J. K., and Knopoff, L. [1974] "Is the sequence of earthquakes in southern California with aftershocks removed, Poissonian?," *Bulletin of the Seismological Society of America*, Vol. 64, No.5, pp. 1363–1367.

Ge, X., Kashani, M. M., Sun, Z., Yang, Y., and Alexander, N. A. [2022] "Exploring the performance of experimentally benchmarked RC bridge pier models when subjected to sequential seismic shocks," *Structures*, Vol. 45, No.2022, pp. 1530–1543.

Gee, R., Peruzza, L., and Pagani, M. [2021] "The power of the little ones: Computed and observed aftershock hazard in Central Italy," *Earthquake Spectra*, Vol. 38, No.1, pp. 702–724.

Ghotbi, A. R., and Taciroglu, E. [2020] "Conditioning criteria based on multiple intensity measures for selecting hazard-consistent aftershock ground motion records," *Soil Dynamics and Earthquake Engineering*, Vol. 139, No.2020, p. 106345.

Goda, K. [2012] "Nonlinear response potential of Mainshock-Aftershock sequences from Japanese earthquakes," *Bulletin of the Seismological Society of America*, Vol. 102, No.5, pp. 2139–2156.

Goda, K., Pomonis, A., Chian, S. C., Offord, M., Saito, K., Sammonds, P., Fraser, S., Raby, A., and Macabuag, J. [2013] "Ground motion characteristics and shaking damage of the 11th March 2011 Mw 9.0 Great East Japan earthquake," *Bulletin of Earthquake Engineering*, Vol. 11, No.1, pp. 141–170.

Goda, K., and Taylor, C. A. [2012] "Effects of aftershocks on peak ductility demand due to strong ground motion records from shallow crustal earthquakes," *Earthquake Engineering and Structural Dynamics*, Vol. 41, pp. 2311–2330.

Hainzl, S., Brietzke, G. B., and Zöller, G. [2010] "Quantitative earthquake forecasts resulting from static stress triggering," *Journal of Geophysical Research: Solid Earth*, Vol. 115, No.11, pp. 1–9.

Hainzl, S., Zakharova, O., and Marsan, D. [2013] "Impact of aseismic transients on the estimation of aftershock productivity parameters," *Bulletin of the Seismological Society of America*, Vol. 103, No.3, pp. 1723–1732.

Hancock, J., and Bommer, J. J. [2005] "The effective number of cycles of earthquake ground motion," *Earthquake Engineering and Structural Dynamics*, Vol. 34, No.2005, pp. 637–664.

Hardebeck, J. L., Llenos, A. L., Michael, A. J., Page, M. T., and van der Elst, N. [2019] "Updated California aftershock parameters," *Seismological Research Letters*, Vol. 90, No.1, pp. 262–270.

Haselton, C. B., Liel, A. B., and Deierlein, G. G. [2007] "Seismic Collapse Safety and Behavior of Modern Reinforced Concrete Moment Frame Buildings," *Structural Engineering Research Frontiers.*

Haselton, C., Liel, A. B., Lange, S. T., and Deierlein, G. G. [2007] "Beam-Column Element Model Calibrated for Predicting Flexural Response Leading to Global Collapse of RC Frame Buildings, " *Pacific Earthquake Engineering Research Center PEER.*

Hatzigeorgiou, G. D., and Beskos, D. E. [2009] "Inelastic displacement ratios for SDOF structures subjected to repeated earthquakes," *Engineering Structures*, Vol. 31, No.11, pp. 2744–2755.

Hatzigeorgiou, G. D., and Liolios, A. A. [2010] "Nonlinear behaviour of RC frames under repeated strong ground motions," *Soil Dynamics and Earthquake Engineering*, Vol. 30, No.10, pp. 1010–1025.

Henkhaus, K., Pujol, S., and Ramirez, J. [2013] "Axial Failure of Reinforced Concrete Columns Damaged by Shear Reversals," *Journal of Structural Engineering*, Vol. 139, No.7, pp. 1172–1180.

Herak, M. [2020] "Conversion between the local magnitude (Ml) and the moment magnitude (mw) for earthquakes in the croatian earthquake catalogue," *Geofizika*, Vol. 37, No.2, pp. 197–211.

Ibarra, L. F., Medina, R. A., and Krawinkler, H. [2005] "Hysteretic models that incorporate strength and stiffness deterioration," *Earthquake Engineering and Structural Dynamics*, Vol. 34, pp. 1489–1511.

Iervolino, I., Giorgio, M., and Chioccarelli, E. [2016] "Markovian modeling of seismic damage accumulation," *Earthquake Engineering and Structural Dynamics*, Vol. 45, pp. 441–461.

Iervolino, I., Giorgio, M., and Polidoro, B. [2014] "Sequence-based probabilistic seismic hazard analysis," *Bulletin of the Seismological Society of America*, Vol. 104, No.2, pp. 1006–1012.

Iñarritu, P. G. de Q., Šipčić, N., Kohrangi, M., and Bazzurro, P. [2021] "Effects of Pre-existing Damage on Fragility of URM and RC Frame Buildings," in *Energy-based Seismic Engineering*. IWEBSE. Lecture Notes in Civil Engineering (Cham: Springer). Vol. 155.

Iñarritu, P. G. de Q., Šipčić, N., Alvarez-Sanchez, L., Kohrangi, M., and Bazzurro, P. [2023] "A closer look at hazard- consistent ground motion record selection for building- specific risk assessment : Effect of soil characteristics and accelerograms ' scaling," *Earthquake Spectra*, Vol. 00, No.0, pp. 1–38.

Jalayer, F. [2003] "Direct Probabilistic Seismic Analysis : Implementing Non-Linear Dynamic Assessments," *Ph.D. Thesis*, Department of Civil and Environmental Engineering, Stanford University.

Jalayer, F., and Ebrahimian, H. [2016] "Seismic risk assessment considering cumulative damage due to aftershocks," *Earthquake Engineering and Structural Dynamics*, Vol. 46, No.3, pp. 369–389.

Jayaram, N., and Baker, J. W. [2008] "Statistical tests of the joint distribution of spectral acceleration values," *Bulletin of the Seismological Society of America*, Vol. 98, No.5, pp. 2231–2243.

Jayaram, N., Lin, T., and Baker, J. W. [2011] "A Computationally efficient ground-motion selection algorithm for matching a target response spectrum mean and variance," *Earthquake Spectra*, Vol. 27, No.3, pp. 797–815.

Jeon, J.S. [2013] "Aftershock vulnerability assessment of damaged reinforced concrete buildings in California," *Ph.D. Thesis*, Georgia Institute of Technology.

Jeon, J.S., DesRoches, R., Lowes, L. N., and Brilakis, I. [2015] "Framework of aftershock fragility assessment-case studies: older California reinforced concrete building frames," *Earthquake Engineering and Structural Dynamics*, Vol. 44, No.15, pp. 2617–2636.

Jeon, J. S., Mangalathu, S., Song, J., and Desroches, R. [2019] "Parameterized Seismic Fragility Curves for Curved Multi-frame Concrete Box-Girder Bridges Using Bayesian Parameter Estimation," *Journal of Earthquake Engineering*, Vol. 23, No.6, pp. 954–979.

Kazama, M., and Noda, T. [2012] "Damage statistics (Summary of the 2011 off the Pacific Coast of Tohoku Earthquake damage)," *Soils and Foundations*, Vol. 52, No.5, pp. 780–792.

Kiani, J., Camp, C., and Pezeshk, S. [2018] "On the number of required response history analyses," *Bulletin of Earthquake Engineering*, Vol. 16, No.11, pp. 5195–5226.

Kohrangi, M., Bazzurro, P., and Vamvatsikos, D. [2016] "Vector and scalar IMs in structural response estimation, Part II: Building demand assessment," *Earthquake Spectra*, Vol. 32, No.3, pp. 1525–1543.

Kohrangi, M., Bazzurro, P., Vamvatsikos, D., and Spillatura, A. [2017] "Conditional spectrum-based ground motion record selection using average spectral acceleration," *Earthquake Engineering and Structural Dynamics*, Vol. 44, pp. 657–675.

Kohrangi, M., Vamvatsikos, D., and Bazzurro, P. [2017] "Site dependence and record selection schemes for building fragility and regional loss assessment," *Earthquake Engineering and Structural Dynamics*, Vol. 46, No.10, pp. 1625–1643.

Kunnath, S. K., El-Bahy, A., Taylor, A. W., and Stone, W. C. [1997] "Cumulative seismic damage of reinforced concrete bridge piers," Report No. NCEER-97–0006. Buffalo, NY: *National Center for Earthquake Engineering Research*, State University of New York at Buffalo.

Kunnath, S. K., Reinhorn, A. M., and Abel, J. F. [1991] "A computational tool for evaluation of seismic performance of reinforced concrete buildings," *Computers and Structures*, Vol. 41, No.1, pp. 157–173.

Lanzano, G., Sgobba, S., Luzi, L., Puglia, R., Pacor, F., Felicetta, C., D'Amico, M., Cotton, F., and Bindi, D. [2019] "The pan-European Engineering Strong Motion (ESM) flatfile: compilation criteria and data statistics," *Bulletin of Earthquake Engineering*, Vol. 17, No.2, pp. 561–582.

Leborgne, M. R., and Ghannoum, W. M. [2013] "Analytical Element for Simulating Lateral-Strength Degradation in Reinforced Concrete Columns and Other Frame Members," *Journal of Structural Engineering,* ASCE, 140(7), 04014038 04014031–04014012.

Lee, C. S., and Han, S. W. [2018] "Computationally effective and accurate simulation of cyclic backbone of old reinforced concrete columns," *Engineering Structures*, Vol. 173, pp. 892–907.

Li, Y. [2012] "The shaking table tests column database and evaluation of drift capacity models for non-ductile columns," *M.Sc. Thesis*, THE UNIVERSITY OF BRITISH COLUMBIA.

Li, Y., Song, R., and Van De Lindt, J. W. [2014] "Collapse fragility of steel structures subjected to earthquake mainshock-aftershock sequences," *Journal of Structural Engineering*, Vol. 140, No.12, p. 4014095.

Lignos, D. G., and Krawinkler, H. [2011] "Deterioration Modeling of Steel Components in Support of Collapse Prediction of Steel Moment Frames under Earthquake Loading," *Journal of Structural Engineering*, Vol. 137, No.11, pp. 1291–1302.

Lilliefors, H. W. [1969] "On the Kolmogorov-Smirnov Test for the Exponential Distribution with Mean Unknown," *Journal of the American Statistical Association,* Vol. 64, No.325, pp. 387–389.

Lin, T., Harmsen, S. C., Baker, J. W., and Luco, N. [2013] "Conditional spectrum computation incorporating multiple causal earthquakes and ground-motion prediction models," *Bulletin of the Seismological Society of America*, Vol. 103, No.2 A, pp. 1103–1116.

Llenos, A. L., and Michael, A. J. [2020] "Regionally optimized background earthquake rates from ETAS (Robere) for probabilistic seismic hazard assessment," *Bulletin of the Seismological Society of America*, Vol. 110, No.3, pp. 1172–1190.

Lolli, B., Randazzo, D., Vannucci, G., and Gasperini, P. [2020] "The Homogenized Instrumental Seismic Catalog (HORUS) of Italy from 1960 to Present," *Seismological Research Letters, XX*, pp. 1–15.

Lombardi, A. M. [2017] "The epistemic and aleatory uncertainties of the ETAS-type models: An application to the Central Italy seismicity," *Scientific Reports*, Springer US, Vol. 7, No.1, pp. 1–9.

Lombardi, A. M., and Marzocchi, W. [2007] "Evidence of clustering and nonstationarity in the time distribution of large worldwide earthquakes," *Journal of Geophysical Research: Solid Earth*, Vol. 112, No.B02303.

Luco, N., and Bazzurro, P. [2007] "Does amplitude scaling of ground motion records result in biased nonlinear structural drift responses?," *Earthquake Engineering and Structural Dynamics*, Vol. 12, pp. 1813–1835.

Luco, N., Bazzurro, P., and Cornell, C. A. [2004] "Dynamic versus static computation of the residual capacity of a mainshock-damaged building to withstand an aftershock.," *13th World Conference on Earthquake Engineering,* Vancouver, Canada.

Luen, B., and Stark, P. B. [2012] "Declustering and Poisson Tests," *Geophysical Journal International*, Vol. 189, No.1, pp. 691–700.

Lynn, A. C., Moehle, J. P., Mahin, S. A., and Holmes, W. T. [1996] "Seismic evaluation of existing

reinforced concrete building columns," *Earthquake Spectra*, Vol. 12, No.4, pp. 715–739.

Manabu, Y., Yoshikazu, T., and Nakamura, T. [2004] "Axial Collapse of Reinforced Concrete Columns," *13th World Conference on Earthquake Engineering*, Vancouver, Canada.

Mancini, S., and Marzocchi, W. [2023] "SimplETAS: A Benchmark Earthquake Forecasting Model Suitable for Operational Purposes and Seismic Hazard Analysis," *Seismological Research Letters*. XX, pp. 1–12.

Mangalathu, S., and Jeon, J. [2019] "Machine Learning – Based Failure Mode Recognition of Circular Reinforced Concrete Bridge Columns : Comparative Study," *Journal of Structural Engineering,* Vol. 145, No.10, pp. 04019104.

Marsan, D., and Helmstetter, A. [2017] "How variable is the number of triggered aftershocks?," *Journal of Geophysical Research: Solid Earth*, Vol. 122, No.7, pp. 5544–5560.

Marzocchi, W., Spassiani, I., Stallone, A., and Taroni, M. [2020] "How to be fooled searching for significant variations of the b-value," *Geophysical Journal International*, Oxford University Press, Vol. 220, No.3, pp. 1845–1856.

Marzocchi, W., and Taroni, M. [2014] "Some thoughts on declustering in probabilistic seismic-hazard analysis," *Bulletin of the Seismological Society of America*, Vol. 104, No.4, pp. 1838–1845.

McNally, K. C., González-Ruiz, J. R., and Stolte, C. [1986] "Seismogenesis of the 1985 great (MS=8.1) Michoacan, Mexico earthquake," *Geophysical Research Letters*. Vol. 13, No.6, pp. 585–588.

Meletti, C., Marzocchi, W., D'Amico, V., Lanzano, G., Luzi, L., Martinelli, F., Pace, B., Rovida, A., Taroni, M., Visini, F., and Group, M. W. [2021] "The new Italian seismic hazard model (MPS19)," *Annals of Geophysics*, Vol. 64, No.1.

Mizrahi, L., Nandan, S., and Wiemer, S. [2021] "The Effect of Declustering on the Size Distribution of Mainshocks," *Seismological Research Letters,* Vol. XX, pp. 1–10.

Mo, Y. L., and Wang, S. J. [2000] "Seismic behavior of RC columns with various tie configurations," *Journal of Structural Engineering*, Vol. 126, No.10, pp. 1122–1130.

Molchan, G. M., and Dmitrieva, O. E. [1992] "Aftershock identification: methods and new approaches," *Geophysical Journal International*, Vol. 109, No.3, pp. 501–516.

Nandan, S., Ouillon, G., Wiemer, S., and Sornette, D. [2017] "Objective estimation of spatially variable parameters of epidemic type aftershock sequence model: Application to California," *Journal of Geophysical Research: Solid Earth*, Vol. 122, No.7, pp. 5118–5143.

O'Reilly, G. J. [2021] "Seismic intensity measures for risk assessment of bridges," *Bulletin of Earthquake Engineering*, Vol. 19, pp. 3671–3699.

O'Reilly, G. J., and Sullivan, T. J. [2019] "Modeling Techniques for the Seismic Assessment of the Existing Italian RC Frame Structures," *Journal of Earthquake Engineering*, Vol. 23, No.8, pp. 1262–1296.

Ogata, Y. [1988] "Statistical Models for Earthquake Occurrences and Residual Analysis for Point Processes," *American Statistical Association*, Vol. 83, No.401, pp. 9–27.

Ogata, Y. [1998] "Space-Time Point-Process Models for Earthquake Occurrences," *Annals of the Institute of Statistical Mathematics*, Vol. 50, No.2, pp. 379–402.

Ogata, Y., and Zhuang, J. [2006] "Space-time ETAS models and an improved extension," *Tectonophysics*, Vol. 413, No.2006, pp. 13–23.

Omori, F. [1894] "On the Aftershocks of Earthquake," *Journal of the College of Science, Imperial University of Tokyo*, Vol. 7, pp. 111–200.

Orlacchio, M., Chioccarelli, E., Baltzopoulos, G., and Iervolino, I. [2021] "State-Dependent Seismic Fragility Functions for Italian Reinforced Concrete Structures: Preliminary Results," *Proceedings of the 31st European Safety and Reliability Conference*, pp. 1591–1598.

Pagani, M., Monelli, D., Weatherill, G., Danciu, L., Crowley, H., Henshaw, P., Butler, L., Nastasi, M., Panzeri, L., Simionato, M., and Vigano, D. [2014] "OpenQuake Engine : An Open Hazard (and Risk) Software for the Global Earthquake Model," *Seismological Research Letters*, Vol. 85, No.3, pp. 692–702.

Page, M. T., and van der Elst, N. J. [2018] "Turing-Style Tests for UCERF3 Synthetic Catalogs," *Bulletin of the Seismological Society of America*, Vol. XX, No.Xx, pp. 1–13.

Page, M. T., van Der Elst, N., Hardebeck, J., Felzer, K., and Michael, A. J. [2016] "Three ingredients for improved global aftershock forecasts: Tectonic region, time-dependent catalog incompleteness, and intersequence variability," *Bulletin of the Seismological Society of America*, Vol. 106, No.5, pp. 2290–2301.

Pagni, C. A., and Lowes, L. N. [2006] "Fragility functions for older reinforced concrete beam-column joints," *Earthquake Spectra*, Vol. 22, No.1, pp. 215–238.

Panagiotakos, T. B., and Fardis, M. N. [2001] "Deformations of Reinforced Concrete Members at Yielding and Ultimate," *ACI Structural Journal*, Vol. 98, No.2, pp. 135–148.

Papadopoulos, A., Kohrangi, M., and Bazzurro, P. [2020] "Mainshock-consistent ground motion

record selection for aftershock sequences," *Earthquake Engineering and Structural Dynamics*, Vol. 49, No.8, pp. 754–771.

Papadopoulos, A., Bazzurro, P., and Marzocchi, W. [2021] "Exploring probabilistic seismic risk assessment accounting for seismicity clustering and damage accumulation: Part I. Hazard analysis," *Earthquake Spectra*, Vol. 37, No.2, pp. 803–826.

Papadopoulos, A., Kohrangi, M., and Bazzurro, P. [2019] "Correlation of spectral acceleration values of mainshock-aftershock ground motion pairs," *Earthquake Spectra*, Vol. 55, No.1, pp. 39–60.

Park, B. Y., and Ang, A. H.-S. [1985] "Mechanistic seismic damage model for reinforced concrete," *Journal of Structural Engineering*, Vol. 1111, pp. 722–739.

Park, Y. J., Ang, A. H. S., and Wen, Y. K. [1987] "Damage-Limiting Aseismic Design of Buildings," *Earthquake Spectra*, Vol. 3, No.1, pp. 1–26.

Pedone, L., Gentile, R., Galasso, C., and Pampanin, S. [2023] "Energy-based procedures for seismic fragility analysis of mainshock-damaged buildings," *Frontiers in Built Environment*, 9:1183699.

Peresan, A., and Gentili, S. [2020] "Identification and characterisation of earthquake clusters : a comparative analysis for selected sequences in Italy and adjacent regions," *Bollettino di Geofisica Teorica ed Applicata*, Vol. 61, No.1, pp. 57–80.

Perus, I., Biskinis, D., Fajfar, P., Fardis, M. N., Grammatikou, S., Krawinkler, H., and Lignos, D. [2014] "The SERIES database of RC elements," *2nd European Conference on Earthquake Engineering and Seismology*, Istanbul, Turkey.

Petersen, M. D., Shumway, A. M., Powers, P. M., Mueller, C. S., Moschetti, M. P., Frankel, A. D., Rezaeian, S., McNamara, D. E., Luco, N., Boyd, O. S., Rukstales, K. S., Jaiswal, K. S., Thompson, E. M., Hoover, S. M., Clayton, B. S., Field, E. H., and Zeng, Y. [2020] "The 2018 update of the US National Seismic Hazard Model: Overview of model and implications," *Earthquake Spectra*, Vol. 36, No.1, pp. 5–41.

Petracca, M., Candeloro, F., and Camata, G. [2017] "STKO User Manual," Pescara: ASDEA Software Technology.

Porter, K., Kennedy, R., and Bachman, R. [2006] "Developing Fragility Functions for Building Components for ATC-58, " Redwood City, California, USA.

Raghunandan, M., Liel, A. B., and Luco, N. [2015] "Aftershock collapse vulnerability assessment of reinforced concrete frame structures," *Earthquake Engineering and Structural Dynamics*, Vol. 44, No.3, pp. 419–439.

Reasenberg, P. [1985] "Second-Order Moment of Central California Seismicity, 1969-1982," *Journal of Geophysical Research*, Vol. 90, No.B7, pp. 5479–5495.

Reasenberg, P. A., and Jones, L. M. [1989] "Earthquake Hazard After a Mainshock in California," *Science*, Vol. 243, No.4895, pp. 1173–1176.

Ribeiro, F. L. A., and Barbosa, A. R. [2015] "General implementation of Modified Ibarra- Medina-Krawinkler models for concentrated plasticity models and finite length plasticity," *OpenSees Days*, Fisciano, Italy.

Rossetto, T., and Elnashai, A. [2003] "Derivation of vulnerability functions for European-type RC structures based on observational data," *Engineering Structures*, Vol. 25, No.10, pp. 1241–1263.

Rovida, A., Locati, M., Camassi, R., Lolli, B., and Gasperini, P. [2020] "The Italian earthquake catalogue CPTI15, " *Bulletin of Earthquake Engineering*, Vol. 18, pp. 2953–2984.

Ruiz-García, J., and Negrete-Manriquez, J. C. [2011] "Evaluation of drift demands in existing steel frames under as-recorded far-field and near-fault mainshock-aftershock seismic sequences," *Engineering Structures*, Vol. 33, No.2, pp. 621–634.

Ryu, H., Luco, N., Uma, S. R., and Liel, A. B. [2011] "Developing fragilities for mainshock-damaged structures through incremental dynamic analysis," *Proceedings of the Ninth Pacific Conference on Earthquake Engineering*, Auckland, New Zealand.

Savage, W. U. [1972] "Microearthquake clustering near Fairview Peak, Nevada, and in the Nevada Seismic Zone," *Journal of Geophysical Research*, Vol. 77, No.35, pp. 7049–7056.

Seif, S., Mignan, A., Zechar, J. D., Werner, M. J., and Wiemer, S. [2017] "Estimating ETAS: The effects of truncation, missing data, and model assumptions," *Journal of Geophysical Research: Solid Earth*, Vol. 122, No.1, pp. 449–469.

Sextos, A., De Risi, R., Pagliaroli, A., Foti, S., Passeri, F., Ausilio, E., Cairo, R., Capatti, M. C., Chiabrando, F., Chiaradonna, A., Dashti, S., De Silva, F., Dezi, F., Durante, M. G., Giallini, S., Lanzo, G., Sica, S., Simonelli, A. L., and Zimmaro, P. [2018a] "Local site effects and incremental damage of buildings during the 2016 Central Italy Earthquake sequence," *Earthquake Spectra*, Vol. 34, No.4, pp. 1639–1669.

Sezen, H. [2000] "Seismic Behavior and Modeling of Reinforced Concrete Building Columns," *Ph.D. Thesis*, University of California, Berkeley.

Sezen, H., and Moehle, J. P. [2004] "Shear Strength Model for Lightly Reinforced Concrete Columns," *Journal of Structural Engineering*, Vol. 130, No.11, pp. 1692–1703.

Sgobba, S., Felicetta, C., Lanzano, G., Ramadan, F., and Amico, M. D. [2021] "NESS2.0 : An Updated Version of the Worldwide Dataset for Calibrating and Adjusting Ground- Motion Models in Near Source," *Bulletin of Seismological Society of America*, Vol. 11, No.5, pp. 2358-2378.

Shcherbakov, R., Nguyen, M., and Quigley, M. [2012] "Statistical analysis of the 2010 M w 7.1 Darfield earthquake aftershock sequence," *New Zealand Journal of Geology and Geophysics*, Vol. 55, No.3, pp. 305–311.

Shcherbakov, R., Turcotte, D. L., and Rundle, J. B. [2005] "Aftershock statistics," *Pure and Applied Geophysics*, Vol. 162, No.6–7, pp. 1051–1076.

Shin, T. [2000] "Some Seismological Aspects of the 1999 Chi-Chi Earthquake in Taiwan," *TAO*, Vol. 11, No.3, pp. 555–566.

Shokrabadi, M., and Burton, H. V. [2018] "Risk-based assessment of aftershock and mainshock-aftershock seismic performance of reinforced concrete frames," *Structural Safety*, Vol. 73, No.2018, pp. 64–74.

Shome, N., and Cornell, C. A. [1999] "Probabilistic Seismic Demand Analysis of Nonlinear Structures," *Program Technical Report RMS-35*. John A. Blume Earthquake Engineering Centre, Department of Civil and Environmental Engineering, Stanford University.

Shome, N., Cornell, C. A., Bazzurro, P., and Eduardo Carballo. [1998] "Earthquakes, records and nonlinear responses," *Earthquake Spectra*, Vol. 14, No.3, pp. 469–500.

Shome, N., and Williams, C. [2014] "Aftershock risk in Japan following Tohoku earthquake," *Proceedings of the 10th US National Conference on Earthquake Engineering,* Anchorage, Alaska.

Šipčić, N., Kohrangi, M., Papadopoulos, A. N., Marzocchi, W., and Bazzurro, P. [2022] "The Effect of Seismic Sequences in Probabilistic Seismic Hazard Analysis," *Bulletin of the Seismological Society of America*, No.Xx, pp. 1–16.

Sivaramakrishnan, B. [2010] "Non-linear modeling parameters for reinforced concrete columns subjected to seismic loads," *M.Sc. Thesis*, The University of Texas at Austin.

Spacone, E. [1996] "Fibre beam-column model for non-linear analysis of RC frames : part II. Applications," *Earthquake Engineering and Structural Dynamics*, Vol. 25, pp. 727–742.

Spassiani, I., and Marzocchi, W. [2018] "How likely does an aftershock sequence conform to a single Omori law behavior?," *Seismological Research Letters*, Vol. 89, No.3, pp. 1118–1128.

Spillatura, A., Kohrangi, M., Bazzurro, P., and Vamvatsikos, D. [2021] "Conditional spectrum record selection faithful to causative earthquake parameter distributions," *Earthquake Engineering and*

Structural Dynamics, Vol. 50, No.10, pp. 2653–2671.

Stallone, A., and Marzocchi, W. [2019] "Features of seismic sequences are similar in different crustal tectonic regions," *Bulletin of the Seismological Society of America*, Vol. 109, No.5, pp. 1594–1604.

Stiphout, T. Van, Zhuang, J., Marsan, D., Service, S. S., and Zurich, E. T. H. [2012] "Theme V – Models and Techniques for Analyzing Seismicity Seismicity Declustering," *Community Online Resource for Statistical Seismicity Analysis*.

Tanaka, H. [1990] "Effect of lateral confining reinforcement on the ductile behaviour of reinforced concrete columns," *Ph.D. Thesis*, University of Canterbury.

Tarbali, K., and Bradley, B. A. [2016] "The effect of causal parameter bounds in PSHA-based ground motion selection," *Earthquake Engineering and Structural Dynamics*, Vol. 45, No.9, pp. 1515–1535.

Taroni, M., Marzocchi, W., Schorlemmer, D., Werner, M. J., Wiemer, S., Zechar, J. D., Heiniger, L., and Euchner, F. [2018] "Prospective CSEP evaluation of 1-Day, 3-month, and 5-Yr earthquake forecasts for Italy," *Seismological Research Letters*, Vol. 89, No.4, pp. 1251–1261.

Taucer, F. F., Spacone, E., and Filippou, F. C. [1991] "A Fiber Beam-Column Element for Seismic Response Analysis of Reinforced Concrete Structures," *Earthquake Engineering Research Center College of Engineering,* Report No. UCB/EERC-91/17, University of California, Berkeley.

Teng, B. G., and Baker, J. W. [2019] "Seismicity declustering and hazard analysis of the Oklahoma–Kansas Region," *Bulletin of the Seismological Society of America*, Vol. 109, No.6, pp. 2356–2366.

Thun, J. L. Von, Roehm, L. H., a. Scott, G., and Wilson, J. A. [1988] "Earthquake ground motions for design and analysis of dams," *Geotechnical special publication*, Vol. 20, pp. 463–481.

Tsalouchidis, K. T., and Adam, C. [2022] "Amplitude scaling of ground motions as a potential source of bias: Large-scale investigations on structural drifts," *Earthquake Engineering and Structural Dynamics*, Vol. 57, pp. 2904–2924.

Umehara, H., and Jirsa, J. O. [1982] "*Shear Strength and Deterioration of Short Reinforced Concrete Columns Under Cyclic Deformations*," *PMFSEL Report No. 82-3,* Department of Civil Engineering, University of Texas at Austin.

Utsu, T. [1961] "A statistical study on the occurrence of aftershocks," *Geophysical magazine*, Vol. 30, No.4, pp. 521–605.

Utsu, T. [1966] "A Statistical Significance Test of the Difference in b-value between Two Earthquake Groups," *Journal of Physics of the Earth*, Vol. 14, No.2, pp. 37–40.

Utsu, T., and Ogata, Y. [1995] "The centenary of the Omori formula for a decay law of aftershock activity," *Journal of Physics of the Earth*, Vol. 43, No.1, pp. 1–33.

Vamvatsikos, D., and Cornell, C. A. [2002] "Incremental Dynamic Analysis," *Earthquake Engineering and Structural Dynamics,* Vol. 31, No.3, pp. 491–514.

Van Houtte, C., Bannister, S., Holden, C., Bourguignon, S., and Mcverry, G. [2017] "The New Zealand strong motion database," *Bulletin of the New Zealand Society for Earthquake Engineering*, Vol. 50, No.1, pp. 1–20.

Wang, Q., Jackson, D. D., and Zhuang, J. [2010] "Missing links in earthquake clustering models," *Geophysical Research Letters*, Vol. 37, No.21, pp. 1–5.

Wei, H., Asce, S. M., Shohet, I. M., Skibniewski, J., Asce, M., and Shapira, S. [2016] "Assessing the Lifecycle Sustainability Costs and Benefits of Seismic Mitigation Designs for Buildings," *Journal of Architectural Engineering*, Vol. 22, No.1, pp. 1–13.

Wells, D. L., and Coppersmith, K. J. [1994] "New empirical relationships among magnitude, rupture length, rupture width, rupture area, and surface displacement," *Bulletin of Seismological Society of America*, Vol. 84, No.4, pp. 974–1002.

Wen, W., Zhai, C., Ji, D., Li, S., and Xie, L. [2017] "Framework for the vulnerability assessment of structure under mainshock-aftershock sequences," *Soil Dynamics and Earthquake Engineering*, Vol. 101, pp. 41–52.

Wiemer, S. [2000] "Introducing probabilistic aftershock hazard mapping," *Geophysical Research Letters*, Vol. 27, No.20, pp. 3405–3408.

Woessner, J., Laurentiu, D., Giardini, D., Crowley, H., Cotton, F., Valensise, G., Arvidsson, R., Basili, R., Hiemer, S., Meletti, C., Musson, R. W., Rovida, A. N., Sesetyan, K., and Stucchi, M. [2015] "The 2013 European Seismic Hazard Model : key components and results," *Bulletin of Earthquake Engineering*, Vol. 13, No.12, pp. 3553–3596.

Yeo, G. L., and Cornell, C. A. [2009] "A probabilistic framework for quantification of aftershock ground-motion hazard in California : Methodology and parametric study," *Earthquake Engineering and Structural Dynamics*, Vol. 38, pp. 45–60.

Zaliapin, I., and Ben-Zion, Y. [2016] "A global classification and characterization of earthquake clusters," *Geophysical Journal International*, Vol. 207, No.1, pp. 608–634.

Zaliapin, I., and Ben-Zion, Y. [2020] "Earthquake Declustering Using the Nearest-Neighbor Approach in Space-Time-Magnitude Domain," *Journal of Geophysical Research: Solid Earth*, Vol. 125, No.4, pp. 0–2.

Zaliapin, I., Gabrielov, A., Keilis-Borok, V., and Wong, H. [2008] "Clustering Analysis of Seismicity and Aftershock Identification," *Physical Review Letters*, Vol. 101, No.01, p. 015801.

Zeris, C. A., and Mahin, S. A. [1991] "Behavior of Reinforced Concrete Structures Subjected to Biaxial Excitation," *Journal of Structural Engineering*, Vol. 117, No.9, pp. 2657–2673.

Zhai, C. H., Wen, W. P., Li, S., Chen, Z. Q., Chang, Z., and Xie, L. L. [2014] "The damage investigation of inelastic SDOF structure under the mainshock-aftershock sequence-type ground motions," *Soil Dynamics and Earthquake Engineering*, Elsevier, Vol. 59, pp. 30–41.

Zhang, L., Werner, M. J., and Goda, K. [2020] "Variability of ETAS Parameters in Global Subduction Zones and Applications to Mainshock – Aftershock Hazard Assessment," *Bulletin of Seismological Society of America,* Vol. XX, pp. 0–0.

Zhang, Y., Burton, H. V., Sun, H., and Shokrabadi, M. [2018] "A machine learning framework for assessing post-earthquake structural safety," *Structural Safety*, Vol. 72, pp. 1–16.

Zhu, R. G., Lu, D. G., Yu, X. H., and Wang, G. Y. [2017] "Conditional mean spectrum of aftershocks," *Bulletin of the Seismological Society of America*, Vol. 107, pp. 1940–1953.

Zhuang, J., Ogata, Y., and Vere-Jones, D. [2004] "Analyzing earthquake clustering features by using stochastic reconstruction," *Journal of Geophysical Research: Solid Earth*, Vol. 109, No.5, pp. 1–17.

Zhuang, J., Ogata, Y., and Wang, T. [2017] "Data completeness of the Kumamoto earthquake sequence in the JMA catalog and its influence on the estimation of the ETAS parameters," *Earth, Planets and Space*, Vol. 69, No.1, pp. 1–12.

Zhuang, J., Werner, M. J., and Harte, D. S. [2013] "Stability of earthquake clustering models: Criticality and branching ratios," *Physical Review E - Statistical, Nonlinear, and Soft Matter Physics*, Vol. 88, No.6.

Zhuang, L., Yin, P., and Pang, Y. [2022] "E-Cloud: Efficient seismic fragility assessment of structures based on enhanced cloud analysis," *Earthquake Spectra*, Vol. 00, No.0, pp. 1–23.

Zimos, D. K., Mergos, P. E., and Kappos, A. J. [2015] "Shear Hysteresis Model for Reinforced Concrete Elements Including the Post-Peak Range," *Proceedings of the 5th Thematic Conference on Computational Methods in Structural Dynamics and Earthquake Engineering (COMPDYN 2015)*, Crete Island, Greece.

APPENDICES

APPENDIX A.

A1. ETAS parameter estimation for different auxiliary windows

Table A.1 shows the estimates of the ETAS parameter values for different lengths of the auxiliary window. One can see that there is no significant difference between these sets (the maximum difference is 8%).

Table A.1. Estimated values of ETAS parameters for different lengths of the auxiliary window

ETAS parameter estimates	Region 1			Region 2		
	2 years	5 years	10 years	2 years	5 years	10 years
v	0.92	0.93	0.91	0.945	0.95	0.95
A (events/day/km^2)	0.093	0.093	0.093	0.09	0.09	0.09
c (days)	0.02	0.019	0.019	0.0054	0.0054	0.0051
p	1.18	1.19	1.19	1.08	1.08	1.08
d (km^2)	0.9	0.86	0.849	1.66	1.62	1.62
q	2	2.05	2.16	1.81	1.82	1.89
γ (magnitude^{-1})	0.59	0.6	0.63	0.36	0.36	0.36

A2. Additional Turing-style tests for ETAS simulated catalogs

In addition to the tests presented in Section 2.5, we present here three additional tests where we compare the instrumental HORUS catalogue with the 500 stochastic catalogues simulated with the ETAS model, for the period of 1983-2020, conditioned on the two previous years of seismicity.

10-day seismicity rate

Figure A.1 shows the cumulative fraction of seismicity rates in 10-day windows in the instrumental HORUS catalogue and 500 ETAS-generated synthetic catalogues. Our goal here is not to compare the seismicity rates but rather to compare the distribution of the

quiet (i.e., lower end of the distribution) and active (i.e., higher end of the distribution) periods. To that end, we normalized the seismicity rates with the mean rate. For both considered regions we see good agreement between the ETAS-generated catalogues and observed seismicity given by the HORUS catalogue.

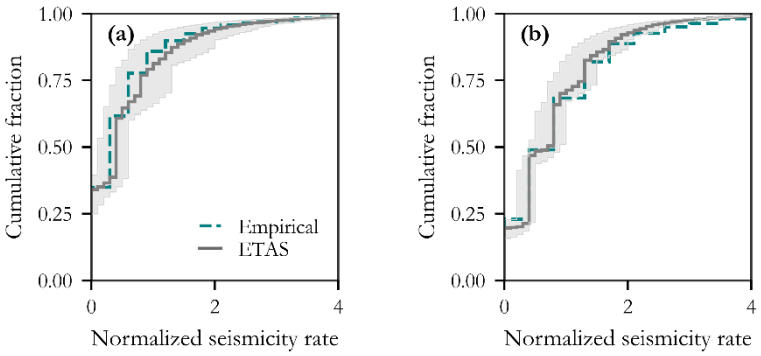

Figure A.1. Cumulative distribution of the normalized seismicity rate ($M_w \geq 3$) for 10-day windows for (a) Region 1 and (b) Region 2. The green dashed line refers to the instrumental HORUS catalogue, the solid grey line to the median of 500 ETAS-generated catalogues, and the shaded area represents the 5th and 95th percentiles of the ETAS simulations.

Spatial distribution

Figure A.2 shows the spatial distribution of $M_w \geq 3.5$ earthquakes for instrumental HORUS and stochastic ETAS catalogs normalized with the total number of events in the considered region. One can observe that, as expected, ETAS-generated maps are more diffuse, but that overall shape looks similar.

To better understand the differences between the ETAS-generated catalogues and HORUS instrumental catalogue, we calculated the 2D interevent distance between every pair of events in each catalogue. Figure A.3 shows the cumulative fraction of events within a certain distance. We can see that the observed events fall within the 5th and 95th percentiles of the 500 stochastic ETAS catalogs. In Region 1, observed events have a steeper slope which indicates more loose spatial clustering, while in Region 2, this slope is lower, i.e., observed events have tighter spatial clustering.

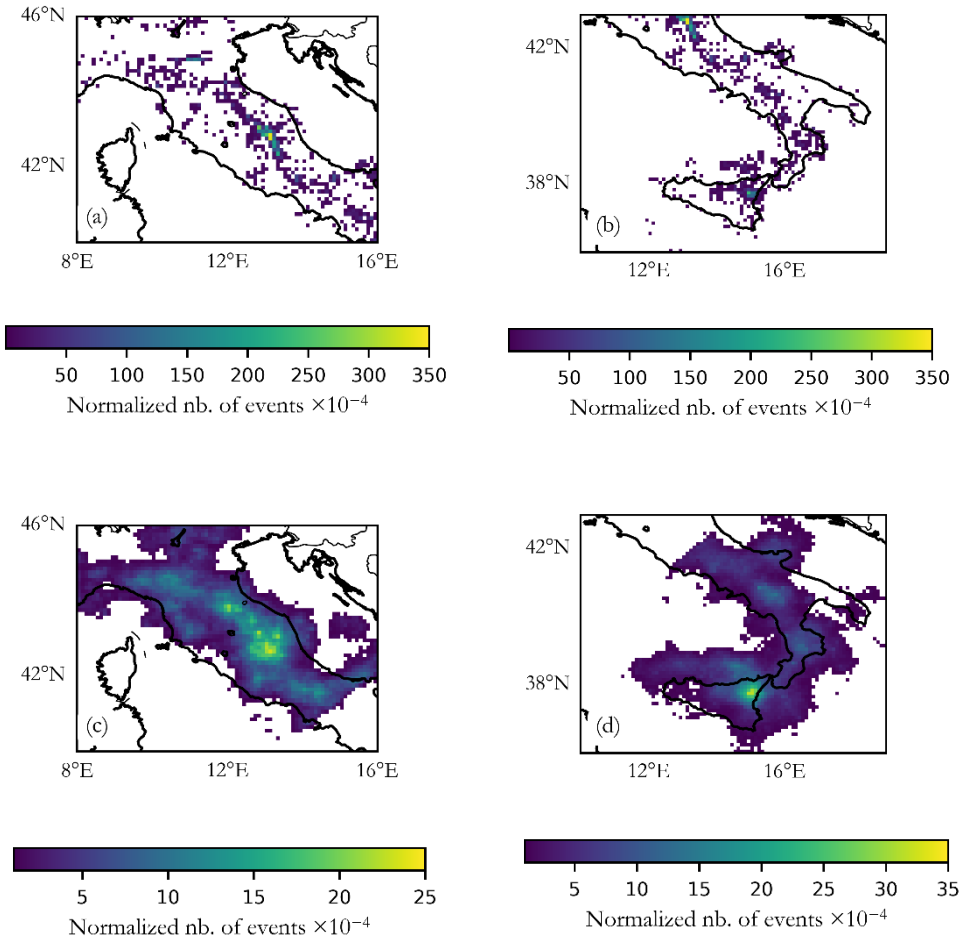

Figure A.2. Number of events with $M_w \geq 3.5$ normalized by the total number of events in the considered region. HORUS instrumental catalogue in (a) Region 1 and (b) Region 2; the median of the 500 ETAS-generated catalogues in (c) Region 1 and (d) Region 2.

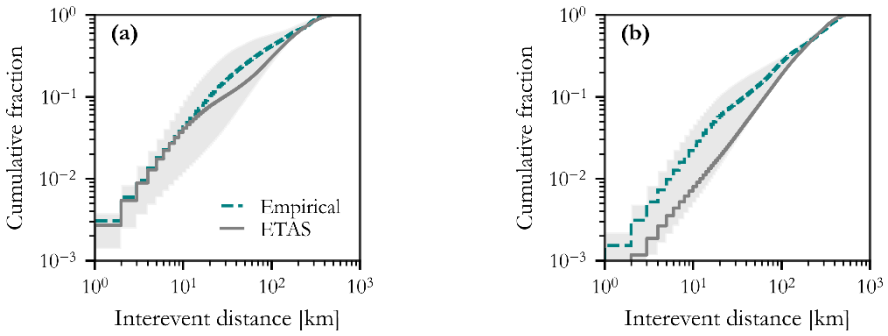

Figure A.3. The fraction of $M_w \geq 3.5$ event pairs within the given interevent distance for (a) Region 1 and (b) Region 2. The green dashed line refers to the instrumental HORUS catalogue, the solid grey line to the median of 500 ETAS-generated catalogues, and the shaded area represents the 5th and 95th percentiles of the ETAS simulations.

Aftershock productivity

In order to compare the aftershock productivity between the HORUS instrumental catalogues and 500 stochastic ETAS-generated catalogues, we first identified the seismic sequences using Gardner and Knopoff [1974] method. We considered only the events with magnitude $M_w \geq 4$. We then counted the number of aftershocks in each identified sequence within different time windows: one day, five days, and ten days after the mainshock event. Even though there is a good agreement between empirical data and ETAS on average, we can see some differences on a sequence-to-sequence basis. Figure A.4 shows more sequence-to-sequence variability in the HORUS catalogue for all time windows considered.

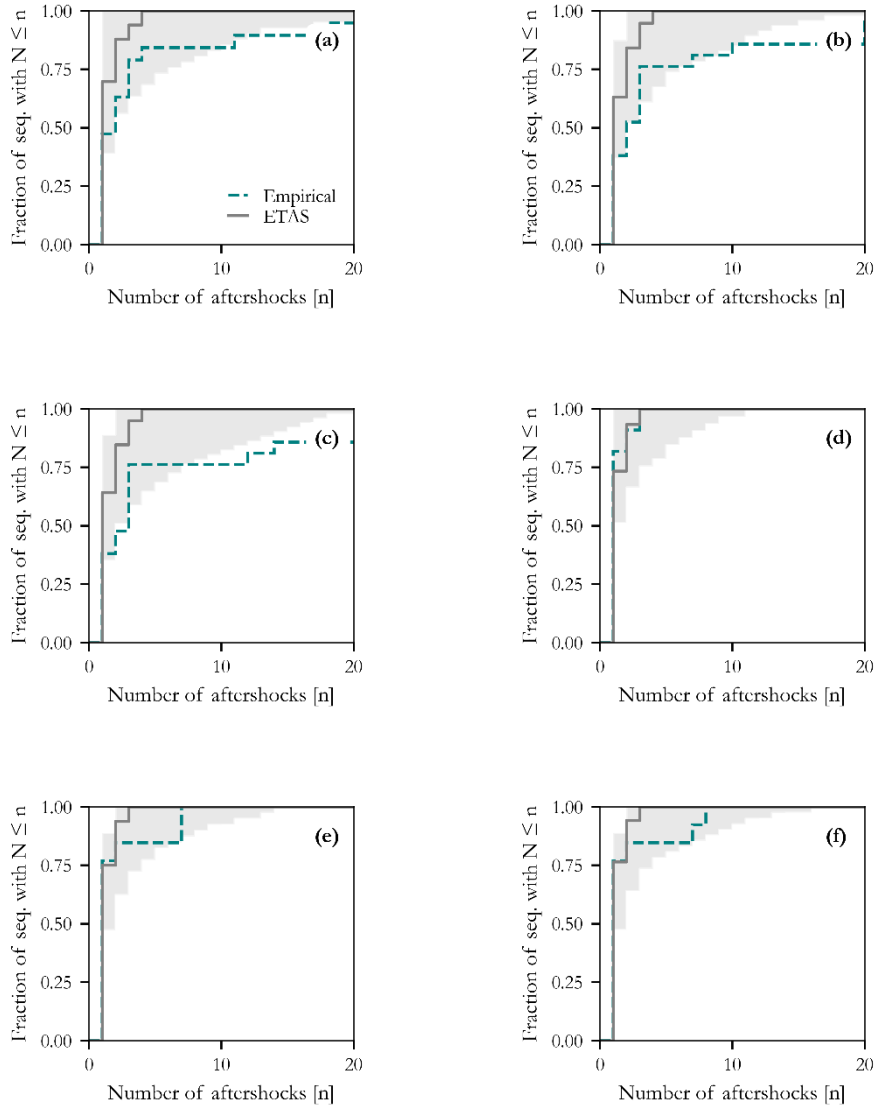

Figure A.4. The fraction of $M_w \geq 4.0$ aftershocks in the identified sequences in Region 1 within (a) one day, (b) five days and (c) ten days after the mainshock event. Results for Region 2 are illustrated in (d), (e) and (f). The green dashed line refers to the instrumental HORUS catalogue, the solid grey line to the median of 500 ETAS-generated catalogues, and the shaded area represents the 5th and 95th percentiles of the ETAS simulations.

A3. Spatial distribution of events in declustered catalogues

Figure A.5 shows the spatial distribution of the entire(non-declustered) catalogue and the distribution of the catalogues declustered with the three different methods, namely Garnder and Knopoff [1974] (GK), Zaliapin et al. [2008] (ZNN) and Reasenberg [1985] (R85). These values are derived by counting the number of events within each grid cell and calculating the median across the 500 simulated catalogs. It is important to note that these values are normalized because our focus is on the spatial distribution rather than the actual rates. One can see that the spatial distribution of the GK-declustered and ZNN-declustered catalogue is very similar, while the R85-declustered catalogue maintains more events in the central part of the considered region (i.e., Region 1).

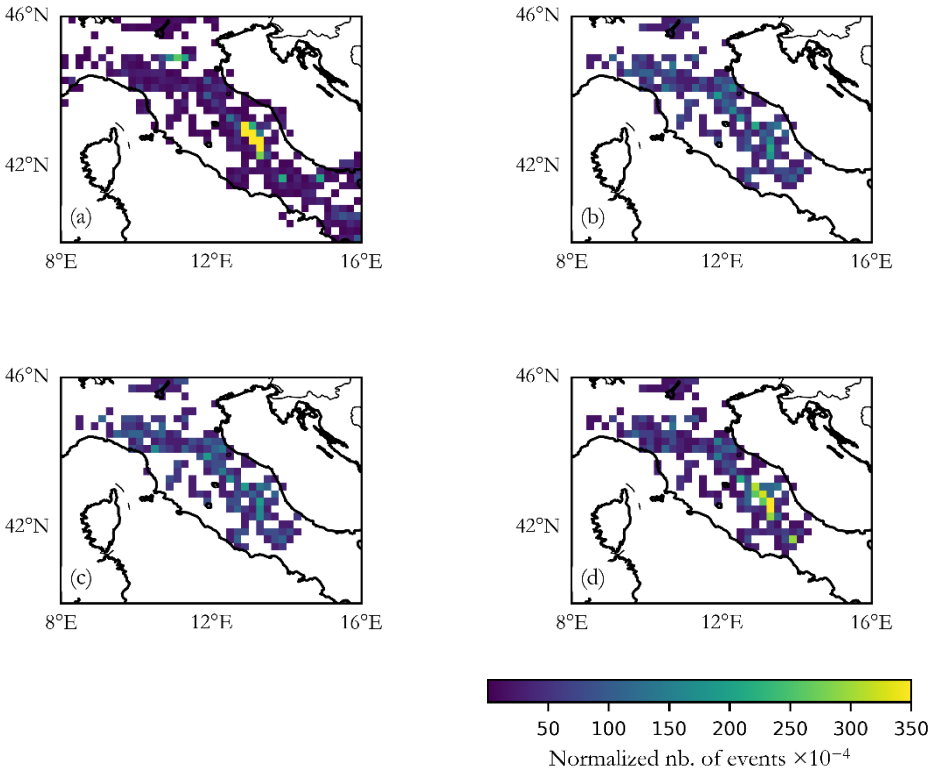

Figure A.5. Number of events with $M_w \geq 3.5$ normalized by the total number of events in the region for (a) non-declustered, (b) GK-declustered, (c) ZNN-declustered and (d) R85-declustered catalogue.

A4. Spatial distribution of events in the Omori and ETAS models

Figure A.6 shows the spatial distribution of events obtained from the 500 ETAS and Omori stochastic catalogues (for different declustering methods). Similar to Figure A.5, we illustrate the normalized number of events. The figures below show that the spatial distribution of the ETAS and Omori-generated events is very similar for GK and ZNN cases, while some differences are observed for the R85 case as more events are kept in the central part of the considered region (i.e., Region 1).

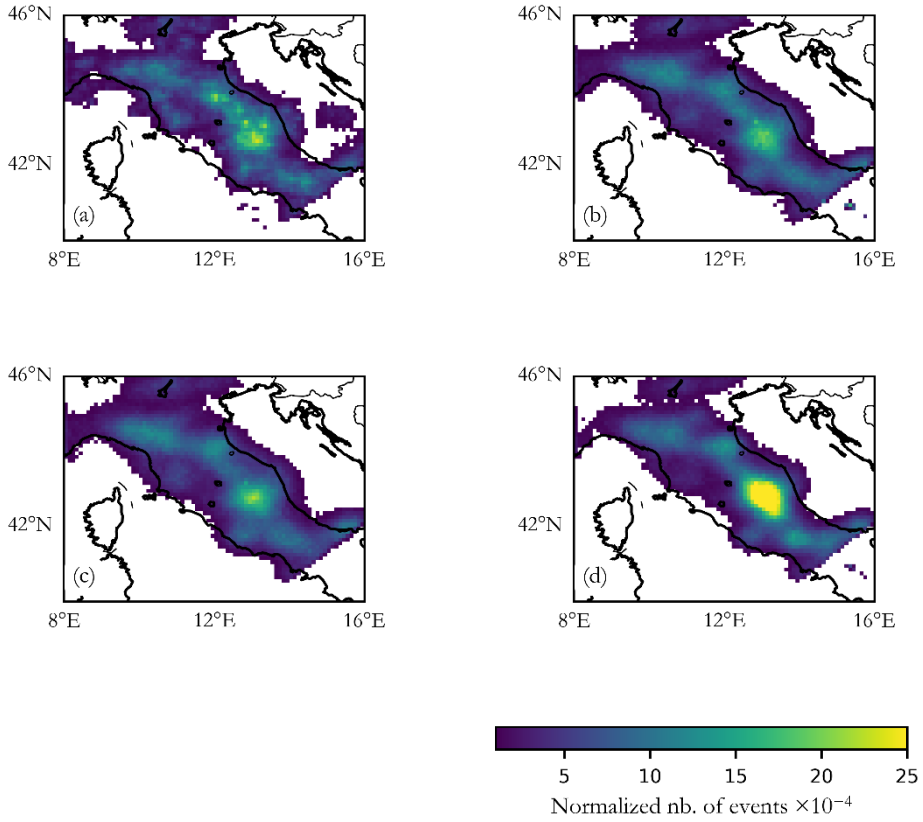

Figure A.6. Number of events with $M_w \geq 3.5$ normalized by the total number of events in the region for (a) ETAS, (b) GK-Omori, (c) ZNN-Omori and (d) R85-Omori models. Median values are illustrated.

APPENDIX B.

B1. Database of RC columns

To compile the experimental test database (referred to as DB in this thesis), we used two primary sources:

a) Data gathered by the ACI committee 369, as described in more detail in Sivaramakrishnan [2010], as the primary source for the database;
b) Database developed for the SERIES research project, described in more detail in Perus et al. [2014];

Both databases extend from the Pacific Earthquake Engineering Research Center (PEER) Structural Database [Berry et al. 2004], supplemented with additional experiments extracted from various published reports. Only rectangular RC columns are included in the database and all specimens are subjected to the pseudo-static cyclic loading. Force-displacement histories within the compiled database were obtained either directly from researchers or digitized from force-displacement plots in source documents.

Given the diverse test configurations of the columns (single cantilever, double-ended, double-curvature), force-displacement histories were standardized to correspond to the cantilever case for consistency. The compiled database includes a total of 370 specimens, with 54 from the SERIES and 316 from the ACI369 database. Of these, 251 columns are flexure-dominated, 36 are shear-dominated, and the remaining 83 are flexure-shear dominated. Each column can be identified by the column name given by the authors who conducted the test or by the test number that we assigned to it. Additionally, for every column, we provide information about the source database (ACI369 or SERIES) and the reference of the source document. Properties available include geometrical and material properties, reinforcing details, test configuration, applied axial load, and other relevant information, as listed and described in more detail in Table B.1. In addition to the properties outlined in Table B.1, two supplementary pieces of information are included: 'Comments,' offering additional insights into the experiments if necessary, and 'Data quality,' indicating the reliability of available data. Instances where results from sectional analysis significantly diverged from experimental data led to the categorization of data as unreliable. In some cases, columns were excluded due to inconsistencies between the provided force-displacement data and the results in reference papers.

Furthermore, as explained in Section 4.2, we extracted the values corresponding to the characteristic points on the force-displacement curve, such as the cracking point, yielding point, capping point, and point where ultimate displacement is reached. In addition to the values extracted from the data, we provide the values reported by the authors of the experiments or extracted from source documents, where available. A description of these parameters is given in Table B.2.

Table B.1. Description of the properties available in the compiled database.

Configuration	1 for single cantilever, 2 for double-ended, and 3 for double-curvature	E_c	modulus of elasticity of concrete, calculated as $4700\sqrt{f_c}$ [MPa] (ACI 318-08), where not given
Failure	1 for flexure, 2 for shear, and 3 for a flexure-shear mode of failure. For the definition of the failures, see Berry and Eberhard (2003)	f_{yl}, f_{ul}	yield and ultimate stress of longitudinal reinforcement
P-delta	effect of axial load on force-displacement data, see Berry and Eberhard (2003) for details	f_{yt}, f_{ut}	yield and ultimate stress of transverse reinforcement
h, b, d	height, width, and effective depth of the cross-section, calculated as the distance between the most compressive fiber of concrete to the center of gravity of tensile reinforcement	d_{bl}, d_{bt}	diameter of longitudinal and transverse reinforcement
c	concrete cover of the cross-section	N_b	total number of longitudinal bars
L, L_{top}, L_{bot}	L is the shear span of the specimen, while L_{top}, L_{bot} are as explained in Berry and Eberhard [2003]	n_{bw}, n_{bh}	number of bars between the corner bars along the width and height of the cross-section
L_{mea}	elevation at which lateral column displacement was measured	s	spacing of transverse reinforcement
a/d	aspect ratio	ρ_l, ρ_t	longitudinal and transverse reinforcement ratio
P, ν	applied axial load and axial force ratio calculated as: $\frac{P}{A_g f_c'}$	ω	volumetric transverse reinforcement ratio, calculated as the ratio of transverse reinforcement volume and the volume of concrete
f_c, f_r	compressive strength (at 28 days) and modulus of rupture of concrete. The latter is calculated as $0.622\sqrt{f_c}$ [MPa] (ACI 318-08), where not given	$N_{v,pp}$, $N_{v,pl}$	number of transverse shear bars in cross-section perpendicular and parallel to the load

Table B.2. Description of the parameters extracted from the available data

d_{cr}	displacement at the cracking point, found using sectional analysis	d_{scr}	displacement at the shear cracking
F_y, d_y	force and displacement at the yielding point	d_{lsy}	displacement at the longitudinal steel yielding
d_{cap}	displacement corresponding to the maximum force	$d_{w,scr}$	displacement at the widening of the shear cracking
F_{max}	maximum force extracted from the available force-displacement data (refers to the data where P-delta effects are removed)	$d_{on,spall}$	displacement at the onset of concrete spalling
d_u	maximum displacement recorded during the experiment	$d_{sig,spall}$	displacement at the significant concrete spalling
$F_{max,bas}$	maximum force calculated following Haselton et al. [2007]	d_{buckl}	displacement at the point of bar buckling
d_{fcr}	displacement at the flexural cracking	d_{fract}	displacement at the fracture of the longitudinal bar
d_{lcr}	displacement at the longitudinal cracking	d_{ax}	displacement at the axial capacity loss

The assembled database is available for download at: NevenaSipcic (Nevena) (github.com). On this link, one can find four *.pkl data files, one with the properties of the columns, one with the extracted values of the characteristic points, one with the reported values of the characteristic points (where available), and finally one with the force-displacement data for each experiment.

B2. Shake table tests used for DI validation

Table B.3 shows the estimated values of DI and maximum drift(Δ) for the 23 shake-table tests that were used for validation. All considered columns fail in flexure-shear mode so the values reported in the table correspond to the damage states as defined in Table 4.4 and Table 4.5, for DI and maximum drift, respectively. DI is calculated using Equation (4.10) and β value of 0.15. In the case of DI for DS1 obtained values are very small positive values so, to simplify, we report them here as 0.01 in all cases. More details about these experiments can be found in Li [2012].

Table B.3. Shake table tests used for validation with the estimated values of DI and maximum drift Δ (in %), for the three damage states. B and H are the width and height of the column's cross-section.

Test	Specimen name	B[mm]xH[mm]	DI1	DI2	DI3	Δ1	Δ2	Δ3
1	NCREE-2009- HCFS-B1	200x200	0.01	0.35	1.07	1.2	1.73	2.74
2	NCREE-2009-HCFS-C1	200x200	0.01	0.47	1.02	1.5	2.58	4.1
3	NCREE-2009-MCFS-A1	200x200	0.01	0.26	0.98	1.0	2.02	3.6
4	NCREE-2009-MCFS-B1	200x200	0.01	0.98	1.02	0.8	2.15	2.28
5	NCREE-2009-MCFS-C1	200x200	0.01	0.94	1.04	1.0	2.15	2.5
6	NCREE-2007-S1-C1	250x250	0.01	0.20	0.95	1.5	2.46	6.28
7	NCREE-2007-S1-C2	250x250	0.01	0.28	1.08	0.7	1.43	3.35
8	NCREE-2005-P2-C1	150x150	0.01	0.4	1.04	1.0	2.77	4.98
9	NCREE-2005-P2-C2	150x150	0.01	0.26	0.95	1.0	2.66	4.98
10	NCREE-2005-L-C1	150x150	0.01	0.32	0.85	1.0	3.64	8.48
11	NCREE-2005-L-C2	150x150	0.01	0.2	0.74	1.0	2.74	8.5
12	Shin 2005-II-1W	152.5x152.5	0.01	0.16	0.76	1.12	2.26	4.26
13	Shin 2005-II-2W	152.5x152.5	0.01	0.25	0.65	1.3	2.79	4.88
14	Shin 2005-II-7W	152.5x152.5	0.01	0.30	0.64	1.23	2.52	3.4
15	Shin 2005-II-8W	152.5x152.5	0.01	0.17	0.49	1.3	2.15	3.63
16	Shin 2005-III-4E	152.5x152.5	0.01	0.35	0.83	1.8	2.63	3.83
17	Shin 2005-III-4W	152.5x152.5	0.01	0.18	0.82	1.13	2.03	3.83
18	Shin 2005-III-6E	152.5x152.5	0.01	0.01	0.69	1.2	1.75	3.35
19	Shin 2005-III-6W	152.5x152.5	0.01	0.3	0.67	1.18	2.73	4.28
20	Shin 2005-III-10E	152.5x152.5	0.01	0.15	0.87	1.21	1.85	3.16
21	Shin 2005-III-10W	152.5x152.5	0.01	0.23	0.86	1.2	1.81	2.48
22	Elwood 2002-S1	230x230	0.01	0.23	1.05	1.0	2.35	6.07
23	Elwood 2002-S2	230x230	0.01	0.24	0.95	1.0	1.58	3.82

B3. MODIMKPeakOriented02 material model: OpenSees parameters

Table B.4 shows the parameters used to define the *MODIMKPeakOriented02* material model and the calculation of these parameters in our particular case.

Table B.4. OpenSees parameters and equations used to define *MODIMKPeakOriented02* material model

Parameter	Description	Calculation
$*matTag*	Integer tag identifying material	integer
$*K0*	Elastic stiffness	M_y / θ_y
$*as_Plus*	Strain hardening ratio for positive loading direction.	$(M_c / M_y - 1) \cdot \theta_y / \theta_{pc}$
$*as_Neg*	Strain hardening ratio for negative loading direction.	$(M_c / M_y - 1) \cdot \theta_y / \theta_{pc}$
$*My_Plus*	Yield moment for positive loading direction.	Sectional analysis
$*My_Neg*	Yield moment for negative loading direction.	Sectional analysis
$*Lamda_S*	Cyclic degradation parameter for strength degradation.	$\theta_y \cdot \lambda$
$*Lamda_C*	Cyclic degradation parameter for post-capping stiffness degradation.	$\theta_y \cdot \lambda$
$*Lamda_K*	Cyclic degradation parameter for reloading stiffness degradation.	$\theta_y \cdot \lambda$
$*Lamda_A*	Cyclic degradation parameter for unloading stiffness degradation.	$\theta_y \cdot \lambda$
$*c_S*	Rate of strength degradation.	1.0
$*c_C*	Rate of post-capping stiffness degradation.	1.0
$*c_K*	Rate of reloading stiffness degradation.	1.0
$*c_A*	Rate of unloading stiffness degradation.	1.0
$*theta_p_Plus*	Pre-capping rotation for positive loading direction.	$\theta_{c,pl}$
$*theta_p_Neg*	Pre-capping rotation for negative loading direction.	$\theta_{c,pl}$
$*theta_pc_Plus*	Post-capping rotation in the positive direction.	θ_{pc}
$*theta_pc_Neg*	Post-capping rotation in the negative direction.	θ_{pc}
$*Res_Pos*	Residual strength ratio for positive loading direction.	0
$*Res_Neg*	Residual strength ratio for negative loading direction.	0
$*theta_u_Plus*	Ultimate rotation capacity for positive loading direction.	$\theta_y + \theta_{c,pl} + \theta_{pc}$
$*theta_u_Neg*	Ultimate rotation capacity for negative loading direction.	$\theta_y + \theta_{c,pl} + \theta_{pc}$
$*D_Plus*	Rate of cyclic deterioration in the positive loading direction. For symmetric hysteretic response use 1.0.	1.0
$*D_Neg*	Rate of cyclic deterioration in the negative loading direction. For symmetric hysteretic response use 1.0.	1.0
$*nFactor*	Elastic stiffness amplification factor	10

APPENDIX C.

C1. Disaggregation results for Perugia

Table C.1. shows the results of the seismic hazard disaggregation in terms of the mean magnitude M and distance R for the site of Perugia. Analyses are performed using OpenQuake software, a magnitude bin width of 0.5 and a distance bin width of 10km. Results for ten intensity levels corresponding to Table 5.1 are shown, for six different conditioning IMs.

Table C.1. The mean magnitude and distance (in km) for Perugia, obtained from seismic hazard disaggregation, for ten intensity levels (IMLs). Results for six different IMs are shown.

	Magnitude (M)						Distance (R[km])					
IML	**Sa (0.2)**	**Sa (0.5)**	**Sa (1.0)**	**Sa (1.5)**	**Sa (2.0)**	**AvgSa (0.2-2)**	**Sa (0.2)**	**Sa (0.5)**	**Sa (1.0)**	**Sa (1.5)**	**Sa (2.0)**	**AvgSa (0.2-2)**
1	5.8	6.0	6.2	6.2	6.3	6.2	24.0	31.4	40.3	45.7	50.0	37.8
2	5.9	6.1	6.3	6.3	6.4	6.3	20.9	27.0	34.5	39.2	43.2	31.9
3	6.1	6.3	6.4	6.5	6.5	6.4	17.5	22.0	27.8	31.6	35.0	25.1
4	6.3	6.5	6.6	6.6	6.7	6.6	11.9	14.0	17.2	19.3	21.5	15.0
5	6.5	6.6	6.7	6.7	6.8	6.7	9.3	10.6	12.7	14.0	15.5	10.9
6	6.6	6.7	6.7	6.8	6.8	6.8	7.0	7.6	8.8	9.5	10.4	7.6
7	6.7	6.7	6.8	6.8	6.9	6.8	6.6	7.0	8.0	8.6	9.3	7.0
8	6.7	6.8	6.8	6.8	6.9	6.9	6.0	6.4	7.2	7.6	8.1	6.3
9	6.8	6.8	6.8	6.9	6.9	6.9	5.6	5.8	6.4	6.7	7.0	5.8
10	6.8	6.9	6.9	6.9	7.0	7.0	5.2	5.2	5.5	5.6	5.8	5.2

C2. Distribution of IMs for IM*=Sa(0.5s) and IM*=Sa(1.5s)

Figure C.1 compares the metrics of the distributions of the IMs using box plots, for the three conditioning periods of 0.5 and 1.5 s. In these figures, the boundaries of each box correspond to the lower and upper quartiles, the line within the box corresponds to the median and the whiskers extend to the minimum and maximum observed values.

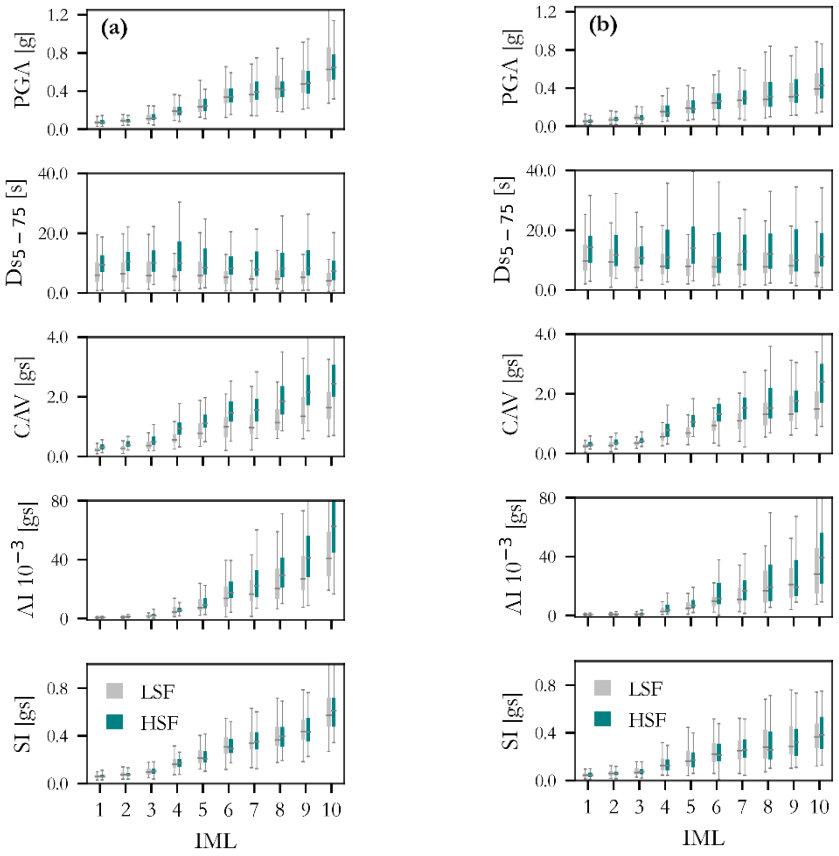

Figure C.1. Metrics of the distributions of the different IMs: PGA, Ds_{5-75}, CAV, AI, and SI from the first to the last row, respectively. Results for the sets of records selected using the IM*=(a) Sa(0.5s), (b) Sa(1.5s).

C3. Structural response estimates: additional results

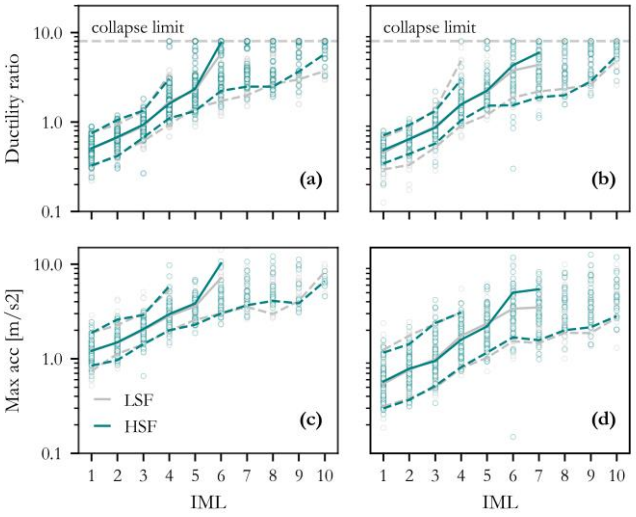

Figure C.2. Response estimates showing the data points, the median and 5th and 95th percentiles of the data in terms of ductility ratio (a, b), and maximum relative acceleration (c, d). Results for the SDOF with T_1 of 0.5 s(a and c) and 1.5 s(b and d) are illustrated. These results pertain to SDOFs with pinching material model.

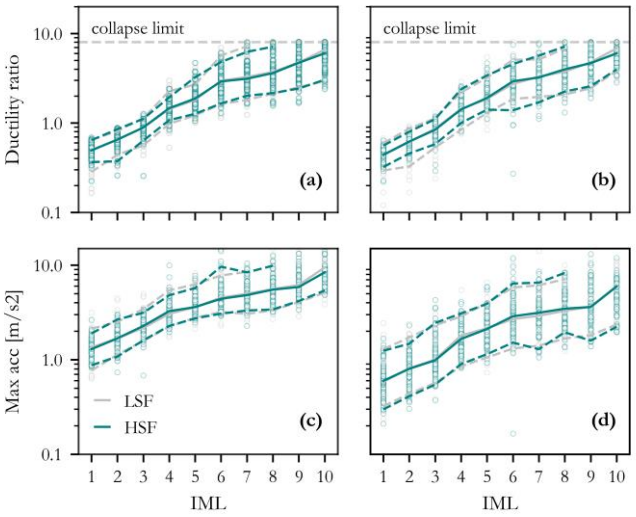

Figure C.3. Response estimates showing the data points, the median and 5th and 95th percentiles of the data in terms of ductility ratio (a, b), and maximum relative acceleration (c, d). Results for the SDOF with T_1 of 0.5 s(a and c) and 1.5 s(b and d) are illustrated. These results pertain to SDOFs with elastic with hardening material model.

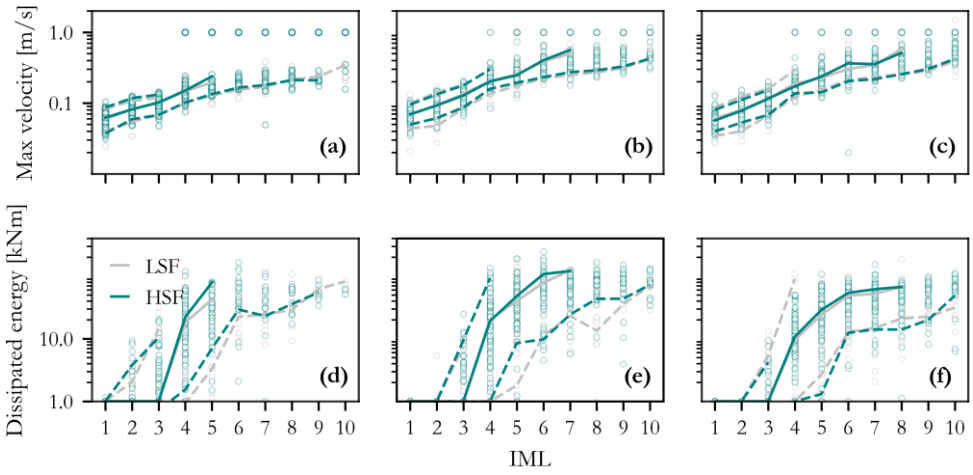

Figure C.4. Response estimates obtained from MSA showing the data points, the median and 5th and 95th percentiles of the data in terms of maximum velocity (a, b, c), and dissipated energy (d, e, f). Results for the SDOF with T_1 of 0.2s(a and d), 1.0s(b and e) and 2.0(c and f) are illustrated. These results pertain to SDOFs with pinching material model.

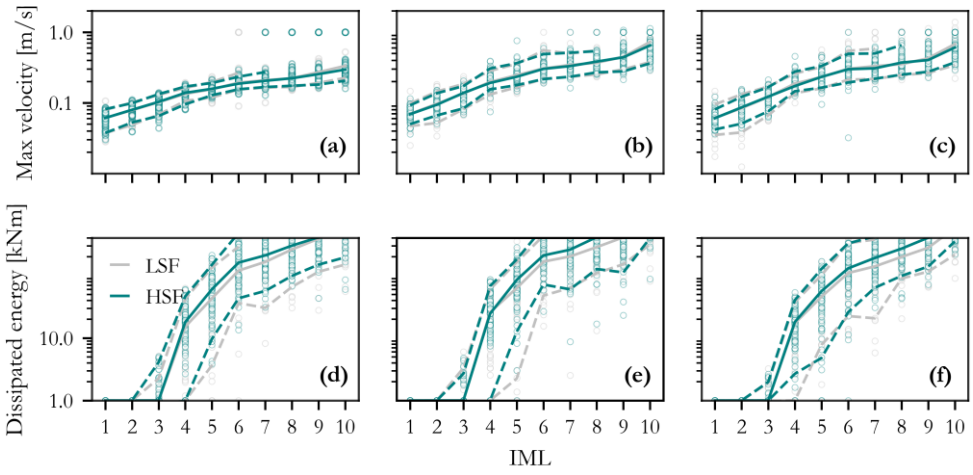

Figure C.5. Response estimates obtained from MSA showing the data points, the median (solid line) and 5th and 95th percentiles (dashed lines) of the data in terms of maximum velocity (a, b, c), and dissipated energy (d, e, f) based on the LSF and HSF sets of ground motions. Results for the SDOF with T_1 of 0.2s(a and d), 1.0s(b and e) and 2.0(c and f) are illustrated. These results pertain to SDOFs with elastic with hardening material model.

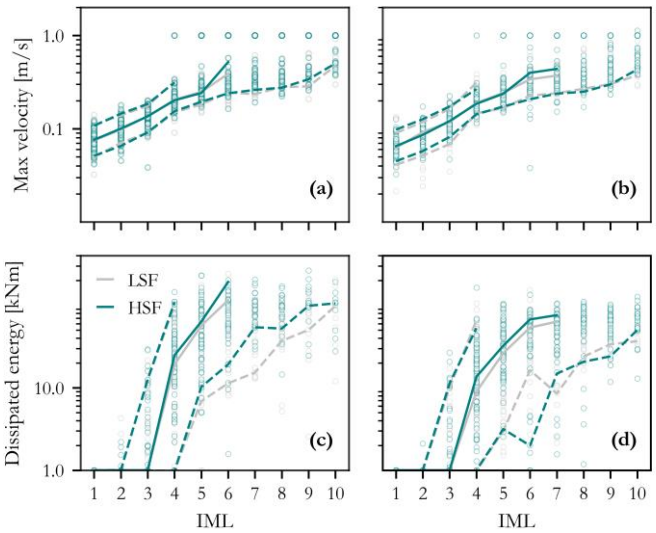

Figure C.6. Response estimates obtained from MSA showing the data points, the median and 5th and 95th percentiles of the data in terms of maximum velocity (a, b), and dissipated energy (c, d). Results for the SDOF with T_1 of 0.5s(a and c) and 1.5 s(b and d) are illustrated. These results pertain to SDOFs with pinching material model.

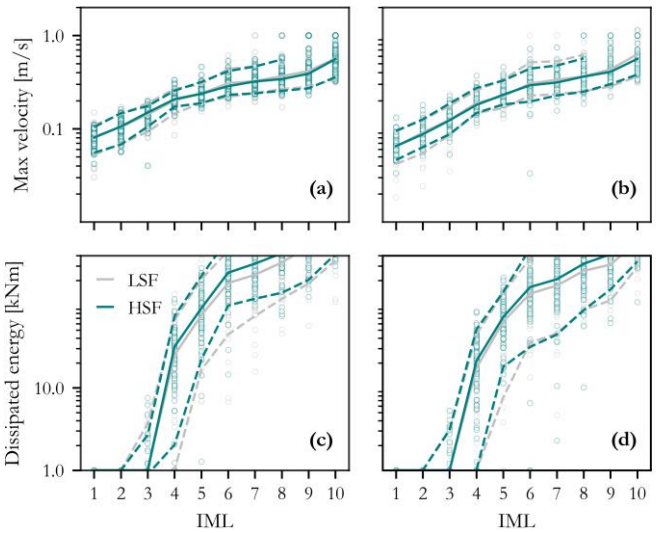

Figure C.7. Response estimates obtained from MSA showing the data points, the median and 5th and 95th percentiles of the data in terms of maximum velocity (a, b), and dissipated energy (c, d). Results for the SDOF with T_1 of 0.5s(a and c) and 1.5s(b and d) are illustrated. These results pertain to SDOFs with elastic with hardening material model.